UNIVERSITY OF SOUTHAMPTON

FACULTY OF ENGINEERING AND THE ENVIRONMENT

Institute of Sound and Vibration Research

Development and analysis of switchable hydromounts for engine mounting

by

Judith Katharine Picken

Thesis for the degree of Doctor of Philosophy

December 2018

UNIVERSITY OF SOUTHAMPTON

ABSTRACT

FACULTY OF ENGINEERING AND THE ENVIRONMENT

Institute of Sound and Vibration Research

Doctor of Philosophy

DEVELOPMENT AND ANALYSIS OF SWITCHABLE HYDROMOUNTS FOR ENGINE MOUNTING

Judith Katharine Picken

Hydromounts are a type of passive engine mount that offer advantages over simple rubber mounts. Hydromounts are tuned to the resonance frequency of the engine on its mounts, providing increased damping. The aim of the current work is to investigate a method for implementing a two-state hydromount and develop a model to describe it. A quarter car model is first used to consider different damping strategies for an engine mounting. Measurements were carried out on a proprietary hydromount and the results were compared to a model with linear and non-linear forms, and the sensitivity of the model to changes in the parameters was studied. The model was optimised using particle swarm optimisation, giving an improved fit, particularly at higher amplitudes. The main mismatch was found at the resonance peak. The hydromount model was then adapted to include a second inertia track and compared with experimental data. Ultimately a good agreement was found and this could be used in designing two inertia track systems. A theoretical analysis of the compliance of an annular diaphragm is presented, and used to aid in the estimation of the compliance of the chambers of the mount along with equi-biaxial inflation of circular rubber diaphragms. For the system studied there was a large variation in calculated compliance with the changes in chamber pressure. Inclusion of the hydromount model in the quarter car model suggested that it is important to have high damping over a large bandwidth to control the behaviour around the resonance.

Experimental work carried out on an adaptive system showed that altering the upper chamber volumetric compliance of a hydromount and controlling a second tuned frequency via a second inertia track could both be successful strategies for implementing a two state mount. A switching mechanism was also developed that relies on the use of a magnetorheological fluid. This versatile solution would potentially allow both retrofitting into existing devices and use in applications other than engine mounts.

Contents

List of Tables

List of Figures

UNIVERSITY OF Southampton

Academic Thesis: Declaration Of Authorship

I, Judith Katharine Picken

declare that this thesis and the work presented in it are my own and has been generated by me as the result of my own original research.

Development and analysis of switchable hydromounts for engine mounting

I confirm that:

1. This work was done wholly or mainly while in candidature for a research degree at this University;
2. Where any part of this thesis has previously been submitted for a degree or any other qualification at this University or any other institution, this has been clearly stated;
3. Where I have consulted the published work of others, this is always clearly attributed;
4. Where I have quoted from the work of others, the source is always given. With the exception of such quotations, this thesis is entirely my own work;
5. I have acknowledged all main sources of help;
6. Where the thesis is based on work done by myself jointly with others, I have made clear exactly what was done by others and what I have contributed myself;
7. Parts of this work have been published as:
   Picken Judith*, Thompson David, Daley Stephen, Dynamic response of two-state hydromounts with twin inertia tracks, *International Congress on Sound and Vibration 24, ICSV24*, London, 2017.

Signed: .....

Date: .....

Acknowledgements

I would like to thank for his support and advice throughout my candidature Professor David Thompson, as my main supervisor and the advice of co-supervisors Professor Mike Brennan and Professor Stephen Daley. I would like to thank my employer the Tun Abdul Razak Research Centre and the Malaysian Rubber Board for providing the resources and support during my candidature. Thanks goes to my colleagues who have also provided support and advice and in some cases practical assistance and in particular Hamid Ahmadi, Alan Harris, Ian Stephens and Julia Gough. Also my thanks are due to Luigi Borrelli who helped with some of the practicals reported within this thesis.

I would also like to thank my partner, David Lowe for his support and proof-reading, my son Matthew for providing plenty of distraction and untimely infections and the as yet unknown one for providing further distractions whilst writing up.

Definitions and Abbreviations

Symbols

A_{d}	Area of the decoupler diaphragm
A_{i}	Cross-sectional area of the inertia track
A_{r}	Effective pumping area of the rubber spring
b_{r}	Damping of the rubber spring
C_1	Compliance of the first chamber
C_2	Compliance of the second chamber
C_3	Compliance of the third chamber
c_1	Damping of car suspension
c_2	Damping of engine mount
C_{dec}	Compliance of the decoupler
C_{d}	Coefficient of discharge (sharp edge orifice formula)
c_{ground}	Damping for groundhook damper
c_{sky}	Damping for skyhook damper
d_{i}	Hydraulic diameter of the inertia track
E	Engine speed
f	Frequency
F_{in}	Force produced by vibration of engine
G	Shear modulus

G'	In-phase shear modulus
G''	Out-of-phase shear modulus
I_{i}	Inertance of the inertia track
I_{i3}	Inertance of the second inertia track
K'	In-phase dynamic stiffness (real part)
K''	Out-of-phase dynamic stiffness (imaginary part)
k_1	Stiffness of car suspension
k_2	Stiffness of engine mount
k_{r}	Stiffness of the rubber spring
l_{i}	Length of the inertia track
m_1	Mass of chassis
m_2	Mass of engine
p	Pressure
p_1	Pressure of the first chamber
p_2	Pressure of the second chamber
p_3	Pressure in the third chamber
p_{atm}	Atmospheric pressure
q_{i}	Flow rate through the inertia track
q_{T}	Flow rate entering the compliant region
q_{i3}	Flow rate through the second inertia track
R^2	Coefficient of determination
R_1	Resistance to volumetric expansion
R_{i}	Resistance to flow through the inertia track
R_{i3}	Resistance to flow through the second inertia track

V	Volume
X	Amplitude of harmonic oscillation
X_1	Amplitude of motion of chassis
x_1	Displacement of chassis
X_2	Amplitude of motion of mounted engine
x_2	Displacement of mounted engine
$X_{2\mathrm{f}}$	Amplitude of displacement of mounted engine from engine-forced vibration
$x_{2\mathrm{f}}$	Displacement of mounted engine from engine-forced vibration
X_{in}	Amplitude of motion of external input
Δp_{12}	Difference in pressure between the first and second chambers
Δ_{d}	Free travel gap of the decoupler
η	Loss factor
η_2	Loss factor due to hysteretic damping in engine mount
μ	Dynamic viscosity of the fluid
ω	Circular frequency of motion of external input
ω_1	Natural frequency of chassis on suspension
ω_2	Natural frequency of mounted engine
ω_{a}	First resonance frequency of quarter car model
ω_{b}	Second resonance frequency of quarter car model
ρ	Density of the fluid
ζ	Damping ratio
ζ_1	Damping ratio for car suspension
ζ_2	Damping ratio of engine mount
ζ_{ground}	Damping ratio for groundhook damper

ζ_{sky}	Damping ratio for skyhook damper

Abbreviations

ECE	Electrically controllable elastomer
ER	Electrorheological
ERF	Electrorheological fluid
FEA	Finite element analysis
LMS	Least mean squares
MCE	Magnetically controllable elastomer
MR	Magnetorheological
MRF	Magnetorheological fluid
NR	Natural rubber
PSO	Particle swarm optimisation
SMA	Shape memory alloy

Chapter 1

Introduction

1.1 Background

An important trend in the automotive industry is for reducing weight to improve fuel efficiency. However, reducing the weight can lead to adverse effects for interior noise, which can also be an important consideration when purchasing a vehicle. There are many sources of noise within a vehicle, but an important one is the engine. The transmission of engine vibrations is mitigated by the use of engine mounts. This work is focussed on engine mountings for internal combustion engines.

An engine mount has three main functions: the first is to support the weight of the engine; the second is to ensure the engine moves with the body of the car when running over rough ground and cornering; and the third is to isolate the vehicle from the engine vibration.

Vibrational excitation of the engine comes from two sources, giving rise to two distinct frequency ranges of engine vibration. The lower frequency range (less than approximately 30 Hz) is often associated with large amplitude and caused by road or wheel input. At higher frequencies (30-200 Hz) the vibration is usually of smaller amplitude, and is caused by the engine out-of-balance forces and the combustion process.

The out-of-balance forces in an internal combustion engine are dependent on the engine speed. The number and the arrangement of cylinders give rise to different

orders being important. For example, in an in-line four cylinder engine the main disturbing force is at twice the engine speed (typically 50 to 130 Hz for engine speeds of 1500 to 4000 rev/min). The main direction of the excitation forces is usually in the vertical direction, and the natural frequency of the mounted engine is tuned to be in the region of 8-12 Hz, to keep it well below the main frequency range of the engine out-of-balance forces. However, this is the range of the wheel input, giving rise to "engine shake", which is the large amplitude vibration at the natural frequency of the engine on its mounts. At idling frequencies there can be significant engine vibration at approximately 30 Hz (twice an engine speed of 900 rev/min), and if the vehicle is stationary there are no other sources of noise or vibration so the disturbance from the engine is more noticeable.

To isolate the vibration caused by the engine-unbalanced disturbances, low elastic stiffness and low damping are needed as the frequency range is high compared to the natural frequency. On the other hand, low damping could cause problems around the resonance frequency, so high damping is preferred to control this. At low frequencies for road input, the ideal mount would be rigid, so the engine moves with the chassis of the car.

Hydromounts are a commonly used type of passive mount that offer improvements in properties over simple rubber mounts, particularly for the low frequency input around the resonance frequency. They are tuned to the resonance frequency of the engine on its mounts. This gives rise to a stiffness change and high damping. The high damping is useful to control the response at the resonance, and the mount acts as a tuned mass damper. The change in stiffness can lead to higher stiffness than desired for the small amplitude higher frequency engine vibration, so decouplers can be used to mitigate this.

As cars become more computerised and "smarter", more complex mounting systems can be included that use smart materials or actuators to allow their properties to be altered in response to the current driving conditions. Depending on how they are used they are termed adaptive, semi-active or active mounting systems. Adaptive mounts typically have an alterable parameter that can be switched on and off or varied to give improved performance under different operating conditions. This can be done either by mechanical means or by the use of smart materials.

Active mounts can require high power inputs, a separate fail-safe system and can

also be significantly more expensive than the alternatives. Semi-active mounts are used as a compromise, avoiding the complexity of the fully active system, whilst providing some of the benefits.

1.2 Scope of this thesis

This thesis explores passive hydromounts and twin track adaptive mounts. In Chapter 2 the current literature is reviewed, starting with smart materials suitable for application to adaptive and active mounts. The literature on hydromounts is then reviewed with a focus on modelling. Adaptive and active engine-mounting systems are also considered. From the review of the literature, the detailed aims and objectives of the thesis are elaborated.

In Chapter 3 a quarter car model, which consists of half the engine sitting on the suspension (and the wheel) of a quarter of the car, is created. Different theoretical strategies for isolating the car engine are considered. Vibration inputs from the base (wheels) and the engine are considered separately. The mount is modelled as a spring with a damper, and various types of damping models and damping strategies are considered.

In Chapter 4 an existing hydromount model, with linear and non-linear forms, is optimised for a proprietary mount, which has been experimentally tested. A study of the effect of the parameters in the model is carried out. To give an improved fit to the measured data, the model is optimised using particle swarm optimisation which is exploited to consider further potential non-linearities in the model.

Experimental work to investigate potential methods for providing a two-state mount is described in Chapter 5. This also introduces a switching mechanism. Smart materials are used in this chapter: specifically a magnetically controllable elastomer (MCE) and a magnetorheological fluid (MRF), to allow the behaviour of the adaptive mount to be controlled using a magnet.

Chapter 6 further considers an adaptive mount with two inertia tracks. The hydromount model from Chapter 4 is expanded to include the second inertia track, and the compliances of the top and bottom chambers are considered theoretically.

Finally in Chapter 7, the model for the hydromount and the two inertia track mount are introduced into the quarter car model considered earlier, to show the effect of these mounting systems on a vehicle.

Conclusions and recommendations for further work are summarised in Chapter 8.

1.3 Contributions

There are several parts of this thesis which form original contributions to the existing body of work.

1. Simple rubber mounts have been considered with frequency dependent complex stiffness in a quarter car model, to give a more realistic model of the performance of rubber mounts as compared to a purely hysteretic model.

2. An existing non-linear hydromount model was applied to a proprietary hydromount and the parameter selection was optimised using particle swarm optimisation, allowing a simultaneous optimisation to occur across many variables.

3. Experimental work examines potential methods of controlling the first chamber compliance of a hydromount and switching on and off a second inertia track, using magnetically active smart materials. A switching mechanism that works for both systems was developed.

4. Theory on equi-biaxial extension of rubber has been applied to calculate the volumetric compliance of diaphragms within the mount. This theory was extended to annular diaphragms.

5. A model for a hydromount with two inertia tracks and a third chamber is proposed with some non-linearities considered.

6. The two inertia track model has been included into the quarter car model to demonstrate the benefits of these mounts.

Chapter 2

Literature Review

This chapter examines the current literature. Initially smart materials are considered as these are commonly adaptive and active engine mounts. Hydromounts are reviewed as a passive engine mounting system, before adaptive, semi-active and active systems are considered. This chapter ends with the aims and objectives of this thesis.

2.1 Smart materials

This section considers some materials used in adaptive and active hydromounts, and serves as a background to the literature review on the mounts themselves.

Adaptive and active engine mountings frequently rely on smart materials to give the change in properties that are desired. In this work a magnetorheological fluid is used as part of the switch in the adaptive two inertia track mount considered and solutions involving a magnetically controllable elastomer were considered. The description of smart materials that follows may aid the understanding of the adaptive mounts discussed later in Section 2.3.

Smart materials are materials that have one or more properties that can be significantly altered in a controlled fashion by external stimuli. In the case of smart fluids the most commonly changed property is the viscosity, in solids it is the dimensions. Some examples of currently available smart materials are:

- Controllable fluids:
  - Magnetorheological fluids (MRFs) - viscosity alters with magnetic field
  - Electrorheological fluids (ERFs) - viscosity alters with electric field.
- Piezoelectric materials - produce a voltage when stress is applied and vice versa.
- Electrostrictive materials - shape alters with electric field.
- Magnetostrictive materials - shape alters with magnetic field.
- Magnetically controllable elastomers (MCEs) - modulus and damping alters with magnetic field.
- Electrically controllable elastomers (ECEs) - modulus and damping alters with electric field
- Polymer gels - volume alters with applied field or conditions (absorb liquid).
- Conducting polymers - bend with electrical or chemical energy.
- Shape memory alloys (SMAs) and polymers - shape alters at various temperatures.
- Colour-changing and light-emitting materials. It is unlikely that these have a potential application in engine mounts.

In the field of engine mountings, the piezoelectric effect is mainly used in actuators in active mounts.The electrostrictive effect is much smaller, less linear and more sensitive to external factors (eg temperature) than the piezoelectric effect[1,2]. This means that it is less commonly used. Magnetostriction, the magnetic equivalent of electrostriction, is also quite a small effect even for so-called "giant magnetostriction"[3] which means that its use in an engine mounting application is limited. SMAs tend to be temperature dependent[4] which means use under an engine is complicated by the range of temperatures they would have to face. Although MCEs and ECEs could potentially be used in mounts, the effect tends to be greatest at very small amplitudes[5,6]. The MRFs and ERFs are considered in more detail below.

2.1.1 Controllable fluids

In the 1940s the first patents and papers describing controllable fluids and potential applications were published. Willis Winslow had the first ERF patent[7] and paper[8] describing the ER effect. MRFs were developed by Jacob Rabinow at the US National Bureau of Standards[9,10].

Table 2.1 shows some of the differences between the properties of MRFs and ERFs.

	MRF	**ERF**
Max. Yield Stress	50 to 100 kPa	2 to 5 kPa
Max. Field	∼250 kA/m (limited by saturation)	∼4 kV/mm (limited by breakdown)
Viscosity (η)	0.1 to 1.0 Pa s	0.1 to 1.0 Pa s
Temp. Range	−40 to +150 °C (limited by carrier fluid)	+10 to +90 °C (ionic, DC) −25 to +125 °C (non-ionic, AC)
Stability	Unaffected by most impurities	Cannot tolerate impurities
Density	3 to 4 g/cm^3	1 to 2 g/cm^3
Power Supply	2 to 25 V @ 1 to 2 A (2-50 W)	2 to 5 kV @ 1 to 10 mA (2-50 W)

Table 2.1: Some differences between MRFs and ERFs. Table adapted with additional data, from Carlson et al.[11]

There are three main operational modes for devices using these fluids (see Figure 2.1)[11,12]:

- Pressure-driven flow mode. This has fixed poles and the fluid is forced to flow between them.
- Direct shear mode. The poles move relative to each other but at a fixed distance apart.
- Squeeze-flow or film mode. The poles move towards each other forcing the fluid out from the gap between them.

Applications of these fluids may use one or sometimes multiple modes simultaneously.

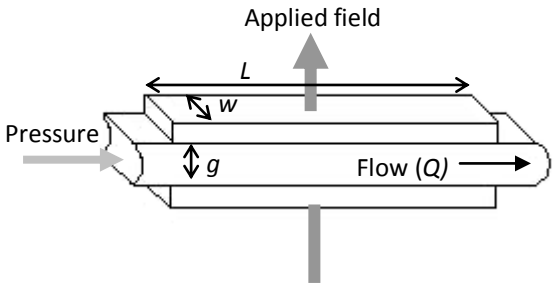

(a) Pressure driven flow mode

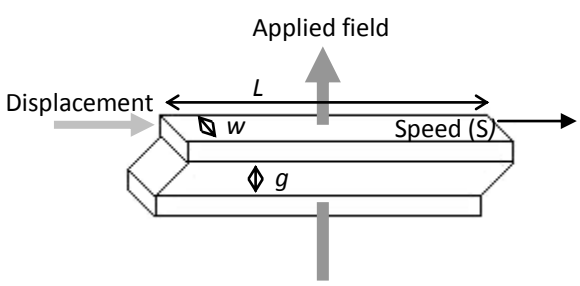

(b) Direct shear mode

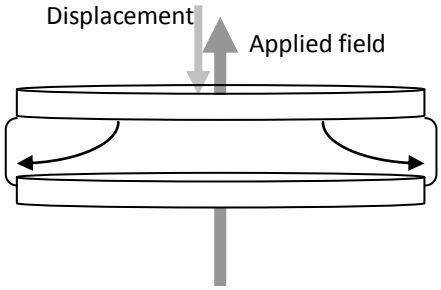

(c) Squeeze-flow mode

Figure 2.1: Operational modes of controllable fluids

Colloids are a mixture of a dispersed phase spread evenly through a continuous medium which can be in the same or different states. At least one dimension of the dispersed phase should be mesoscopic (in the nanometre region). They should be (kinetically) stable[13]. MRFs and ERFs are not colloids, although some mistakenly refer to them as such. Some of the chemistry important for the stability of colloids is also applicable to improve the stability of the fluids. These sorts of controllable fluids will settle over time due to the micrometre size of the particles and in some cases their high density compared with the fluid.

There are many models for describing the rheological behaviour of MRFs and ERFs; a discussion of many of these and their relation to different types of viscometer is provided by Choi et al.[14]. It is typically found that in the off-state the fluids exhibit Newtonian behaviour, but in the on-state they behave like Bingham fluids with a yield stress associated with them.

Magnetorheological fluids

There are two sorts of fluid that respond to a magnetic field:

- Ferrofluids are composed of nanoscale magnetic particles suspended in a carrier fluid[15]. The random movement of the particles is larger than the force pulling them together, as they are smaller than a magnetic domain. Although there are numerous applications for this class of fluid, these fluids do not have a controllable parameter suitable for an adaptive mount.

- The term MRF refers to liquids that solidify in the presence of a magnetic field. An MRF typically consists of 1-10 μm multi-domain particles, made up of a soft ferromagnetic material, which are suspended in a non-magnetic fluid[16]. Some literature confusingly refers to MRFs as ferrofluids, in this work the distinction made here will be kept.

In an MRF, the magnetorheological effect is produced by the ordering of suspended particles into linear chains parallel to the applied magnetic field due to magnetic polarisation of the particles[17]. The presence of these chains greatly restricts the flow of the fluid, increasing the viscosity of the suspension. To overcome this effect and reattain a low viscosity state requires the application of a force greater than the yield stress of the MRF, which is dependent on the strength of the applied magnetic field.

Although MRFs initially show an approximately linear response to the strength of the applied field, sufficiently high field strengths will cause saturation as the particles reach their maximum polarisation. Complete saturation is normally achieved with field strengths in excess of $0.4/\mu_0$ A/m (where $\mu_0 = 4\pi \times 10^-7$, the permeability of free space), when the intrinsic induction (also known as the polarisation density) of the MRF is ϕJ_s, (where ϕ is the volume percent of particles in the fluid and J_s is the saturation polarization of the particulate material)[17]. To quote an example given in the literature[12], a fluid that contains 30% iron by volume (J_s=2.1 T) will be saturated at a flux density of about (0.3)(2.1)=0.63 T. The response to the application and withdrawal of the magnetic field is highly reversible, with very little hysteresis observed.

While high yield strength and non-settling particles are frequently considered the most desirable features for an MRF, these particular features are not necessarily the most critical properties[18]. Provided the settled particles do not form a hard sediment, the suspension can usually be quickly redispersed by the normal motion of the device in use. Therefore, it is sufficient for most applications to have an MRF that soft settles, i.e. redisperses easily, and trying to make it stable may

actually degrade characteristics such as off-state viscosity. An exception to this is found in applications where the device will be inactive for long periods and the behaviour of the first few cycles is critical. Here fluid stability issues will be very important, and so MRFs for these applications are often formulated as thixotropic gels.

However, nanowires being incorporated into the fluid in the place of the spherical particles can improve the tendency of the ferromagnetic particles to settle. The length remains similar in size to the spheres, but the diameter of the wire is in the order of 100 nm[19]. Due to the reduction in volume (and therefore weight) the rate of settling is significantly improved.

Although it is necessary for an MRF to have a high yield stress, it is also important that it possesses a low off-state viscosity, particularly for applications such as "sky-hook" damping[18]. The off-state viscosity is influenced by many factors, including[17]:

- temperature;
- the magnitude and orientation of any residual applied field;
- the concentration and density of particles;
- the particle size and shape distribution;
- the properties of the carrier fluid;
- any additional additives, such as dispersing agents, in the suspension.

Genç[20] carried out a study into stability, redispersibility and factors affecting on and off-state behaviour. It was found that even small remnant magnetism in the particles, can cause agglomeration and increase the off-state viscosity. This means that careful choice has to be put into the material of the particles. The off-state measurements demonstrated that the fluid was in fact non-Newtonian and underwent shear-thinning.

It is in the nature of MRFs that they will gradually degrade over time, at a rate that depends on both the intrinsic properties of the MRF and the application for which it is used. One common problem is 'In Use Thickening', where the off-state viscosity increases as the MRF is subjected to long term stresses[18]. The

cause is believed to be abrasion of the magnetic particles, causing fragments to flake off into the suspension. These fragments are expected to be highly shaped and will have a very high surface area to volume ratio, and so will produce a relatively large effect of the rheology of the suspension. The particles will also abrade any other surfaces that are exposed to the MRF, which may also lead to reduced device functionality. Zhang et al.[21] looked at the effect of particle size on wear. The larger particles showed more deterioration in the properties considered (shear stress, sedimentation stability and off-state viscosity). They also examined the particles with a scanning electron microscope and found that some of the particles were visibly worn, i.e. no longer spherical.

Electrorheological fluids

ERFs are suspensions of conductive particles in a carrier fluids. The change in viscosity is proportional to the applied potential. Most of the points mentioned under MRFs are true for ERFs too.

Stanway et al.[22] looked at the squeeze-flow mode of operation of ERFs with a view to applications in vibration isolation. They designed and tested a damper under a mass. They found they were able to reduce the resonance magnification from 12 to 2.5. By switching the field off at higher frequencies (above this resonance) good vibration isolation is achieved.

Hong et al.[23] suggested an interesting proposition to incorporate piezoelectric ceramics into a ER damper. A displacement applied to piezoelectric materials gives rise to an electric voltage. This voltage is used to generate the electric field to control the ERF. This means that the size of the electric field will be proportional to the applied displacement. This also means it is self-powered. They found the vibration suppression was good at low frequencies and large vibration amplitudes, but the high frequency performance was not as good.

ERFs are less desirable for the present application than MRFs, refer to Table 2.1. The comparatively high voltages required make these fluids less attractive than MRFs. The intolerance to impurities is another disadvantage. However, there are examples of people using ERFs in mounts, see Section 2.3.

2.1.2 Smart rubbers

Magnetically controllable elastomers

MCEs are solid analogues of MRFs. However, MCEs work in the pre-yield region. They consist of magnetisable particles within an elastomer matrix. On the application of a magnetic field, the modulus of the rubber can increase by up to 60%[24] due to the interactions between the particles and the field. One of the advantages over MRFs is that the particles do not settle under gravity.

Their response is quicker than that of MRFs as the particles do not need to move and MCEs remove the problems with sedimentation and aggregation present in MRFs. However, the increase in modulus is small compared with the change in viscosity of MRFs and the largest effects are seen at low shear strain, of about 1-2%[25] .

MCEs can be cured in a magnetic field, which causes them to align, or without which causes the particles to be isotropic. Ahmadi et al.[6] looked at this effect using double shear test pieces, cured and tested with and without magnets. The elastomer matrix was natural rubber (NR). They found that curing in the presence of a magnetic field produced a much stiffer compound than otherwise, even without testing under a magnetic field (the ratio of the shear moduli at 0.17% strain cured with magnetic field to cured without magnetic field was 3.3), and the loss angle was also increased (from 10° to 15°). Curing in the magnetic field increased the non-linearity as measured by the ratio of the shear modulus at 0.17% shear strain to 5% shear strain. They found that at high (5%) shear strains curing the compound in a magnetic field did not lead to a greater rise in the shear modulus of the MCE when a magnetic field is applied to the component, but at very small strain there is an advantage to curing in a magnetic field. The rise in shear modulus with the application of a magnetic field under testing at high strains was modest (a ratio of tested with to tested without of approximately 1.3 at all frequencies for samples both cured with and without a magnetic field). They concluded that MCEs are best suited to applications where the strain in the rubber is very small, as this region demonstrates the greatest change in modulus upon application of a magnetic field. Curing the rubber in the presence of a magnetic field produces a larger difference in the modulus between the with and without field testing conditions at low strains. However, for high shear strains curing the compound under a magnetic field does not lead to greatly improved

behaviour over that cured without a magnetic field. Pre-straining the rubber reduces the size of the magnetic field dependent behaviour. This reduction is more significant when the compound is cured within the magnetic field. These results suggest that for applications where the dynamic strains are not very small the benefits from curing the rubber in a magnetic field may not be significant.

The work of Blom and Kari[26–28] concentrated on the use of MCEs in the audible frequency region. They claimed increases in modulus of up to 115% at 0.0084% strain for NR and silicone rubber based MCEs in the frequency range from 100 to 1000 Hz. The rubbers they used have a 33% loading of water-atomised, irregularly shaped, randomly distributed iron particles. They also then used the rubbers as torsionally and axially excited isolators to improve the performance of the isolator. They concluded that it has a great potential in the audible frequency range to reduce transmitted noise by quickly and reversibly shifting the resonance frequencies of the system. This can be used to help with internal resonances or wave effects of the material as well. It is difficult to say what the improvement of changing the internal resonances is, because the greatly increased mass of the elastomer will bring the internal resonances to lower frequencies, and the paper does not compare a rubber without the iron filler to establish this effect, so the benefits may not be as great as stated.

Lokander and Sternberg[29,30] found that large irregularly shaped particles created a large MR effect (due to the comparatively low critical particle volume concentration), and argued that poorly dispersed carbonyl iron particles would behave similarly due to the resemblance of clumps of the material to large irregular particles. Although it was not investigated in their work, it is likely that the large and irregular particle shapes will have a detrimental effect on the long term durability of the elastomer. They also found that the choice of elastomer matrix (experimenting with nitrile rubber with varying acrylonitrile content and a butadiene-natural rubber mix) had little effect on the MR effect. On the other hand, plasticisers improved the effect. The increase in damping they considered so small as to be of little practical use. They found that the MR effect was double in isotropic MCEs compared with the comparable anisotropic MCE. This is surprising and contradicts some of the other work reviewed in this section, although all the increases were modest compared with the claims of other papers. They found that there was an optimum filler concentration for the isotropic rubber dependent on the size and shape of the particle and based on the critical particle volume concentration, but above this although the modulus increased,

the percentage increase was much diminished due to the higher starting modulus.

Guan et al.[31] explored the magnetostrictive effect of MCEs. They used carbonyl iron in a matrix of silicone rubber. They found that magnetostriction increases with the volume fraction of iron. The highest effect was observed when the particles were aligned perpendicular to the field (183 ppm) and the lowest when they where orientated parallel to the applied field (56 ppm). The magnetostriction tended to saturate at a magnetic field of 400 kA/m and this saturation magnetostriction was higher than the magnetostriction of carbonyl iron alone (which the authors quote as 10 ppm). They also found some magnetostriction would remain after longer tests, meaning that there was an increase in the set.

There are a number of papers considering the theory and the modelling of the material[26,32–38]. From one of these computational studies[32] it was found that the optimum volume fraction of iron particles would be 27%, although there was no validation by experimental results.

There are so many different potential elastomer matrices and types and quantities of iron particles it is not surprising that the size of the effect observed varies so much between the papers. Also the strain and frequency regimes examined vary quite a lot between the papers, also making comparisons hard.

Electrically controllable elastomers

These are very similar in principle to the MCEs, but rely on electric fields to change the properties which can mean comparatively high voltages. Unlike with MCEs the electric current flow through the material due to the electric field needs to be considered[39]. This is an important consideration not just for power consumption but also for heat build-up and material degradation. This was investigated using a material consisting of conductive carbonaceous particles and silicone rubber (which is an electrical insulator) for which the mechanical properties had been previously investigated[5]. The ER effect was very dependent on the volume fraction of particles, with the higher volume fractions showing the largest effects, so because of the large effect a volume fraction of 50% was chosen for the majority of the work. As for MCEs the effect diminishes as the strain increases. Also it was shown that for materials with a higher zero-field modulus the percentage increase was reduced. Increasing the electric field strength from 0

to 2.0 kV/mm resulted in an increasing ER effect. However, despite the advantage to the ER effect of the low modulus rubbers it was found that these rubbers drew the largest current, so there is a compromise between maximising the ER effect and minimising the power consumption.

Unlike MCEs it is possible to get a response out of the material using a dielectric polymer with no filler. The effect of the application of an electric field on a number of different dielectric polymers was studied by Ludeelerd et al.[40]. At 1kV/mm the rise in the modulus has not saturated, although they did not take the electric field higher. The poly(acrylate) copolymer AR70 showed the largest ER effect (232%) when the percentage increase was considered (as opposed to absolute increase). For small additions of polypyrrole particles (up to 5% by volume) with no external electric field the modulus increases linearly. However, as they disrupt the dipole interactions with a field the increase is non-linear with the particle increase.

Polyisoprene (it is unclear whether NR or synthetic *cis*-1,4-polyisoprene is used- as it is sourced from Aldrich it is likely to be synthetic, but it has been implied that it is synonymous with natural rubber[41]) and polythiophene/polyisoprene blends have been examined by Puvanatvattana et al.[42]. They looked at the effect of cross-linking on the ER effect (they used a peroxide cure system and a 1% strain amplitude). They found that polyisoprene behaved like an electrostrictive polymer (i.e. there was a quadratic relationship between the response and the applied electric field). Cross-linking increases the stiffness of NR, so unsurprisingly they found that the largest modulus was for the highest cross-link ratio (7) under an electric field, but the largest ER effect was for the elastomer with the lowest cross-link ratio (the optimum ratio was found to be 3) where an ER effect of up to 60% was observed. As the cross link ratio of 3 had the largest effect this was chosen to look at the effect of the addition of polythiophene. The largest effect (an increase of 110%) was obtained for 20% by weight of polythiophene.

Modelling has been carried out by Liu et al.[43]. Shiga et al.[44] also considered the theory behind the behaviour.

There is even more variety in the literature for ECEs than for MCEs because dielectric polymers can have an effect without the need for particles and there are many more variations of particles that are used due to the large number of materials that are at least partially electrically conductive, unlike the restrictions

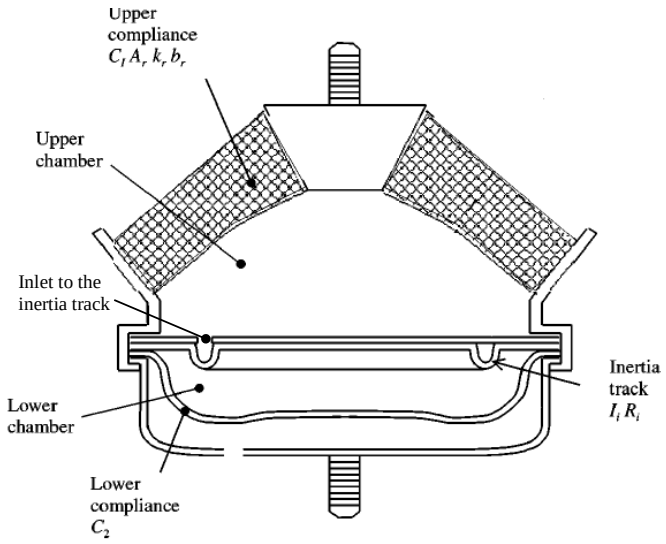

Figure 2.2: Diagram of a hydromount adapted from Geisberger et al. [46]

of ferromagnetic materials that are chosen for MCEs.

2.2 Passive hydromounts

Frequently in the literature and in this thesis, K' and K'' are used to describe dynamic stiffness. They are the real and imaginary parts respectively of the dynamic stiffness. K' is the elastic part of the stiffness, referred to as in-phase stiffness, and K'' is the loss part of the stiffness, referred to as out-of-phase stiffness.

$$K* = K' + jK'' \tag{2.1}$$

A hydromount is a passive mount that consists of a rubber spring and two fluid-filled chambers. The chambers are connected by an inertia track, which allows the fluid to flow between the chambers (Figure 2.2). It exploits a Helmholtz resonance to provide a tuned mass damping system[45].

A Helmholtz resonator consists of a fluidic mass subjected to a restoring force, undergoing periodic motion. In a hydromount, the oscillating column of fluid in the inertia track provides the inertance for the fluid resonator. The restoring force is governed by the stiffness of the primary rubber element.

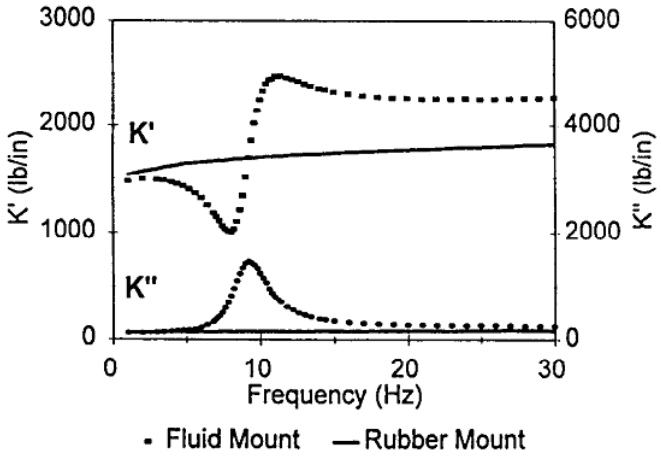

Figure 2.3: Behaviour of a hydromount with and without fluid[47]

The inertia track is a channel, usually circular or a spiral, through which the liquid has to travel between the two chambers; adjusting the length and diameter of the track allows the resonance frequency of the mount to be tuned. The lengths can be of the order of 100 to 200 mm and the diameter in the order of 10 mm. Typically the compliance of the first chamber governs the resonance frequency of the engine on the mounts. The stiffness behaviour of a typical hydromount with and without fluid can be seen in Figure 2.3[47].

The important characteristics are the stiffness and damping at the resonance frequency of the engine on its mounts, with the latter needing to be sufficiently high to control the response, and the high frequency stiffness and damping, both of which are desirable to be low to provide good isolation.

There have been many studies of hydromounts that demonstrate the improvements they produce in both ride comfort and noise levels[48–51]. Brach and Haddow[52] discuss the sources of engine vibration and therefore the requirements for a hydromount.

The dip in the dynamic stiffness is tuned to the resonance of the engine in the vertical direction, so ideally a mount would have the minimum in the stiffness as close to 0 $\mathrm{N.m^{-1}}$ as possible and the peak to be as low as possible. Although there are improvements in the damping and stiffness around the resonance frequency of the mount, the high frequency stiffness is usually larger than the equivalent elastomeric mount. To improve the high frequency performance, decouplers can be incorporated, as the higher frequency engine vibration is normally small. For small amplitude vibration a decoupled hydromount behaves like a rubber spring,

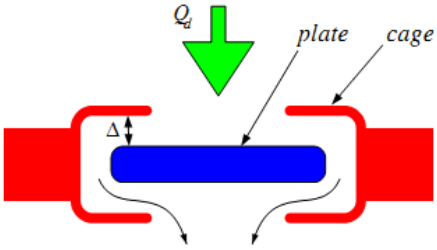

Figure 2.4: Diagram of a free type decoupler[54]

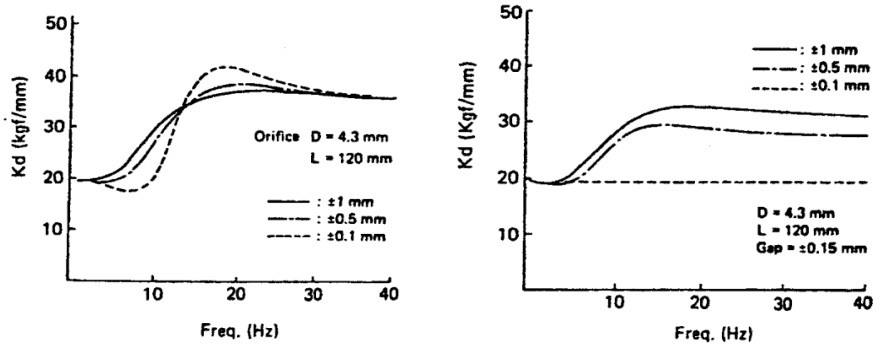

(a) inertia track dimensions given (b) decoupler dimensions given

Figure 2.5: Dynamic stiffness of a hydromount at different amplitudes (a) without decoupler and (b) with decoupler[55]

as the inertia track is bypassed[53].

There are two sorts of decoupler: fixed and free. A fixed decoupler consists of a rubber diaphragm separating the two chambers; it is able to accommodate small amplitude oscillations without forcing the fluid through the inertia track. The fraction of displaced fluid accommodated is dependent upon the compliance, C_{dec}. A free decoupler consists of a hole bypassing the inertia track linking the two chambers, with a diaphragm in it. This diaphragm is able to move a limited distance up and down before sealing the hole and forcing the fluid through the inertia track (see Figure 2.4). The fraction of displaced fluid accommodated is dependent upon the diaphragm area, A_d and free travel gap, Δ_d. The dynamic stiffness of a mount with and without a decoupler can be seen in Figure 2.5 (a) and (b).

The effects of inertia track parameters (cross-sectional area and length) and top chamber stiffness have been investigated by Lee et al.[56] and by Singh et al.[57]

Different types of hydraulic mount systems have been modelled from one-degree-of-freedom to multi-degree-of-freedom systems, and as linear and non-linear

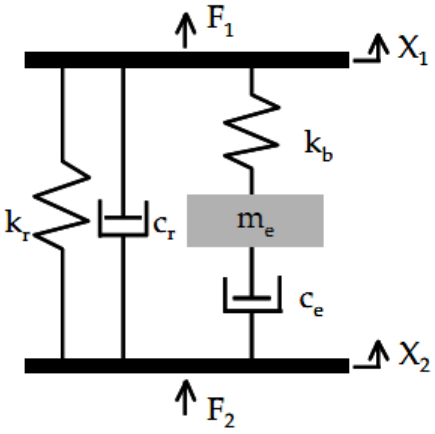

Figure 2.6: Mechanical model for hydromount[66]

systems[48,49,56–62]. A detailed discussion of hydraulic mount modelling is given by Flower[63]. To design a mount with the desired stiffness, genetic neural networks have been employed[64,65]. This method does not rely on an understanding of the mechanics of the hydromount, unlike the modelling. Instead, by using the experimental results of a number of different mount configurations, an optimum design configuration or predictions of the behaviour under different inputs can be obtained.

A purely mechanical model for a hydromount (see Figure 2.6) has been shown by Lee et al.[66] not to take into account the symmetry of the actual component. This is represented by the following four-pole stiffness matrix:

$$\begin{pmatrix} F_1 \\ F_2 \end{pmatrix} = \overbrace{\begin{pmatrix} k_{11} & k_{12} \\ k_{21} & k_{22} \end{pmatrix}}^{\text{four pole stiffness matrix}} \begin{pmatrix} x_1 \\ x_2 \end{pmatrix} \tag{2.2}$$

All the components of the four pole stiffness matrix should be equal but in the mechanical model this is not true. In fact only k_{11} agrees with the experimental behaviour of the mount (see Figure 2.7).

Singh et al.[57] proposed a hydro-mechanical model for hydromounts:

$$K(i\omega) = \frac{-i\alpha_3^3 - \alpha_2\omega^2 + i\alpha_1\omega + \alpha_0}{-\beta_2\omega^2 + i\beta_1\omega + \beta_0} \tag{2.3}$$

where $\alpha_3 = b_\mathrm{r}C_1C_2R_\mathrm{d}I_\mathrm{i}$, $\alpha_2 = C_1C_2R_\mathrm{d}(b_\mathrm{r}R_\mathrm{i} + k_\mathrm{r}I_\mathrm{i}) + b_\mathrm{r}I_\mathrm{i}(C_1 + C_2) + A_\mathrm{r}^2C_2R_\mathrm{d}I_\mathrm{i}$,

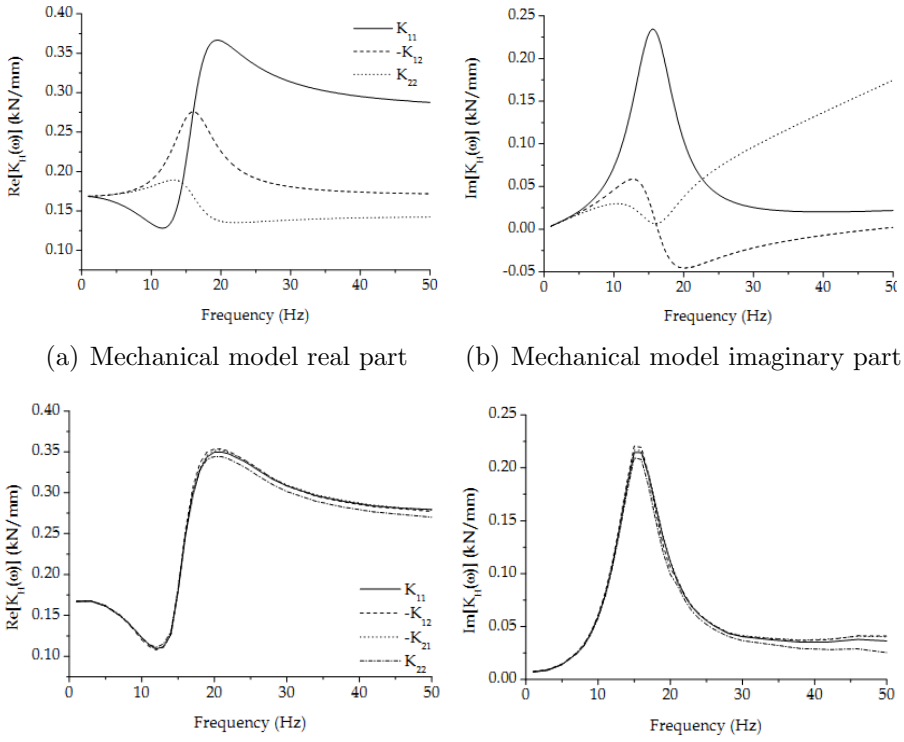

(a) Mechanical model real part (b) Mechanical model imaginary part

(c) Hydromount real part (d) Hydromount imaginary part

Figure 2.7: Four-pole stiffness of mechanical model and hydromount[66]

$\alpha_1 = b_\mathrm{r}(R_\mathrm{i}+R_\mathrm{d})(C_1+C_2)+k_\mathrm{r}C_1C_2R_\mathrm{d}R_\mathrm{i}+k_\mathrm{r}I_\mathrm{i}(C_1+C_2)+A_\mathrm{r}^2I_\mathrm{i}+A_\mathrm{r}^2C_2R_\mathrm{d}R_\mathrm{i}$, $\alpha_0 = k_\mathrm{r}(R_\mathrm{i}+R_\mathrm{d})(C_1+C_2)+A_\mathrm{r}^2(R_\mathrm{i}+R_\mathrm{d})$, $\beta_2 = C_1C_2R_\mathrm{d}I_\mathrm{i}$, $\beta_1 = C_1C_2R_\mathrm{d}R_\mathrm{i}+I_\mathrm{i}(C_1+C_2)$ and $\beta_0 = (R_\mathrm{i}+R_\mathrm{d})(C_1+C_2)$.

The parameters of the model, which can be seen in Figure 2.8, are the stiffness of the rubber spring, k_r; the damping of the rubber spring, b_r; the pumping area of the rubber spring A_r; the volumetric compliance of the first chamber, C_1; the compliance of the second chamber, C_2; the resistance to flow through the inertia track, R_i; and the inertance in the inertia track, I_i. The last two parameters are dependent on the fluid properties, such as viscosity, and the inertia track dimensions.

A number of assumptions are made when modelling a hydromount[67], including:

- Fluid inertia in upper and lower chambers are negligible;
- Pressure fields in upper and lower chambers are hydrostatic pressure fields and the pressure gradient is negligible;
- Mass of the main rubber spring and lower diaphragm are negligible;

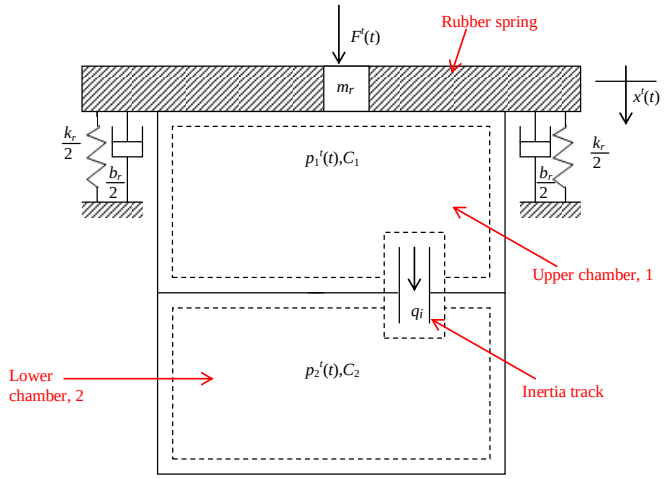

Figure 2.8: Hydro-mechanical model for a hydromount. Adapted from Singh et al.[57]

- Stiffness and damping of the lower diaphragm are negligible;
- Fluid is incompressible and its density is constant throughout the mount.

The model described by Equation (2.3), in its initial form, assumes linear parameters for the mount and can predict the general features of the dynamic behaviour of hydromounts reasonably reliably. These are: a) the frequency at which the phase angle of the dynamic stiffness of the mount reaches its maximum and; b) the form of the complex dynamic stiffness of the mount. This linear approach could be used as a design tool for establishing the main geometrical design of a mount. However, hydromounts exhibit non-linear force deformation response, and hence accurate prediction of their dynamic behaviour requires a model that is capable of catering for their various non-linear characteristics. A good review of this model and discussion of the non-linearities incurred is given by Adiguna et al.[68]

Further work on modelling with an emphasis on the equivalent damping of the inertia track was described by Lee and Kim[69]. Wang et al.[70] looked at developing a type of graphic modelling based on results from finite element analysis (FEA). FEA modelling of mounts has been carried out by various authors[71–74]. On the whole a good correlation between experimental results and the simulation was found, in both the time and the frequency domains. Ahn et al.[75] used a "genetic algorithm with simplex method" to optimise the design of a hydromount. They aimed to decrease the "notch stiffness"(the minimum stiffness which is tuned to the engine resonance frequency), whilst minimising the effect of this on

the high frequency stiffness. They found it to be better than another method (sequential quadratic programming), but it required more computational time. Christopherson and Jazar[54,76] look in detail at the mathematical modelling and the FEA simulation for describing hydromounts. The emphasis seemed to be on decoupled mounts, one with a free-type decoupler, relying on the fluid pressure to move it and the other with a direct decoupler, where a decoupler like a free-type one was directly coupled to the top of the mount. The free decoupler mount essentially had three chambers connected to each other in series, with the flow through the inertia track controlled by the movement of the decoupler. Although there was some comparison of quasi-static experimental data with the FEA simulation, there was no comparison with experiment for the frequency-dependent behaviour. He and Singh[77] attempt to simplify the model detailed above, and they find some success. Although not as accurate as the full model it gives reasonable predictions.

replacedThere are many sources of non-linear behaviour in hydraulic mountsThere are many types of non-linear behaviour in hydromounts. Clearly the non-linear behaviour with respect to frequency provides the characteristic hydromount performance, and there are other non-linear behaviours, for example with respect to temperature. In this thesis the discussion of non-linearities will focus on those that are amplitude dependent. There are many sources of this, such as:

- The decoupler, if the mount has one;
- The inertia track, mainly consisting of the resistance to flow through the inertia track;
- The stiffness and damping of the rubber spring;
- The effective pumping area;
- The compliances of the upper and lower chambers;
- The vacuum phenomenon.

These are discussed further in the following subsections.

2.2.1 Decoupler

If present in the hydraulic mount, a decoupler is the most obvious cause of non-linearity. The use of a decoupler means that the hydraulic mount will have a distinctive small amplitude behaviour (whilst the coupler is in action) and a different large amplitude behaviour (when the decoupler has reached its limit and the fluid is forced through the inertia track). The change in behaviour is discontinuous. This means that often people incorporate a switching mechanism in their models to account for the decoupler behaviour[46,68,78]. Another source of non-linearity found only with the floating decoupler is the resistance to flow of the decoupler. Ohadi and Maghsoodi[79] considered it necessary to add turbulent terms to the resistance of their free decoupler. They also added a term to the resistance to take into account where the floating disc in the free decoupler is. Other work incorporating non-linear decoupler behaviour into models includes Ushijima and Dan[80] and Golnaraghi and Jazar[81].

2.2.2 Inertia track

When modelling the inertia track the assumptions usually made[67] are that:

- The fluid is incompressible;
- The influence of gravity is neglected;
- The properties are uniform at cross-sections at the beginning and the end of the inertia track;
- The relative velocity of the fluid along the track is constant;
- The inertia track is straight;
- Cross-sections taken along the track have the same shape.

The inertance is defined as the pressure per unit volume velocity. For a circular tube the following equation can be used to estimate I_i, the inertance of the inertia track.

$$I_\mathrm{i} = \frac{\rho l_\mathrm{i}}{A_\mathrm{i}} \tag{2.4}$$

where l_i is the effective length of the inertia track, A_i is the cross-sectional area of the inertia track and ρ is the density of the fluid.

According to Adiguna et al.[68] this is an acceptable approximation as more accurate approximations would require lengthy analysis. The effective length is not necessarily actual length. It is likely to be between 1.0 and 1.33 times greater. This is because when the track stops the flow does not cease, but carries on into the chamber a short way.

Generally, the resistance to flow, R relates the change in pressure, p across a tube to the flow rate through the tube, q, as shown here:

$$q = \frac{p}{R} \tag{2.5}$$

As a linear value for use in the model, the resistance to flow was assumed by Singh et al.[57] to be constant and given by :

$$R_\mathrm{i} = \frac{128\mu l_\mathrm{i}}{\pi d_\mathrm{i}^4} \tag{2.6}$$

where μ is the viscosity of the fluid and d_i is the hydraulic diameter. For this the flow is assumed to be laminar and through a circular tube.

The resistance to flow is, in fact, the gradient of the graph of the steady state pressure drop, Δp_{12}, versus the steady flow rate, q_i[68]. This relationship is non-linear. The linear equation underestimates the actual resistance as it does not take into account end effects and pressure drop due to cornering. It also does not take into account turbulent flow that might be caused by the sharp edge orifice. A more suitable equation is suggested by Adiguna et al.[68] to describe the non-linear relationship between Δp_{12} and q_i ; the sharp edge orifice formula:

$$q_\mathrm{i} = C_d A_\mathrm{i} \sqrt{\frac{2\Delta p_{12}}{\rho}} \tag{2.7}$$

C_d, the coefficient of discharge, is dependent on the edges, surface finishes and roundness of the hole. For a perfectly sharp edge C_d is 0.60, a chamfered edge can change it to be up to 0.9 and a radius could increase it to 0.98[82]. However, chamfers and radii are difficult to recreate and can create extra variables to consider when trying to predict flow. The best method for getting a value for

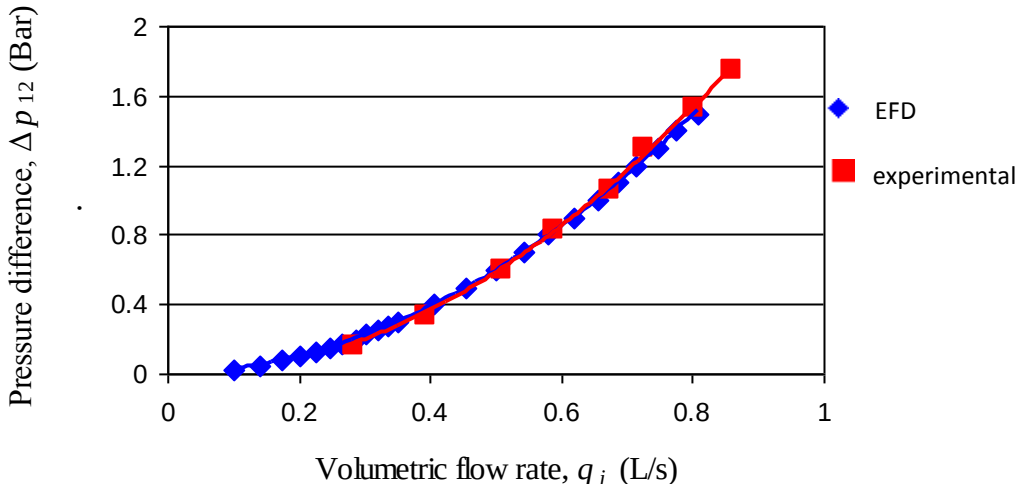

Figure 2.9: Pressure flow relationship for the inertia track[6]

resistance is by curve fitting to experimental results. However, in the work of Adiguna et al.[68] the non-linear sharp edge orifice formula gives a value of the right order of magnitude, whereas their values with the linear formula differed by an order of magnitude. Ohadi and Maghsoodi[79] also consider turbulent terms for the resistance to flow.

Ahmadi et al.[6] studied this effect both experimentally and using a computer fluid behaviour simulation package (Engineering Fluid Dynamics). They found close agreement between the model and the experiment and the curve was quadratic (see Figure 2.9). They found the relationship to be:

$$\Delta p_{12} = 2.23 q_{\mathrm{i}}^2 + 0.07 q_{\mathrm{i}} \tag{2.8}$$

2.2.3 Stiffness and damping

Geisberger et al.[46] discuss the non-linearities of the stiffness and damping. The stiffness and damping of the rubber spring have been assumed to be linear, following the Voigt model (frequency and amplitude invariant). At low frequencies, the stiffness and the damping are much less than those of the mount, and frequency invariance is a reasonable approximation although at higher frequencies the error increases. The stiffness and the damping of filled rubber components do show amplitude dependence. There is also a dependence upon the preload. However, these parameters could be improved by taking experimental results for the rubber

spring at different amplitudes, preloads and frequencies and using them in the appropriate simulation.

2.2.4 Effective pumping area

There is a dependence of the effective pumping area on the preload[46]. A preload results in a mean displacement of the rubber, which alters the effective pumping area.

2.2.5 Compliances

Compliance is defined by:

$$C = \frac{\Delta V}{\Delta p} \tag{2.9}$$

where ΔV is the change in volume and Δp is the change in applied pressure.

The compliance of the chambers is dependent upon the applied preload. Adiguna et al.[68] studied the static pressure as a function of preload. They found that if the preload was less than a certain value the static pressure was equal to atmospheric pressure, because of the high compliance of the lower chamber. In addition, the values for the upper chamber compliance at preloads of 800 N and 1200 N were similar to each other, but significantly lower than that for a 0 N preload. The bottom chamber compliance was non-linear and demonstrated hysteresis during loading and unloading. For the lower chamber, a cubic polynomial fit to the compliance was found to be quite good. The upper chamber was shown by Adiguna et al.[68] to be dependent upon the preload, though linear for positive compliances at a given preload.

Another problem with the compliance according to Colgate et al.[78] and Geisberger et al.[46] is that the compliances of the upper and lower chambers do not take into account bulge damping effects. This is the damping caused by the volume expansion. For the upper chamber, Geisberger et al.[46] solved this problem by introducing another parameter, R_1 to represent the resistance to volumetric expansion. They introduced the following equation into the model:

$$C_1 \dot{p}_1 = q_\mathrm{T} + C_1 R_1 \dot{q}_\mathrm{T} \tag{2.10}$$

where C_1 is the compliance of the upper chamber, p_1 is the upper chamber pressure and q_T is the flow entering the compliant region.

C_1 and R_1 are functions of the steady state volume amplitude, the preload and the frequency of excitation. Not altering the lower chamber compliance is justified as its value (as long as it is significantly higher than the upper chamber compliance) has little effect on the system dynamics.

He and Singh [83] carry out an investigation into the non-linearities of the top and bottom chamber compliances. They introduced a multi-staged variable $C_1(p_1)$ and a variable $C_2(x_{\text{mean}})$ and found that the time domain results for their hydromount can be greatly improved. Wang et al. [84] also looked at the non-linearities in hydromounts including volumetric compliance.

2.2.6 Vacuum phenomenon

The vacuum phenomenon has been discussed by Adiguna et al. [68] and Kim and Singh [85]. When $p_1 < p_{atm}$, where p_{atm} is the atmospheric pressure, the compliance of the upper chamber is negative. Under these conditions, air dissolved in the fluid (usually a glycol and water mixture) would come out of solution and result in a mixture of gas and liquid phases present. Ahmadi et al. [6] also found this to be true experimentally.

It is not easy to determine the level of pre-dissolved gas in the liquid. To get around this problem, Kim and Singh [85] assumed an initial amount of air in the upper chamber with a volume of 0.025 cm^3 in a 40 cm^3 total volume. However, Adiguna et al. [68] considered the dynamic stiffness characteristics of the mount under both compression and expansion conditions. They suggested that the mount would behave as a non-linear system with a bi-linear stiffness curve. They created a piecewise linear system with a vacuum stiffness, and the usual stiffness. This resulted in the empirical equation:

$$\frac{dV}{dp} = ap^n + b \tag{2.11}$$

where n is a polytropic coefficient (a suitable value is found to be between 7 and 10), a is approximately 10^{-60} and b is the gradient of the p-V curve at the operating point $p_1 = p_{\text{atm}}$. This shows a sharp but continuous change from one

stiffness regime to the other as a is very small.

2.2.7 Further issues

Lee et al.[66] argued that using a lumped mass to model the inertia effect of the fluid is unsuitable. This is because a point stiffness model is being compared with experimental results in the form of a transfer stiffness. They pointed out that these mechanical models only considered one point-stiffness whilst ignoring a further point stiffness and the transfer stiffness. They admit that the point stiffness of a vibration isolation element is the same as the transfer stiffness as long as inertia effects are negligible. Therefore, if the end of the hydraulic mount is attached to a fixed frame the difference between the point stiffness and the transfer stiffness would be negligible as the transmitted force has no effect on the underlying frame.

Another concern is whether experimental results for harmonic excitation give an accurate portrayal of what may occur in a car. It is realistic to contemplate that the hydraulic mount may be expected to be simultaneously ensuring the engine moves with the car body and isolating the car from the engine vibration. Consideration of this form of composite function is given by Colgate et al.[78]. They found that the mount's ability to isolate from high frequency, small amplitude inputs is significantly degraded by the simultaneous occurrence of low frequency, large amplitude vibrations. They concluded that a fixed rather than a floating decoupler might go some way to solve this issue. They also found that the piecewise linear model and the equivalent linearisation technique they used (the major contributor to non-linearity they considered was the decoupler) was able to model the composite behaviour well. Their piecewise linear model includes a large amplitude model which is virtually identical to the one used by Singh et al.[57].

Adiguna et al.[68] investigated their non-linear model's response to transient inputs with reasonable success. The model they use is a non-linear adapted form of the linear model proposed by Singh et al.[57].

Lee and Singh[86] stated that despite much work being done on experimental and analytical characterisation of hydromounts, the inclusion of these results into system models is open to interpretation. This is because the tests and simulations

almost always used a fixed base to calculate the transfer stiffness. Their argument is based on the four pole stiffnesses not being equal in the mechanical models, whereas the fluid model does not have this problem. Later[87] they included their model in a quarter car model and demonstrated the effect of amplitude dependence on this system. They also argue[88] that normal consideration of hydromounts usually ignores the harmonics their non-linearity imposes on to the simple sinusoidal input.

2.2.8 In summary

The design of passive engine mounts involves managing a compromise between two or more conflicting requirements. On one hand, for effective isolation of the cabin from engine vibration, generated by the movement of engine parts during ignition cycles, the mount is required to be as soft as possible. On the other hand, to prevent engine shake a stiff, highly damped mount is required. Hydromounts have been developed to try to achieve this compromise. Although hydromounts are widely used in the automotive industry and perform well, they are tuned to one specific frequency, that of the resonance of the vertical motion of the engine mount on the rubber spring.

Passive hydraulic mounts cannot resolve all the problems that arise during vehicle operation. Ushijima et al.[55] reported that a conventional hydraulic mount with a decoupler displayed excellent characteristics when subjected to simple sinusoidal inputs but was not practical for superimposed inputs because of the significant non-linearity of the decoupler. Also the design of such frequency- and amplitude-dependent systems and the hydraulic mount's sensitivity to the alteration of structural parameters can result in several iterations being required, during which the parameters of the mounts are tuned to solve the particular vibration problem existing in the target vehicle. This retuning involves a compromise in which the performance in a particular frequency range may be sacrificed for better performance in other frequency ranges. The variations between vehicles and the inherent inaccuracy in the manufacture of mount parts may significantly change the desired dynamic response and further reduce the mount performance.

2.3 Adaptive and semi-active mounts

Adaptive mounts are mounts where the properties are changed to improve the performance of the mount based on an input. They may have two or more modes, like "on" and "off" modes, or a changeable parameter that varies continuously across the range of interest.

2.3.1 Changing parameters

Foumani et al.[89] carried out a sensitivity analysis to determine which parameters of a hydromount it was best to alter in an adaptive mount. This was based purely on the best results, not which might be easiest to alter. Some parameters mainly adjust the magnitude of the peak stiffness of the mount, but keep the resonance frequency the same, whereas other parameters have a bigger effect on the frequency; they do not appear to have considered the difference between these effects. Having identified both the high stiffness and low stiffness behaviour to be critical, it is not surprising that they concluded that the upper chamber compliance is the best parameter to alter, as it has an important role in determining the high and low frequency stiffness. They showed that to achieve good performance with varying upper chamber compliance, an on-off mechanism is all that is required, as opposed to a continuous variable.

An adaptive mount based on a hydromount was proposed by Kim and Singh[90]. They stated that the low frequency performance of the engine mount with the inertia track characteristics was desirable. However, at high frequencies (above 100 Hz) there are undesirable resonances that can affect the noise, vibration and harshness response. They aimed to create a more ideal isolation system that behaves like a soft rubber mount at high frequencies, and concluded that the technology is promising.

Truong and Ahn[91] proposed a semi-active mount that has an inertia track with a controllable area. The area of the inertia track is controlled by a moving disc. They managed to reduce significantly the transmissibility over a large frequency range by optimising the inertia track area, and also modelled the behaviour.

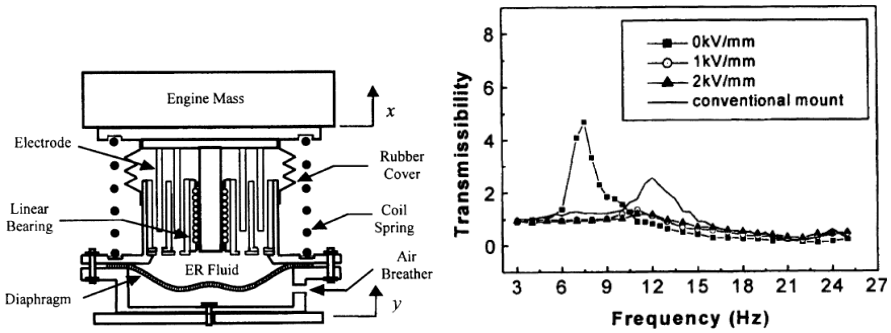

(a) Configuration (b) Transmissibility

Figure 2.10: Mixed mode ER engine mount from Choi et al.[98]

2.3.2 Adaptive mounts with smart materials

Hong et al.[92] exploited the squeeze film mode of controllable fluids. They showed significant reduction in the vibration of a frame with the use of their ERF mounts with an optimal controller. Duclos[93] proposed a tuneable flow mode ER fluid filled mount with multiple inertia paths containing valves to control the flow of fluid. Morishita and Mitsui[94] introduced plate-type electrodes to a flow mode ER mount to enable them to look at the electrode gap parameters. A squeeze-flow mode ER fluid mount was developed by Williams et al.[95]. Choi and Choi[96] suggested that a shear-mode mount might overcome some of the problems encountered in previous designs. They also looked at a mixed mode ERF engine mount exploiting both the shear mode and the pressure-driven flow mode, which they both modelled and tested experimentally. The experimental transmissibility as well as the configuration of the mount are shown in Figure 2.10. It can be seen that changing from the conventional mount to the ER mount shifts the resonance of the system to a lower frequency, and increasing the magnetic field can damp and move the transmissibility peaks. They also designed the hardware control system required. Using a similar mount and model to the previous example and using a skyhook controller, Choi and Song[97] improved the transmissibility of their vehicle model with three engine mounts.

Hong et al.[99] claimed that it is straight-forward to manufacture an ERF mount for small to medium-sized passenger vehicles, where the dead load is of the order of 70 kg, but they anticipated problems with the design and manufacture of mounts for a larger dead load. They came up with a design suitable for 200 kg. Their work showed that merely applying the field did not much alter the transmissibility of

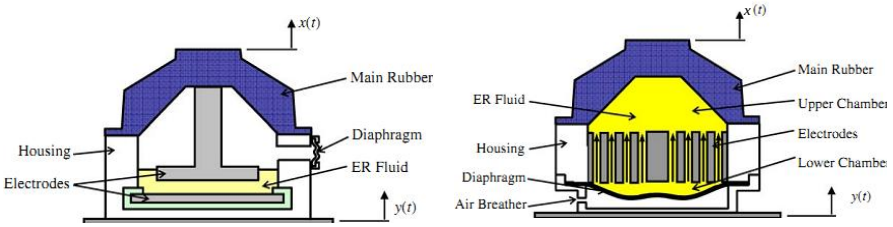

(a) squeeze-flow mount (b) Pressure driven flow mount

Figure 2.11: ER mounts for different fluid modes proposed by Hong et al. [102]

the mount. However, they achieved much improved transmissibility by employing a skyhook controller in the frequency regime below 30 Hz.

Jeong et al. [100] developed two ER squeeze-flow mounts designed for differing dead loads to control the vibration of flexible structures. They found, with both experiment and simulation, a significant improvement in the vibration control using their control mechanism. The authors modelled the noise radiated from a cylindrical shell and found significant improvements when their mount was included. Jung et al. [101] used ER mounts to control the vibration of a flexible beam structure with a proportional-integral-derivative controller. The mode of operation is the squeeze-flow mode. Hong et al. [102] go on to compare the performance of pressure-driven flow mode and squeeze-flow mode mounts (see Figure 2.11) designed for a dead load of 200 kg with a skyhook controller. It was found that for small excitations the squeeze-flow mount performed better.

MRFs can be used as an on/off type system or one where the viscosity can be changed to a number of different values, or even in a continuous range [93,103,104]. Ushijima et al. [104] and Petek et al. [105] used this principle to increase damping at resonance and reduce the transmissibility for shock excitation.

Ahn et al. [106] discussed the design of an MR engine mount based on a hydromount. An MR valve is used to open and close the inertia track as required. The purpose of the mount was to overcome the shortcomings of conventional mounts at frequencies above the resonance. The mount they used had an external inertia track to aid the easy switching of the mount in its development process. They included a model and a control scheme. The mount stiffness and transmissibility resulting from their optimum control scheme can be seen in Figure 2.12.

Multi-purpose magnetorheological isolators were investigated by Brigley et al. [107]. This work used all three fluid modes to overcome problems of using individual

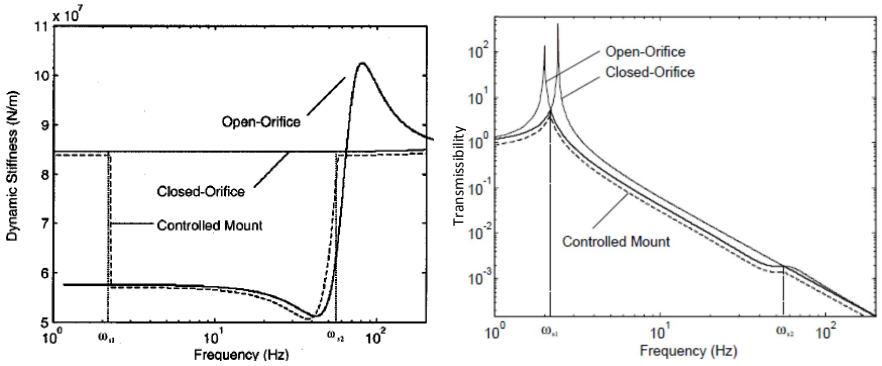

(a) Dynamic stiffness vs frequency (b) Transmissibility vs frequency

Figure 2.12: The behaviour of the MR engine mount with open and closed inertia track from Ahn et al.[106]

modes (eg squeeze-flow mode is only effective at low amplitudes; pressure-driven flow mode requires large electrodes etc.). Interestingly they seem to be using it as a damper rather than an isolator. They found that the damping was highest at low frequencies and low amplitudes. Their model underestimated the storage modulus although good agreement was shown for the loss modulus.

York et al.[108] proposed an MRF embedded in an elastomer and used this in a novel isolator. They found that it was possible to control the dynamic stiffness and damping over a wide frequency and strain amplitude ranges. They stated that this has superior frequency performance to similar squeeze mode dampers.

Similar to the work mentioned above on ER mounts, Choi et al.[109] also carried out work on a mixed mode MR mount controlling vibration in flexible structures. This mount utilises the pressure-driven flow mode and the shear mode (see Figure 2.13). Using their optimal control system they found significant improvements in controlling the acceleration and displacement of their structure compared with using the mount passively. Ciocanel et al.[110] also proposed a mixed mode MRF mount, using the pressure-driven flow mode and the squeeze-flow mode. They found that combining the modes resulted in improved effectiveness of the mount.

Lord Corporation[111] have developed glycol-based MRFs for use in applications where they come into contact with rubber, as oils can cause certain types of rubber to swell. They tried two types of mount using these fluids: the first only had a MRF valve while the second had an MRF valve and an inertia track (see Figure 2.14). The off-state behaviour of both mounts was similar, being governed by the flow of liquid through the annular gap. For the former, when the magnetic

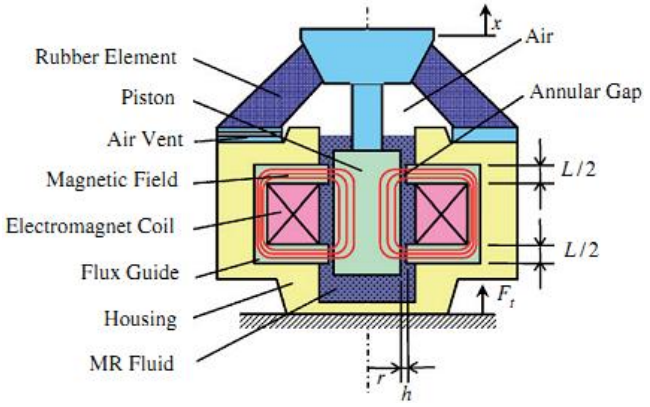

Figure 2.13: The configuration of a mixed mode MR engine mount from Choi et al.[109]

field was active, there was no fluid flow between the two chambers, so the stiffness and damping were governed by the rubber properties, meaning little frequency dependence. For the on-state of the second mount, as the magnetic field was increased more and more fluid was forced through the inertia track increasing the dominance of the frequency-dependent hydromount type behaviour. Another study on a MRF valve mount[112] considered both radial and annular flow paths. They adjusted the magnetic field to allow a controllable yield stress and post-yield viscosity, thereby controlling and maximising the damping of the mount.

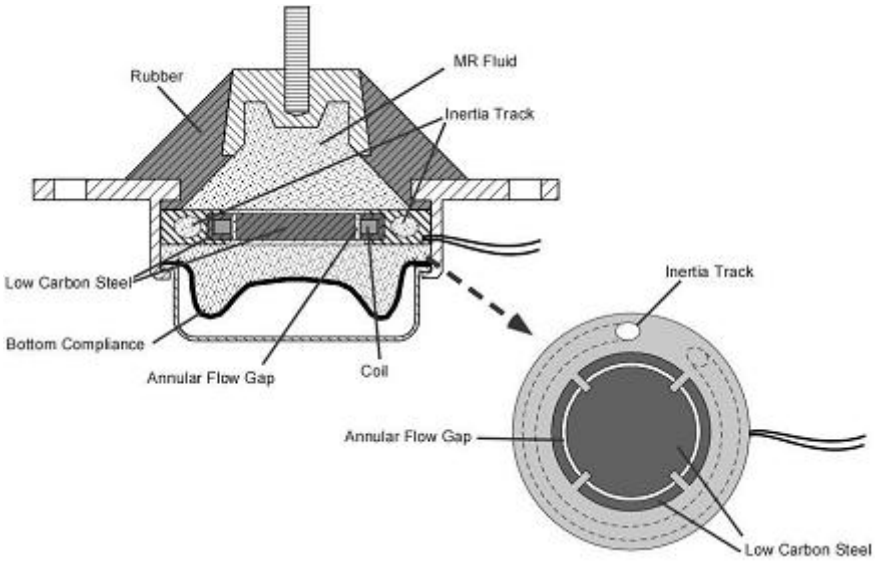

Figure 2.14: The schematic diagram for the MR engine mount from Barber and Carlson[111]

Patent US5088699[113] reports an active engine mount based on the use of an ERF as the fluid in a hydraulic mount. This makes use of the pressure driven

flow mode where the electrodes are held constant, but the flow is altered by the change in properties of the fluids. Electrodes are positioned both in partitioned chambers and in the orifices between the chambers. To damp the low frequency, small amplitude vibrations produced by engine idling, a voltage is applied across the auxiliary chamber. This increases the yield stress, effectively fixing the fluid in this chamber in position. The orifice has no voltage across it, allowing the fluid in the orifice to resonate freely and produce damping. When subjected to conditions associated with engine shaking (low frequency, large amplitude) a voltage is applied across the orifices also. The increased flow resistance produces a large damping effect. Finally, when subjected to high frequency vibration, all electric fields are switched off. This allows the elastomeric components of the engine mount to vibrate freely, causing increased damping. Other similar techniques to the above to produce ERF-based active engine mounts are also reported[114,115].

Ahmadian and Ahn[116] proposed an alteration which aimed to improve the dynamic stiffness performance of the mount. Using an MRF valve which when switched on reduced the peak stiffness meant that the higher frequency performance was improved. However, if the valve remained switched on the minimum stiffness (the notch stiffness) was increased which was a disadvantage to the performance at the resonance frequency of the engine. The minimum stiffness could be regained by switching off the MRF valve.

2.3.3 Altering resonance frequencies

It is possible to actively adjust the resonance frequency of the mount by varying the length and cross-sectional area of the orifice or inertia track[117,118]. Tikani et al.[119] considered changing the inertia track profile using a rubber cylinder in the centre of the inertia track (see Figure 2.15). The rubber cylinder could be compressed by a linear solenoid actuator to change the profile of the inertia track. They mathematically modelled the system and demonstrated that a significant improvement over a passive system was possible. Wang et al.[120] aimed to achieve similar results with a screw thread mechanism that could alter both the cross-sectional area and the length simultaneously via a single actuator. They state that controlling either the length or the cross-sectional area alone does not give a broad enough range of frequencies. They also considered that it could be used as a design tool for speeding up the process of passive hydromount design as the

optimum parameters can be found quickly.

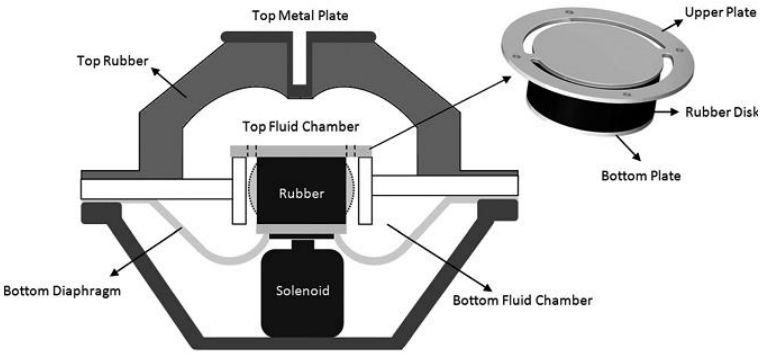

Figure 2.15: The configuration of a mount where the shape of the inertia track can be changed from Tikani et al. [119]

Multiple inertia tracks are a way of altering the mount behaviour, if they can be switched "on" and "off" as required. This type of design can provide two or more notch stiffnesses tuned to different frequencies. Barszcz et al. [121] successfully modelled a mount which has multiple inertia tracks between the same two chambers.

There are alternative means of providing two notch stiffnesses. For example, Vahdati [122] modelled a system with three successive chambers connected, each chamber connected to the following chamber by an inertia track. Tikani et al. [123] proposed a system to get two notches in which a second MRF-filled hydromount is suspended inside a passive hydromount. The vibrations are passed to the inner hydromount though a spring and a fabric diaphragm.

Although Koo and Ahmadian [124] were interested in tuned vibration absorbers they also discuss a number of control techniques. These include velocity-based on-off groundhook control, velocity-based continuous groundhook control, displacement-based on-off groundhook control, and displacement-based continuous groundhook control. For their work they found the displacement-based ones the best.

2.4 Active mounts

Active mounts work by cancelling the applied force. To achieve this requires a suitable control system as well as actuators, both of which are reviewed in the following subsections. To achieve active control energy is required continuously,

so although active mounts can potentially achieve better control, adaptive mounts are a lower energy alternative.

2.4.1 Control

For active control, filters are often used as part of the control system. Widrow et al.[125] provided a theoretical treatment of the advantages and limitations of fixed and adaptive filters, and some applications. They also provide the proof of the use of notch filters for a single frequency noise. A good general source for more information on active control is Elliot[126] and this literature review will focus on control strategies in the literature for active mounts.

There are a number of algorithms available to optimise the filter and the control system, one of the most common being the least mean squares (LMS) algorithm and variants of it. Hills et al.[127] compared two of the algorithms used for active mounts, the filtered-X LMS and their new error-driven minimal controller synthesis (Er-MCSI) adaptive controller[128].

Olsson[129] looked at a multi-input multi-output feedback controller for active engine mounts. The aim was to achieve broadband vibration isolation. The engine was a five-cylinder diesel engine. Two software packages were used - ADAMS and Matlab/Simulink. Apart from extreme situations (eg high ramping speed or engine torque) the controller appeared to work successfully.

On the other hand Lee and Lee[130] looked at a feedforward control system. Part of the idea of a feedforward system is to save money on the cost of the sensors required for feedback control. Their mount included an electromagnetic actuator (see Figure 2.17). They concluded that the feedforward technique was feasible and demonstrated reductions in the transmitted force of up to 13 dB over the 20 to 100 Hz frequency range.

2.4.2 Actuators

Actuators turn electrical signals into linear movement. In an active control system they are used to provide an opposing reaction to any external motion, cancelling it out. This provides isolation from both high and low frequency vibrations, and

at both large and small amplitudes. High frequency vibration can be reduced by applying a force at the same frequency and amplitude, but 180° out of phase to the applied vibration. Low frequency vibration, such as the transients produced by driving over a pothole, can be countered by vertically displacing the engine with the actuators. However, for this to work effectively the response of the system has to be almost instantaneous. There are a number of different types of actuators that have been used, including electromagnetic, hydraulic and piezoelectric. Each type of actuator has its own advantages and disadvantages. Bandwidth, force, response time and displacement are all important characteristics which differ for different types of actuator. The characteristics for each main type of actuator are summarised in table 2.2 below. Each type of actuator will be described in greater detail afterwards.

	Electromagnetic	**Hydraulic**	**Piezoelectric**
Bandwidth	Very broad	Medium	Very broad
Force	High	Very high	High
Response time	Fast	Slow	Fast
Displacement	Large	Very large	Small

Table 2.2: The characteristics for each of the main types of actuator. Data summarised from Huber et al.[131].

Hydraulic Actuators

Hydraulic actuators rely on the incompressibility of liquids, and consist of a piston in a fluid-filled cylinder. The difference in pressure between the two sides of the piston govern the motion. Hydraulic actuators can produce very high forces and large displacements, but have relatively slow response times compared with other types of actuator. The response to different frequency inputs is reasonable, but again not as good as other actuator types. Although they can achieve large amplitudes, the lower amplitude response is coarse compared with other types of actuator[131,132].

A range of innovations in the design and control of hydraulic actuators have been reported in the patent literature. For example, a method to reduce the electric power consumed by the hydraulic pump was described in Togashi and Nakano[133]. This involved the reduction of the pressurisation range of a hydraulic pump

attached to the hydraulic actuator, as well as the addition of a second hydraulic pump to allow replacement of leaking oil. They also described in a separate patent[134] how a hydraulic active mount can be modified in order to control the lateral swing of a hydraulic actuator piston. It additionally reports how the degradation of a seal on the hydromount can be prevented by controlling the lateral swing of the actuator piston. Another patent by Togashi and Nakano[135] describes how engine-generated shake vibration can be reduced by the enlargement of the amplitude of a hydraulic actuator. Finally, Togashi et al.[136] reports the use of a rubber mount to prevent the transmission of vibration from a solenoid-controlled valve used to control the oil pressure in a hydraulic actuator.

Electromagnetic Actuators

Electromagnetic actuators contain a permanent magnet and a coil. When a current is passed through the coil, a magnetic force is produced which causes the magnet to be attracted or repelled. Assuming the coil and magnet are not fixed relative to each other, a displacement of the two will result. The magnitude of the actuating force is directly proportional to the applied voltage. This can be varied to produce actuation at a wide range of frequencies and amplitudes[131].

Electromagnetic actuators can produce a high magnitude force and a large displacement, both of which are very useful characteristics for actuators used in active mounts. The response time is also very fast, and they can produce outputs at a wide range of frequencies. This makes them very popular for use in active engine mounts. Typical designs for an electromagnetic actuator for use in an active mount is given in patent US5718418[137] (Figure 2.16) and Lee and Lee[130] (Figure 2.17).

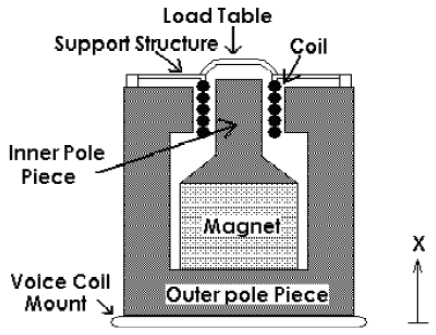

Figure 2.16: Typical design of an electromagnetic actuator[137]

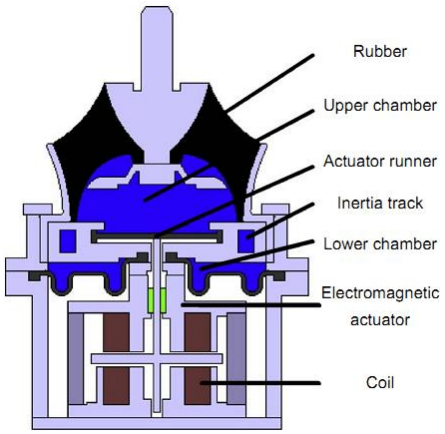

Figure 2.17: Design of a hydromount incorporating an electromagnetic actuator[130]

Miller et al.[138] used an electromagnetic actuator with a hydromount and described a model for it. This mount is designed for jet turbofan engines in aircraft. Given that they used a linear model, it seems to fit remarkably well, which suggests some of the parameters are fitted. It also seems that the model is only for the passive behaviour. The frequency response of the dynamic stiffness of their engine mount can be seen in Figure 2.18. The mount is activated between 25 and 100 Hz as this is the frequency range with significant aircraft vibration. The active mount's dynamic stiffness can be up to 100 times lower than the stiffness of the passive mount alone.

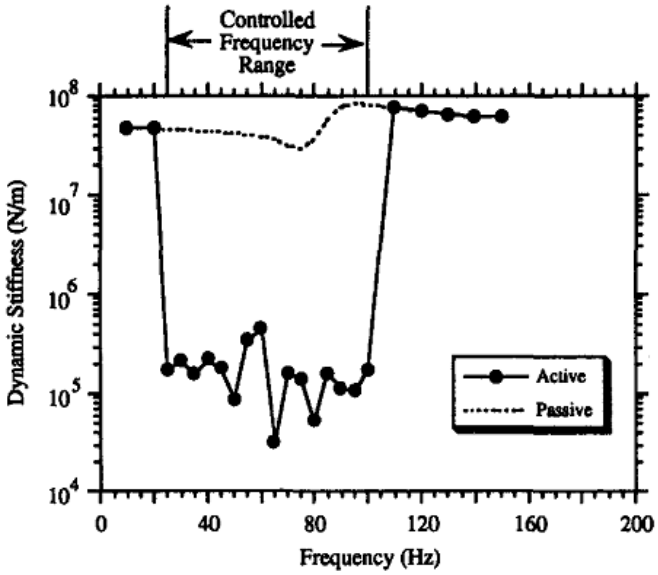

Figure 2.18: Frequency response of a hydromount incorporating an electromagnetic actuator[138]

Nakaji et al.[139] also chose electromagnetic actuators for their active control mount

system. They used two hydromounts with electromagnetic actuators and for control used the synchronized filtered-X LMS (SFX) algorithm. The SFX is said to have many of the advantages of the filtered-X LMS algorithm but with a lower computational load. It is, however, limited to cyclic phenomena. The paper is a little confusing, as it lists and explains the disadvantages of the SFX but at the end of "adaptation direction error" it says this may be considered an advantage. The sampling frequency needs to be sufficiently higher than the maximum control frequency for this control system to work well. They replaced two of four engine mounts in a four cylinder vehicle and they managed to reduce the floor vibration and booming noise.

Lee and Lee[140] also used combinations of hydromounts but unlike the examples above they complicated matters by not having the actuator incorporated into the passive mount. Separate spring elements were placed between the actuators and the engine. They used a filtered X-LMS algorithm. They used a pivot model for the passive engine mount, but ignored the compliance of the lower chamber, although as this is soft this is probably a reasonable approximation. Despite including a decoupler in their mount, their passive model also ignores this. The full active engine mount model did include a decoupler (as the piston) and lower chamber stiffness. The amplitude and the transmitted force were largest in idling state, which were measured to be 0.22 mm and 70 N respectively. They calculated that the actuator force required was approximately 50 N and the stroke needed to be at least 0.7 mm over the frequency range 20 to 50 Hz. For an ordinary vehicle it is surprising that the lower frequency region is ignored, unless the authors are relying on the passive hydromount to be adequate for the engine vibration at approx 10 Hz, or the rubber mount is really stiff hence increasing the engine-on-mount resonance. The performance of the actuator declines at high frequencies, and actually started deteriorating before the end of their frequency range of interest.

Because electromagnetic actuators are technically quite straightforward, the key feature is the control system. A typical control system is comprised of[141]:

- a data map comprising amplitude and/or phase data with respect to torque values of a vehicle engine. This is the unique feature of the system reported in the patent.
- means for detecting actual torque values of the vehicle engine;

- means for determining one of the amplitude and/or phase data with respect to one of the actual values based on the data map;
- a signal generator for generating a control signal comprising an amplitude and a phase.

One example of how a electromagnetic actuator can be modified to reduce vibration is found in patent JP2005239084[142]. In particular, it attempts to reduce the effect of small amplitude vibrations of medium to high frequency, as produced by idling engine vibration. This is achieved by the addition of an elastic stopper projection attached to the actuator, causing a shock-absorbing restriction. A second example is the invention of an electromagnetic actuator with reduced operating resistance when in motion, with claims of improvements in energy efficiency[143]. This was achieved by changing the fluid pressure in a liquid chamber within which the actuator is semi-submerged. Another modification[144] included an active decoupling system comprising a decoupler mass attached to a coil in a permanent magnetic field. The control system causes the decoupler mass to be set into motion to provide additional vibration control.

With a view to modern engine requirements,[145] described a solenoid valve based active engine mount which could satisfy variable displacement and hybrid engines. Their design was retrofittable to a passive hydromount, and they examined several driving conditions. This mount is further developed[146] with some adjustments and using a low cost modified conventional solenoid valve.

Pneumatic Control of Engine Mount Properties

US6422545[147] explained how imposing vacuum pressure on elastomeric decoupler discs can allow the mount to operate at a dynamic stiffness substantially below the static stiffness of the same mount, providing improved low amplitude vibration isolation. In effect the vacuum is behaving as an actuator, causing the engine mount to counter the vibrations produced by the engine. A similar proposal[148] also considered the control system used to calculate the vacuum output based on the operating conditions of the engine.

Another patent based on negative pressure control of an active engine mount is JP2003214484[149]. Two valves with different valve strokes are used selectively, in accordance with the input received from engine sensors, to alter the air pressure

in a chamber connected to other, fluid-filled chambers. These in turn change the vibration characteristics of the engine mount, allowing the transmission of engine vibration to be decreased over a wide range of engine speeds.

A different scheme for using pneumatic pressure to control the variation of damping characteristics has also been proposed by Kojima[150]. In this case the air pressure is varied both positively and negatively, as opposed to just negatively in the above examples.

Other active engine mounts

There is a wide range of techniques described in the patent literature to actively adjust the engine mount properties. One of the most straightforward[151] has hydraulic mount contains a piston which oscillates at a frequency corresponding to the vibration produced by the engine, but 180° out of phase. The piston moves within a fluid-filled chamber, with an orifice above the piston head and another one below. These are each connected to another fluid-filled chamber, one either side of the bushing supporting the engine. As the piston moves, the pressure increases on one side of the bushing and decreases on the other side, producing a force on the bushing. This opposes the engine vibration transmitted through the bushing, reducing its amplitude.

A good example of a complete active engine mount system which possesses the full range of attributes necessary for an ideal system is given in US2001032919[152]. In this patent a fluid-filled pressure receiving chamber is attached to another chamber by two orifices, with the dimensions of these orifices tuned so as to damp vibration at frequencies corresponding to engine shaking and idling engine vibration respectively. This is achieved by resonance of the fluid within the orifices, which can be opened and closed by valves in response to signals from the control system. The pressure receiving chamber is also bounded by an oscillating disc, powered by an electromagnetic actuator, which vibrates so as to damp high frequency vibrations. This engine mount design, from Tokai Rubber Industries Ltd., is very similar to that found in a number of other patents from the same company.

Another patent[153] also looks at a complete active engine mount system. This involves a hydraulic mount and a piezoelectric actuator system, allowing the

decoupling of high-frequency vibration, such as engine noise, from low-frequency vibration, such as road noise. A similar system was also reported[154], except that the piezoelectric actuator is replaced by an electromagnetic actuator.

US5101929[155] and US5310017[156] both describe an active control mount based on a number of gas/liquid-filled cylinders. The two phases are separated by an impermeable diaphragm, with the gas-filled section sealed and the liquid-filled section attached to a reservoir of much greater volume. This means that the gas-filled section acts as a cushion, whilst the constant pressure provided by the liquid reservoir produces a restoring force.

Sui et al.[157] use a piezoelectric actuator, stating the advantages of low power consumption, fast response time and the lack of wear as justification for using them in their mount design. To obtain large enough displacements they use a stack of piezoelectric discs connected electrically in a parallel circuit. They only model the system in a car, but the model suggests good isolation may be achievable (approximately an 80% reduction in the amplitude of the vibration). In this process the phase of the vibration is shifted, but they only considered vibration from the engine, not due to road input.

Jeon et al.[158] continued the work of Lee et al.[159] and used a combination of two MR mounts and a piezostack actuator to replace three simple rubber mounts. The two MR mounts were placed on either side of the engine with the piezostack at one of the other ends. The MR mounts control were used as roll mounts, controlling the low frequency performance, whereas the piezostack was used to control the high frequency engine vibration. The MR and piezostack mounts were analysed by experiment, whereas the system with the engine was considered theoretically, feeding in the experimental data.

Active mounts can achieve good control, but are dependent on a suitable control system, they require a passive fail-safe system. There is the question about whether the active system should be in series with the passive system (and therefore supporting the weight) or in parallel (and therefore needing to counteract the passive system). The power demands also can be very high. Adaptive mounts can offer many of the benefits of active control, but are generally simpler and cheaper to implement and have lower energy consumption. This thesis focuses on adaptive mounts.

2.5 Concluding remarks

There is limited literature on hydromounts with multiple inertia tracks. Christopherson and Jazar[54,76] describe a decoupled mount with essentially three chambers and Vahdati[122] describes a three-chambered, two inertia tracked mount, but both these are connected in series, unlike the model proposed in this thesis. Barszcz et al.[121] modelled a mount which has multiple inertia tracks between the same two chambers, which also differs from the work in this thesis where there are single inertia tracks leading to individual chambers. This work aims to study this in more detail, both experimentally and by developing a model for a two inertia track, three chamber mount.

2.6 Aims and objectives

The aim of this project is to develop and test ideas for a switchable hydromount. To aid the design and understanding of the benefits of such a mount it is important to have a working model for this switchable hydromount.

To achieve this aim, the following objectives have been identified:

1. Develop understanding of the parameters affecting the performance of a hydromount by carrying out measurements and by implementing a dynamic model of the hydromount
2. Experimentally explore possibilities for a two state mount and a mechanism by which to switch the mount between the two states
3. Develop a dynamic model for this switchable mount to give increased understanding of its performance
4. Examine the potential benefits of such a mount when installed in a vehicle.

Chapter 3

Quarter-Car Model

In this chapter the car is modelled as a quarter-car model with simple engine mounts. This is used to assess the characteristics which might be beneficial for a mount. The model is used again later in Chapter 7 to examine the effect of the hydromounts.

The car is simplified as a two-degree-of-freedom system, so vibration not in the vertical direction is ignored. This is termed a quarter-car model due to the neglect of pitch and roll. This also simplifies the system by neglecting the modal vibration of the car. There are two types of input to the engine mounting system which can be considered. The mount can be base-excited due to the road and wheel input (Figure 3.1) and it can undergo forced vibration from the input due to excitation the engine.

The car body, tyres and the suspension system are lumped together into the first mass, spring and damper (m_1, k_1 and c_1) with natural frequency $\omega_1 = \sqrt{(k_1/m_1)}$ and damping ratio $\zeta_1 = c_1/2m_1\omega_1$ (for the car body without engine). The second mass, spring and damper (m_2, k_2 and c_2) represent the engine and the stiffness and damping of its mounts respectively, with natural frequency $\omega_2 = \sqrt{(k_2/m_2)}$ and damping ratio $\zeta_2 = c_2/2m_2\omega_2$ (for the engine on its mounts on a rigid base). This set-up is different from the typical car model which considers the sprung mass supported by the suspension and the unsprung mass, but for this work it is the motion of the engine and the car body due to engine forcing that is of interest.

For the present simulations m_1 is taken to be 250 kg, approximately one quarter

of the vehicle mass. As the engine is situated at the front of the vehicle, half of its mass is included in the model and so for this work m_2 is taken as 50 kg. If there are four engine mounts, the stiffness of two would be appropriate to include in the quarter-car model of 0.2 $\mathrm{MNm^{-1}}$each, giving k_2 as 0.4 $\mathrm{MNm^{-1}}$. For the damping ratio (ζ_2) of the engine mount various values are considered. The suspension stiffness for a standard car is usually tuned such that the natural frequency falls between 1 and 1.5 Hz and the damping is usually around 40% of the critical damping[160]. In this chapter the natural frequency, $\omega_1/2\pi$, is taken to be 1.5 Hz. Further it is assumed that the tyre stiffness is much greater than that of the suspension. Therefore, as they are in series, the suspension stiffness dominates so k_1 is taken to be that of the suspension. The damping of the tyres is usually assumed to be negligible, so only the suspension damping is used for c_1. These assumptions are reasonable as the stiffness of the tyres is approximately 200 $\mathrm{kNm^{-1}}$ (about 10 times that of k_1), and the damping ratio is approximately 1.5% (which given that the unsprung mass is approximately 10% of the total weight of the vehicle, makes the damping much smaller than c_1), although both these values are very dependent upon the inflation of the tyres and their speed of rotation (the damping ratio is as high as 10% when the car is barely moving)[161]. The values used in the model can be seen in Table 3.1.

Variable	**Value**	**Unit**
m_1	250	kg
k_1	22.2	$\mathrm{kNm^{-1}}$
ζ_1	0.4	
m_2	50	kg
k_2	0.4	$\mathrm{MNm^{-1}}$
ζ_2	varies	

Table 3.1: Values of the variables used in the quarter car model

In this chapter various methods of describing the damping of the engine mount are compared. The aim is to identify which gives the best performance for both situations (base excitation and engine-forced vibration). For base excitation, ideally the car body and the engine should move at the same amplitude, in-phase, so that the car engine moves with the rest of the car. For engine-forced vibration, it is undesirable for the vibration to be transmitted from the engine to the car body.

First passive systems with viscous and hysteretic damping are considered. The work is then extended to look at the effects of including skyhook and groundhook damping in the system.

3.1 Modal frequencies

For a two-degree-of-freedom system there will be two resonance frequencies, which are shifted from ω_1 and ω_2 as the two systems are coupled. For the case where there is no damping, the modal frequencies, ω_a and ω_b can be calculated for the two-degree-of-freedom system. For free vibration there is no input into the system. The equations of motion are[162]:

$$\begin{aligned} m_1\ddot{x}_1 + k_2(x_1 - x_2) + k_1 x_1 &= 0 \\ m_2\ddot{x}_2 + k_2(x_2 - x_1) &= 0 \end{aligned} \tag{3.1}$$

If the motion at all points is harmonic i.e. $x_i = X_i e^{j\omega t}$ then X_i is the amplitude of the motion at point i. Further $\dot{X}_i = j\omega X_i$ and $\ddot{X}_i = -\omega^2 X_i$. Equation (3.1) can be rewritten in the form of a matrix equation:

$$\begin{pmatrix} -k_2 & k_2 - m_2\omega^2 \\ k_2 + k_1 - m_1\omega^2 & -k_2 \end{pmatrix} \begin{pmatrix} X_1 \\ X_2 \end{pmatrix} = \begin{pmatrix} 0 \\ 0 \end{pmatrix} \tag{3.2}$$

For non-zero solutions for the displacements, the determinant of the matrix must be zero:

$$\begin{vmatrix} -k_2 & k_2 - m_2\omega^2 \\ k_2 + k_1 - m_1\omega^2 & -k_2 \end{vmatrix} = 0 \tag{3.3}$$

This gives rise to a quadratic equation in ω^2 of the form:

$$m_1 m_2 \left(\omega^2\right)^2 - \left((k_2 + k_1)m_2 + k_2 m_1\right)\omega^2 + k_1 k_2 = 0 \tag{3.4}$$

To solve for ω^2, the quadratic formula can be used. This gives rise to two solutions for ω^2 of the form:

$$\omega^2_{\mathrm{a,b}} = \frac{(1+\mu)\,\omega_2^2 + \omega_1^2 \mp \sqrt{\left(\mu\omega_2^2 + \omega_1^2\right)^2 + 2\omega_2^2\left(\mu\omega_2^2 - \omega_1^2\right) + \omega_2^4}}{2} \tag{3.5}$$

where μ is the mass ratio (m_2/m_1). For the assumed parameters the two modal frequencies are at 1.4 Hz and 15.6 Hz.

The lower frequency, $\omega_a/2\pi$, is shifted down with respect to $\omega_1/2\pi$ which is 1.5 Hz. This is because at low frequencies the spring of stiffness k_2 barely moves and m_2 appears as additional mass. The higher frequency, $\omega_b/2\pi$, is shifted up with respect to $\omega_2/2\pi$ (14.2 Hz), as the lower mass, m_1 appears as additional mass, in series with m_2.

For both of the types of input, when the movement of each mass is compared with the input, there are two resonances. For the first resonance both the masses are moving in phase with each other and for the second resonance the two masses are 180° out of phase with each other.

3.2 Passive systems with viscous damping

This section considers the base-excitation and the engine-forced vibration situations for an engine mount with a viscous damper. The force due to a viscous damper is proportional to the velocity ($\dot{x}$). The addition of damping will shift the resonance frequencies from those calculated in Section 3.1.

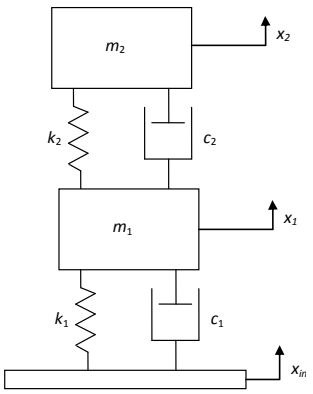

Figure 3.1: Passive two-degree-of-freedom representation of the car and engine, base excited

3.2.1 Base excitation

A diagram for the system with base excitation can be seen in Figure 3.1. The equations of motion for this system are:

$$\begin{aligned} m_1\ddot{x}_1 + c_2(\dot{x}_1 - \dot{x}_2) + k_2(x_1 - x_2) + c_1(\dot{x}_1 - \dot{x}_{\text{in}}) + k_1(x_1 - X_{\text{in}}) &= 0 \\ m_2\ddot{x}_2 + c_2(\dot{x}_2 - \dot{x}_1) + k_2(x_2 - x_1) &= 0 \end{aligned} \tag{3.6}$$

If harmonic motion is assumed at circular frequency ω, then Equation (3.6) can be written as:

$$\frac{X_2}{X_{\text{in}}} = \frac{2\zeta_1\frac{j\omega}{\omega_1} + 1}{-\frac{k_2}{k_1}\left(\frac{\omega}{\omega_2}\right)^2 + \left(2\zeta_1\frac{j\omega}{\omega_1} + 1 - \left(\frac{\omega}{\omega_1}\right)^2\right)\left(\frac{2\zeta_2\frac{j\omega}{\omega_2} - \left(\frac{\omega}{\omega_2}\right)^2 + 1}{2\zeta_2\frac{j\omega}{\omega_2} + 1}\right)} \tag{3.7}$$

The magnitude and phase of this transmissibility, representing the motion of the engine relative to a road input, are shown in Figure 3.2.

As ω tends to 0, X_2/X_{in} tends to 1, while at high frequencies it tends to

$$\lim_{\omega > \omega_2} \frac{X_2}{X_{\text{in}}} = \left(\frac{j2\zeta_2\omega_1^2\omega_2}{\omega^3} - \frac{4\zeta_1\zeta_2\omega_1\omega_2}{\omega^2}\right) \tag{3.8}$$

Initially, the imaginary term dominates, meaning the expression tends to 0 at a rate of -60 dB/decade above the resonances and the phase is 90°. However, ultimately at very high frequencies the decay becomes -40 dB/decade when the real term is dominant, and the phase tends to 180°. There are two peaks, one for ω_{a} and one for ω_{b}, as it is a two degree of freedom system (see Figure 3.2(a)). The height of the peaks is controlled mainly by the values of ζ_1 and ζ_2 respectively. The phase undergoes significant changes at both of the resonances (Figure 3.2(b)) and is $-90°$ above the first resonance frequency and 90° above the second. Increasing ζ_2, the damping ratio of the mount, again reduces the high frequency roll-off and reduces the height of the second resonance peak, although it has little effect on the first resonance.

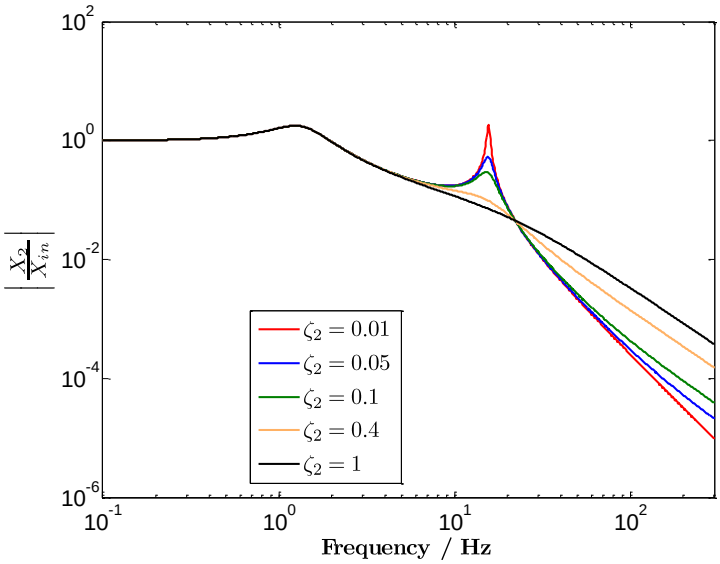

(a) $|X_2/X_{\text{in}}|$ versus frequency

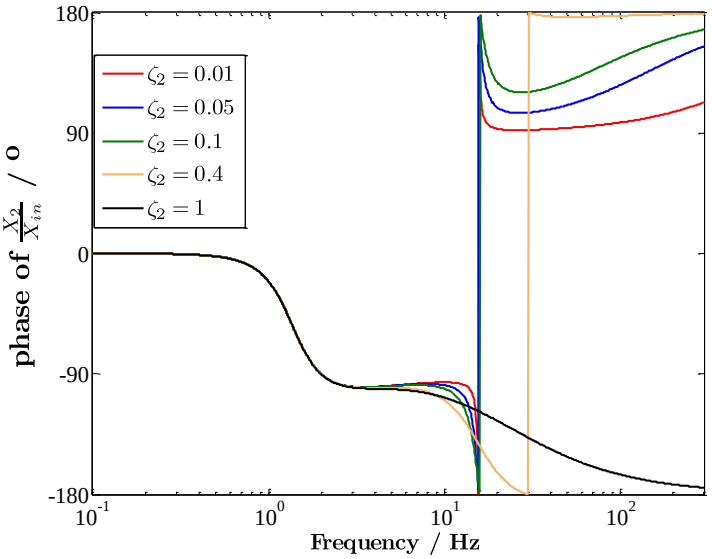

(b) Phase of X_2/X_{in} versus frequency

Figure 3.2: The variation of X_2/X_{in} with frequency for base excitation for various damping ratios, ζ_2

A similar equation can be derived when considering the movement of m_1:

$$\frac{X_1}{X_{\text{in}}} = \frac{2\zeta_1 \frac{j\omega}{\omega_1} + 1}{-\left(\frac{\omega}{\omega_1}\right)^2 - \frac{k_2}{k_1}\left(2\zeta_2 \frac{j\omega}{\omega_2} + 1\right)\left(\frac{\left(\frac{\omega}{\omega_2}\right)^2}{2\zeta_2 \frac{j\omega}{\omega_2} - \left(\frac{\omega}{\omega_2}\right)^2 + 1}\right) + 2\zeta_1 \frac{j\omega}{\omega_1} + 1} \tag{3.9}$$

This behaviour is very similar to that of X_2/X_{in} in Equation (3.7), see Figure 3.3. The major differences are that there is an anti-resonance in the response at approximately ω_2 before reaching the second resonance at ω_{b}, where the car body has a large response. This anti-resonance is caused by the second mass-spring (m_2 and k_2) system forming a dynamic absorber at ω_2. This is shifted slightly away from ω_2 by the introduction of damping to the engine mounting. Also, the decay at high frequencies is less severe than for X_2, at -20 dB/decade. This gradient is due to the expression becoming dominated by $j2\zeta_1(\omega_1/\omega)$, because ζ_1 is high. The phase angle suggests that the system is damping controlled ($-90°$) above the first resonance frequency; whereas below this it is stiffness controlled. At the second resonance the phase goes through a peak before returning to $-90°$. Increasing ζ_2, the damping of the mount, reduces the depth of the anti-resonance and the height of the second resonance but does not have any effect on the high frequency behaviour as this is only determined by ω_1 and ζ_1.

Using Equation (3.6) above, the ratio X_2/X_1 can be found:

$$\frac{X_2}{X_1} = \frac{2\zeta_2 \frac{j\omega}{\omega_2} + 1}{2\zeta_2 \frac{j\omega}{\omega_2} - \left(\frac{\omega}{\omega_2}\right)^2 + 1} \tag{3.10}$$

It is this relative motion that is the most important for the engine mount as ideally the engine will move with the car body and not resonate at its natural frequency. Graphs for the modulus and the phase of X_2/X_1 can be seen in Figure 3.4. As ω tends to 0 X_2/X_1 tends to 1, and in the low frequency region the phase angle is 0; this means the masses move together. As the frequency is increased a peak is reached at ω_2, the natural resonance frequency of the engine on its mounts. This occurs because m_1 is stationary, but m_2 is still moving (as can be seen in Figures 3.2(a) and 3.3(a)). This peak is controlled by the damping of the mount, and the height of the peak is $|1 - j/(2\zeta_2)|$. Above the resonance frequency the phase changes to $-180°$, meaning that the masses are now moving in opposite directions. At high frequencies the ω^2 the denominator of Equation (3.10) dominates and

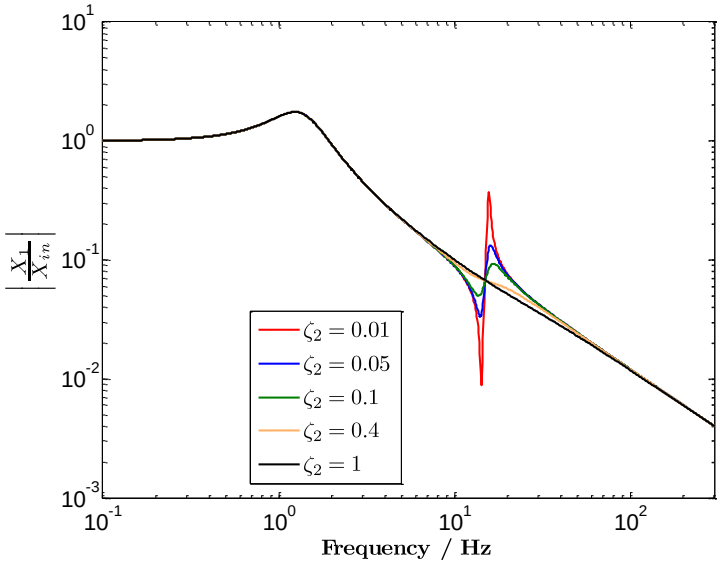

(a) $|X_1/X_{\text{in}}|$ versus frequency

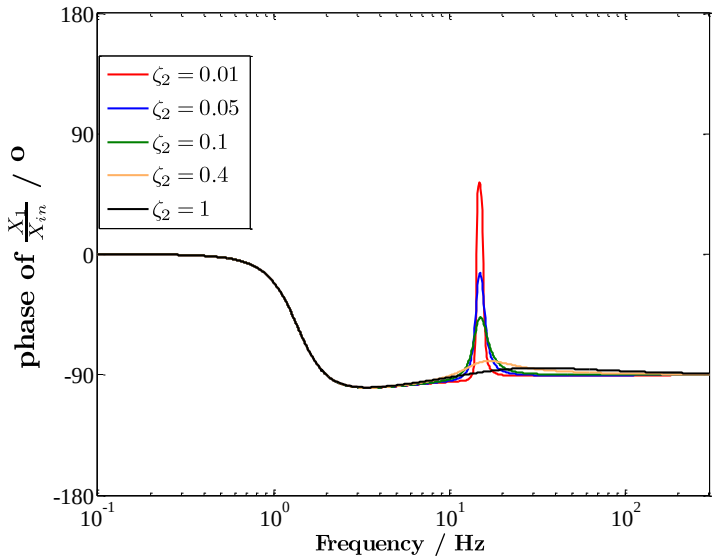

(b) Phase of X_1/X_{in} versus frequency

Figure 3.3: The variation of X_1/X_{in} with frequency for base excitation for various damping ratios, ζ_2

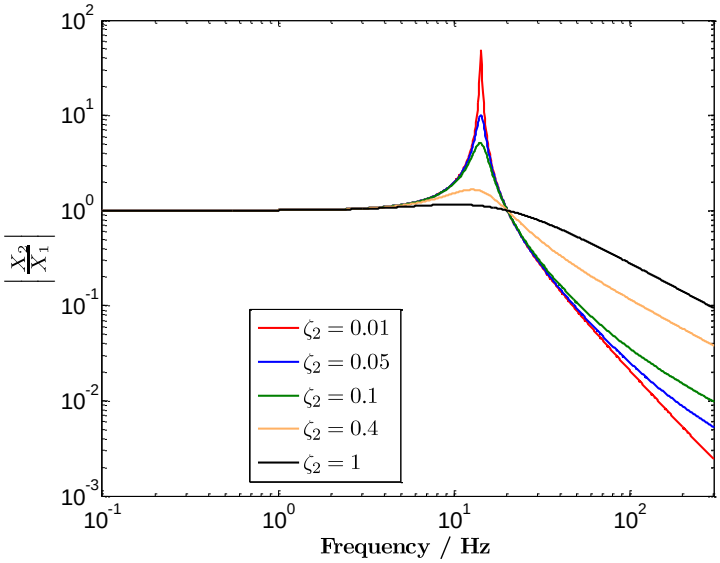

(a) $|X_2/X_1|$ versus frequency

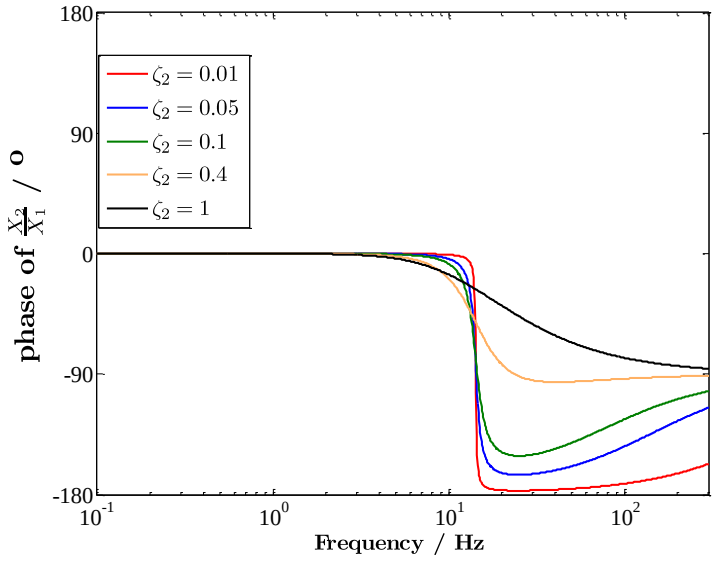

(b) Phase of X_2/X_1 versus frequency

Figure 3.4: The variation of X_2/X_1 with frequency for base excitation for various damping ratios, ζ_2

this means that the value of X_2/X_1 tends to $-j2\zeta_2(\omega_2/\omega) - (\omega_2/\omega)^2$. Initially, immediately above ω_2, the dominant part of the equation is $(\omega_2/\omega)^2$ and the gradient of this decay is -40 dB/decade with a phase of $-180°$. At very high frequencies, the decay becomes -20 dB/decade and the phase is $-90°$ where the term $j2\zeta_2(\omega_2/\omega)$ becomes dominant. As ζ_2 is increased, the -20 dB/decade region is reached more quickly. Very high damping thus improves the performance at the resonance as the peak is reduced, but at high frequencies the movement of the two masses is out-of-phase meaning there is no benefit in having the high damping above the resonance.

3.2.2 Engine-forced vibration

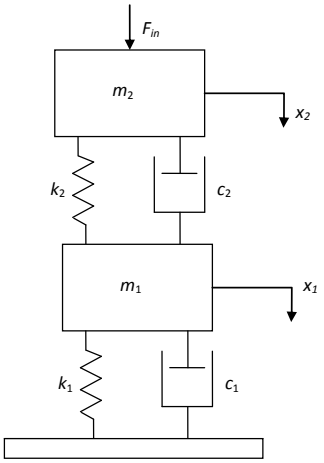

Figure 3.5: Passive two-degrees-of-freedom representation of the car and engine, engine-forced

If the assumption is made that the base is stationary and there is a force applied to the top of m_2 then the equations of motion for this system are:

$$\begin{aligned} m_1\ddot{x}_1 + c_2(\dot{x}_1 - \dot{x}_2) + k_2(x_1 - x_2) + c_1\dot{x}_1 + k_1x_1 &= 0 \\ m_2\ddot{x}_2 + c_2(\dot{x}_2 - \dot{x}_1) + k_2(x_2 - x_1) &= f_{\text{in}} \end{aligned} \tag{3.11}$$

In order to express the responses in a non-dimensional form similar to the previous section, the amplitudes X_1 and X_2 are normalised to $X_{2\text{f}}$, the amplitude of the displacement of m_2 under the imposed force with no spring or damper attached. This satisfies $f_{\text{in}} = m_2\ddot{x}_{2\text{f}}$ and for simple harmonic motion $F_{\text{in}} = -m_2\omega^2X_{2\text{f}}$. This

leads to the coupled equations:

$$\begin{aligned} m_1\ddot{x}_1 + c_2(\dot{x}_1 - \dot{x}_2) + k_2(x_1 - x_2) + c_1\dot{x}_1 + k_1x_1 &= 0 \\ m_2\ddot{x}_2 + c_2(\dot{x}_2 - \dot{x}_1) + k_2(x_2 - x_1) &= m_2\ddot{x}_{2\mathrm{f}} \end{aligned} \tag{3.12}$$

As in the previous section harmonic motion is assumed at circular frequency ω, i.e. $x_i = X_i e^{j\omega t}$, giving:

$$\frac{X_2}{X_{2\mathrm{f}}} = \frac{\left(\frac{\omega}{\omega_2}\right)^2}{\left(\frac{\omega}{\omega_2}\right)^2 + \left(2\zeta_2\frac{j\omega}{\omega_2} + 1\right)\left(\frac{\left(\frac{\omega}{\omega_1}\right)^2 - 2\zeta_1\frac{j\omega}{\omega_1} - 1}{2\zeta_1\frac{j\omega}{\omega_1} + 1 - \left(\frac{\omega}{\omega_1}\right)^2 + \frac{k_2}{k_1}\left(2\zeta_2\frac{j\omega}{\omega_2} + 1\right)}\right)} \tag{3.13}$$

Unlike the previous equations, this ratio tends to 0 as ω tends to 0. This is due to the scaling by $X_{2\mathrm{f}}$, which introduces the ω^2 term into the numerator. It increases at approximately 40 dB/decade as, for small ω, the equation tends to $m_2(k_2 + k_1)\omega^2/k_1k_2$, whilst the phase is 180°, until it reaches a small peak for the first resonance at approximately ω_{a} (see Figure 3.6). It dips before reaching the second resonance at approximately ω_{b}. The dip corresponds to an anti-resonance where m_2 would be stationary, but due to the high damping it is not as pronounced as the anti-resonance in Equation (3.9) (see Figure 3.3(a)). At this anti-resonance m_1 forms a dynamic absorber, with both springs (k_1 and k_2) in parallel, so without the addition of damping it would occur at $\sqrt{((k_1 + k_2)/m_1)}$. Above the second resonance, at high frequencies, $X_2/X_{2\mathrm{f}}$ tends to 1 as the first term dominates in the denominator and cancels with the numerator and the phase tends to 0°. This means that m_2 is behaving as though there is no k_2 or c_2, so the chassis does not affect the motion of the engine. Increasing ζ_2 has no effect on the high or low frequency behaviour, but it does reduce the depth of the anti-resonance and the height of the second resonance.

The more important result is how the car body moves as a result of the forced input from the engine. This is given by:

$$\frac{X_1}{X_{2\mathrm{f}}} = \frac{\left(\frac{\omega}{\omega_2}\right)^2}{\left(\frac{\omega}{\omega_2}\right)^2\left(\frac{2\zeta_1\frac{j\omega}{\omega_1} + 1 - \left(\frac{\omega}{\omega_1}\right)^2 + \frac{k_2}{k_1}\left(2\zeta_2\frac{j\omega}{\omega_2} + 1\right)}{\frac{k_2}{k_1}\left(2\zeta_2\frac{j\omega}{\omega_2} + 1\right)}\right) + \frac{k_1}{k_2}\left(\left(\frac{\omega}{\omega_1}\right)^2 - 2\zeta_1\frac{j\omega}{\omega_1} - 1\right)} \tag{3.14}$$

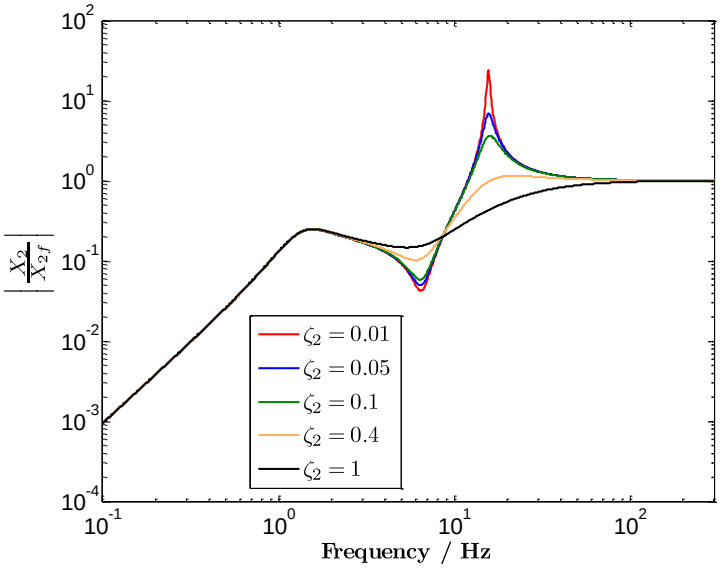

(a) $|X_2/X_{2\mathrm{f}}|$ versus frequency

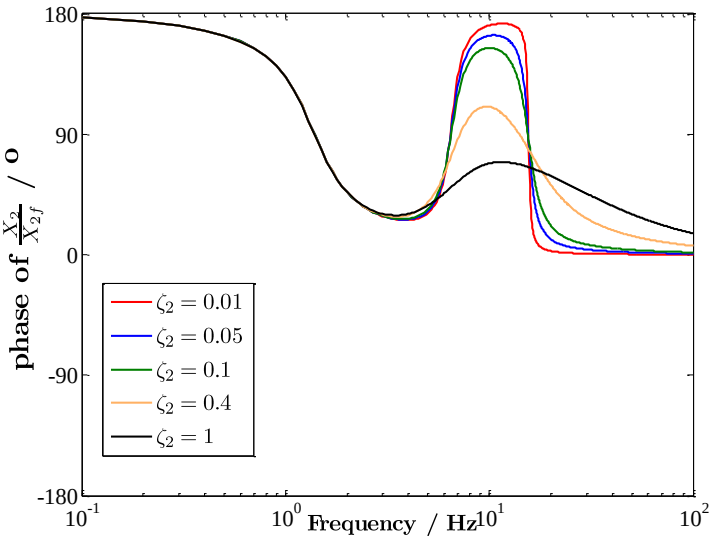

(b) Phase of $X_2/X_{2\mathrm{f}}$ versus frequency

Figure 3.6: The variation of $X_2/X_{2\mathrm{f}}$ with frequency for engine forcing for various damping ratios, ζ_2

This is plotted in Figure 3.7. This behaves similarly at low frequencies to $X_2/X_{2\mathrm{f}}$ in Equation (3.13), starting at 0 when ω is 0 and then increasing at 40 dB/decade whilst the phase is 180° (see Figure 3.7(b)), but in this case the ratio tends to $m_2\omega^2/k_1$. The first resonance again appears at approximately ω_a. The second resonance can again be seen at approximately ω_b (see Figure 3.7(a)). At higher frequencies $X_1/X_{2\mathrm{f}}$ tends to zero at −20 dB/decade due to the ratio tending to $-j2\zeta_2 k_2/(m_1\omega_2\omega)$. Increasing ζ_2 has a beneficial effect in reducing the second resonance peak, but it has a detrimental effect on the high frequency behaviour with the reduction in the high frequency fall-off. Ideally ζ_2 should be as close to 0 as possible across the frequency range above ω_b, as this will mean the engine vibration are not being transmitted to the chassis, but at ω_b the damping should ideally be large.

The relative motion of the two masses can also be considered:

$$\frac{X_1}{X_2} = \frac{\frac{k_2}{k_1}\left(2\zeta_2\frac{j\omega}{\omega_2}+1\right)}{2\zeta_1\frac{j\omega}{\omega_1}+1-\left(\frac{\omega}{\omega_1}\right)^2+\frac{k_2}{k_1}\left(2\zeta_2\frac{j\omega}{\omega_2}+1\right)} \tag{3.15}$$

For small ω, this ratio tends to $1/(1+k_1/k_2)$, which in this instance, where $k_1/k_2 \approx 0.05$, is close to 1. For low ζ_2, it has a peak at approximately $\sqrt{(k_1+k_2)/(m_1)}$, but this is lowered due to the high value of ζ_1. As ζ_2 is increased this frequency reduces until it is approximately $\sqrt{(k_1+k_2)/(m_1+m_2)}$. This peak corresponds to the anti-resonance observed in Figure 3.6(a). At high frequencies the equation simplifies to $-j2\zeta_2 k_2/(m_1\omega_2\omega) - k_2/(m_1\omega^2)$. Initially the real part dominates the high frequency behaviour, decaying at −40 dB/decade and with a phase of 180° (Figure 3.8(b)), but at very high frequencies, the imaginary part becomes the most important part, with the curve decaying at −20 dB/decade and a phase of −90°. Increasing the ζ_2 reduces the magnitude of the resonance peak and reduces the roll-off at high frequencies, changing the point at which the −40 dB/decade slope switches to −20 dB/decade.

3.2.3 Summary

For base excitation high damping in the engine mount is desirable at the second resonance frequency. At higher frequencies neither the high damping nor the low damping situation are ideal, but the amplitude of the input to the system will

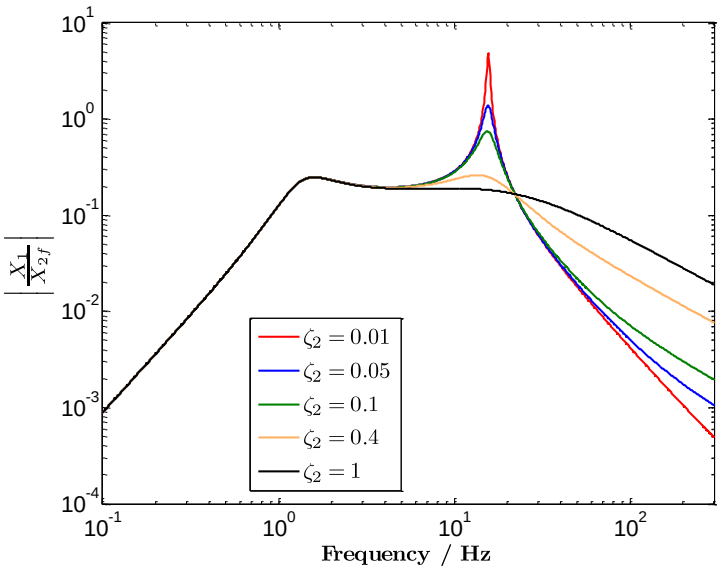

(a) $|X_1/X_{2\mathrm{f}}|$ versus frequency

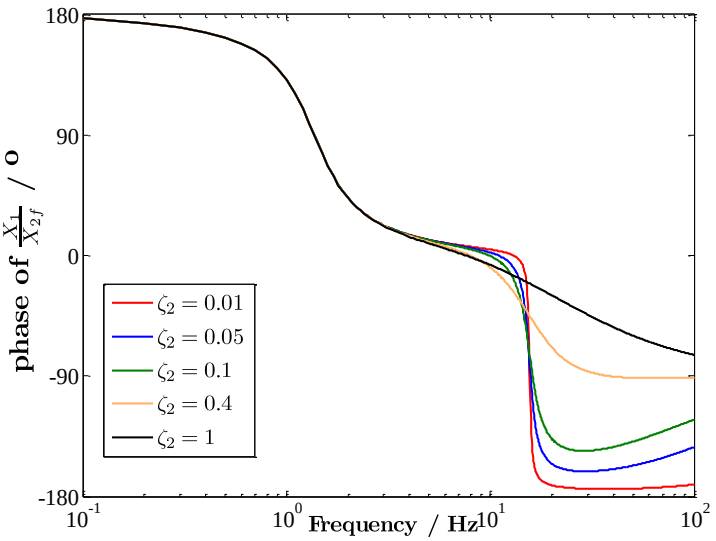

(b) Phase of $X_1/X_{2\mathrm{f}}$ versus frequency

Figure 3.7: The variation of $X_1/X_{2\mathrm{f}}$ with frequency for engine forcing for various damping ratios, ζ_2

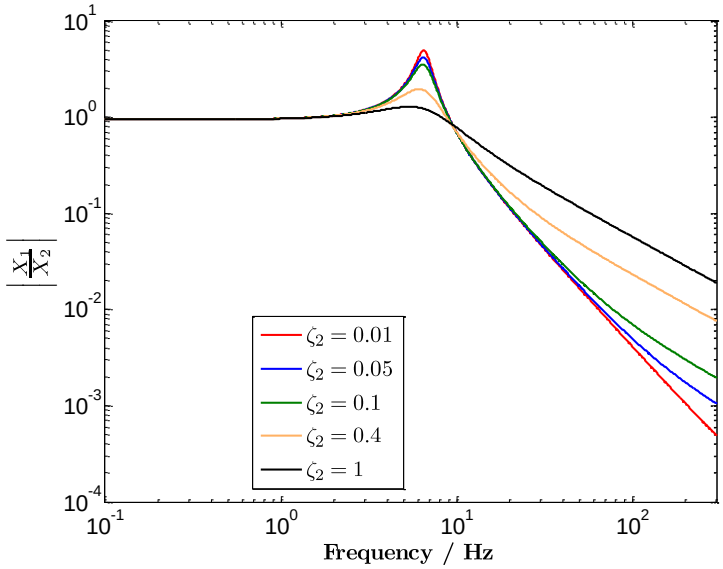

(a) $|X_1/X_2|$ versus frequency

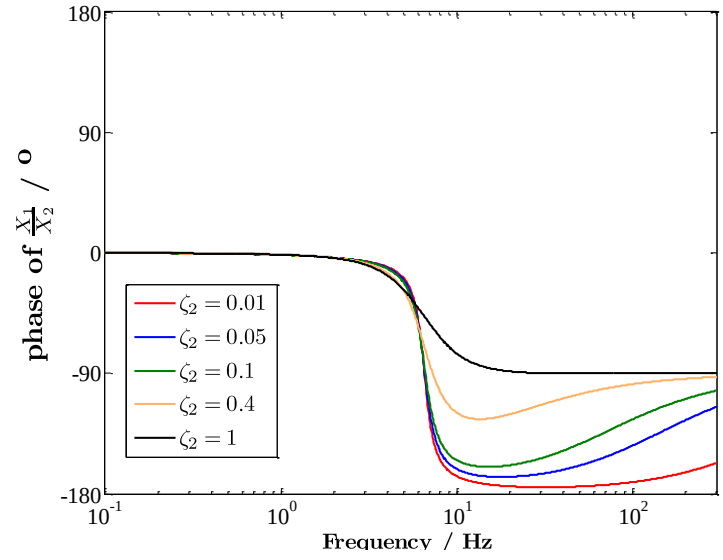

(b) Phase of X_1/X_2 versus frequency

Figure 3.8: The variation of X_1/X_2 with frequency for engine forcing for various damping ratios, ζ_2

be fairly small. This is especially true as they will have been filtered through the suspension system with its resonance of 1.5 Hz. For engine-forced vibration high damping is only desirable at low frequencies, including the engine-mounting resonance, whereas for high frequency isolation a lower value of damping is more desirable.

3.3 Passive systems with hysteretic damping in the mount

The majority of the parameters are kept the same, with the only changes being to k_2 and c_2. For the suspension, viscous damping is a good model. However, hysteretic damping is often considered a better description for a simple rubber mount as the damping of natural rubber does not show the frequency dependence seen with viscous damping. With hysteretic damping, the force is proportional to the displacement amplitude. So hysteretic damping is introduced by replacing k_2 and c_2 by $k_2(1 + j\eta_2)$ where η_2 is the loss factor. To give an equivalent damping force at ω_2, η_2 is chosen to be equal to $2\zeta_2$. This hysteretic damping model is not causal and as such can only be used as a model for the steady-state vibration for harmonic excitation. Again, two types of inputs to the engine mounting system will be considered, base excitation and engine forced vibration.

3.3.1 Base excitation

Assuming harmonic motion at circular frequency ω, the equations of motion in Equation (3.6) become:

$$\begin{aligned} m_1\ddot{X}_1 + k_2(1 + j2\zeta_2)(X_1 - X_2) + c_1(\dot{X}_1 - \dot{X}_{\text{in}}) + k_1(X_1 - X_{\text{in}}) &= 0 \\ m_2\ddot{X}_2 + k_2(1 + j2\zeta_2)(X_2 - X_1) &= 0 \end{aligned} \tag{3.16}$$

This leads to:

$$\frac{X_2}{X_{\text{in}}} = \frac{2\zeta_1\frac{j\omega}{\omega_1} + 1}{-\frac{k_2}{k_1}\left(\frac{\omega}{\omega_2}\right)^2 + \left(2\zeta_1\frac{j\omega}{\omega_1} + 1 - \left(\frac{\omega}{\omega_1}\right)^2\right)\left(\frac{1+j2\zeta_2-\left(\frac{\omega}{\omega_2}\right)^2}{1+j2\zeta_2}\right)} \tag{3.17}$$

The magnitude and phase are plotted in Figure 3.9. As ω tends to 0, X_2/X_{in} tends to 1 and at high frequencies it tends to $2\zeta_1(j-2\zeta_2)\omega_1\omega_2^2/\omega^3$, which means that the decay is -60 dB/decade, with the phase somewhere between 90° and 180°. The lower frequency behaviour is similar to that found for the viscous damper, with two resonance frequencies (at approximately ω_{a} and ω_{b}). Increasing ζ_2 reduces the height of the second resonance, as seen previously.

Also, a similar equation can be derived for the movement of m_1:

$$\frac{X_1}{X_{\text{in}}} = \frac{2\zeta_1\frac{j\omega}{\omega_1}+1}{-\left(\frac{\omega}{\omega_1}\right)^2 - \frac{k_2}{k_1}\left(j2\zeta_2+1\right)\left(\frac{\left(\frac{\omega}{\omega_2}\right)^2}{1+j2\zeta_2-\left(\frac{\omega}{\omega_2}\right)^2}\right)+2\zeta_1\frac{j\omega}{\omega_1}+1} \tag{3.18}$$

At low frequencies this relationship tends to 1 (see Figure 3.10(a)). As ζ_1 is large, at high frequencies the equation tends to $-j2\zeta_1(\omega_1/\omega)$ and $-90°$ (see Figure 3.10(b)). The behaviour is very similar to that of the base excited case with the viscous damper.

The expression for X_2/X_1 is:

$$\frac{X_2}{X_1} = \frac{1+j2\zeta_2}{1+j2\zeta_2-\left(\frac{\omega}{\omega_2}\right)^2} \tag{3.19}$$

Again, it is this relative motion that is the most important. This can be seen in Figure 3.11. When ω tends to 0, X_2/X_1 tends to 1, and in the low frequency region the phase angle is 0°. The low frequency behaviour is very similar to that for a viscous damper (see Figure 3.3(a)). As the frequency is increased a peak is reached at ω_2, the natural frequency of the engine on its mounts. This peak is controlled by the damping of the mount, and the height of the peak is $1-j/(2\zeta_2)$, as for the viscous damping case. At high frequencies the last term in the denominator of the equation dominates and this means that the value of X_2/X_1 tends to $-\omega_2^2(1+j2\zeta_2)/\omega^2$. The gradient of this decay is -40 dB/decade. The phase behaves reasonably similarly to that for the viscous damping, although at high frequencies, the lack of frequency dependence of the phase means that the phase tends to a constant value between $-180°$ and $-90°$, dependent on the value of ζ_2. Increasing ζ_2 has a similar effect at low frequencies to that found for the viscous damper, but at high frequencies the decay is much less dependent on

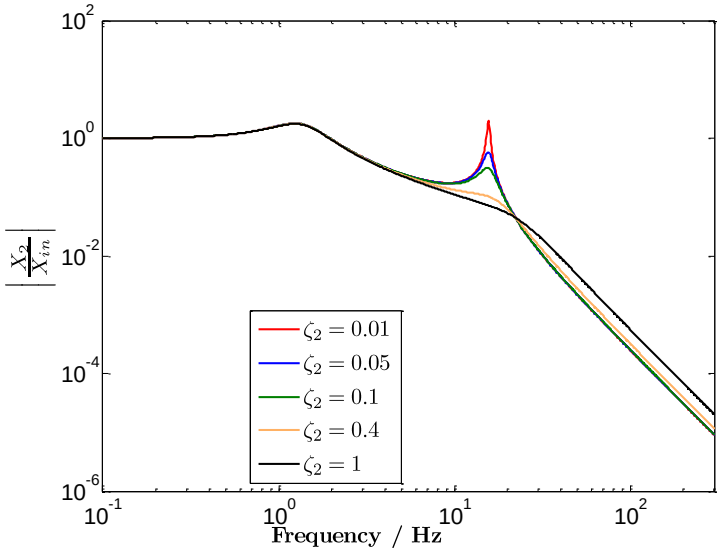

(a) $|X_2/X_{\text{in}}|$ versus frequency

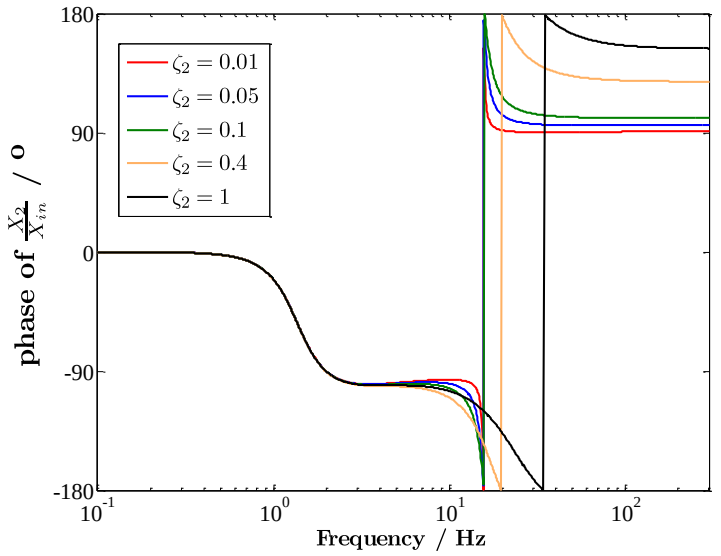

(b) Phase of X_2/X_{in} versus frequency

Figure 3.9: The variation of X_2/X_{in} with frequency for base excitation for values of the damping ratio, ζ_2, with hysteretic damping in the mounts

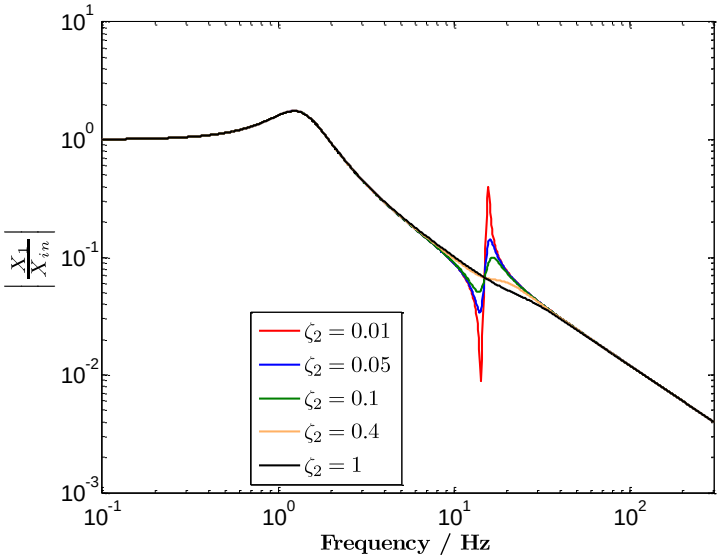

(a) $|X_1/X_{\text{in}}|$ versus frequency

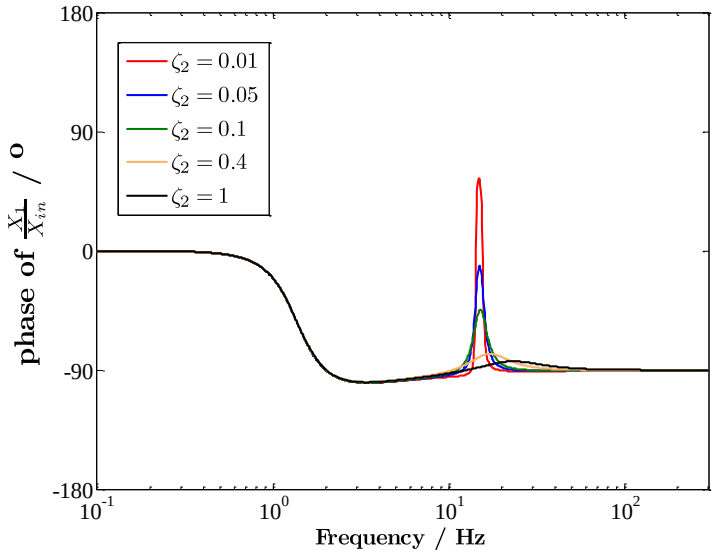

(b) Phase of X_1/X_{in} versus frequency

Figure 3.10: The variation of X_1/X_{in} with frequency for base excitation for values of the damping ratio, ζ_2, with hysteretic damping in the mounts

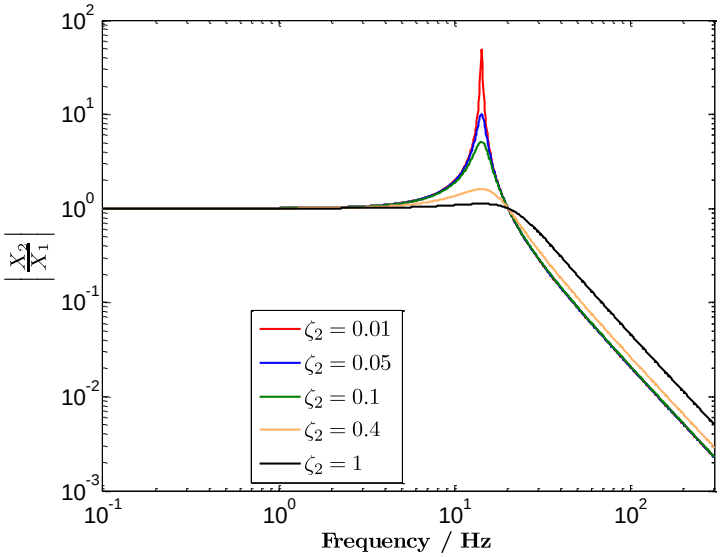

(a) $|X_2/X_1|$ versus frequency

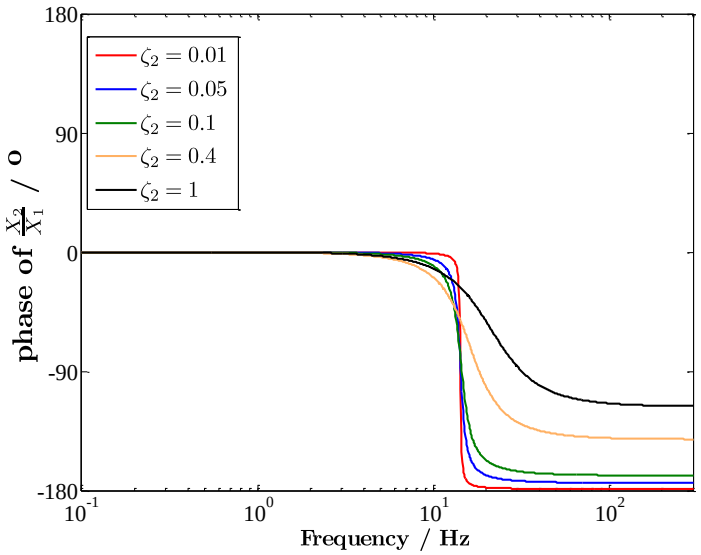

(b) Phase of X_2/X_1 versus frequency

Figure 3.11: The variation of X_2/X_1 with frequency for base excitation for values of the damping ratio, ζ_2, with hysteretic damping in the mounts

the value of ζ_2, with the decay following at a -40 dB/decade slope even at very high frequencies for all ζ_2.

3.3.2 Engine-forced vibration

As in the previous section harmonic motion is assumed at circular frequency ω and so for engine-forced vibration, the equations of motion are:

$$\begin{aligned} m_1\ddot{X}_1 + k_2(1+j2\zeta_2)(X_1 - X_2) + c_1\dot{X}_1 + k_1X_1 &= 0 \\ m_2\ddot{X}_2 + k_2(1+j2\zeta_2)(X_2 - X_1) &= F_{\text{in}} \end{aligned} \tag{3.20}$$

Again, in order to give the results in non-dimensional form, they are scaled by the vibration of mass, m_2, in the absence of the mounts, $(X_{2\text{f}})$. The relation $f_{\text{in}} = m_2\ddot{x}_{2\text{f}}$ is used leading to:

$$\begin{aligned} m_1\ddot{X}_1 + k_2(1+j2\zeta_2)(X_1 - X_2) + c_1\dot{X}_1 + k_1x_1 &= 0 \\ m_2\ddot{X}_2 + k_2(1+j2\zeta_2)(X_2 - X_1) &= m_2\ddot{X}_{2\text{f}} \end{aligned} \tag{3.21}$$

This leads to:

$$\frac{X_2}{X_{2\text{f}}} = \frac{\left(\frac{\omega}{\omega_2}\right)^2}{\left(\frac{\omega}{\omega_2}\right)^2 + (j2\zeta_2+1)\left(\frac{\left(\frac{\omega}{\omega_1}\right)^2 - 2\zeta_1\frac{j\omega}{\omega_1} - 1}{2\zeta_1\frac{j\omega}{\omega_1} + 1 - \left(\frac{\omega}{\omega_1}\right)^2 + \frac{k_2}{k_1}(j2\zeta_2+1)}\right)} \tag{3.22}$$

At high frequencies this tends to 1 with a 0° phase angle (see Figure 3.12), which again means that the engine behaves as if it is a free mass. At low frequencies there is dependence on the value of ζ_2, as the equation tends to $\omega^2(1 + k_2/k_1(1 + j2\zeta_2)/(\omega_2^2(1 + j2\zeta_2))$. However, as can be seen in Figure 3.12(a), in practice there is very little difference for the different values of ζ_2. The behaviour between the two extremes is similar to that for the viscous damper.

Again, it is interesting to consider how the car body moves as a result of the

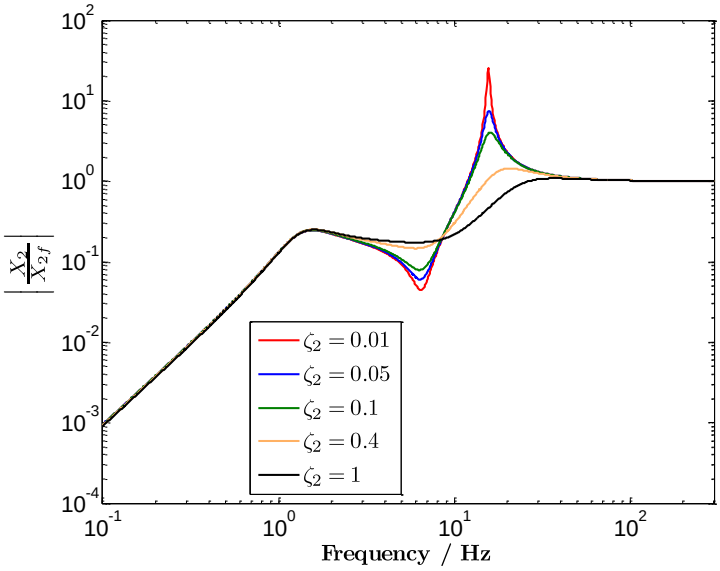

(a) $|X_2/X_{2\mathrm{f}}|$ versus frequency

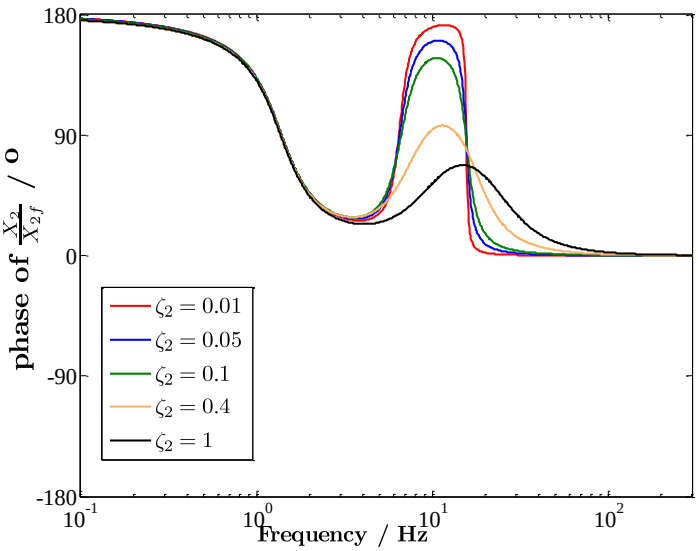

(b) Phase of $X_2/X_{2\mathrm{f}}$ versus frequency

Figure 3.12: The variation of $X_2/X_{2\mathrm{f}}$ with frequency for engine forcing for values of the damping ratio, ζ_2, with hysteretic damping in the mounts

forced input to the engine. This is given by:

$$\frac{X_1}{X_{2\mathrm{f}}} = \frac{\left(\frac{\omega}{\omega_2}\right)^2}{\left(\frac{\omega}{\omega_2}\right)^2 \left(\frac{2\zeta_1 \frac{j\omega}{\omega_1} + 1 - \left(\frac{\omega}{\omega_1}\right)^2 + \frac{k_2}{k_1}(j2\zeta_2+1)}{\frac{k_2}{k_1}(j2\zeta_2+1)} \right) + \frac{k_1}{k_2}\left(\left(\frac{\omega}{\omega_1}\right)^2 - 2\zeta_1 \frac{j\omega}{\omega_1} - 1 \right)} \tag{3.23}$$

As the frequency tends to 0, this tends to $\omega^2 m_2/k_1$ and the phase is 180° (as seen in Figure 3.13). At high frequencies the decay is -40 dB/decade and the phase tends to somewhere between $-90°$ and $-180°$. At these frequencies the equation tends to $-k_2(1 + j2\zeta_2)/(m_1\omega^2)$.

From Equation (3.21) the following relation can be found:

$$\frac{X_1}{X_2} = \frac{\frac{k_2}{k_1}(j2\zeta_2 + 1)}{2\zeta_1 \frac{j\omega}{\omega_1} + 1 - \left(\frac{\omega}{\omega_1}\right)^2 + \frac{k_2}{k_1}(j2\zeta_2 + 1)} \tag{3.24}$$

Unlike the previous example of viscous damping, as the frequency tends to 0 the value that X_1/X_2 tends to is dependent on ζ_2 (see Figure 3.14(a)), although it is close to 1 as it is given by $(1+j2\zeta_2)/(k_1/k_2+1+j2\zeta_2)$ and again $k_1/k_2 \approx 0.05$. At high frequencies the equation tends to $k_2(1+j2\zeta_2)/m_1\omega^2$, meaning that the decay is -40 dB/decade and the phase tends to a constant value between $-90°$ and $-180°$. Compared with the viscous damper case the decay at high frequencies is greater and independent on the value of ζ_2. High values of ζ_2 still reduce the peak at the resonance frequency.

3.3.3 Summary

The behaviour seen for hysteretic damping is more desirable than that of the viscous damper, because if high damping is used to reduce the response at the second resonance, there is better decay at high frequencies and the other features are very similar to those of the viscous damper. However, the hysteretic damper model is not causal which means it can only be used in the frequency domain. To give better agreement with physical systems, frequency (and temperature) dependence need to be included.

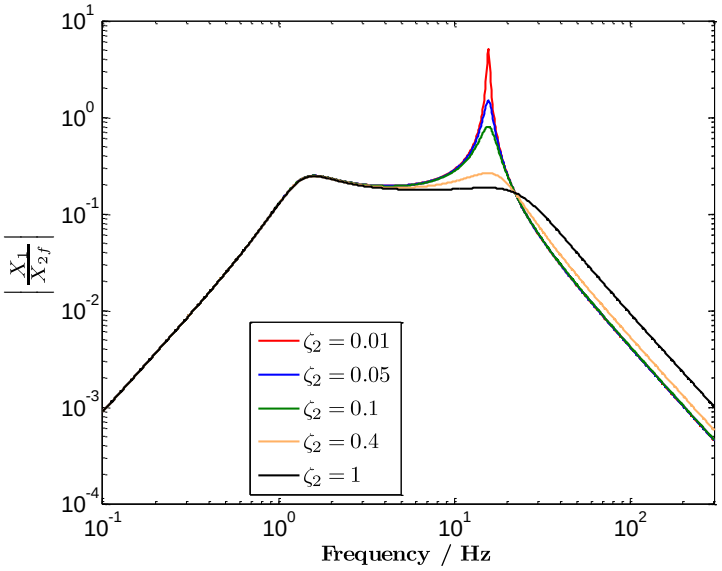

(a) $|X_1/X_{2\mathrm{f}}|$ versus frequency

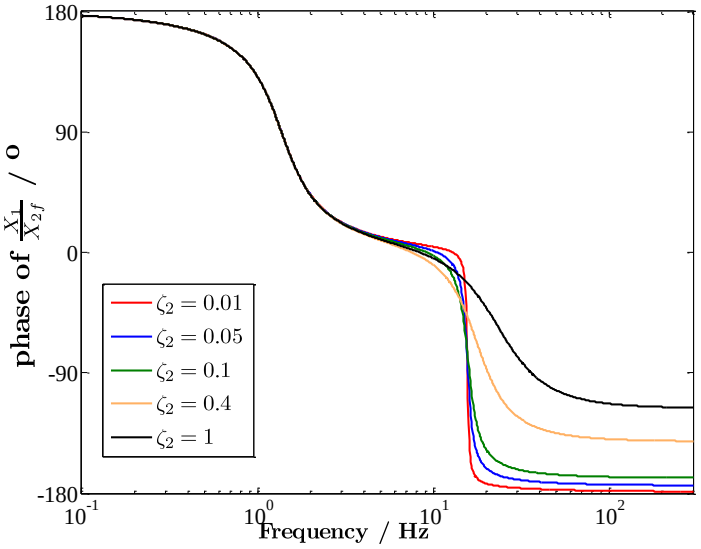

(b) Phase of $X_1/X_{2\mathrm{f}}$ versus frequency

Figure 3.13: The variation of $X_1/X_{2\mathrm{f}}$ with frequency for engine forcing for values of the damping ratio, ζ_2, with hysteretic damping in the mounts

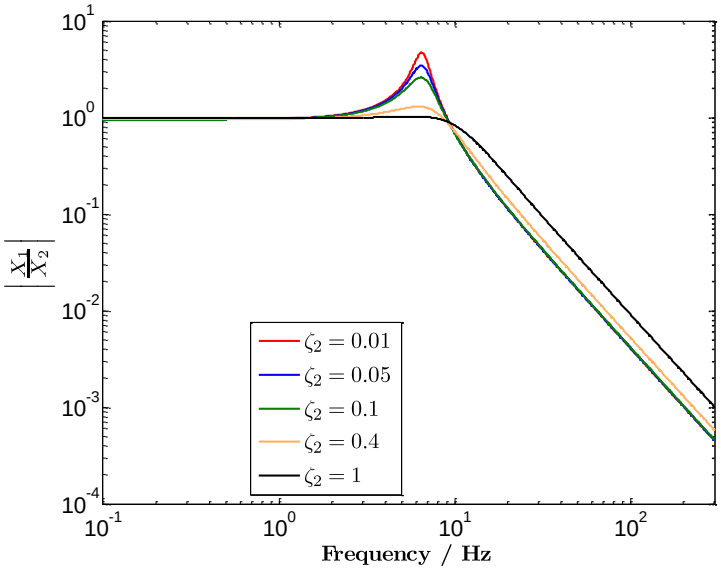

(a) $|X_1/X_2|$ versus frequency

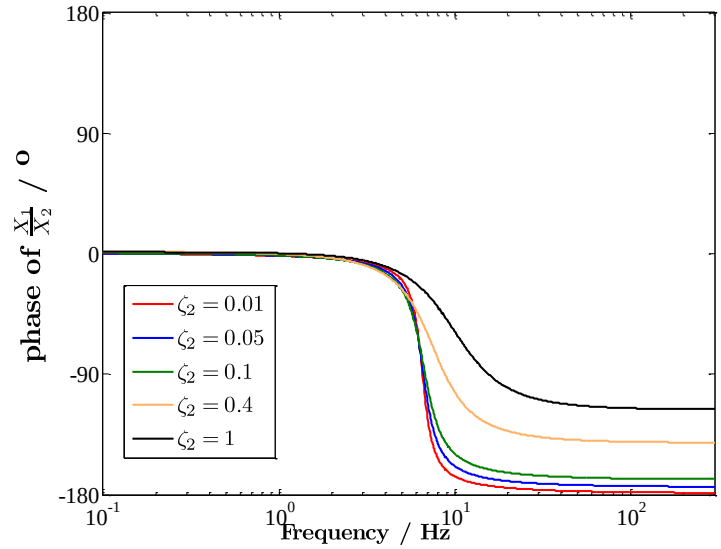

(b) Phase of X_1/X_2 versus frequency

Figure 3.14: The variation of X_1/X_2 with frequency for engine forcing or values of the damping ratio, ζ_2, with hysteretic damping in the mounts

3.4 Frequency dependence of complex stiffness for elastomers

For elastomers, the in-phase shear modulus is related to the out-of-phase shear modulus by the following relation[163]:

$$\frac{dG'}{d(\ln f)} = \frac{2G''}{\pi} \tag{3.25}$$

This arises from an approximation to the Kronig-Kramers relations, which can be used to infer causality into a physical system.

The loss factor, η, is defined:

$$\eta = \frac{G''}{G'} \tag{3.26}$$

If it is assumed, for the simplest case, that η is independent of frequency and temperature then the following expression can be obtained by substituting Equation (3.26) into Equation (3.25) and integrating:

$$G' = G_0 f^{\frac{2\eta}{\pi}} \tag{3.27}$$

where G_0 is the value of G' at $f = 1$.

The assumption that η is constant is reasonable away from the glass transition region for the elastomer, i.e. at sufficiently high temperatures and low frequencies[164]. As a result of the engine's operating temperature, it is likely that any standard elastomer used in an engine mount would be above its glass transition for the majority of the time used and this assumption would be reasonable.

So at two arbitrary frequencies, f_p and f_q, the ratio of G' is:

$$\frac{G'(f_\mathrm{q})}{G'(f_\mathrm{p})} = \left(\frac{f_\mathrm{q}}{f_\mathrm{p}}\right)^{\frac{2\eta}{\pi}} \tag{3.28}$$

The shear modulus, G, is related to the stiffness, k, via the cross-sectional area and the length of the sample which are both assumed constant for a given sample.

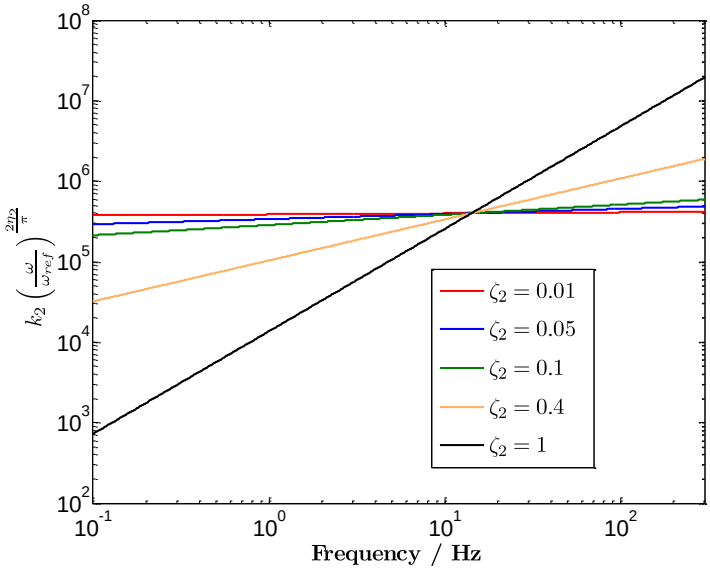

Figure 3.15: The dependence of the stiffness on the frequency for various values of ζ_2

So $G \propto k$, and it follows that:

$$\frac{k'(f_\mathrm{q})}{k'(f_\mathrm{p})} = \left(\frac{f_\mathrm{q}}{f_\mathrm{p}}\right)^{\frac{2\eta}{\pi}} \tag{3.29}$$

This can be used to determine the frequency dependence of both the in-phase and the out-of-phase stiffness of the spring for a given, constant loss factor. This means that the stiffness becomes $k_2(\omega/\omega_\mathrm{ref})^{2\eta_2/\pi}(1+j\eta_2)$ where k_2 is the stiffness at a reference frequency ω_ref. To avoid shifting the resonance of the mount on its spring, ω_ref is chosen to be ω_2. The values of the stiffness for the various values of η_2 (which is the same as $2\zeta_2$) can be seen in Figure 3.15. Substituting this for the stiffness and damping components of the equations in Sections 3.3.1 and 3.3.2, this model can be considered.

3.4.1 Base excitation

Assuming harmonic motion and a circular frequency of ω, the equations of motion for the base excited system are:

$$\begin{aligned} m_1\ddot{x}_1 + k_2\left(\frac{\omega}{\omega_2}\right)^{\frac{2\zeta_2}{\pi}}(1+j\zeta_2)(x_1-x_2) + c_1(\dot{x}_1-\dot{x}_{\text{in}}) + k_1(x_1-X_{\text{in}}) &= 0 \\ m_2\ddot{x}_2 + k_2\left(\frac{\omega}{\omega_2}\right)^{\frac{2\zeta_2}{\pi}}(1+j\zeta_2)(x_2-x_1) &= 0 \end{aligned} \tag{3.30}$$

This leads to:

$$\frac{X_2}{X_{\text{in}}} = \frac{2\zeta_1\frac{j\omega}{\omega_1}+1}{-\frac{k_2}{k_1}\left(\frac{\omega}{\omega_2}\right)^2 + \left(2\zeta_1\frac{j\omega}{\omega_1}+1-\left(\frac{\omega}{\omega_1}\right)^2\right)\left(\frac{\left(\frac{\omega}{\omega_2}\right)^{\frac{4\zeta_2}{\pi}}(1+j2\zeta_2)-\left(\frac{\omega}{\omega_2}\right)^2}{\left(\frac{\omega}{\omega_2}\right)^{\frac{4\zeta_2}{\pi}}(1+j2\zeta_2)}\right)} \tag{3.31}$$

This is shown in Figure 3.16. The inclusion of the frequency dependence of the hysteretic damping mainly affects the high frequency response. There are still two resonance frequencies (at ω_{a} and ω_{b}), although these are shifted due to the changing stiffness. This shift is particularly visible for ω_{b} at high levels of damping. For the very high values of ζ_2 ($\zeta_2 > \pi/4$), the behaviour is not as good as for the viscous damper. However, for the lower values of damping the behaviour is improved with respect to the viscous damper (see Figure 3.2(a)). At high frequencies the phase tends to a value between $-180°$ and $-90°$, dependent on the value of ζ_2.

The following expression is derived for the ratio of X_1 to X_{in}:

$$\frac{X_1}{X_{\text{in}}} = \frac{2\zeta_1\frac{j\omega}{\omega_1}+1}{-\left(\frac{\omega}{\omega_1}\right)^2 - \frac{k_2}{k_1}\left(\frac{\omega}{\omega_2}\right)^{\frac{4\zeta_2}{\pi}}(j2\zeta_2+1)\left(\frac{\left(\frac{\omega}{\omega_2}\right)^2}{\left(\frac{\omega}{\omega_2}\right)^{\frac{4\zeta_2}{\pi}}(1+j2\zeta_2)-\left(\frac{\omega}{\omega_2}\right)^2}\right) + 2\zeta_1\frac{j\omega}{\omega_1}+1} \tag{3.32}$$

This is shown in Figure 3.17. The lower frequency behaviour is similar to that of the hysteretic damper (Figure 3.10). The resonance and anti-resonance frequencies are shifted due to the frequency and damping dependence of the stiffness, and this is most visible for the anti-resonance and the second resonance (ω_{b}) at the higher values of the damping. The high frequency behaviour, like that

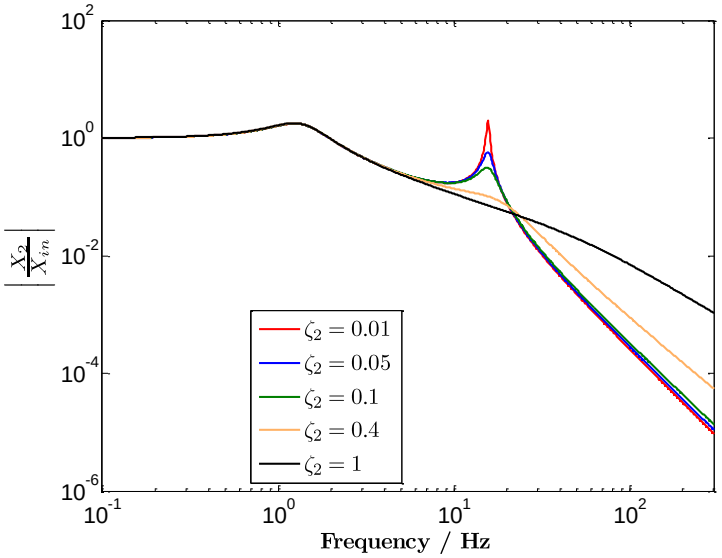

(a) $|X_2/X_{\text{in}}|$ versus frequency

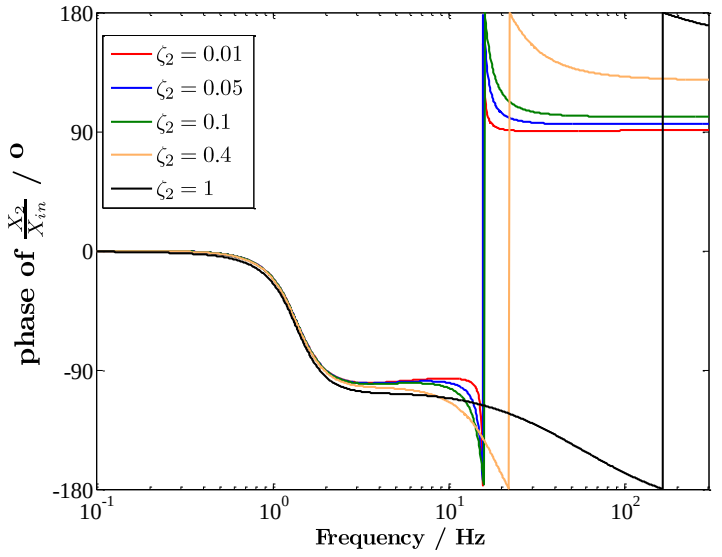

(b) Phase of X_2/X_{in} versus frequency

Figure 3.16: The variation of X_2/X_{in} with frequency for base excitation for values of the damping ratio, ζ_2, with frequency dependent hysteretic damping in the mounts

for the hysteretic damper and the viscous damper is dependent upon ζ_1 and not, therefore, affected by the frequency dependence. In the phase plot (Figure 3.17(b)) the shifting of the resonance frequency for the high levels of damping is clear when compared with Figure 3.10(b).

Considering the ratio of X_2 to X_1:

$$\frac{X_2}{X_1} = \frac{\left(\frac{\omega}{\omega_2}\right)^{\frac{4\zeta_2}{\pi}} (1 + j2\zeta_2)}{\left(\frac{\omega}{\omega_2}\right)^{\frac{4\zeta_2}{\pi}} (1 + j2\zeta_2) - \left(\frac{\omega}{\omega_2}\right)^2} \tag{3.33}$$

Looking at Figure 3.18, at and below the resonance frequency the behaviour is virtually identical to that seen for the hysteretic damper. This resonance occurs at ω_2, although particularly for the higher levels of damping this is shifted more than seen previously (as damping will shift the resonance frequency slightly). This is because the stiffness at frequencies higher than ω_2 is increased with increasing damping. At high frequencies it can be seen that the inclusion of the frequency dependence compromises the high frequency advantage of the hysteretic damper, particularly for high values of the damping ratio, ζ_2. This is because at high frequencies the equation now has a frequency dependence. Very high ζ_2 is now detrimental to the high frequency behaviour when compared with the viscous damper. For the lower values of ζ_2 (up to $\pi/4$) this frequency-dependent damping is still advantageous. The phase at high frequencies tends to a value between -180° and -90°, dependent on the value of ζ_2, although these values are different from those for the hysteretic damper.

3.4.2 Engine-forced vibration

When harmonic motion is assumed, the equations of motion for the engine-forced vibration system are:

$$\begin{aligned} m_1\ddot{x}_1 + k_2\left(\frac{\omega}{\omega_2}\right)^{\frac{2\eta_2}{\pi}}(1 + j\eta_2)(x_1 - x_2) + c_1\dot{x}_1 + k_1x_1 &= 0 \\ m_2\ddot{x}_2 + k_2\left(\frac{\omega}{\omega_2}\right)^{\frac{2\eta_2}{\pi}}((1 + j\eta_2)(x_2 - x_1) &= m_2\ddot{x}_{2\mathrm{f}} \end{aligned} \tag{3.34}$$

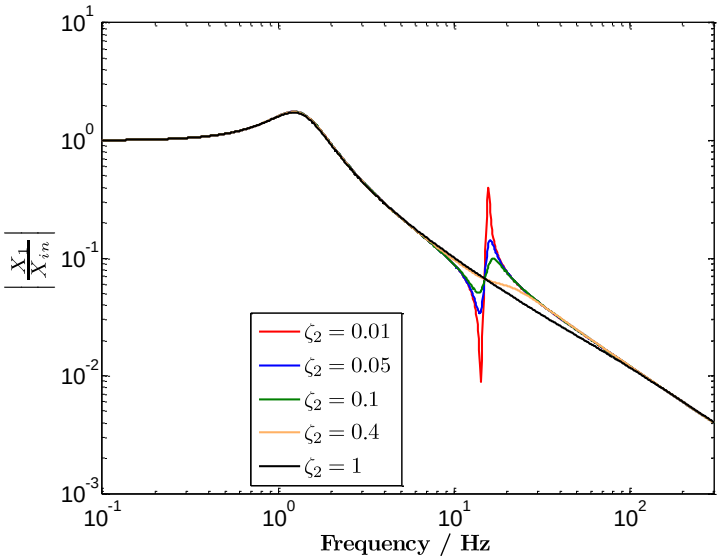

(a) $|X_1/X_{\text{in}}|$ versus frequency

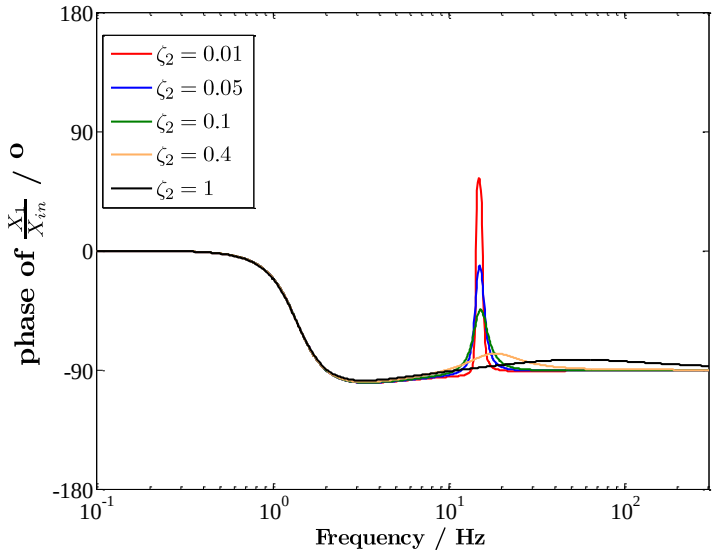

(b) Phase of X_1/X_{in} versus frequency

Figure 3.17: The variation of X_1/X_{in} with frequency for base excitation for values of the damping ratio, ζ_2, with frequency dependent hysteretic damping in the mounts

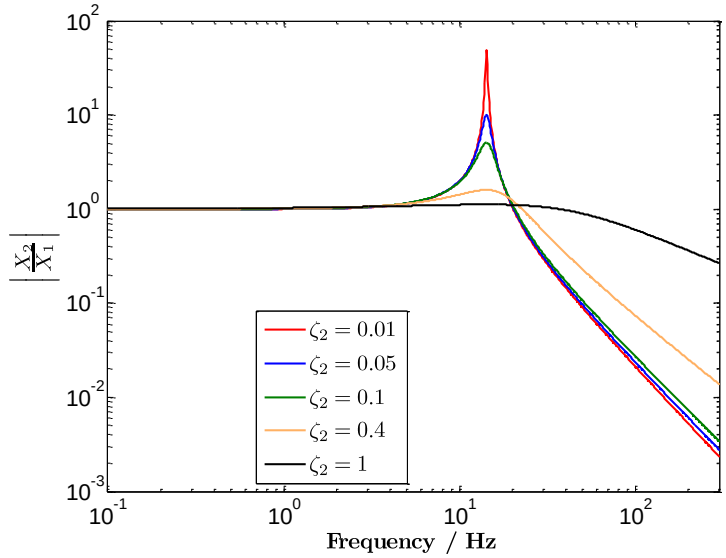

(a) $|X_2/X_1|$ versus frequency

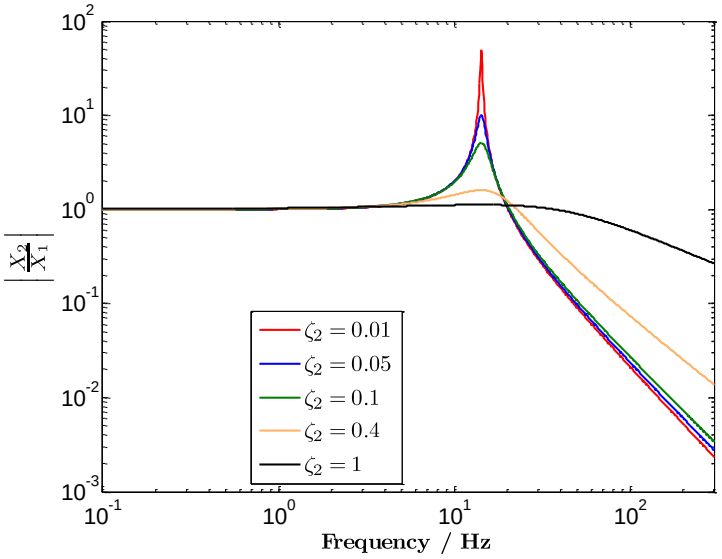

(b) Phase of X_2/X_1 versus frequency

Figure 3.18: The variation of X_2/X_1 with frequency for base excitation for values of the damping ratio, ζ_2, with frequency dependent hysteretic damping in the mounts

This leads to:

$$\frac{X_2}{X_{2\mathrm{f}}} = \frac{\left(\frac{\omega}{\omega_2}\right)^2}{\left(\frac{\omega}{\omega_2}\right)^2 + \left(\frac{\omega}{\omega_2}\right)^{\frac{4\zeta_2}{\pi}} (j2\zeta_2 + 1) \left(\frac{\left(\frac{\omega}{\omega_1}\right)^2 - 2\zeta_1 \frac{j\omega}{\omega_1} - 1}{2\zeta_1 \frac{j\omega}{\omega_1} + 1 - \left(\frac{\omega}{\omega_1}\right)^2 + \frac{k_2}{k_1}\left(\frac{\omega}{\omega_2}\right)^{\frac{4\zeta_2}{\pi}} (j2\zeta_2+1)} \right)} \tag{3.35}$$

This is shown in Figure 3.19. The behaviour is similar to that found for the hysteretic damper (Figure 3.12). However, there are a few notable differences. The first is the low frequency behaviour. Increasing ζ_2 affects the rate at which the response tends to 0, as the frequency tends to 0. The high values of ζ_2 show significantly higher values of $|X_2/X_{2\mathrm{f}}|$ at low frequencies. The next difference is at the first resonance peak. Increasing the value of ζ_2 also increases the height of this peak slightly. Further, the resonances and anti-resonance are shifted in frequency as the damping increases. The high frequency limit of 1 is still observed. The differences are again caused by the introduction of the frequency and damping dependent stiffness.

For the response of the lower mass:

$$\frac{X_1}{X_{2\mathrm{f}}} = \frac{\left(\frac{\omega}{\omega_2}\right)^2}{\left(\frac{\omega}{\omega_2}\right)^2 \left(\frac{2\zeta_1 \frac{j\omega}{\omega_1} + 1 - \left(\frac{\omega}{\omega_1}\right)^2 + \frac{k_2}{k_1}\left(\frac{\omega}{\omega_2}\right)^{\frac{4\zeta_2}{\pi}} (j2\zeta_2+1)}{\frac{k_2}{k_1}\left(\frac{\omega}{\omega_2}\right)^{\frac{4\zeta_2}{\pi}} (j2\zeta_2+1)} \right) + \frac{k_1}{k_2}\left(\left(\frac{\omega}{\omega_1}\right)^2 - 2\zeta_1 \frac{j\omega}{\omega_1} - 1\right)} \tag{3.36}$$

This is shown in Figure 3.20. The behaviour until the second resonance is reached, is not affected by ζ_2 and the inclusion of the frequency and damping dependence into the stiffness is not noticeable. The second resonance corresponding to ω_{b} is shifted slightly. Also, the rate of decay at high frequencies is significantly affected for high values of damping. The inclusion of the frequency and damping dependence of the stiffness also affects the phase at high frequencies.

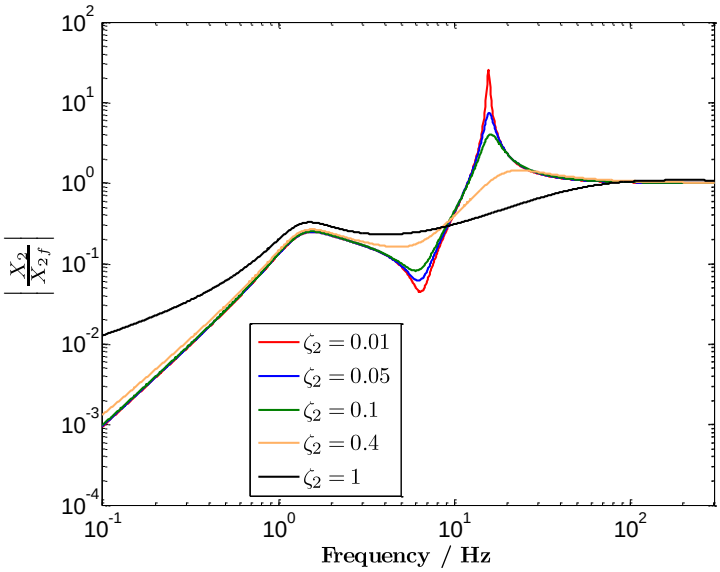

(a) $|X_2/X_{2\mathrm{f}}|$ versus frequency

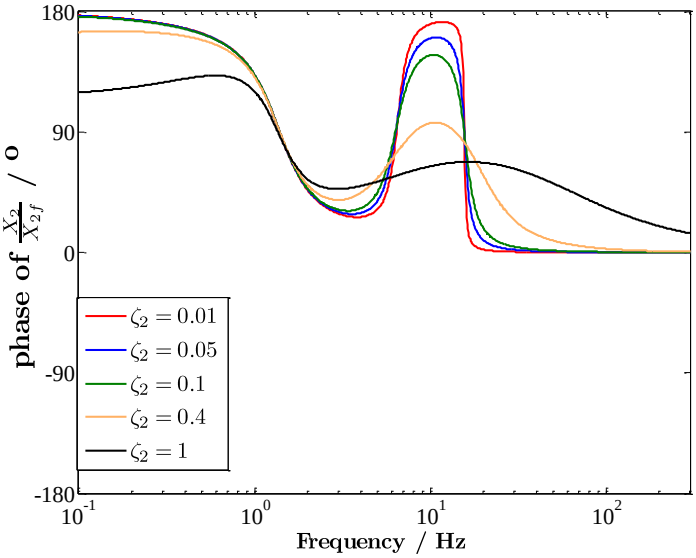

(b) Phase of $X_2/X_{2\mathrm{f}}$ versus frequency

Figure 3.19: The variation of $X_2/X_{2\mathrm{f}}$ with frequency for engine forcing for values of the damping ratio, ζ_2, with frequency dependent hysteretic damping in the mounts

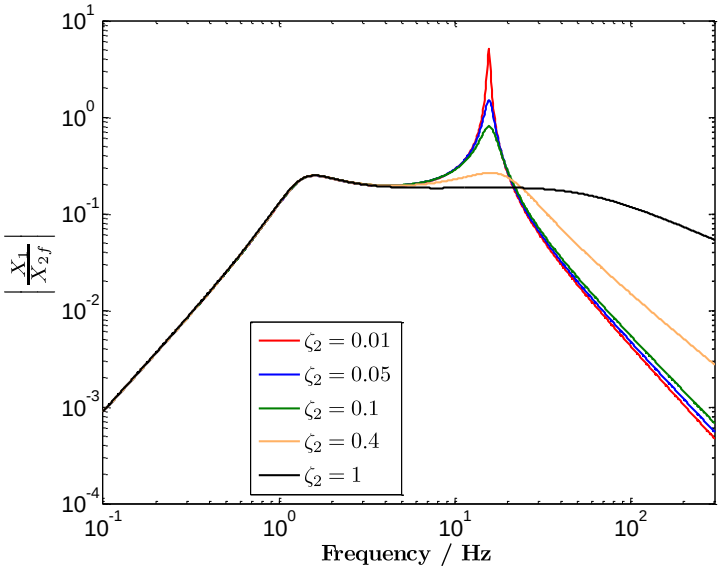

(a) $|X_1/X_{2\mathrm{f}}|$ versus frequency

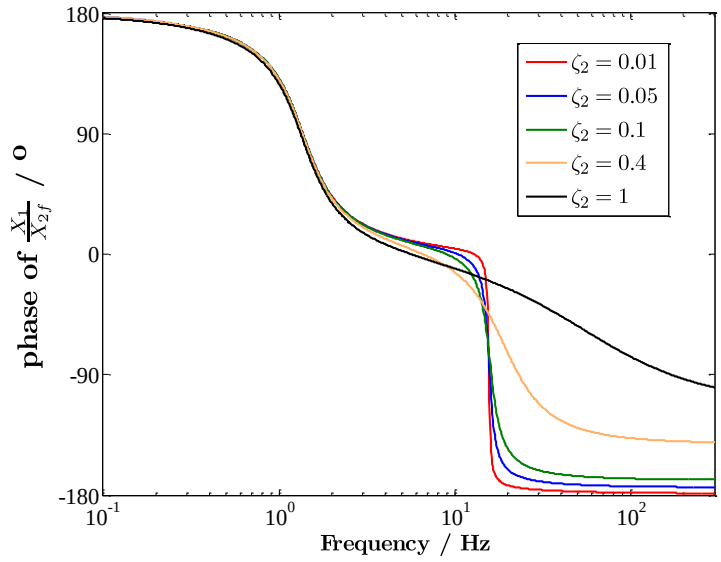

(b) Phase of $X_1/X_{2\mathrm{f}}$ versus frequency

Figure 3.20: The variation of $X_1/X_{2\mathrm{f}}$ with frequency for engine forcing for values of the damping ratio, ζ_2, with frequency dependent hysteretic damping in the mounts

From Equation (3.34) an expression for X_1/X_2 can be derived:

$$\frac{X_1}{X_2} = \frac{\frac{k_2}{k_1}\left(\frac{\omega}{\omega_2}\right)^{\frac{4\zeta_2}{\pi}}(j2\zeta_2+1)}{2\zeta_1\frac{j\omega}{\omega_1}+1-\left(\frac{\omega}{\omega_1}\right)^2+\frac{k_2}{k_1}\left(\frac{\omega}{\omega_2}\right)^{\frac{4\zeta_2}{\pi}}(j2\zeta_2+1)} \tag{3.37}$$

This is plotted in Figure 3.21. Similar to the hysteretic damping case, as the frequency tends to 0 the asymptotic limit for X_1/X_2 is dependent on ζ_2. However, in this case for the high values of damping it is no longer close to 1 as the frequency and damping dependence of the stiffness plays a role. For the high damping levels (e.g. $\zeta_2 = 1$) the low frequency value is significantly less than 1. At high frequencies, as for the base excitation case above, the rate of decay is dependent on ζ_2 and the phase tends to a constant value between $-90°$ and $-180°$. High ζ_2 still reduces the peak at the resonance frequency and it shifts the resonance to a lower frequency (this is due to the shift in the anti-resonance from Equation (3.35)). This is as a result of the frequency and damping dependence of the stiffness.

3.4.3 Summary

It should be noted that in modelling the behaviour of a viscoelastic mount, the high values of damping used in these models are unlikely to be achieved in practice with an elastomer, especially at the elevated temperatures likely to be found under a car engine. If they were achieved using an elastomer, the elastomer would have to be operating near its glass transition, making the assumption that η_2 is not frequency or temperature dependent not valid. However, the lower values for the damping would be achievable and the assumptions still valid. Typically the value of damping ratio for natural rubber varies between approximately 0.02 and 0.2 (the former for an unfilled formulation and the latter for a specially formulated high damping compound).

The advantages of the hysteretic damper observed in Section 3.3 over the viscous damper are reduced by the inclusion of the frequency and damping dependence of the stiffness. The high frequency behaviour for the lower values of the damping is still desirable when compared with the viscous damper. High damping is still advantageous around the resonance frequencies and not desirable at high

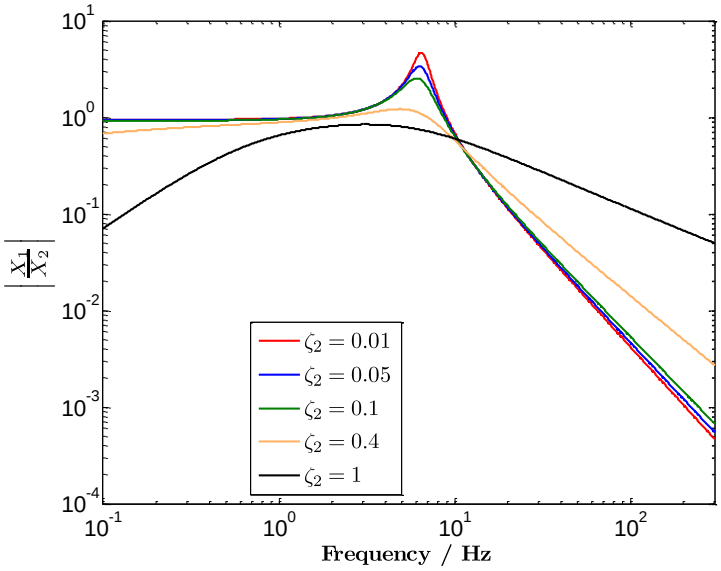

(a) $|X_1/X_2|$ versus frequency

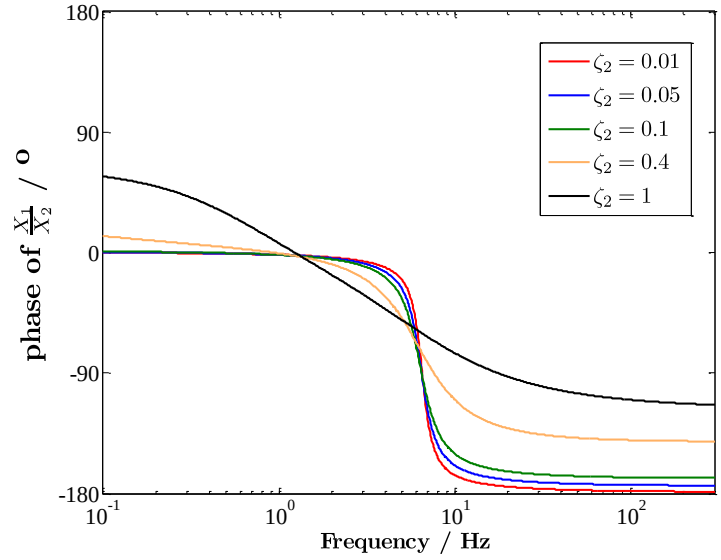

(b) Phase of X_1/X_2 versus frequency

Figure 3.21: The variation of X_1/X_2 with frequency for engine forcing for values of the damping ratio, ζ_2, with frequency dependent hysteretic damping in the mounts

frequencies. The low frequency behaviour is also affected by the damping and is not as desirable as in the hysteretic and the viscous cases.

As mentioned above, it is not possible in practice to have a passive, solely elastomer based mount with ζ_2 as high as 1, or even 0.4. Other methods to introduce higher damping include using a hydromount and using an adaptive or active or control system. The latter is considered in the next sections.

3.5 Skyhook damper

The skyhook damper is a theoretical approach, where a damper is attached in this case between the upper mass (the engine) and a fixed reference point, to achieve better characteristics. A diagram for the skyhook damper set-up can be seen in Figure 3.22 for base excitation.

Active and semi-active control often aims to achieve these characteristics of damping via algorithms. For active control skyhook damping can be approximated by the inclusion of an actuator between the engine and the chassis, replacing or in parallel with the passive mount. The output from this actuator is set to be proportional to the velocity of the engine mass and can be achieved via feed-forward or feed-back control. In practice the actuator also will exert a force on the chassis, but this is neglected in the present analysis.

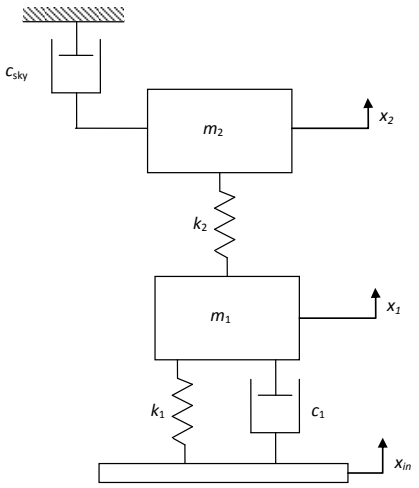

Figure 3.22: Two-degrees-of-freedom system with a skyhook damper, base excited

3.5.1 Base excitation

The equations of motion for the system, with base excitation, shown in Figure 3.22 are:

$$\begin{aligned} m_2\ddot{x}_2 + c_{\text{sky}}\dot{x}_2 + k_2(x_2 - x_1) &= 0 \\ m_1\ddot{x}_1 + k_2(x_1 - x_2) + c_1(\dot{x}_1 - \dot{x}_{\text{in}}) + k_1(x_1 - X_{\text{in}}) &= 0 \end{aligned} \tag{3.38}$$

Writing $c_{\text{sky}} = 2\zeta_{\text{sky}}k_2/\omega_2$, then as in the examples above, expressions can be derived for the relative movements of the masses with respect to each other and the input under steady-state harmonic motion. This leads to:

$$\frac{X_2}{X_{\text{in}}} = \frac{1 + 2\zeta_1\frac{j\omega}{\omega_1}}{\left(\frac{k_2}{k_1} + 1 + 2\zeta_1\frac{j\omega}{\omega_1} - \left(\frac{\omega}{\omega_1}\right)^2\right)\left(1 + 2\zeta_{\text{sky}}\frac{j\omega}{\omega_2} - \left(\frac{\omega}{\omega_2}\right)^2\right) - \frac{k_2}{k_1}} \tag{3.39}$$

This is shown in Figure 3.23. Interestingly, unlike any of the previous cases, ζ_{sky} has a significant effect on the peak response of the first resonance. This is because both masses move together at the first resonance, so any damping dependent on the relative displacements of the two masses (like the viscous or the hysteretic examples), does not affect the resonance. However, the damping to the motion caused by ζ_{sky} is dependent on the motion of m_2 which has a peak at this resonance. At low frequencies X_2/X_{in} tends to 1 as before. At high frequencies the decay is -60 dB/decade with a phase of 90° which suggests it is damping-controlled. The equation tends to $j2\zeta_1\omega_2^2\omega_1/\omega^3$ at high frequencies meaning it is independent of ζ_{sky}, although it is dependent upon ζ_1.

Considering the motion of m_1 with respect to the input:

$$\frac{X_1}{X_{\text{in}}} = \frac{1 + 2\zeta_1\frac{j\omega}{\omega_1}}{-\left(\frac{\omega}{\omega_1}\right)^2 + \frac{k_2}{k_1}\left(\frac{2\zeta_{\text{sky}}\frac{j\omega}{\omega_2} - \left(\frac{\omega}{\omega_2}\right)^2}{1 + 2\zeta_{\text{sky}}\frac{j\omega}{\omega_2} - \left(\frac{\omega}{\omega_2}\right)^2}\right) + 1 + 2\zeta_1\frac{j\omega}{\omega_1}} \tag{3.40}$$

This is shown in Figure 3.24. At low frequencies this tends to 1. At high frequencies it tends to $j2\zeta_1\omega_1/\omega$. This decays as -20 dB/decade and the phase goes to $-90°$. Again the response at both the resonances shows dependence on the value of ζ_{sky}.

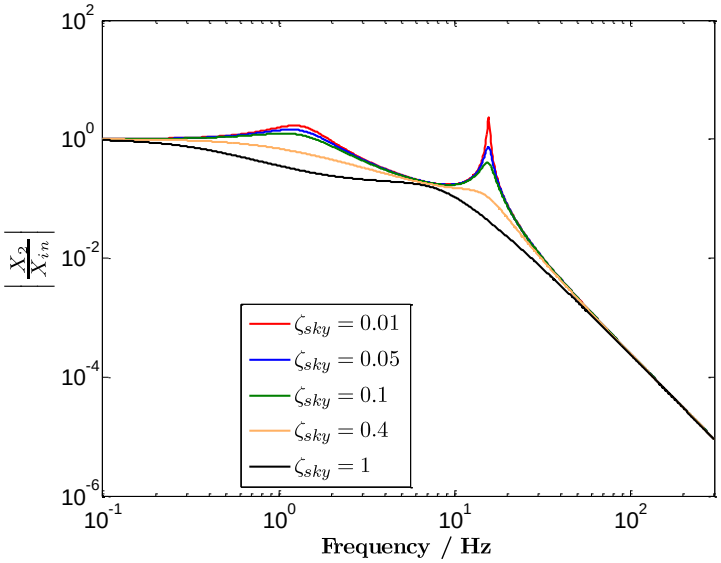

(a) $|X_2/X_{\text{in}}|$ versus frequency

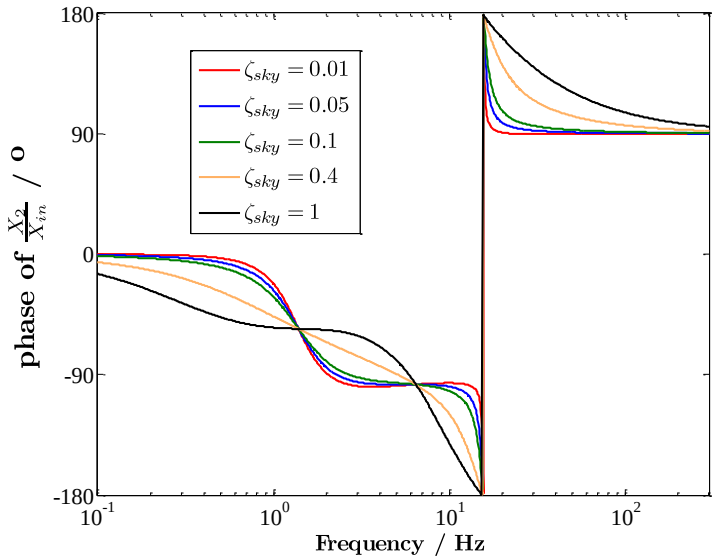

(b) Phase of X_2/X_{in} versus frequency

Figure 3.23: The variation of X_2/X_{in} with frequency for base excitation for various values of the damping ratio, ζ_{sky}, for the skyhook damper

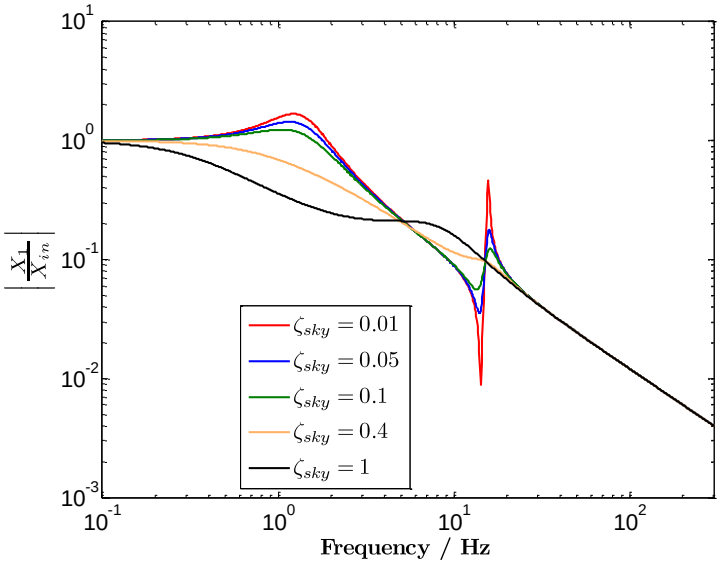

(a) $|X_1/X_{\text{in}}|$ versus frequency

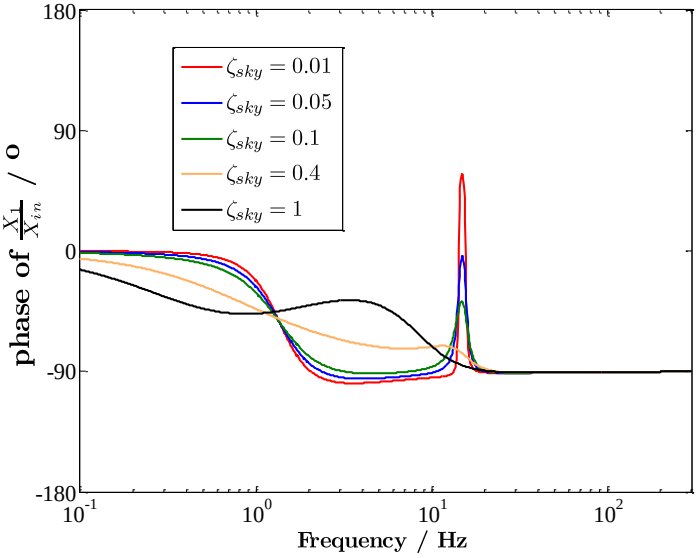

(b) Phase of X_1/X_{in} versus frequency

Figure 3.24: The variation of X_1/X_{in} with frequency for base excitation for various values of the damping ratio, ζ_{sky}, for the skyhook damper

The other ratio to consider for the base excitation case is:

$$\frac{X_2}{X_1} = \frac{1}{1 + 2\zeta_{\text{sky}}\frac{j\omega}{\omega_2} - \left(\frac{\omega}{\omega_2}\right)^2} \tag{3.41}$$

which is shown in Figure 3.25. As the frequency approaches 0, X_2/X_1 tends to 1. At high frequencies there is no dependence on the damping as the equation tends to $(\omega_2/\omega)^2$, so there is a -40 dB/decade decline and the phase is 180° as there is no $j\zeta_{\text{sky}}$ term in the numerator (compare Equation (3.10) for viscous damping). This is because the skyhook damper is assumed not to be connected to m_1. The high frequency behaviour is even more desirable than that of the hysteretic damper, as there is no penalty to having larger damping at all. The response at the resonance is $-j/2\zeta_{\text{sky}}$ and the phase is $-90°$. This means that the peak is lower than that with either the hysteretic damper or the viscous damper for all values of damping of the second mass, and as ζ_{sky} increases the value at the resonance actually drops below 1 (the best achievable for the other types). In fact $\zeta_{\text{sky}} = 0.5$ gives a value of exactly 1 at the resonance frequency. It is, therefore, possible to achieve a similar response with a lower level of damping compared with the hysteretic and viscous damping cases. Due to the phase relation, the fact that the amplitude can go below 1 at the resonance is not necessarily desirable. This is because below the resonance frequency for high damping the response starts dropping below 1 and the two masses stop being in phase. Ideally for low frequency base excitation inputs (for example going over a bump in the road), the car and engine should move in phase (together), so the engine does not hit the bonnet of the car (or the upper stops). The best compromise might be to use the sky-hook damper with high damping for base excitation around and above the resonance frequency, but the hysteretic or the viscous damper at low frequencies.

3.5.2 Engine-forced vibration

Similarly the equations of motion for the forced vibration case are:

$$\begin{aligned} m_1\ddot{x}_1 + k_2(x_1 - x_2) + c_1\dot{x}_1 + k_1x_1 &= 0 \\ m_2\ddot{x}_2 + c_{\text{sky}}\dot{x}_2 + k_2(x_2 - x_1) &= f_{\text{in}} \end{aligned} \tag{3.42}$$

Again letting $F_{\text{in}} = -m_2\omega^2X_{2\text{f}}$ for harmonic motion allows the following equation

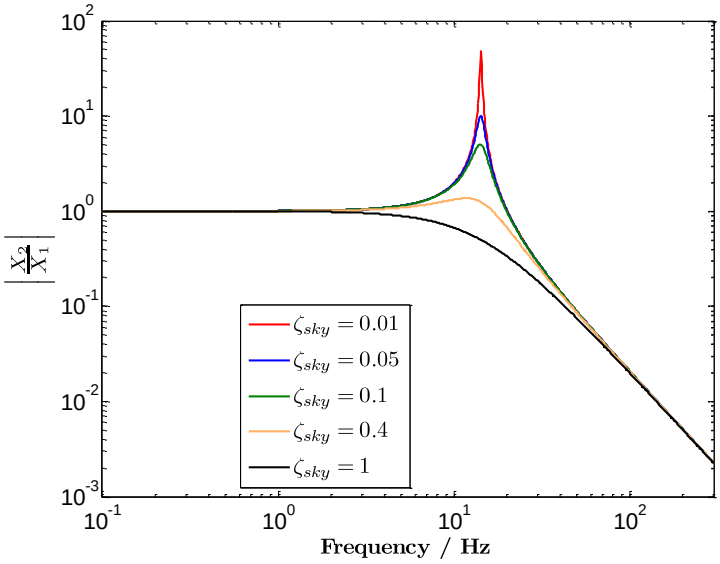

(a) $|X_2/X_1|$ versus frequency

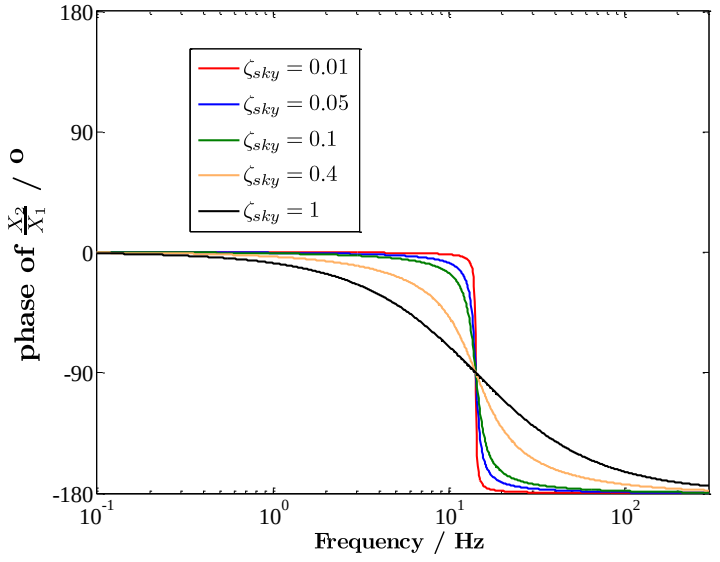

(b) Phase of X_2/X_1 versus frequency

Figure 3.25: The variation of X_2/X_1 with frequency for base excitation for various values of the damping ratio, ζ_{sky}, for the skyhook damper

to be derived:

$$\frac{X_2}{X_{2\mathrm{f}}} = \frac{\frac{\omega^2 m_2}{k_1}}{\left(\left(\frac{\omega}{\omega_2}\right)^2 - 2\zeta_{\mathrm{sky}}\frac{j\omega}{\omega_2} - 1\right)\left(1 + 2\zeta_1\frac{j\omega}{\omega_1} - \left(\frac{\omega}{\omega_1}\right)^2\right) + \frac{k_2}{k_1}\left(\left(\frac{\omega}{\omega_2}\right)^2 - 2\zeta_{\mathrm{sky}}\frac{j\omega}{\omega_2}\right)} \tag{3.43}$$

The response can be seen in Figure 3.26. As the frequency tends to 0, $X_2/X_{2\mathrm{f}}$ tends to $\omega^2(k_2 + k_1)/\omega_2^2 k_1$, which has a gradient of 40 dB/decade. At high frequencies the equation tends to 1. The highest value of ζ_{sky} gives an interesting behaviour, where the peak values at the resonances have been significantly shifted, although the 90° phase is at the same frequency. The second resonance peak occurs at a lower frequency than those for the other values of ζ_{sky} and is nearer the anti-resonance in the others. At high frequencies the phase goes to 0°, but at low frequencies it is 180°. As seen previously, the high frequency behaviour suggests that the engine is behaving like the uncoupled mass.

For the response of the chassis

$$\frac{X_1}{X_{2\mathrm{f}}} = \frac{\left(\frac{\omega}{\omega_2}\right)^2}{\left(\frac{\omega}{\omega_2}\right)^2 - 2\zeta_{\mathrm{sky}}\frac{j\omega}{\omega_2} + \frac{\left(\frac{\omega}{\omega_1}\right)^2 - 2\zeta_1\frac{j\omega}{\omega_1} - 1}{1 + \frac{k_2}{k_1} + 2\zeta_1\frac{j\omega}{\omega_1} - \left(\frac{\omega}{\omega_1}\right)^2}} \tag{3.44}$$

which is plotted in Figure 3.27. As the frequency tends to 0 the ratio tends to $\omega^2 m_2/k_1$, which has a gradient of −40 dB/decade. At high frequencies the decay is also 40 dB/decade with the equation becoming $m_2\omega_2^2/m_1\omega^2$. At high levels of damping, the first resonance is not clearly visible. In fact it is arguable that the largest effect of sky-hook damping is visible here. A smaller peak in the resonance is beneficial for the transmission of the engine vibration to the chassis and using a sky-hook damper can achieve better values than are achieved with either the hysteretic damper or the viscous damper. The high frequency behaviour is better than both the viscous and the hysteretic dampers because it is not dependent on the high value of the damping.

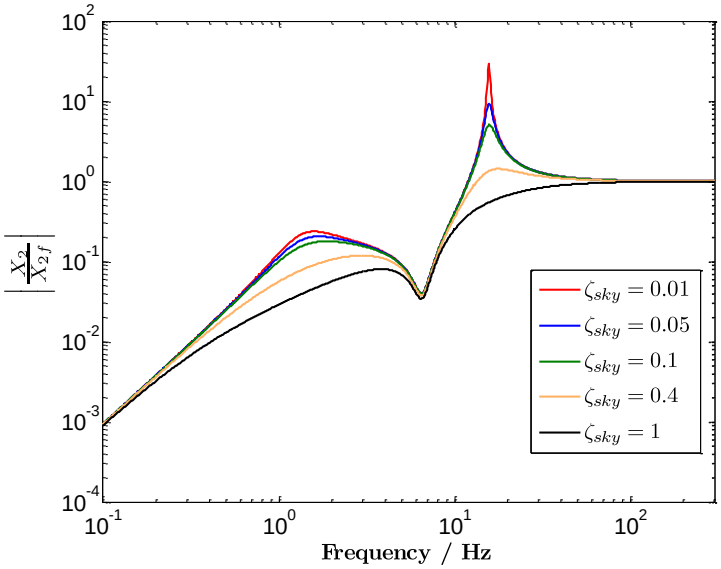

(a) $|X_2/X_{2\mathrm{f}}|$ versus frequency

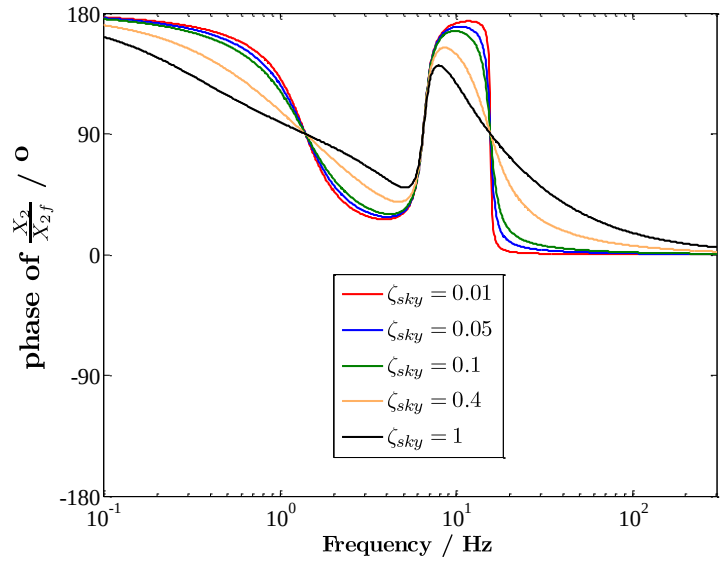

(b) Phase of $X_2/X_{2\mathrm{f}}$ versus frequency

Figure 3.26: The variation of $X_2/X_{2\mathrm{f}}$ with frequency for engine forcing for various values of the damping ratio, ζ_{sky}, for the skyhook damper

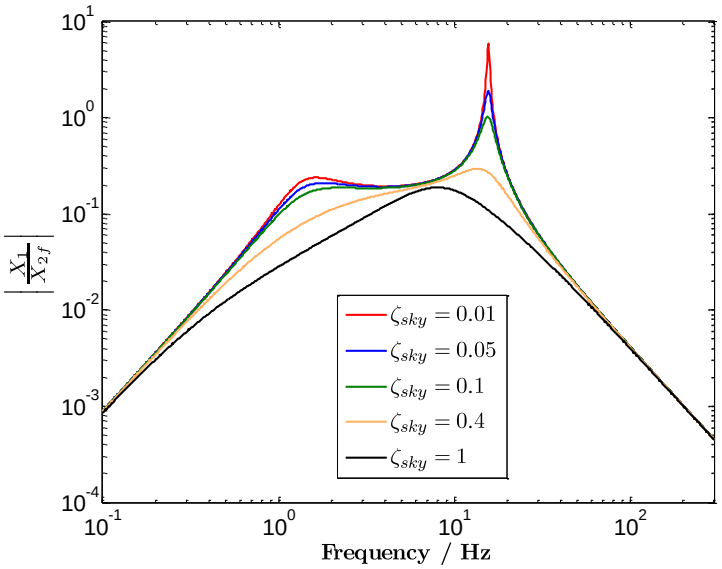

(a) $|X_1/X_{2\mathrm{f}}|$ versus frequency

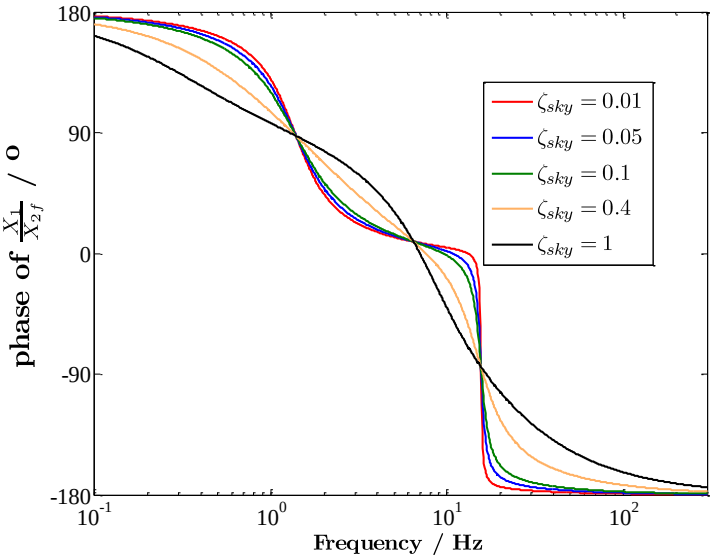

(b) Phase of $X_1/X_{2\mathrm{f}}$ versus frequency

Figure 3.27: The variation of $X_1/X_{2\mathrm{f}}$ with frequency for engine forcing for various values of the damping ratio, ζ_{sky}, for the skyhook damper

The next ratio considered is:

$$\frac{X_1}{X_2} = \frac{\frac{k_2}{k_1}}{1 + \frac{k_2}{k_1} + 2\zeta_1 \frac{j\omega}{\omega_1} - \left(\frac{\omega}{\omega_1}\right)^2} \tag{3.45}$$

This is shown in Figure 3.28. The value of ζ_{sky} does not have any effect, as it is not contained in Equation (3.45). However, this ratio is not as important to consider as $X_1/X_{2\text{f}}$. As the frequency goes to 0 the ratio tends to $1/(k_1/k_2+1)$, as in the viscous damping case. At high frequencies the equation tends to $k_2/m_1\omega^2$. This means that the decay is again -40 dB/decade and the phase angle is $-180°$.

3.5.3 Summary

Overall it is beneficial to have skyhook damping for frequencies above the engine resonance, ω_2, but below this it could be detrimental for the base excitation case and beneficial for the engine-forced vibration case for the reasons discussed above.

One advantage of using an algorithm with an actuator is that very high values for the damping are achievable. It is also possible to have different regimes in different frequency regions by changing the response of the actuator depending on the frequencies detected by the control accelerometers. The actuator could give a force like that of a viscous damper, or a hysteretic damper, or with different values of damping for the skyhook damper. However, this would require power input.

3.6 Groundhook damper

The groundhook damper approach is similar to that of the skyhook approach, but with the damper between the lower mass (in this case the car body) and the fixed reference point (see Figure 3.29).

Although this approach as described here is also purely theoretical, it is possible to achieve this sort of response using a control algorithm. In this case, the output of the actuator would be proportional to the velocity of the chassis and achieved through feed-forward or feed-back control.

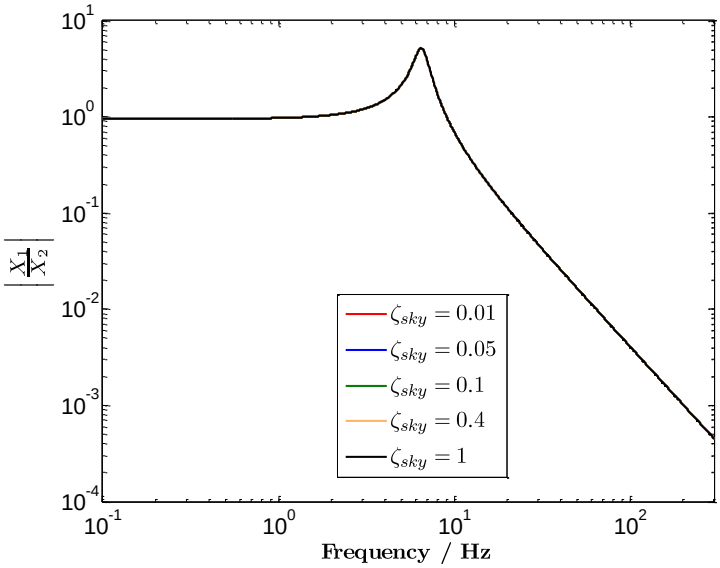

(a) $|X_1/X_2|$ versus frequency

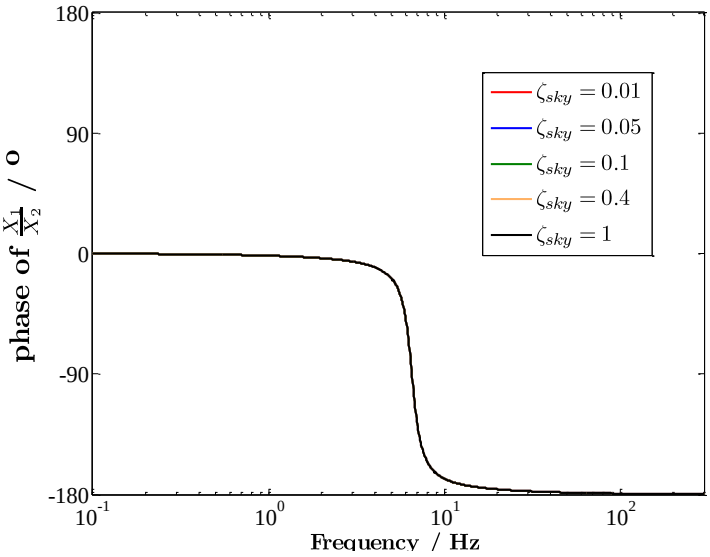

(b) Phase of X_1/X_2 versus frequency

Figure 3.28: The variation of X_1/X_2 with frequency for engine forcing for various values of the damping ratio, ζ_{sky}, for the skyhook damper

3.6.1 Base excitation

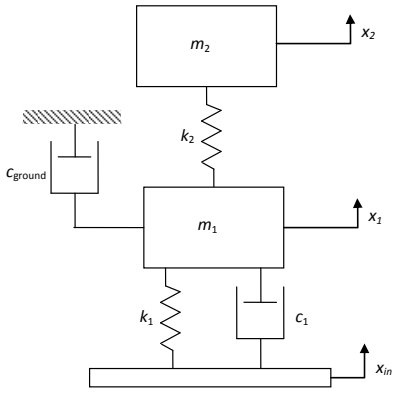

Figure 3.29: Two-degrees-of-freedom system with a groundhook damper, base excited

For the case of base excitation (Figure 3.29) the following equations of motion apply:

$$\begin{aligned} m_1\ddot{x}_1 + c_{\text{ground}}\dot{x}_1 + k_2(x_1 - x_2) + c_1(\dot{x}_1 - \dot{x}_{\text{in}}) + k_1(x_1 - X_{\text{in}}) &= 0 \\ m_2\ddot{x}_2 + k_2(x_2 - x_1) &= 0 \end{aligned} \tag{3.46}$$

Assuming that $\zeta_{\text{ground}} = c_{\text{ground}}/2m_2\omega_2$, under steady-state harmonic motion these give:

$$\frac{X_2}{X_{\text{in}}} = \frac{1 + 2\zeta_1\frac{j\omega}{\omega_1}}{\left(1 - \left(\frac{\omega}{\omega_2}\right)^2\right)\left(1 + 2\zeta_1\frac{j\omega}{\omega_1} + 2\zeta_{\text{ground}}\frac{k_2 j\omega}{k_1\omega_2} - \left(\frac{\omega}{\omega_1}\right)^2\right) + \frac{m_2}{k_1}\omega^2} \tag{3.47}$$

The response can be seen in Figure 3.30. This relation also tends to 1 at low frequencies, but at high frequencies it tends to $j2\zeta_1\omega_2^2\omega_1/\omega^3$. This means that the ratio decays at -60 dB/decade and the phase tends to 90°. As for the sky-hook damping the value of ζ_{ground} affects the height of the first resonance. This is because it is dependent on the absolute motion of the first mass, rather than on the relative motion between the masses. As seen in Figure 3.32, the masses are moving at the same amplitude as each other, in phase, so there is no relative motion. There is little effect of the damping on the second resonance, so having

high groundhook damping in this region is not beneficial.

The ratio of X_1/X_{in} is also considered:

$$\frac{X_1}{X_{\text{in}}} = \frac{1 + 2\zeta_1 \frac{j\omega}{\omega_1}}{1 + 2\zeta_1 \frac{j\omega}{\omega_1} - \left(\frac{\omega}{\omega_1}\right)^2 + \frac{k_2}{k_1}\left(2\zeta_{\text{ground}} \frac{j\omega}{\omega_2} + \frac{\left(\frac{\omega}{\omega_2}\right)^2}{\left(\frac{\omega}{\omega_2}\right)^2 - 1}\right)} \tag{3.48}$$

This is shown in Figure 3.31. This also tends to 1 at low frequencies, but at high frequencies it tends to $-j2\zeta_1\omega_1/\omega$. This means that the equation decays at -20 dB/decade and the phase tends to $-90°$. As above, the value of ζ_{ground} affects the height of the first resonance, but has only limited effect on the second resonance.

Finally for the base excitation case the ratio of the two responses is derived as:

$$\frac{X_2}{X_1} = \frac{1}{1 - \left(\frac{\omega}{\omega_2}\right)^2} \tag{3.49}$$

This behaves like a single-degree-of-freedom system with no damping. At low frequencies X_2/X_1 tends to 1 with a 0° phase and at high frequencies it goes to $(\omega_2/\omega)^2$ (Figure 3.32). The high frequency decay is -40 dB/decade. At the resonance the response is infinite. There is no effect on the response due to changes in the value of ζ_{ground}. For this base-excitation situation, at the resonance, this is clearly unsuitable for keeping the chassis and mount moving together. However, this assumes that there is no source of damping between the two masses. Any mount located between the masses would provide some damping although this might be very small.

3.6.2 Engine-forced vibration

For the engine-forced vibration situation, this is basically the same situation as the base-excitation case above with the assumption made that the base is a fixed reference point. This means that the damping provided by the groundhook damper is adding to that provided by the suspension (c_1 in Section 3.2.2). For this model there is still no damping considered between the two masses. The

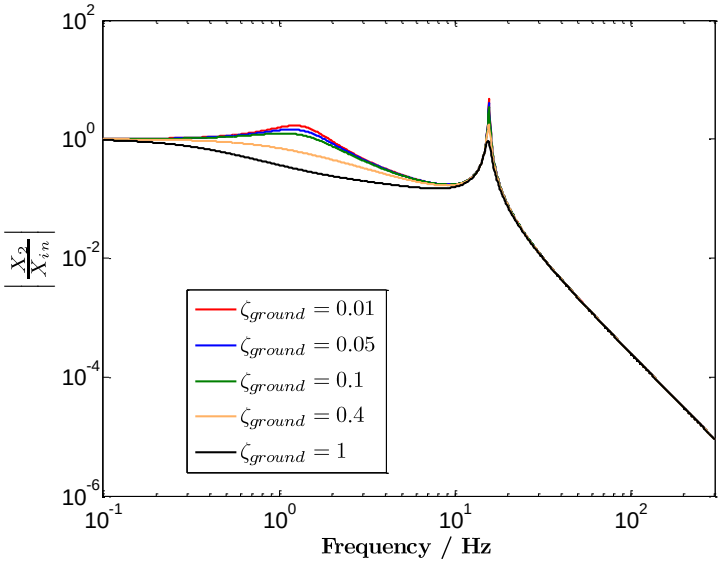

(a) $|X_2/X_{\text{in}}|$ versus frequency

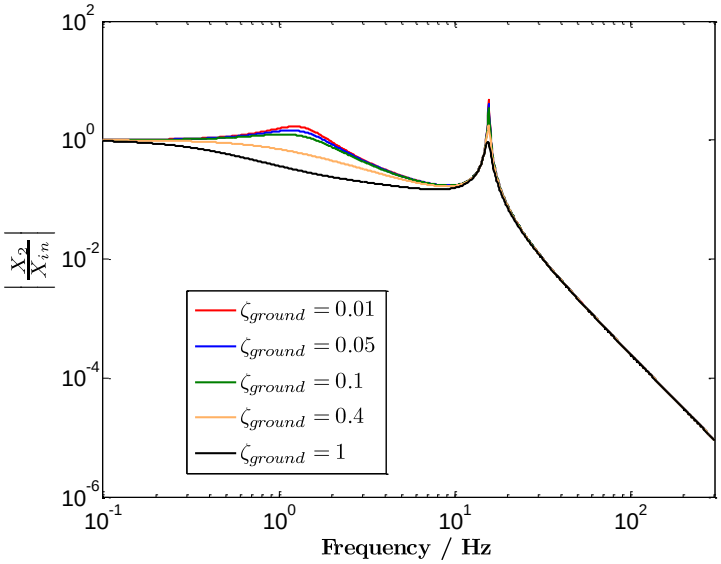

(b) Phase of X_2/X_{in} versus frequency

Figure 3.30: The variation of X_2/X_{in} with frequency for base excitation for various values of the damping ratio, ζ_{ground}, for the groundhook damper

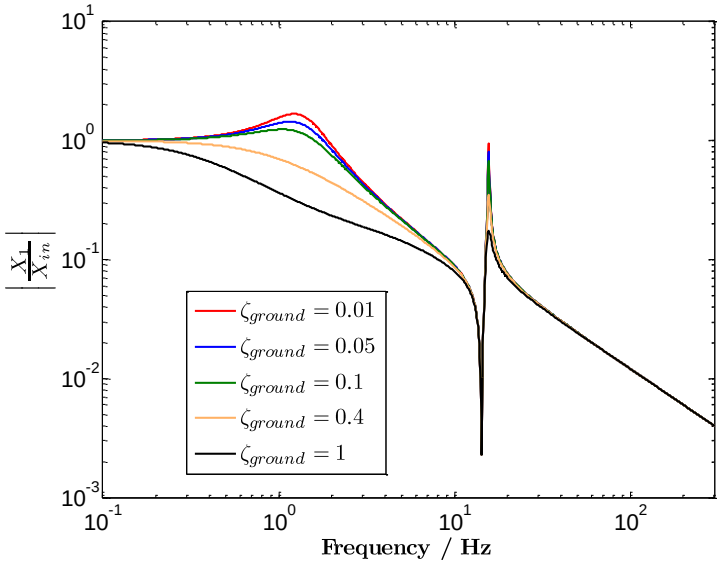

(a) $|X_1/X_{\text{in}}|$ versus frequency

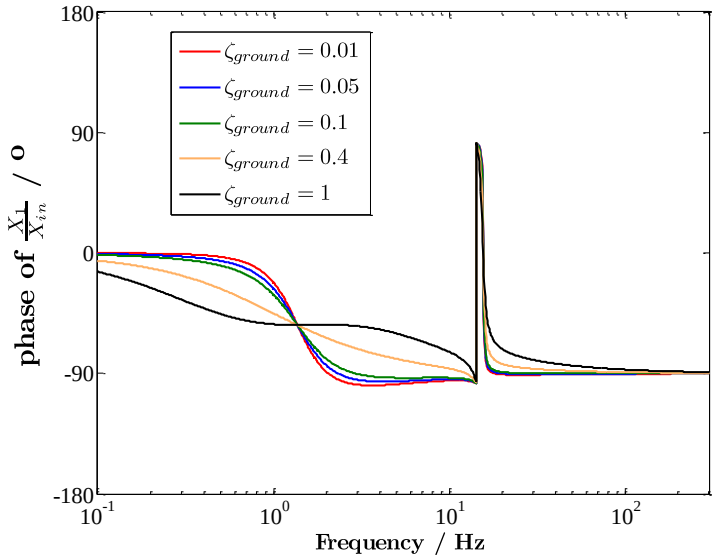

(b) Phase of X_1/X_{in} versus frequency

Figure 3.31: The variation of X_1/X_{in} with frequency for base excitation for various values of the damping ratio, ζ_{ground}, for the groundhook damper

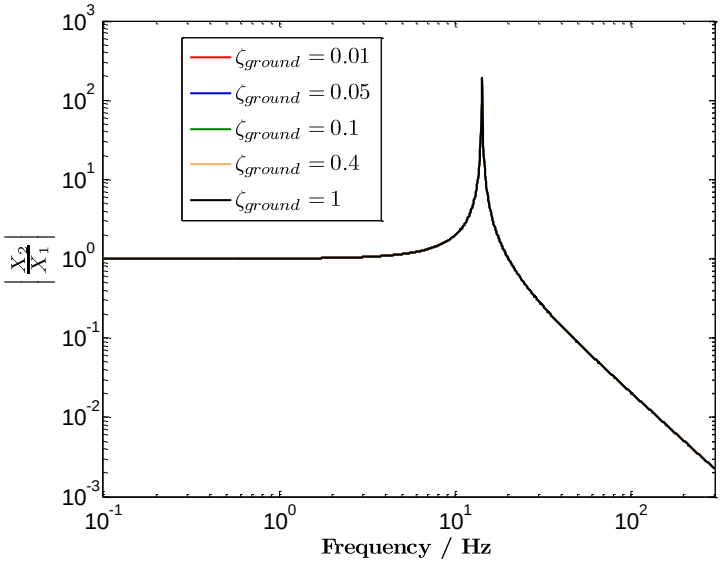

(a) $|X_2/X_1|$ versus frequency

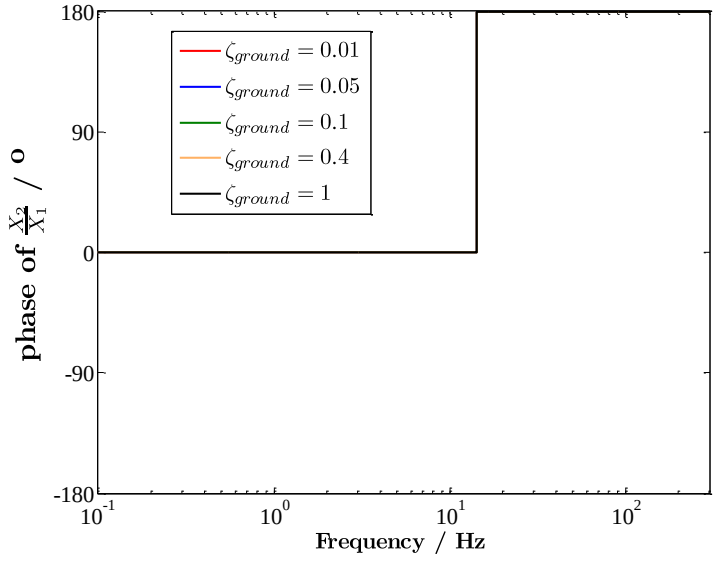

(b) Phase of X_2/X_1 versus frequency

Figure 3.32: The variation of X_2/X_1 with frequency for base excitation for various values of the damping ratio, ζ_{ground}, for the groundhook damper

equations of motion are:

$$\begin{aligned} m_1\ddot{x}_1 + c_{\text{ground}}\dot{x}_1 + k_2(x_1 - x_2) + c_1\dot{x}_1 + k_1 x_1 &= 0 \\ m_2\ddot{x}_2 + +k_2(x_2 - x_1) &= m_2\ddot{x}_{2\text{f}} \end{aligned} \tag{3.50}$$

As in the previous section harmonic motion is assumed, i.e. $x_i = X_i e^{j\omega t}$ and i.e. $f_{\text{in}} = F_{\text{in}} e^{j\omega t}$, giving:

$$\frac{X_2}{X_{2\text{f}}} = \frac{\left(\frac{\omega}{\omega_2}\right)^2}{\left(\frac{\omega}{\omega_2}\right)^2 + \left(\frac{1}{\frac{k_1}{k_2} 2\zeta_1 \frac{j\omega}{\omega_1} + \frac{k_1}{k_2} - \frac{k_1}{k_2}\left(\frac{\omega}{\omega_1}\right)^2 + 2\zeta_{\text{ground}}\frac{j\omega}{\omega_2} + 1}\right)} \tag{3.51}$$

This is shown in Figures 3.33(a) and 3.33(b). As the frequency tends to 0, the response tends to zero at 40 dB/decade. The relation tends to $\omega^2(k_1/k_2 + 1)/\omega_2^2$. At high frequencies it tends to 1 as seen in Figure 3.33(a) and the phase tends to 0°. This suggests that the engine is behaving as though it is not coupled to the chassis. Both the first resonance and the anti-resonance are significantly affected by altering ζ_{ground}; however, there is not much effect on the second resonance.

The more important relation is how the car body moves as a result of the forced input to the engine. This is given by:

$$\frac{X_1}{X_{2\text{f}}} = \frac{\left(\frac{\omega}{\omega_2}\right)^2}{\left(\left(\frac{\omega}{\omega_2}\right)^2 - 1\right)\left(\frac{k_1}{k_2} 2\zeta_1 \frac{j\omega}{\omega_1} + \frac{k_1}{k_2} - \frac{k_1}{k_2}\left(\frac{\omega}{\omega_1}\right)^2 + 2\zeta_{\text{ground}}\frac{j\omega}{\omega_2} + 1\right) + 1} \tag{3.52}$$

which is shown in Figure 3.34. As the frequency goes to zero, this tends to $\omega^2/\omega_2^2(1 - k_1/k_2)$. This means there is a 40 dB/decade increase at the lowest frequency up to the region of the first resonance, with a phase of 180°. At high frequencies again the response tends to 0. The relation becomes $k_2\omega_1^2/k_1\omega^2$, so the decay is at −40 dB/decade and the phase −180°. There is a good effect when increasing ζ_{ground} on the first resonance frequency; however, there is little effect on the second resonance frequency.

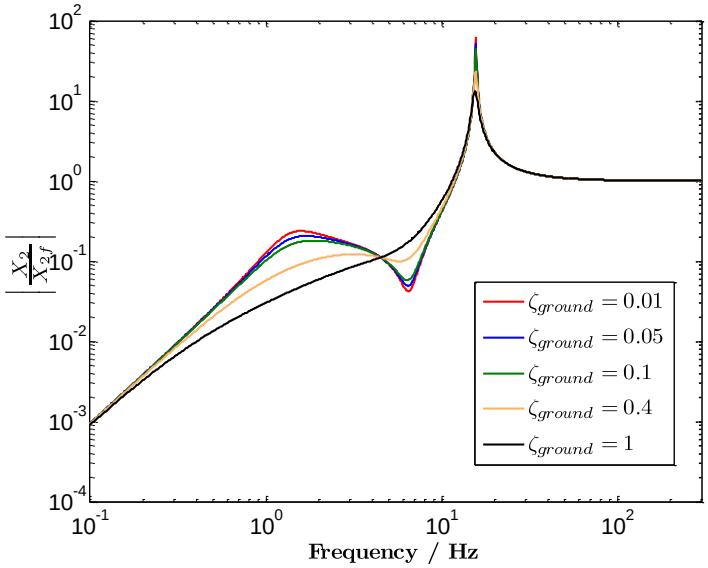

(a) $|X_2/X_{2\mathrm{f}}|$ versus frequency

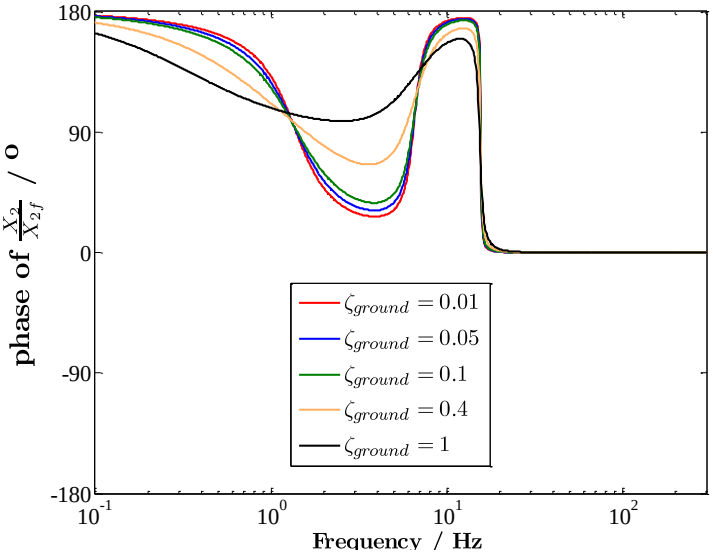

(b) Phase of $X_2/X_{2\mathrm{f}}$ versus frequency

Figure 3.33: The variation of $X_2/X_{2\mathrm{f}}$ with frequency for engine forcing for various values of the damping ratio, ζ_{ground}, for the groundhook damper

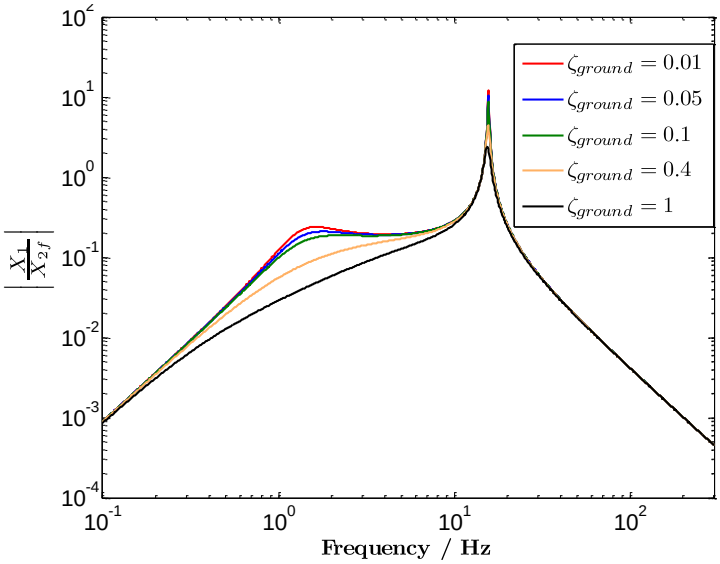

(a) $|X_1/X_{2\mathrm{f}}|$ versus frequency

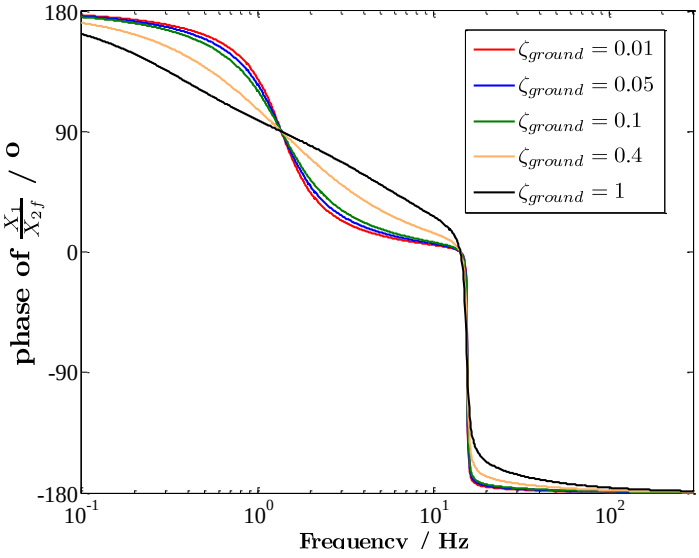

(b) Phase of $X_1/X_{2\mathrm{f}}$ versus frequency

Figure 3.34: The variation of $X_1/X_{2\mathrm{f}}$ with frequency for engine forcing for various values of the damping ratio, ζ_{ground}, for the groundhook damper

Finally, the ratio of the two responses is given by:

$$\frac{X_1}{X_2} = \frac{1}{\frac{k_1}{k_2} 2\zeta_1 \frac{j\omega}{\omega_1} + \frac{k_1}{k_2} - \frac{k_1}{k_2}\left(\frac{\omega}{\omega_1}\right)^2 + 2\zeta_{\text{ground}} \frac{j\omega}{\omega_2} + 1} \tag{3.53}$$

This is shown in Figure 3.35. This has one resonance frequency, the response of which is altered significantly by the value of ζ_{ground}. The high and low frequency regions do not depend on ζ_{ground}. At low frequencies, the trend is similar to that seen before, with the response tending to $1/(1 + k_1/k_2)$ and the phase to 0°. At high frequencies the relation tends to $k_1\omega_1^2/k_1\omega^2$with a phase of −180°. The decay is at −40 dB/decade.

3.6.3 Summary

There is some advantage in the forced vibration case to using groundhook damping at low frequencies, where there is a significant alteration to the response at the lower resonance frequency. There is no advantage in using groundhook damping at the higher frequencies as other systems mentioned earlier display better characteristics around ω_2 and ω_{b}. For the base-excitation case, due to the lack of damping between the two masses, groundhook damping is not desirable in comparison with the other cases.

3.7 Conclusions

This chapter considers a two-degree-of-freedom system representing a quarter of a car. This simplified model contains a spring and damper representing the suspension of the car, with a mass for the chassis. A second spring and damper represent the engine mount and the second mass the engine. Excitation is considered both from the base and the forced vibration of the engine, with different types of damping.

Viscous damping has the disadvantage that if high damping is used to reduce the magnitude of the resonances, the high frequency roll-off is not very good. Hysteretic damping improves this, but it is only a theoretical consideration because it is not causal. Using a frequency dependent stiffness, makes the high damping

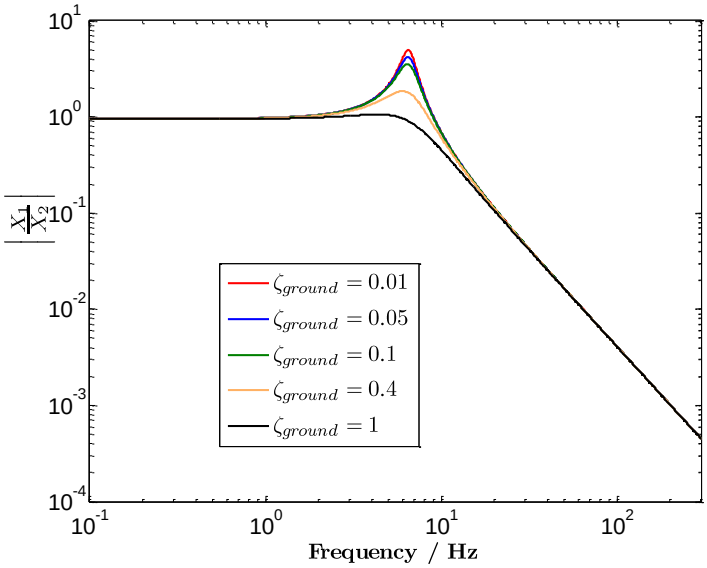

(a) $|X_1/X_2|$ versus frequency

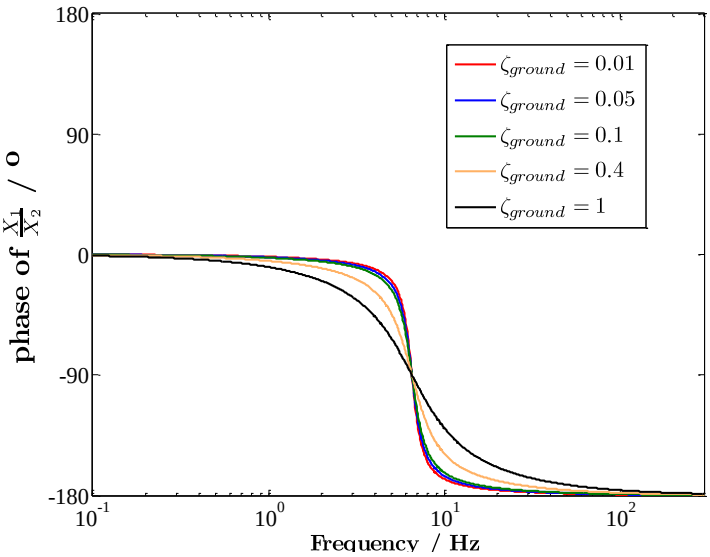

(b) Phase of X_1/X_2 versus frequency

Figure 3.35: The variation of X_1/X_2 with frequency for engine forcing for various values of the damping ratio, ζ_{ground}, for the groundhook damper

situation similar to that of viscous damping at high frequencies. However, there is still some advantage to high frequency roll-off when compared with the viscous damping case for low and moderate damping.

In reality any vehicle is going to undergo excitation from both the base and the engine-forcing at the same time, not separately as considered here. This means that the groundhook damping is not useful away from the low frequency regime to deal with the simultaneous input. Skyhook damping was found to be the best as it reduces the amplitudes at both resonance frequencies (ω_a and ω_b). For the base-excitation case, the transmissibility at ω_2 can be reduced to 1 and below (if required) which is not possible with either the viscous or the hysteretic damping. The roll-off at high frequencies is beneficial when compared with the viscous and hysteretic dampers.

As mentioned previously, it would be hard to find an elastomeric material exhibiting a damping ratio greater than approximately 0.2, unlike the higher values of ζ_2 in the models. However, as the damping for the skyhook and groundhook cases is not a material property this could in fact be achieved.

Although the best properties were found for the skyhook damper, the power requirements mean that a passive or adaptive solution that can provide some of the advantages in performance are more potentially more desirable. The quarter car model from this chapter is used in Chapter 7 to examine the performance of hydromounts and an adaptive system.

Chapter 4

Modelling Hydromounts

This chapter considers the properties of a proprietary passive hydromount, both experimentally and theoretically. This mount is similar to those that have been used for a Jaguar V6 engine and had no decoupler. Initially a set of dynamic stiffness measurements are taken. The behaviour of the mount is first approximated using a linear model, before non-linearities are added to describe the amplitude dependence. The model used here is an existing one[57] from the literature, described in Section 2.2, but it has been applied to and optimised for the proprietary mount.

4.1 Testing of a proprietary hydromount

The dynamic stiffness of a proprietary hydromount was measured at a range of frequencies and amplitudes. The aim of this was to identify the characteristic frequency behaviour of the hydromount and to examine how much amplitude dependence there was. The range of frequencies chosen was large enough so the primary resonance of the mount (expected to be coincident with the resonance of the engine mounted in the vehicle and tuned to 8-12 Hz) would be apparent along with the high and low frequency behaviour. The amplitudes tested covered a range that could be easily tested at 50 Hz, and includes both high amplitude (1 mm) and low amplitude (0.05 mm) cases.

The testing was carried out on a VH7 Schenck servohydraulic machine with a stationary piezoelectric load cell at the bottom and a linear variable differential

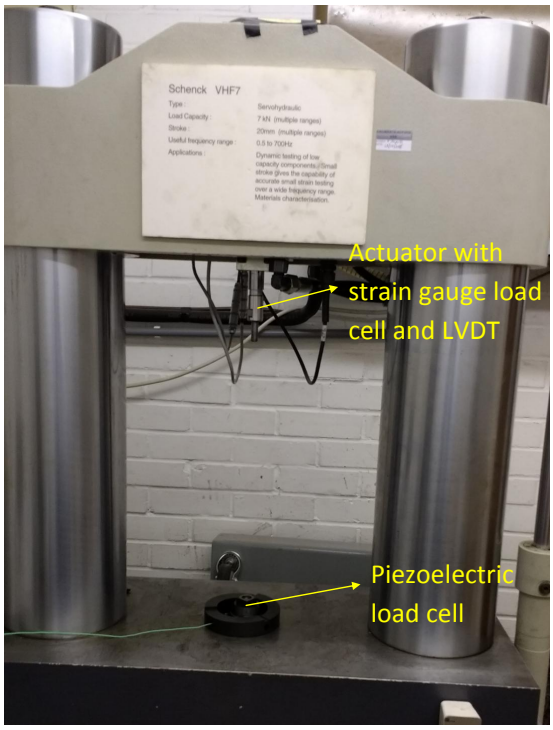

Figure 4.1: The VH7 Schenck machine

transformer (LVDT) measuring the displacement of the actuator at the top (see Figure 4.1). The tests were carried out using a sinusoidal input over a frequency range from 1 to 50 Hz at 1 Hz intervals at amplitudes of 0.05, 0.1, 0.2, 0.3, 0.5 and 1 mm. The dynamic stiffness was measured using a Solartron 1250 Frequency Response Analyzer (FRA), which was used to extract the first harmonic component of the signals for the force and the displacement. The hydromount had a preload of 1000 N applied to it. The results are shown in Figure 4.2.

These results show a single resonance of the mount within the frequency range tested, with the peak in K'' at approximately 10 Hz. There is no decoupler, so there is strong amplitude dependence, with the lowest amplitude showing the highest stiffness response. Increasing the amplitude, although reducing the peak value of K'', increases its frequency bandwidth. K' shows a trough approximately 8 Hz and a peak at approximately 12 Hz, which is within the expected range. At low frequencies (below the resonance) K' is slightly amplitude dependent, with the lowest value being for the highest amplitude, with a value of approximately 350 N mm^{-1}. At high frequencies (above the resonance) K' is again slightly amplitude dependent with the highest amplitude showing the lowest stiffness and the value tends to 550-600 N mm^{-1}. K'' tends to 0 at low frequencies and

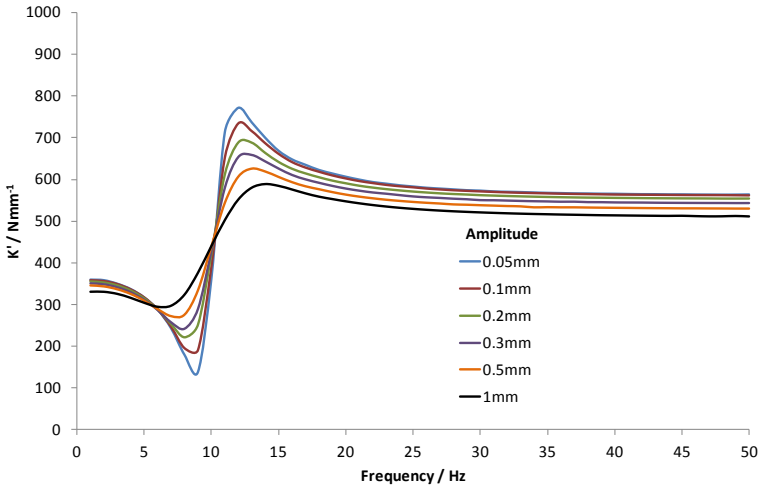

(a) In-phase stiffness

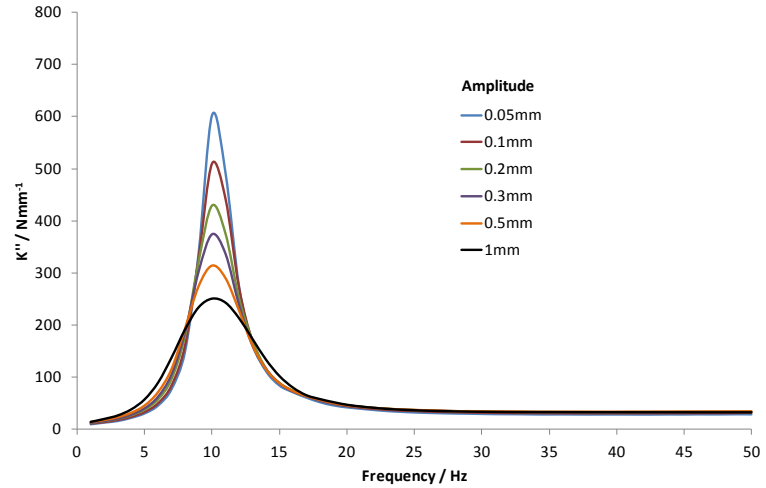

(b) Out-of-phase stiffness

Figure 4.2: The measured stiffness of the proprietary hydromount subject to sinusoidal excitation

25 N mm^{-1} at high frequencies.

The mount was then sectioned and the rubber spring of the hydromount was also tested separately under the same conditions as the full hydromount. The results are shown in Figure 4.3. K' changes very little over the frequency range of 1 to 50 Hz. The assumption that it is constant is reasonable over this frequency range; at 50 Hz the value for K' is only 1.06 times larger than the value at 1 Hz. There is also very little amplitude dependence (suggesting a rubber with little reinforcing filler). The higher amplitudes have lower stiffnesses than the lower amplitudes, as expected for reinforced rubber. The value of approximately 350 N mm^{-1} is very similar to that of the hydromount, and it is the stiffness of this spring that governs the low frequency stiffness of the hydromount. Looking at K'', there is again little frequency dependence, although this is greater than that of K'. The values are low (under 25 N mm^{-1} across all frequencies and amplitudes) as might be expected for a properly cured natural rubber (NR) compound tested at ambient temperature with low levels of reinforcing filler. K'' is highest for the highest amplitude. Due to the low values, the data is noisy, particularly at low amplitudes. The low values provide justification for the assumption that damping of the rubber spring is negligible for the linear model below.

4.2 Linear model for a hydromount

4.2.1 Transfer stiffness

The linear model described by Singh et al.[57] has been used in this work in an attempt to model the frequency dependence of the mounts. This is shown schematically in Figure 4.4. The original equation, expressed in the frequency domain, was given in Section 2.3.1. Here, it has been simplified to remove the decoupler and separated into real and imaginary parts:

$$K'(\omega) = \frac{(\chi_0 - \chi_2\omega^2)(\epsilon_0 - \epsilon_2\omega^2) + \epsilon_1\omega(\chi_1\omega - \chi_3\omega^3)}{(\epsilon_0 - \epsilon_2\omega^2)^2 + \epsilon_1^2\omega^2} \tag{4.1}$$

$$K''(\omega) = \frac{(\chi_1\omega - \chi_3\omega^3)(\epsilon_0 - \epsilon_2\omega^2) - \epsilon_1\omega(\chi_0 - \chi_2\omega^2)}{(\epsilon_0 - \epsilon_2\omega^2)^2 + \epsilon_1^2\omega^2} \tag{4.2}$$

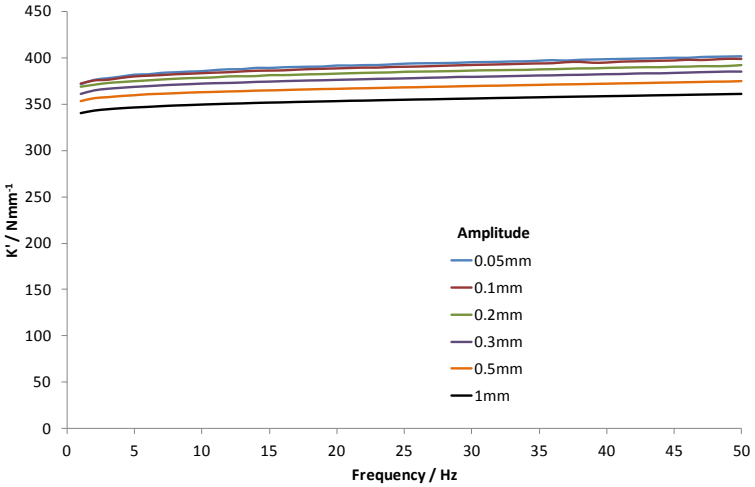

(a) In-phase stiffness

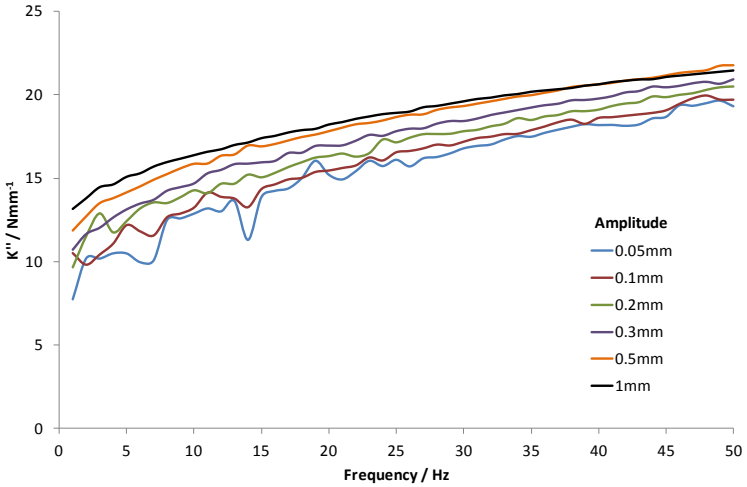

(b) Out-of-phase stiffness

Figure 4.3: The measured stiffness of the spring of the proprietary hydromount subject to sinusoidal excitation

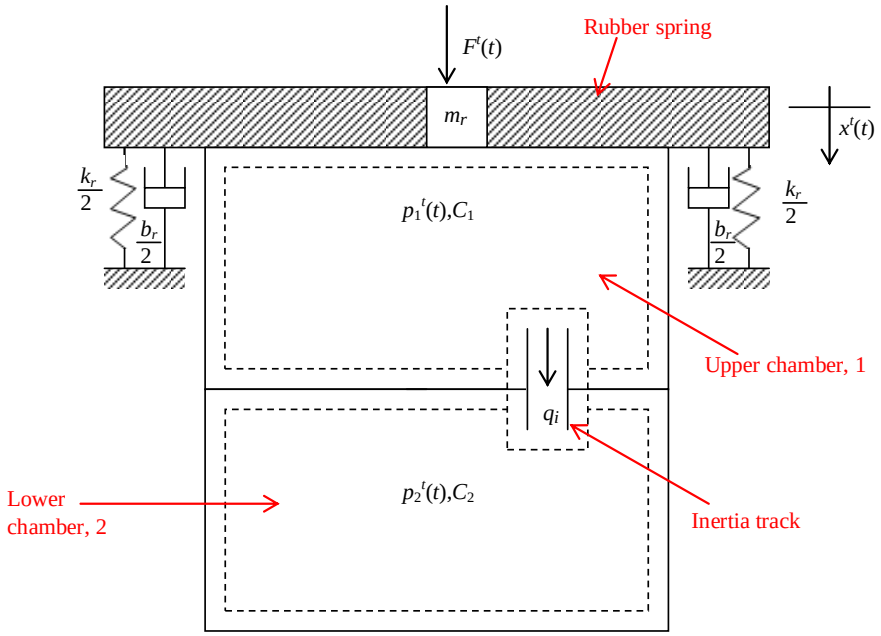

Figure 4.4: Hydro-mechanical model for a hydromount. Adapted from Singh et al.[57]

where:

$$\chi_3 = b_\mathrm{r} C_1 C_2 I_\mathrm{i},$$
$$\chi_2 = b_\mathrm{r} C_1 C_2 R_\mathrm{i} + k_\mathrm{r} C_1 C_2 I_\mathrm{i} + A_\mathrm{r}^2 C_2 I_\mathrm{i},$$
$$\chi_1 = b_\mathrm{r}(C_1 + C_2) + k_\mathrm{r} C_1 C_2 R_\mathrm{i} + A_\mathrm{r}^2 C_2 R_\mathrm{i},$$
$$\chi_0 = k_\mathrm{r}(C_1 + C_2) + A_\mathrm{r}^2,$$
$$\epsilon_2 = C_1 C_2 I_\mathrm{i},$$
$$\epsilon_1 = C_1 C_2 R_\mathrm{i},$$
$$\epsilon_0 = C_1 + C_2.$$

The parameters of the model are the stiffness of the rubber spring, k_r; the damping of the rubber spring, b_r; the pumping area of the rubber spring A_r; the volumetric compliance of the first chamber, C_1; the compliance of the second chamber, C_2; the resistance to flow through the inertia track, R_i (see Equation (4.3) below); and the inertance in the inertia track, I_i (see Equation (4.4)). The last two parameters are dependent on the fluid properties, such as the viscosity, μ, and the density, ρ, and on the inertia track dimensions: the diameter, d_i, and the length, l_i) as follows:

$$R_{\mathrm{i}} = \frac{128\mu l_{\mathrm{i}}}{\pi d_{\mathrm{i}}^4} \tag{4.3}$$

$$I_{\mathrm{i}} = \frac{\rho l_{\mathrm{i}}}{A_{\mathrm{i}}} \tag{4.4}$$

The value for k_{r} was taken from the experimental data for the rubber spring (K' at 1 Hz, see Figure 4.3(a)) and assumed to be constant at all frequencies. The reason for choosing the 1 Hz value across the entire frequency range is because it appears from the experimental results that the low frequency stiffness of the hydromount is very dependent on the stiffness of the rubber spring. At higher frequencies other effects dominate and the exact value of the stiffness of the rubber spring is less important. The value for b_{r} for the rubber spring (K''/ω) is assumed to be 0 for simplicity as the damping in the rubber spring is small ($\eta = K''/K' \lesssim 0.05$).

The resistance to flow through the inertia track, R_{i} was estimated from the linear fluid flow relation given in Equation (4.3). This required knowledge of the hydraulic diameter, d_{i}, but in the proprietary hydromount the inertia track had a square-shaped cross-section. However, this was found to be insignificant compared with the linear equation's under-estimation of R_{i}, which was approximately 10 times lower than the value that gave the best agreement. At this stage the values for the compliance (C_1 and C_2) were chosen such that there was a good agreement in the frequency of the peak K''. All the values used in the model are listed in Table 4.1.

Variable	Value	Unit	Comment
C_1	9.58×10^{-11}	$m^3\ Pa^{-1}$	best-fit
C_2	3.80×10^{-8}	$m^3\ Pa^{-1}$	best-fit
R_i	7.69×10^{7}	$m^4\ s\ kg^{-1}$	best-fit (calculated $\times 10$)
I_i	2.07×10^{6}	$kg\ m^{-4}$	calculated
k_r	3.4×10^{5}	$N\ m^{-1}$	measurement
b_r	0	$N\ s\ m^{-1}$	measurement
A_r	6.17×10^{-3}	m^2	estimated from measurement
A_i	1.0×10^{-4}	m^2	
d_i	0.0113	m	measurement
l_i	0.190	m	measurement
μ	0.0161	$kg\ m\ s^{-1}$	based on glycol at room temperature
ρ	1090	$kg\ m^{-3}$	measurement

Table 4.1: Values of the variables in the linear model for the proprietary mount

Looking at Equation (4.1), as ω tends to 0, the low frequency value of K' goes as follows:

$$\lim_{\omega \to 0} K'(\omega) = \frac{\chi_0}{\epsilon_0} = k_r + \frac{A_r^2}{C_1 + C_2} \tag{4.5}$$

As $C_1 << C_2$ this can be further approximated to $k_r + A_r^2/C_2$. Also $k_r >> A_r^2/C_2$ so at low frequencies $K' \approx k_r$ as the experimental data suggested. Similarly, at high frequencies Equation (4.1) goes as follows:

$$\lim_{\omega \to \infty} K'(\omega) = \frac{\chi_2}{\epsilon_2} \tag{4.6}$$

As b_r is taken as 0 in the current study this further simplifies to $k_r + A_r^2/C_1$, which gives a high frequency asymptote of 738 $N\ mm^{-1}$. This means the high frequency behaviour is strongly affected by the compliance of C_1. For this purpose this mount contains an additional diaphragm inside the upper chamber, which contributes to C_1 without altering k_r which would affect the low frequency stiffness.

The frequency of the peak of K'' can be estimated by assuming that at this frequency the numerator is not changing significantly. This means the frequency

at which the denominator is at its minimum would give the frequency of the maximum of K''. Taking the dominant term from this leads to:

$$\omega^2 \approx \frac{\eta_0}{\eta_2} = \frac{C_1 + C_2}{C_1 C_2 I_\mathrm{i}}. \tag{4.7}$$

As $C_1 << C_2$ this leads to $\omega = \sqrt{1/(C_1 I_\mathrm{i})}$. This gives the frequency at which the maximum value occurs as being 11.3 Hz. This is approximately 4% larger than where the maximum occurs looking at the graph, which means the approximations made are reasonable to give estimate of the frequency. This means the resonance frequency of the hydromount is predominantly determined by these two values. This is not unexpected as the compliance is inversely proportional to stiffness and the inertance gives the 'mass-like' behaviour of the fluid.

The results from the model are compared with the experimental data for the largest amplitude (1.0 mm) and the smallest amplitude (0.05 mm) in Figure 4.5. There is good agreement using the linear model to predict the frequency of the resonance in the response. However, the magnitude of K' and K'' is not predicted well and has no amplitude dependence. It is clear that a non-linear model is required to achieve better prediction of the measured behaviour.

4.2.2 Point stiffness

In Section 2.2, Figure 2.7(c,d) shows that the hydromount transfer and point stiffnesses are approximately equal.[66] Singh et al.[57] also give a linear function for the point stiffness (here simplified to remove the decoupler):

$$K(i\omega) = \frac{\alpha_4\omega^4 - i\alpha_3\omega^3 - \alpha_2\omega^2 + i\alpha_1\omega + \alpha_0}{-\beta_2\omega^2 + i\beta_1\omega + \beta_0} \tag{4.8}$$

where:

$$\begin{aligned}
\alpha_4 &= m_\mathrm{r} C_1 C_2 I_\mathrm{i}, \\
\alpha_3 &= m_\mathrm{r} C_1 C_2 R_\mathrm{i} + b_\mathrm{r} C_1 C_2 I_\mathrm{i}, \\
\alpha_2 &= m_\mathrm{r}(C_1 + C_2) + b_\mathrm{r} C_1 C_2 R_\mathrm{i} + k_\mathrm{r} C_1 C_2 I_\mathrm{i} + A_\mathrm{r}^2 C_2 I_\mathrm{i}, \\
\alpha_1 &= b_\mathrm{r}(C_1 + C_2) + k_\mathrm{r} C_1 C_2 R_\mathrm{i} + A_\mathrm{r}^2 C_2 R_\mathrm{i}, \\
\alpha_0 &= k_\mathrm{r}(C_1 + C_2) + A_\mathrm{r}^2,
\end{aligned}$$

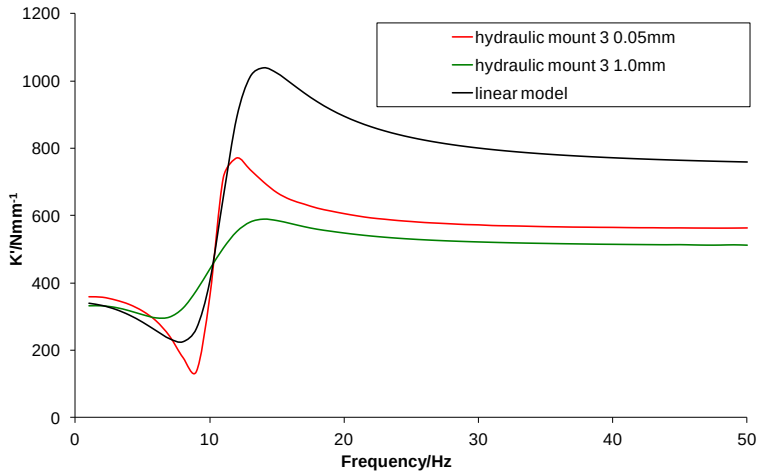

(a) In-phase stiffness

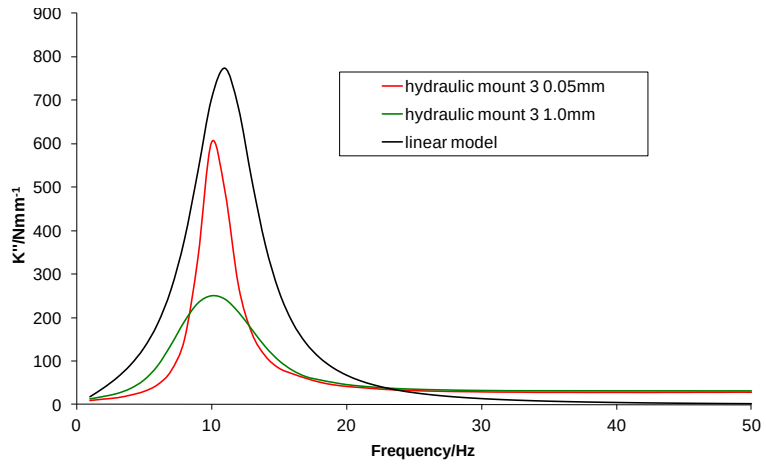

(b) Out-of-phase stiffness

Figure 4.5: The stiffness of the proprietary hydromount subject to sinusoidal excitation using the linear model compared with experimental results

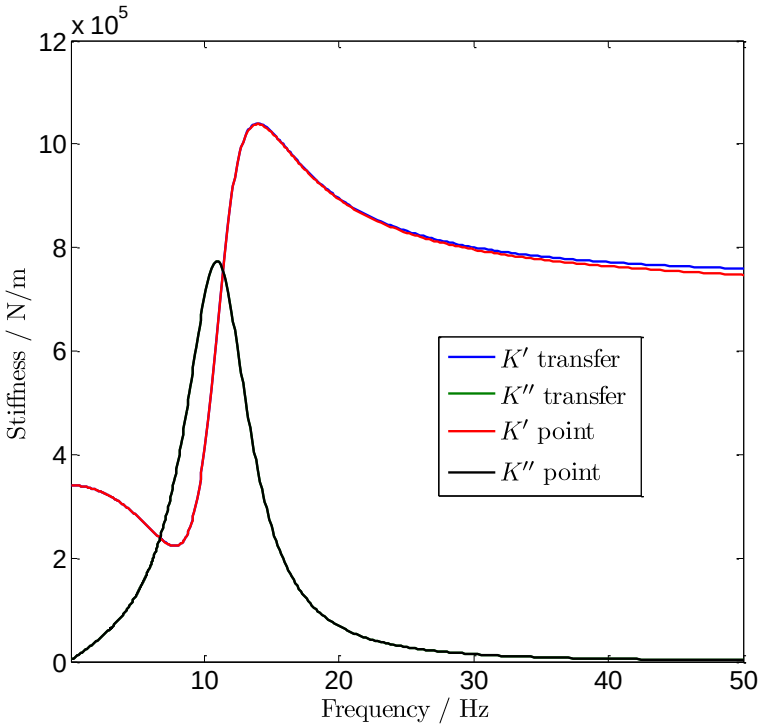

Figure 4.6: The transfer stiffness and the point stiffness of the linear model for the hydromount

$$\beta_2 = C_1 C_2 I_\mathrm{i},$$
$$\beta_1 = C_1 C_2 R_\mathrm{i},$$
$$\beta_0 = C_1 + C_2.$$

The main difference between this and the transfer stiffness in Equations (4.1 and 4.2) is the introduction of an extra parameter, m_r, which is the mass of the rubber spring; consequently, there is the introduction of an ω^4 term. For a test of this the other parameters were kept as in Table 4.1, and m_r was assumed to be 0.124 kg (assuming 20 mm thick rubber with the cross-sectional area A_r and the approximate density of rubber of 1000 kg m^{-3}). The comparison between the point and the transfer stiffness can be seen in Figure 4.6. There is little visible difference around the resonance in either K' or K'', but at the higher frequencies a difference in K' starts to be apparent. The lack of change in K'' may be because b_r is assumed to be zero.

4.3 Non-linear model for a hydromount

4.3.1 Sources of non-linearity

In the literature survey (Section 2.2) many potential sources of amplitude dependent non-linearity were identified including:

- The decoupler, if the mount has one. As the proprietary hydromount being modelled does not have a decoupler, the decoupler part of the model is not included.
- The inertia track, in particular, the effects of the resistance to flow through the inertia track. The non-linearity due to this is considered to be significant and the equations from Ahmadi et al.[6] have been used.
- Stiffness and damping of the rubber spring. Both the stiffness and the damping of the rubber spring vary slightly with amplitude as well as frequency, as seen in Figures 4.3(a) and 4.3(b). Although this is not the most significant non-linear behaviour around the resonance, this should be included to make the high and low frequency behaviour amplitude-dependent.
- Effective pumping area. The compression of the spring is likely to change the exact pumping area of the rubber spring and so this would be amplitude dependent. This is not expected to be significant, compared with the size of the rubber spring and the size of the preload used. This has not been considered further.
- The compliances of the upper and lower chambers. The compliance of both of these is governed by elastomeric diaphragms and the upper chamber also has a rubber spring, all of which are likely to have some amplitude and pressure dependence. For the lower chamber this is not likely to be significant as its compliance has little effect on the dynamic stiffness behaviour. For the upper chamber this dependency may be of more significance, but it is not likely to be highly amplitude dependent as the rubber used appears not to be highly reinforced. The non-linearites of the compliances have therefore been neglected in this consideration.

- The vacuum phenomenon. This occurs when the upper chamber pressure falls below atmospheric pressure, and dissolved air or the liquid itself forms a gas thereby altering the chamber compliance.

4.3.2 Time domain equations

The non-linear model, from Singh et al.[57], is expressed in the time domain model and consists of the integration using the Runge-Kutta method of the following equations:

$$\dot{q}_{\mathrm{i}}(t) = \frac{-R_{\mathrm{i}} q_{\mathrm{i}}(t) + p_2(t) - p_1(t)}{I_{\mathrm{i}}} \tag{4.9}$$

where q_{i} is the volumetric flow rate through the inertia track, p is the pressure in chambers 1 and 2 as indicated by the subscript. This equation describes the flow through the inertia track which is governed by the relative pressures in the two chambers.

$$\dot{p}_1(t) = \frac{A_{\mathrm{r}} \dot{x}(t) - q_{\mathrm{i}}(t)}{C_1} \tag{4.10}$$

$$\dot{p}_2(t) = \frac{q_{\mathrm{i}}(t)}{C_2} \tag{4.11}$$

Equations (4.10) and (4.11) describe the rate of change of the pressure in chambers 1 and 2.

$$F_{\mathrm{T}}(t) = b_{\mathrm{r}} \dot{x}(t) + k_{\mathrm{r}} x(t) + A_{\mathrm{r}} p_1(t) \tag{4.12}$$

where x is the displacement at the top of the mount and F_{T} is the force transmitted to the base of the mount which is assumed not to move. Equation (4.12) represents the sum of the forces that are exerted onto the base of the mount. As the rubber spring is directly bonded to the outer section of the mount, this includes all the forces acting on the spring. The force at the top of the mount would also include a term for the moving mass of the rubber spring.

The values for the input velocity, $\dot{x}(t)$, can be calculated from the input displacement excitation by the central difference method of differentiation (this allows the transient properties and non-sinusoidal inputs to be considered, although the current work is limited to steady-state sinusoidal input). The dynamic stiffness

is calculated from the transmitted force amplitude and the input displacement amplitude. For compatibility with the method used for the experimental testing, the harmonic method[165] was used to calculate the stiffness, which takes the first harmonic component of the displacement input and the force output from the model. The stiffness was calculated in the steady state (significantly after the initial transient had died away). Without the inclusion of the non-linearities, it was confirmed that the time-domain model agreed with the frequency domain model used above. The various non-linear terms are described in the following.

4.3.3 Inertia track

When using the linear model it was found that the inertia track resistance to flow, R_i, was underestimated by Equation (4.3) and to achieve a good fit it had to be increased by a factor of approximately 10 (as given in Table 4.1).

The resistance to flow is the gradient of the graph of the steady state pressure drop, Δp_{12}, versus the steady flow rate, q_i:

$$R_\mathrm{i} = \frac{d\Delta p_{12}}{dq_\mathrm{i}} \tag{4.13}$$

Adiguna et al.[68] found that the linear equation underestimates the actual resistance as it does not take into account end effects and the pressure drop due to cornering. It also does not take into account turbulent flow that might be caused by the sharp edge orifice. They suggested a more suitable equation to describe the non-linear relationship between $\Delta p_{12} = p_2 - p_1$ and q_i; the sharp edge orifice formula:

$$\Delta p_{12} = \frac{\rho q_\mathrm{i}^2}{2C_\mathrm{d}^2 A_\mathrm{i}^2} \tag{4.14}$$

C_d, the coefficient of discharge, is dependent on the edges, surface finishes and roundness of the hole. For a perfectly sharp edge C_d is 0.6, while a chamfered edge can change it to be up to 0.9 and a radius could increase it to 0.98. For the proprietary mount, assuming sharp edges, this equation becomes:

$$\Delta p_{12} = 1.5 \times 10^{11} q_\mathrm{i}^2 \tag{4.15}$$

However, the best method that Adiguna et al.[68] found for obtaining the formula was by curve fitting experimental results of the pressure versus flow rate. For the

proprietary mount, this was done by the present author in Ahmadi et al.[6] and the equation was found to be approximately:

$$\Delta p_{12} = 2.5 \times 10^{11} q_{\mathrm{i}}^2 \tag{4.16}$$

which suggests C_d is less than 0.6. As the cross-section of the inertia track was square, it is not surprising that the theoretical values for C_d do not agree with the observed value. They also found that modelling the flow through the inertia track using Engineering Fluid Dynamics software gave very good agreement with experimental data for measuring the resistance to flow. Substituting Equation (4.16) into Equation (4.13) gives the following expression for R_{i}:

$$R_{\mathrm{i}} = 5 \times 10^{11} q_{\mathrm{i}}. \tag{4.17}$$

4.3.4 Stiffness and damping of the rubber spring

The experimental results for the rubber spring (see Figures 4.3(a) and 4.3(b)) were put into a look-up table, with the value for K' becoming k_{r} and the value for K''/ω becoming b_{r}. Although not strongly frequency dependent, the non-linearity due to the amplitude gives rise to the majority of the difference between the results at different amplitudes, particularly in the high and low frequency regimes. This is a shortcoming of the current approach, because this is only valid for harmonic excitation, but this is not a major issue because K' and K'' and damping are not highly amplitude dependent. To improve this the stiffness could be considered as a function of the speed at which the spring is being deformed. However, this would give a tangential stiffness, not K' and K'' as used here. In this thesis only harmonic excitation has been considered, so the look-up table is appropriate.

4.3.5 Vacuum phenomenon

It is not easy to determine the level of pre-dissolved gas in the liquid. To deal with this problem, Adiguna et al.[68] suggest a bilinear model and the following

equation is adapted from that used in their non-linear model:

$$C_1 = \begin{cases} -7 \times 10^{-45}(101000 + p_1)^7 + 2.5 \times 10^{-10} & p_1 < -25000 \text{ Pa} \\ 1.25 \times 10^{-10} \text{ m}^3 \text{ Pa}^{-1} & \text{otherwise} \end{cases} \tag{4.18}$$

This means for pressures in the upper chamber of below 76000 Pa (25000 Pa below atmospheric pressure) the compliance changes.

4.3.6 Other parameters

The pumping area of the spring, A_r and the value for the upper chamber compliance, C_1, (with $p_1 \geq -25000$ Pa) are difficult to measure accurately. They were therefore adjusted until a good fit was found, although the values obtained were similar in magnitude to those used before. The other parameters were kept the same as those that had been used previously in the linear model, which were based on the dimensions of the component and the density of the fluid.

4.3.7 Using the non-linear model

Table 4.2 lists all the parameters and the values used in the non-linear model. The viscosity of the fluid is no longer used (the resistance to flow is an empirical equation and which implicitly depends upon the viscosity of the fluid among other factors), and the damping of the rubber spring is now included.

Figure 4.7 shows the results of the non-linear model for the proprietary mount. It can be seen that as the amplitude is increased the resonance is shifted to slightly lower frequencies using the model, whereas this did not occur in the experimental results. The effect is more significant at higher amplitudes. However, the trends seen are generally similar to the experimental results; as the amplitude is increased the magnitude of the stiffnesses are reduced, and the bandwidth of the resonance becomes broader.

Results are shown in Figures 4.8 to 4.13 for the different amplitudes in comparison with the experimental results. With these parameters the best agreement for the in-phase stiffness is seen at 0.2 mm amplitude and for the out-of-phase stiffness at 0.1 mm.

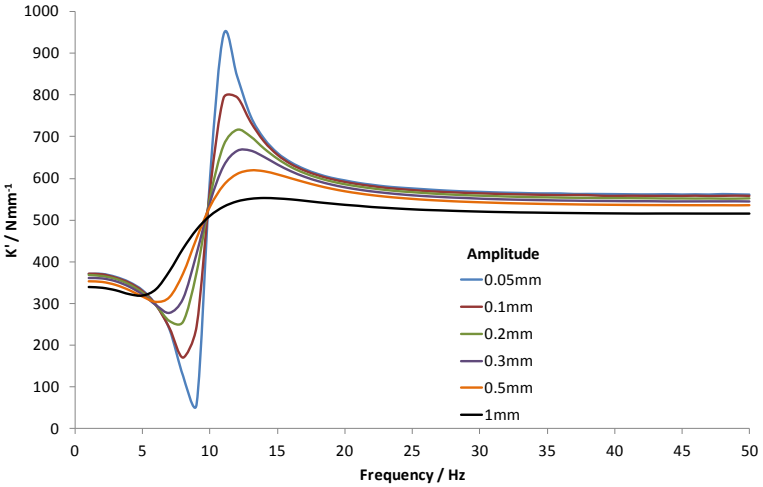

(a) In-phase stiffness

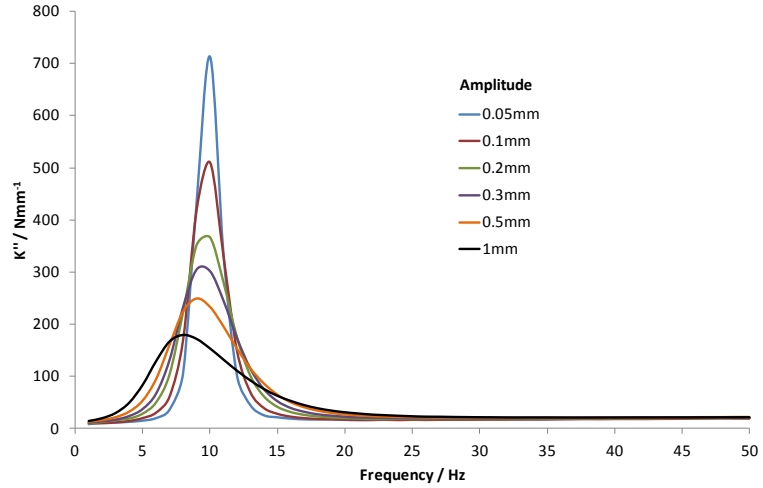

(b) Out-of-phase stiffness

Figure 4.7: The predicted stiffness of the proprietary hydromount subject to sinusoidal excitation obtained using the non-linear model

Variable	Non-linear Model	Linear Model	Units
C_1†	1.25×10^{-10}	9.58×10^{-11}	$m^3\ Pa^{-1}$
C_2	3.80×10^{-8}	3.80×10^{-8}	$m^3\ Pa^{-1}$
R_i	$5 \times 10^{11} q_i$	7.69×10^7	$m^3\ Pa^{-1}$
I_i	2.07×10^6	2.07×10^6	$kg\ m^{-4}$
k_r	from look-up table	3.40×10^5	$N\ m^{-1}$
b_r	from look-up table	0	$N\ m^{-1}\ s^{-1}$
A_r	0.00437	0.00617	m^2
d_i	0.0113	0.0113	m
l_i	0.19	0.19	m
μ	n/a	0.0161	$kg\ m\ s^{-1}$
ρ	1090	1090	$kg\ m^{-3}$

† The non-linear behaviour of C_1 is described in Equation (4.18); the value given here is only that for $p_1 >$ -25000 Pa

Table 4.2: The parameters used in the linear and the non-linear models

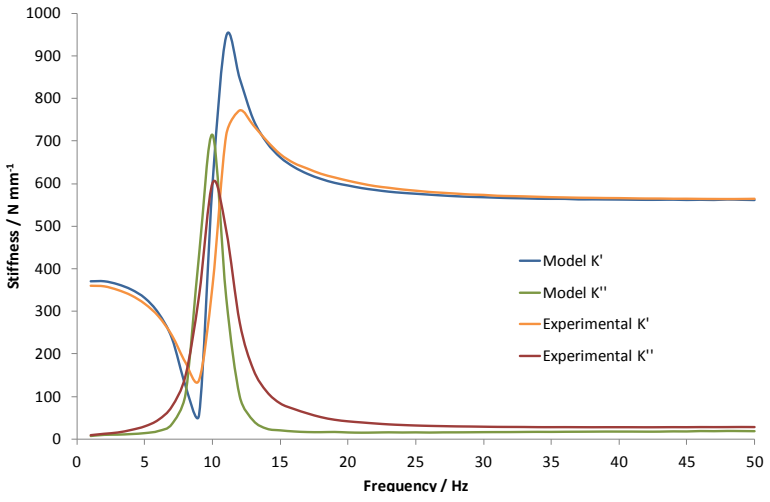

Figure 4.8: Comparison between the non-linear model and the experimental results of the in- and out-of-phase stiffness at 0.05 mm amplitude

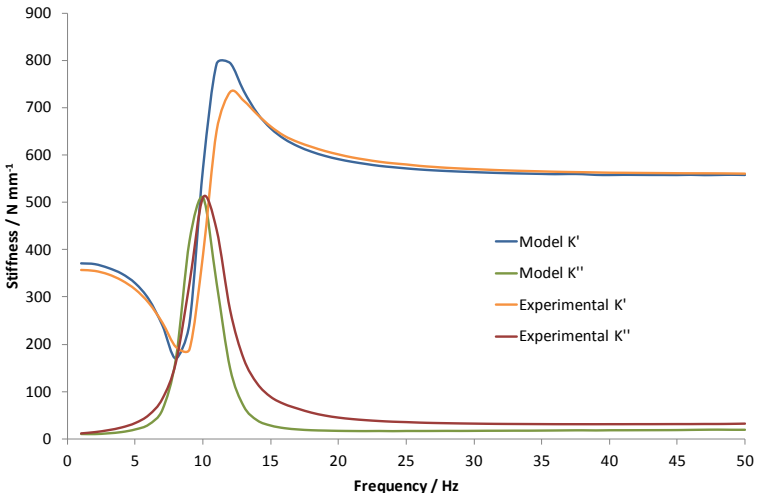

Figure 4.9: Comparison between the non-linear model and the experimental results of the in- and out-of-phase stiffness at 0.1 mm amplitude

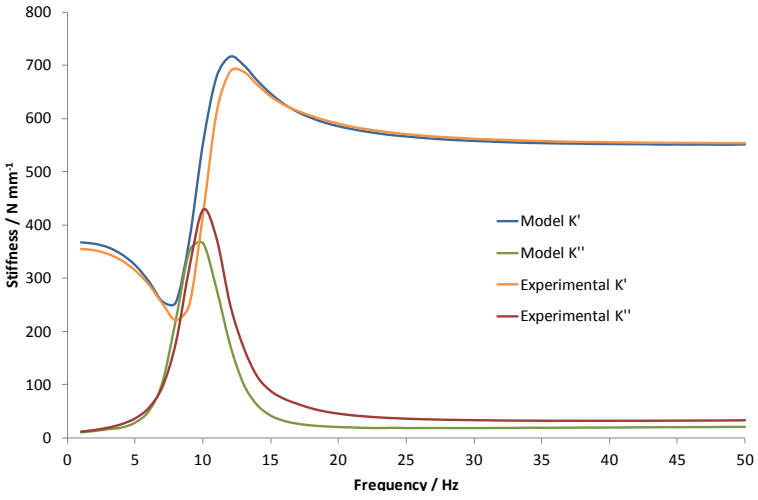

Figure 4.10: Comparison between the non-linear model and the experimental results of the in- and out-of-phase stiffness at 0.2 mm amplitude

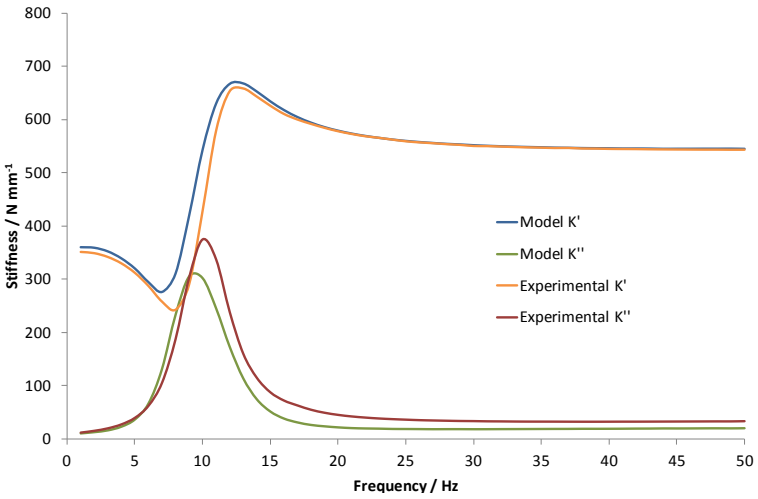

Figure 4.11: Comparison between the non-linear model and the experimental results of the in- and out-of-phase stiffness at 0.3 mm amplitude

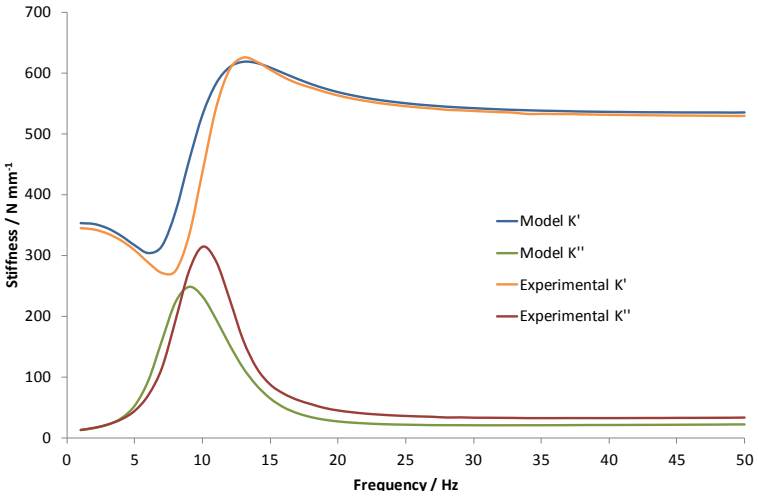

Figure 4.12: Comparison between the non-linear model and the experimental results of the in- and out-of-phase stiffness at 0.5 mm amplitude

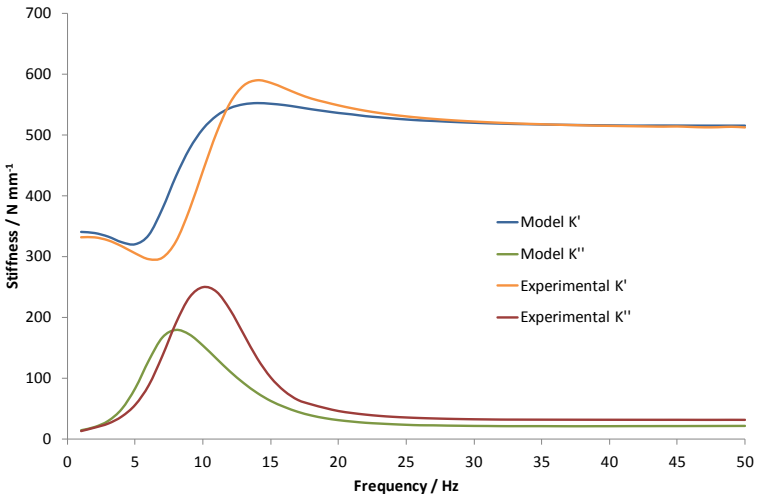

Figure 4.13: Comparison between the non-linear model and the experimental results of the in- and out-of-phase stiffness at 1.0 mm amplitude

4.4 Effect of changing the variables

In an attempt to improve the fit with the experiments, the variables were changed independently to investigate whether altering them had a significant effect.

4.4.1 Area of the rubber spring

The trends of altering the area of the rubber spring, A_r, for a specific amplitude (in this case 0.05 mm) can be seen in Figure 4.14. Reducing A_r to 0.00358 m^2 had the effect of improving the fit of the model to the peaks and troughs in both the in-phase and out-of-phase stiffness. However, at high frequency the in-phase stiffness was significantly lowered. Using this value of A_r at 0.1 mm amplitude (not shown) made the fit worse and the magnitude at the resonance was lower. The best fit for the out-of phase stiffness at this amplitude was achieved with the original value of 0.004365 m^2. The best match for the peak and trough of the in-phase stiffness was with a value of 0.00395 m^2, but again the high frequency asymptote was lowered. The value of 0.0043 m^2, which is very close to the original value, fits the behaviour at 0.2 mm amplitude well for the in-phase stiffness, but the optimum value for matching the peak height in the out-of-phase stiffness is 0.0051 m^2. This worsens the fit above 10 Hz for the in-phase stiffness and emphasises that the peak in the out-of-phase-stiffness is at a slightly lower frequency than the experimental results.

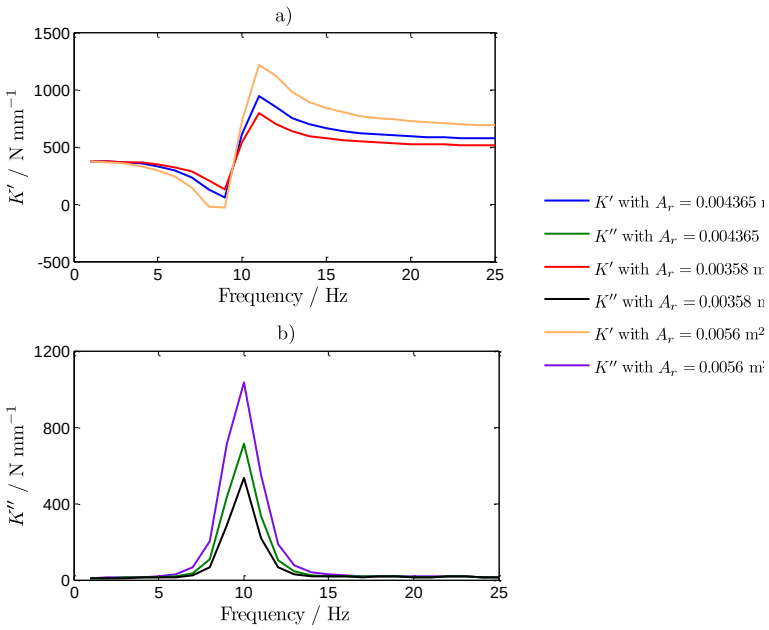

Figure 4.14: The effect of altering the area of the rubber spring, A_r, on the in-phase and out-of-phase stiffness at 0.05 mm amplitude

The trends are similar at 0.3 mm, although here the initial value gives a good fit for the in-phase stiffness peak while the trough is not well matched. The peak in the out-phase stiffness is best matched in magnitude with a value for A_r of 0.0053 m^2: however, it again draws attention to the mismatch in the frequency of the peaks. At 0.5 mm the out-of-phase stiffness was best matched by a value of 0.0056 m^2 and the best matching of the peak of the in-phase stiffness was with a value of 0.0046 m^2. A value of 0.0049 m^2 gives the best match at 1.0 mm amplitude for the in-phase stiffness whereas 0.0059 m^2 matches the peak in the out-of-phase stiffness best.

Altering this parameter had no significant effect on the resonance frequency, mainly controlling the magnitude of the response above the resonance. This supports the finding from the linear model that suggested that the high frequency asymptote was $k_\mathrm{r} + A_\mathrm{r}^2/C_1$. The best match for the high frequency behaviour (significantly above the resonance) at all amplitudes was with the value originally chosen of $A_\mathrm{r} = 0.004365$ m^2.

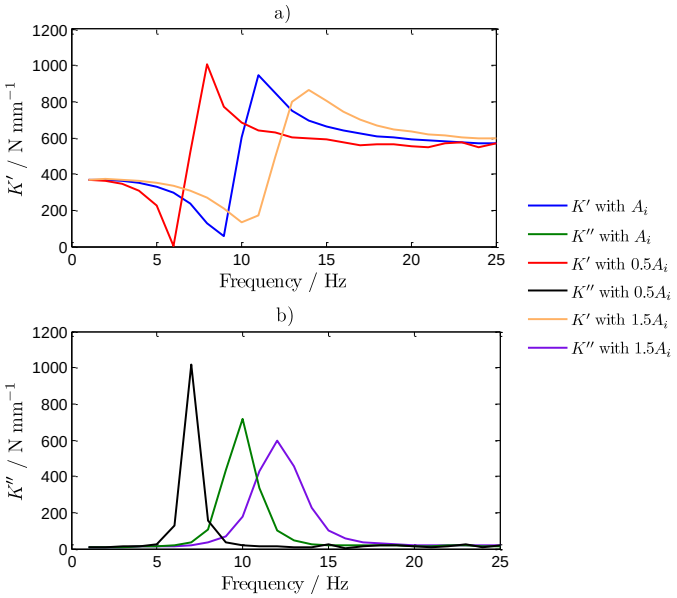

Figure 4.15: The effect of altering the area of the inertia track, A_i, on the in-phase and out-of-phase stiffness at 0.05 mm amplitude

4.4.2 Area of the inertia track

The inertance in the inertia track, $I_\mathrm{i} = \rho l_\mathrm{i}/A_\mathrm{i}$ (Equation (4.4)) is dependent on several variables, including the area of the inertia track, A_i. Altering A_i has little effect on the behaviour away from the resonance frequency as can be seen in Figure 4.15, which shows the situation at 0.05 mm amplitude. Increasing this value not only decreases the height of the peaks in K' and K'' and the depth of the trough in K' but also shifts the resonance to a higher frequency. At 0.05 mm amplitude the resonance frequency was already at a reasonable value. To get the magnitude of the response to fit better, the value of A_i should be increased significantly (by about 50%) and this has a detrimental effect on the agreement of the resonance frequency. Similarly, at 1.0 mm amplitude the value of A_i should be decreased by about 50% to get a good agreement in the peaks of the stiffnesses. This results in the resonance being moved to a lower frequency.

It seems unlikely that the effective area of the inertia track is significantly amplitude-dependent; however, if it is then it would need to be altered in parallel with another parameter which also shifts the resonance frequency.

4.4.3 Effective length of the inertia track

Like the parameter A_i, the length of the inertia track, l_i also is a parameter of the equation for the inertance (Equation (4.4)). It has an effect on the resonance of the hydromounts, but little effect on the high and low frequency behaviour. This is because in the non-linear model, I_i is the only parameter directly dependent on l_i. However, based on the observed behaviour of the inertia track, it is likely that the empirical equation for the resistance to flow through the inertia track would also be dependent on the length of the inertia track. The effective length of the inertia track is likely to be somewhat amplitude dependent, as the effective length will be based to some extent on the speed of the fluid through the inertia track and the increased pressure in the upper chamber due to the imposed displacement. Both of these would be amplitude dependent. Increasing l_i shifts the resonance to a lower frequency and increases the magnitude around the resonance — the same effect as decreasing A_i. To achieve good agreement of the magnitude of the stiffnesses between the experimental data and the model, the resonance frequency would be shifted by a significant amount.

4.4.4 Density of the fluid

The density of the fluid, ρ, is unlikely to be non-linear and the value used is taken from a direct measurement of the fluid. That said, the density does have a significant effect on the resonance behaviour. This can be seen in Figure 4.16, although the magnitude of these changes is too large to be practicable. It is only used in the definition of the inertance or the mass-like properties of the fluid. Increasing it, thereby increasing the 'mass', decreases the frequency at which resonance occurs and increases the height of the peaks and troughs in the stiffness curves.

4.4.5 Resistance to flow in the inertia track

The resistance to flow is already modelled by a non-linear formula (Equation (4.16)). Changing the coefficient in this equation from 2.5×10^{11} N m^{-8} has a significant effect on the magnitude of the peaks and troughs at the resonance whilst leaving the high and low frequency behaviour unchanged. Increasing the

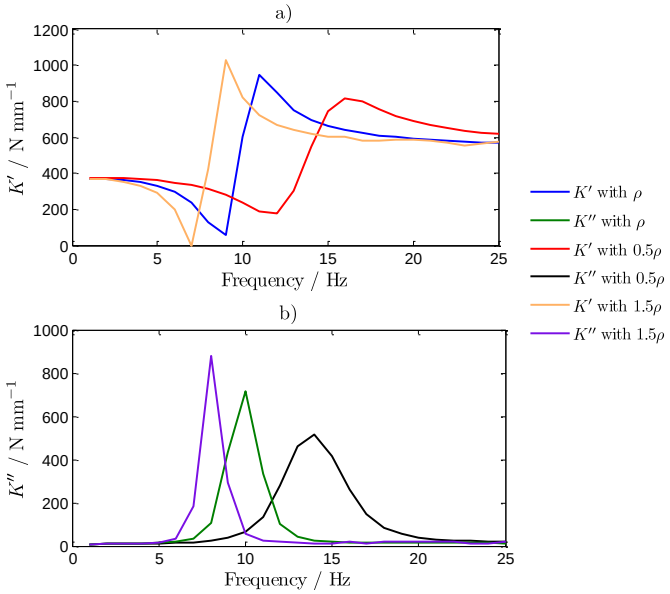

Figure 4.16: The effect of altering the density ρ on the in-phase and out-of-phase stiffness at 0.05 mm amplitude

resistance to flow decreases the height of the peaks and the troughs.

For the 0.05 mm amplitude, increasing the coefficient to 4.13×10^{11} N m^{-8} gives good agreement across all frequencies for both K' and K''. However, the width of the peak in the out-of-phase stiffness is still too narrow. The best result at 1.0 mm amplitude is found with a value of 1.1×10^{11} N m^{-8}; the resonance is still at a slightly lower frequency than that observed experimentally, but the heights of the peaks and the troughs agree well. The width of the out-of-phase stiffness peak is still too narrow.

This parameter does not strongly alter the resonance frequency, nor does it have an effect on the high and low frequency behaviours. However, it is important for governing the strength and bandwidth of the change in stiffness occurring at the resonance.

4.4.6 Compliance of the first chamber

There are a number of parameters that control the compliance of the first chamber in the non-linear model (see Equation (4.18)).

The first to be considered is the value for the compliance in the absence of the vacuum phenomenon, which was taken to be 1.25×10^{-10} m^3 Pa^{-1}. As the compliance of the first chamber, C_1, is the primary stiffness governing the resonance frequency, altering it will have an effect on this frequency. Increasing the compliance (reducing the stiffness) has the effect of lowering the resonance frequency as well as reducing the height of the response. It also affects the results at higher frequencies, above the resonance, where the in-phase stiffness is reduced. At 0.05 mm amplitude a value of 1.67×10^{-10} m^3 Pa^{-1} improves the fit for the magnitude of the K' and K'' at their respective peaks, but reduces the frequency at which they occur, as well as reducing the in-phase stiffness at high frequencies. Reducing C_1 to 7.29×10^{-9} m^3 Pa^{-1} improves the height of the stiffness peaks around the resonance and, unlike the other parameters so far considered, significantly broadens them to match the measured out-of-phase stiffness much better. However, the high frequency behaviour of the in-phase stiffness is significantly worsened becoming much higher than required.

The next value to be considered is the pressure at which the vacuum phenomenon is programmed to take effect. The initial value used for this was 25 kPa below atmospheric pressure. Increasing the magnitude of this value has little effect on the behaviour of the hydromount at 0.05 mm amplitude, but decreasing it significantly changes the behaviour, so that it is unlike the hydromount that was measured. At 1 mm amplitude the changes in behaviour due to the decrease in the magnitude are more pronounced and occur at a higher negative pressure. Also there is a small effect on the behaviour observed by increasing the value; the high frequency stiffness is slightly increased, but the behaviour is not very sensitive to this parameter (away from the point at which the discontinuities appear to become significant).

Changing the exponent in Equation (4.18) from 7 to 6 only has a small effect, increasing the magnitude slightly. On the other hand increasing it to 8 has a detrimental effect, greatly reducing the size of the response. Increasing the value of C_1 by changing either of the other two parameters in Equation (4.18) only has a small effect on the behaviour and reduces the magnitude of the response.

The fit is not very sensitive to these vacuum phenomenon parameters. They could be used for fine-tuning but will not greatly improve the behaviour if changed on their own.

4.4.7 Compliance of the second chamber

The compliance of the second chamber is much greater than that of the first chamber (more than two orders of magnitude). The properties of the hydromount are therefore governed primarily by the characteristics of the first chamber compliance. As long as this remains the case there is negligible effect of altering the actual value of the second chamber compliance. Even decreasing the value so there is about a factor of 10 between the first and second chamber compliance has little visible effect. When the compliances become similar in magnitude there is an effect, and the resonance frequency is increased (as would be expected by the increase in stiffness).

4.4.8 Summary

The non-linear model gives fairly good agreement with measurements on the proprietary hydromount, but there is some uncertainty in the values of some of the parameters. The fit could be improved by using optimisation techniques and the results of this may either suggest more accurate values for some of the parameters currently undetermined or indicate non-linearities in parameters not currently considered to be significantly non-linear. This will be considered in the next section.

4.5 Particle Swarm Optimisation

Particle swarm optimisation (PSO) is a optimisation method inspired by the behaviour of biological organisms such as birds and fish. The algorithm was first developed by Kennedy and Eberhart [166]. Simplistically, a number of 'particles' are used, initially randomly positioned in the search space. After evaluating the results for each particle, the particles move towards the best solution from the previous results. This relatively new technique is designed to be simple, with few parameters and can find the global minimum within the specified search space. It can also be used to find optimised values for several parameters at the same time.

The Matlab code for particle swarm optimisation used in this thesis was downloaded from www.yarpiz.com [167]. The optimisation for each amplitude was run

separately. The cost function was based on a comparison between the non-linear model using the adjusted parameters and the experimental results across the frequency range 1 to 25 Hz. The frequency range was chosen such that the resonance was included without putting undue emphasis on the high frequency behaviour. Also limiting the frequency range speeds up the computation time. The cost function was calculated using:

$$C = \sum_{f=1}^{25} (K'_{\text{mod}} - K'_{\text{exp}})_f^2 + \sum_{f=1}^{25} (K''_{\text{mod}} - K''_{\text{exp}})_f^2. \tag{4.19}$$

where C is the cost, f is the frequency, the subscript 'mod' indicates the non-linear model and the subscript 'exp' indicates the measured data.

Each particle contains a set of parameters, the position of which is initially randomised (with the exception of particle 1, which, with the aim of speeding up the convergence, has its position set to the values of the parameters used in the non-linear model). Each parameter is given a maximum and minimum value which defines the search space. The velocity of each particle is set to 0 at the start. Having evaluated the cost function the particle velocities are updated using the following equation for particle i:

$$\mathbf{v}_i = w\mathbf{v}_{i-1} + c_1 R_1(\mathbf{x}_{i,\text{opt}} - \mathbf{x}_{i-1}) + c_2 R_2(\mathbf{x}_{\text{glob,opt}} - \mathbf{x}_{i-1}) \tag{4.20}$$

where $\mathbf{v}_i$ is the 'velocity' of particle i, w is termed the inertia weight (explained further below), $c_1 = 1.5$ is the personal learning coefficient, $\mathbf{x}_i$ is the position of particle i, $\mathbf{x}_{i,\text{opt}}$ is the optimal position of the particle so far, $c_2 = 2.0$ is the global learning coefficient and $\mathbf{x}_{\text{glob,opt}}$ is the global optimal position so far. R_1 and R_2 are uniformly distributed random numbers between 0 and 1. The inertia weight is initially set to 1, but is adjusted by multiplication by an inertia weight damping ratio (set to 0.99) after each iteration, so the current particle velocity has less influence over the new velocity at higher iterations.

The maximum and minimum velocity are set so that they are factors of 0.1 and -0.1 of the search space for each variable. If these are exceeded the maximum or minimum velocity is chosen instead. After this the new position is calculated:

$$\mathbf{x}_i = \mathbf{x}_{i-1} + \mathbf{v}_i \tag{4.21}$$

Variable	Minimum	Maximum	Units
A_r	0.001	0.01	m^2
C_2	1.00×10^{-8}	1.00×10^{-7}	$\mathrm{m}^4\mathrm{s}^2\mathrm{kg}^{-1}$
A_i	5.0×10^{-5}	5.0×10^{-4}	m^2
l_i	0.10	0.50	m
R_i	$1.00 \times 10^{11} q_\mathrm{i}$	$5.00 \times 10^{11} q_\mathrm{i}$	$\mathrm{m}^4\mathrm{s\ kg}^{-1}$
$a^\dagger$	-1×10^{-50}	0	$\mathrm{m}^3\mathrm{Pa}^{-b-1}$
$b^\dagger$	0	10	
$c^\dagger$	1.0×10^{-10}	1.0×10^{-9}	$\mathrm{m}^4\mathrm{s}^2\mathrm{kg}^{-1}$
$d^\dagger$	-50	-10	kPa
$e^\dagger$	5.0×10^{-11}	1.0×10^{-9}	$\mathrm{m}^4\mathrm{s}^2\mathrm{kg}^{-1}$

† where Equation (4.18) can be written:

$$C_1 = \begin{cases} a(101000 + p_1)^b + c & p_1 < d \\ e & \text{otherwise} \end{cases}$$

Table 4.3: The variables used with maximum and minimum values in the PSO

The new position is checked to ensure it is between the maximum and minimum for each variable. If it is outside the allowed range then the maximum or minimum value is chosen and the velocity is reversed for those variables. The variables considered and the maximum and minimum values for each variable can be seen in Table 4.3.

For this work 100 particles were chosen and 200 iterations were carried out. Figure 4.17 shows the improvement in the optimal global solution for all the amplitudes. The cost function was minimised more effectively for the higher amplitude cases, with the best cost function for the 1.0 mm case. In Figure 4.18 the results from the model using the PSO parameters are compared with the experimental data and the model using the previous parameters. The fit is improved relative to Figures 4.8-4.13 at all amplitudes, but most significantly at higher amplitudes, particularly 1 mm as the cost function data suggests. The main point of mismatch between the model with the PSO parameters and the experimental data is at the resonance peak. The resonance frequency obtained using the optimised parameters matches well at all amplitudes.

The parameters obtained for each amplitude can be seen in Figure 4.19. C_2 is not included. This is because to 5 significant figures there was no variation between the values and it was equal to the maximum allowed value. As has been described in Section 4.4.7, if the value of C_2 is more than two orders of magnitude greater

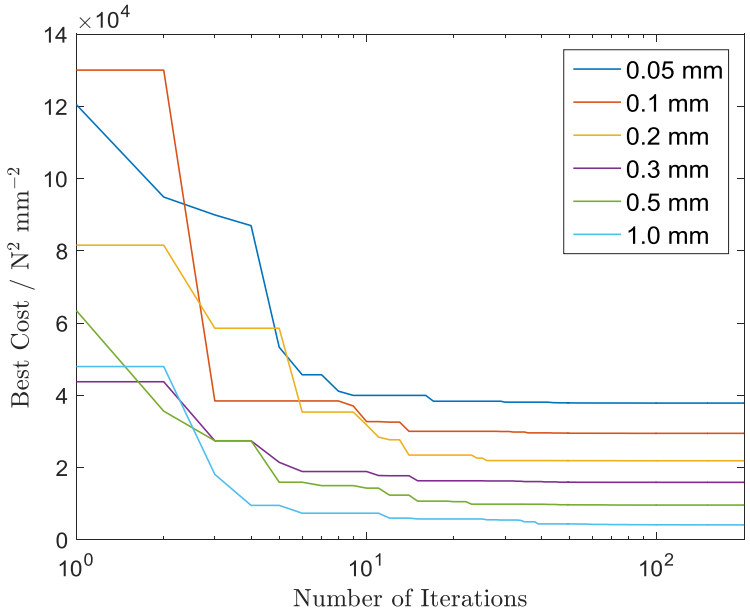

Figure 4.17: The best result from the cost function after each iteration

than C_1 there is little or no effect on the model if C_2 is changed. Therefore, it was felt there would be no great benefit to extending the range of C_2 to improve the fit further.

The other parameters do not show a general trend with changing amplitude, with the possible exception of the coefficient for R_i which appears to show a decrease with increasing amplitude. Using the mean values (across the amplitudes) for each optimised parameter leads to an improvement over the initial values at all amplitudes as shown in Figure 4.20 and the results are very similar to the post PSO values at 0.1 mm and 0.2 mm amplitude. At high amplitudes using the mean values causes the resonance frequency to shift to lower values and at 0.05 mm the peak and trough are poorly predicted.

Assuming that the coefficient for R_i is non-linear, curves were fitted to the data using Microsoft Excel. Table 4.4 shows the coefficient of determination for different curves: the closer to 1 this is, the better the fit of the curve to the experimental data. The exponential fit appears to be best giving the equation:

$$y = 1.92 \times 10^{11} \exp(-1.28x) \tag{4.22}$$

where y is the coefficient of R_i and x is the amplitude. This curve can be seen in Figure 4.21 along with the linear regression line. At 0.5 and 1 mm amplitudes the exponential function agrees very well with the post PSO values for the coefficient

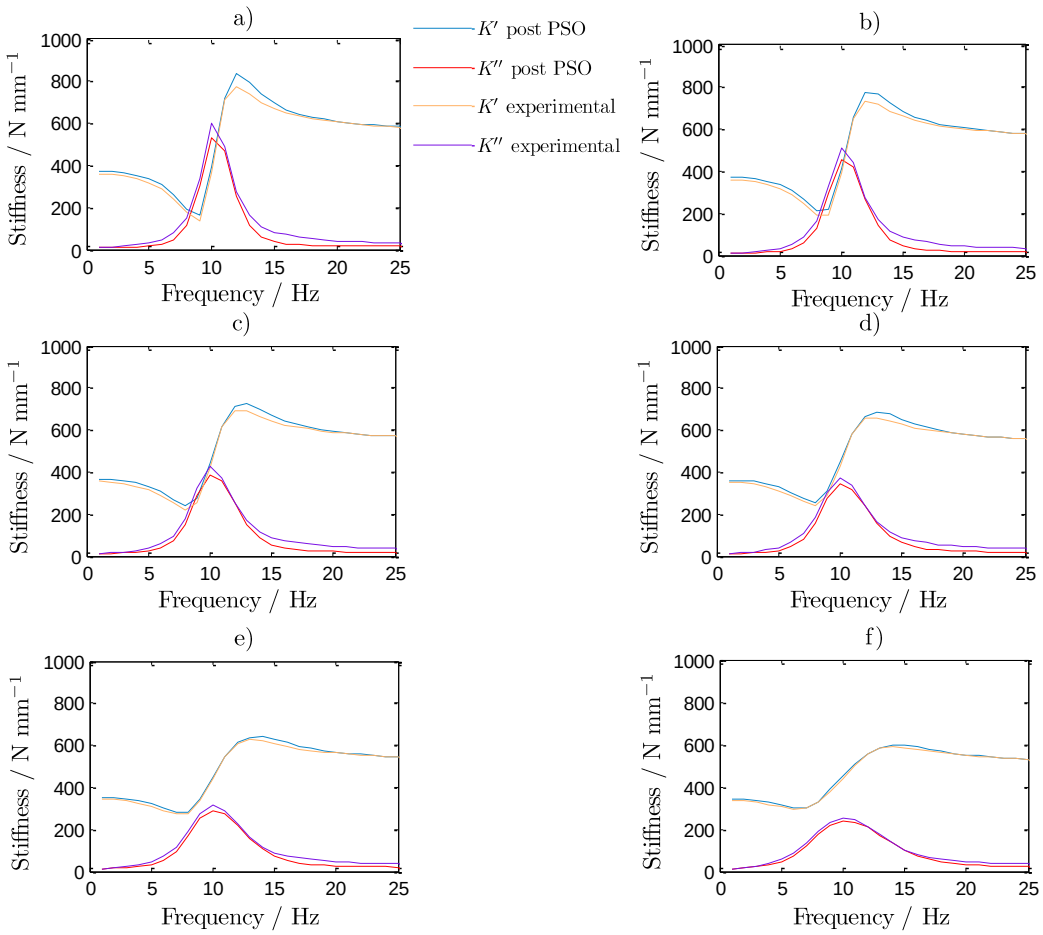

Figure 4.18: Comparison of the model using the parameters optimised with PSO with the experimental results of the in- and out-of-phase stiffness for a) 0.05 mm, b) 0.1 mm, c) 0.2 mm, d) 0.3 mm, e) 0.5 mm and f) 1.0 mm amplitude

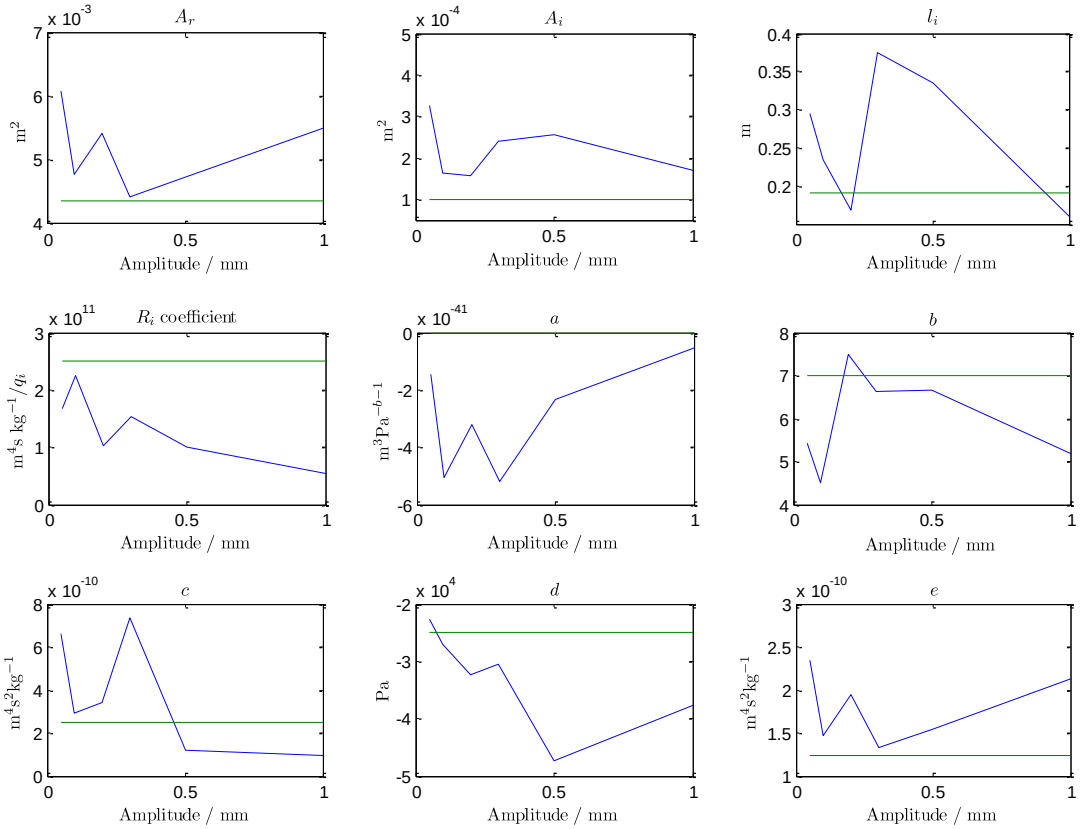

Figure 4.19: The variation of the optimised parameters with amplitude. PSO optimised parameters (blue) and initial parameters (green).

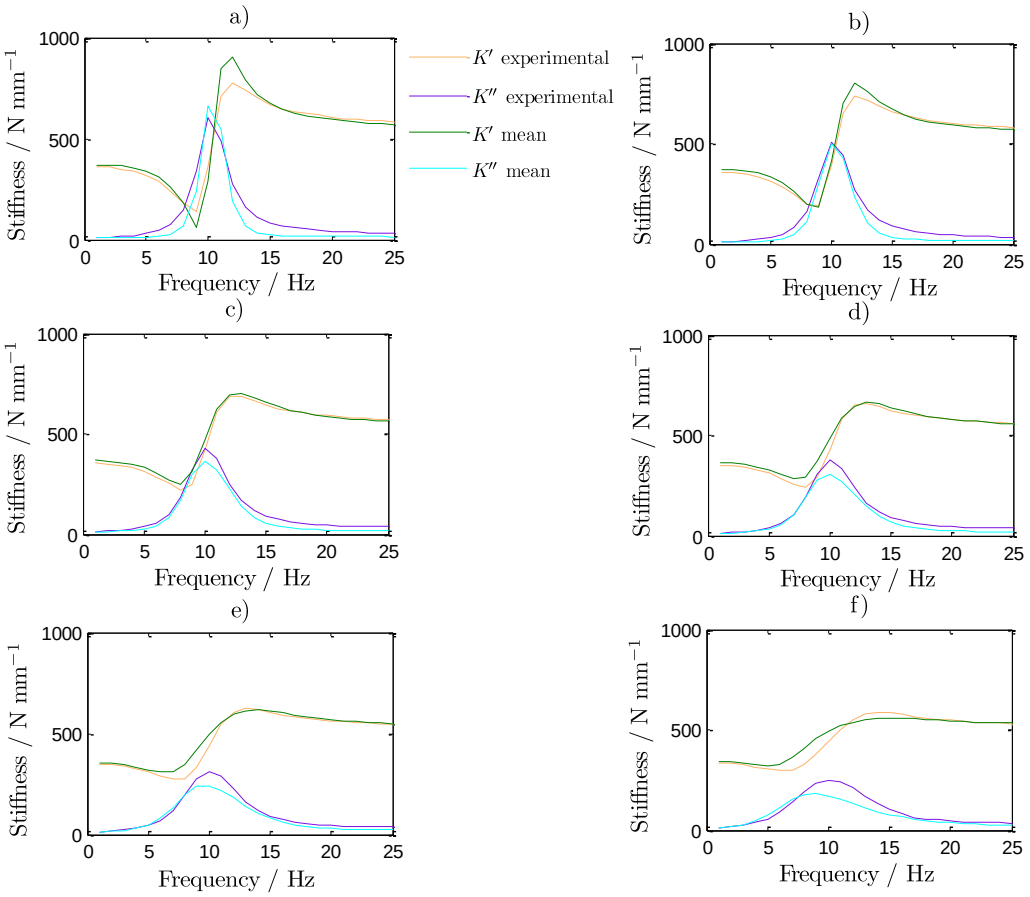

Figure 4.20: Comparison of the model using mean values of the optimised parameters and the experimental data for the in- and out-of-phase stiffness for a) 0.05 mm, b) 0.1 mm, c) 0.2 mm, d) 0.3 mm, e) 0.5 mm and f) 1.0 mm amplitude

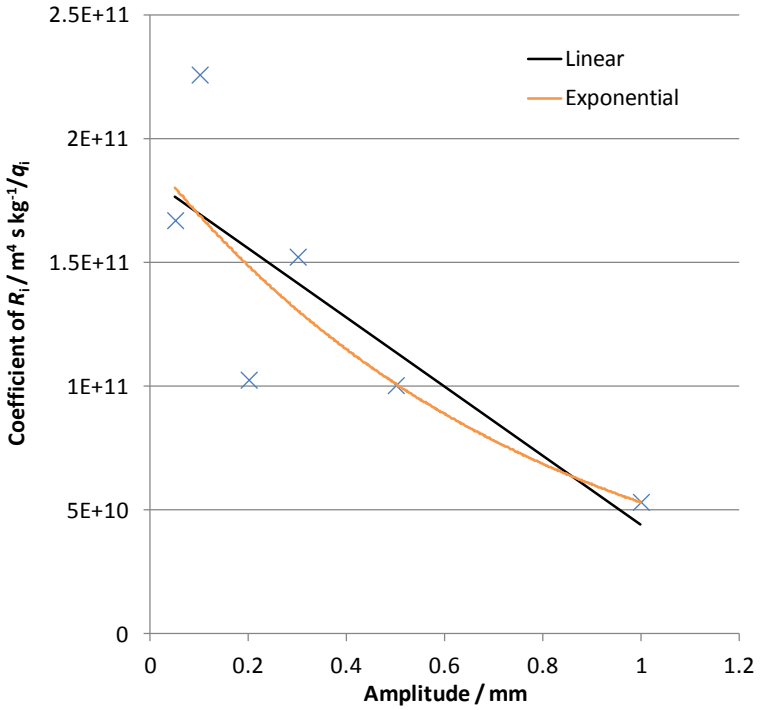

Figure 4.21: Linear and exponential curve-fitting for the coefficient of R_i with respect to dynamic amplitude

of R_i. However, large variations at 0.1 mm and 0.2 mm amplitudes are not well matched by any trend line.

Curve	R^2
Linear	0.65
2$^{\mathrm{nd}}$ order polynomial	0.68
3$^{\mathrm{rd}}$ order polynomial	0.68
Logarithmic	0.63
Power	0.69
Exponential	0.80

Table 4.4: The coefficient of determination (R^2) for different curve fittings

Including the relationship for the coefficient for R_i and using the mean values for all the other values gives rise to the results in Figure 4.22. This generally has an improved fit over using the mean alone, particularly around the resonance. However, at low amplitudes the high frequency asymptote is reduced compared with the experimental data. The prediction of the trough in K' is improved at

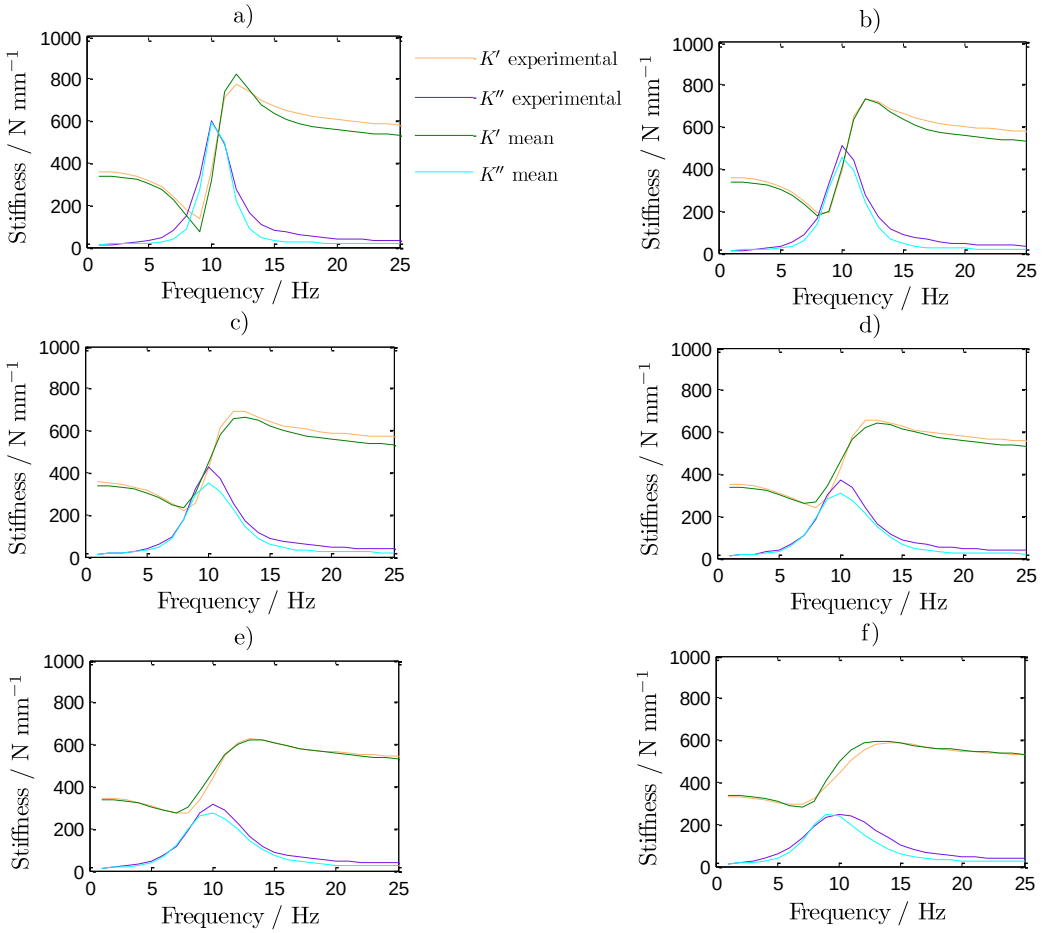

Figure 4.22: Comparison of the model using mean values of the optimised parameters and the exponential function for the coefficient of R_i and the experimental data for the in- and out-of-phase stiffness for a) 0.05 mm, b) 0.1 mm, c) 0.2 mm, d) 0.3 mm, e) 0.5 mm and f) 1.0 mm amplitude

all amplitudes, but the peak response is less well predicted for 0.2 and 0.3 mm amplitude. At high amplitudes the fit is improved.

4.6 Conclusions

The mount tested showed a strong relationship between displacement amplitude and the magnitude of K' and K'', but the frequency of the resonance was not significantly affected by changing the amplitude. The linear model used gave good agreement in predicting the frequency of the resonances, but the magnitude of K' and K'' was not predicted well and it was clear that the inclusion

of non-linear parameters might improve this fit as the magnitude of these is strongly amplitude dependent. Adding the non-linearities improved the fit of the model to the experimental data, but made the frequency of the resonances amplitude dependent. This effect becomes more significant at higher amplitudes. Generally the trends seen are similar to the experimental results, with increases in the amplitude leading to reductions in the magnitude of the stiffnesses, and broadening of the bandwidth of the resonances. With these parameters the best agreement for the in-phase stiffness is seen at 0.2 mm and for the out-of-phase stiffness at 0.1 mm.

From an investigation of the parameters in the model, some have much more effect than others in changing the appearance and position of the features. The area of the rubber spring has no significant effect on the resonance frequency, mainly controlling the magnitude of the response above the resonance. The dimensions of the inertia track (length and area) have an effect on the resonance of the hydromount, but little effect on the high and low frequency behaviour. However, it is likely that the empirical equation for the resistance to flow through the inertia track is also dependent on the dimensions of the inertia track. The effective length of the inertia track is likely to be somewhat amplitude dependent, as it will be based to some extent on the speed of the fluid through the inertia track as well as on the increased pressure in the upper chamber due to the imposed displacement. Density also has a significant effect on the resonance behaviour as it is contained in the definition of the inertance or the mass-like properties of the fluid. Changing the coefficient in the non-linear equation for resistance to flow has a significant effect on the magnitude of the peaks and troughs at the resonance whilst leaving the high and low frequency behaviour unchanged. It is not very sensitive to these vacuum phenomenon parameters, but they could be used for fine-tuning. In this mount, the compliance of the second chamber is much greater than that of the first chamber (approximately two orders of magnitude) and so the properties of the hydromount are governed primarily by the characteristics of the first chamber compliance.

Using PSO to optimise the parameters of the non-linear model improves the fit at all amplitudes. However, the cost function is minimised most effectively at higher amplitudes, with the best cost function and the best fit achieved for the 1.0 mm case. The main point of mismatch between the model with the PSO parameters and the experimental data is at the resonance peak, with the resonance frequency predicted well for all amplitudes. The best-fit parameters do not show a general

trend with changing amplitude, with the possible exception of the coefficient for R_{i} which appears to decrease with increasing amplitude. Using the mean values (across the amplitudes) for each optimised parameter leads to an improvement in the fit at all amplitudes and the results are very similar to the post PSO values at the 0.1 mm and the 0.2 mm amplitudes. At high amplitudes, using the mean values causes the resonance frequency to shift to lower values and at 0.05 mm the peak and trough are poorly predicted. These features can be improved by using the mean values, apart from the coefficient of R_{i} which is described by an exponential function of amplitude. Although this improves the high amplitude resonance frequency prediction and K' behaviour, it is less good at predicting the high frequency behaviour at low amplitudes, or the peak in K' for 0.2 and 0.3 mm. The success of the optimisation technique means it has potential to be used to design a mount to fit a particular idealised behaviour, as well as providing a tool to create a model with good agreement to measured data that can be used in multi-body dynamics simulations of the full vehicle.

Chapter 5

Switching Mechanism

5.1 Concept

The aim of the work done in this chapter is to develop a simply controllable switching mechanism that can be operated using the existing electricity supply from the car battery. It is also desirable to be compact, so that it can fit in the engine bay and under the engine. Ideally it should also be functional at temperatures well above ambient, although that has not been considered in the current work.

The initial idea was to adjust the resonance frequency of a single track hydromount. As discussed in Section 4.4, there are four variables that could be altered to change the resonance frequency of a hydromount:

- the compliance of the first chamber;
- the length of the inertia track;
- the diameter of the inertia track;
- the density of the fluid

The density of the fluid is difficult to alter *in situ*. The length and diameter of the inertia track could be altered, but this would require a complicated mechanism. The compliance of the first chamber, C_1 is the easiest to vary.

In one state, with a very high compliance, most of the volume change due to the movement of the rubber mount would be absorbed in the first chamber, leading to only a small flow through the inertia track resulting from the small pressure difference. The resonance of this state could be tuned to a particular disturbing frequency if required. The other state, with a much lower compliance, would have a much larger effect on the stiffness and the damping provided by the mount as more of the fluid would be forced through the inertia track.

The work in this chapter continues from a promising arrangement presented by Ahmadi et al.[6] to which the author contributed, which used a diaphragm made of magnetically controllable elastomer (MCE). The set-up in Section 5.2.1 is based on this configuration, but with constraint in the off-state.

5.2 Compliance of the first chamber[i]

A series of tests were carried out to evaluate different possible mechanisms to provide a two-state mount. The test rig was designed prior to this project and can be seen in Figure 5.1. It consists of a rubber spring taken from a commercially available mount. The inertia track is a copper pipe, which passes out of the side of the top chamber allowing the bottom of the first chamber to be accessible so that its compliance can be altered using diaphragms. The second chamber compliance is governed by a diaphragm made of unfilled natural rubber. The parameters for this rig can be seen in following Table 5.1.

Parameter	Value	Unit
Diameter of the inertia track	12.5	mm
Length of the inertia track	300	mm
Diameter of the 2nd chamber diaphragm	50	mm

Table 5.1: The dimensions of the mount used to test the compliance

Unless otherwise stated a permanent magnet was used to provide the on-state, with a flux density in the order of 1 T. There was a soft iron ferromagnetic rod

[i]The experimental work presented in this section was carried out by Luigi Borrelli, an undergraduate student from the University of Naples Federico II, with day-to-day supervision by the author. The ideas for the testing configurations resulted from discussions between Luigi Borrelli, and TARRC staff Hamid Ahmadi, Alan Harris and the author.

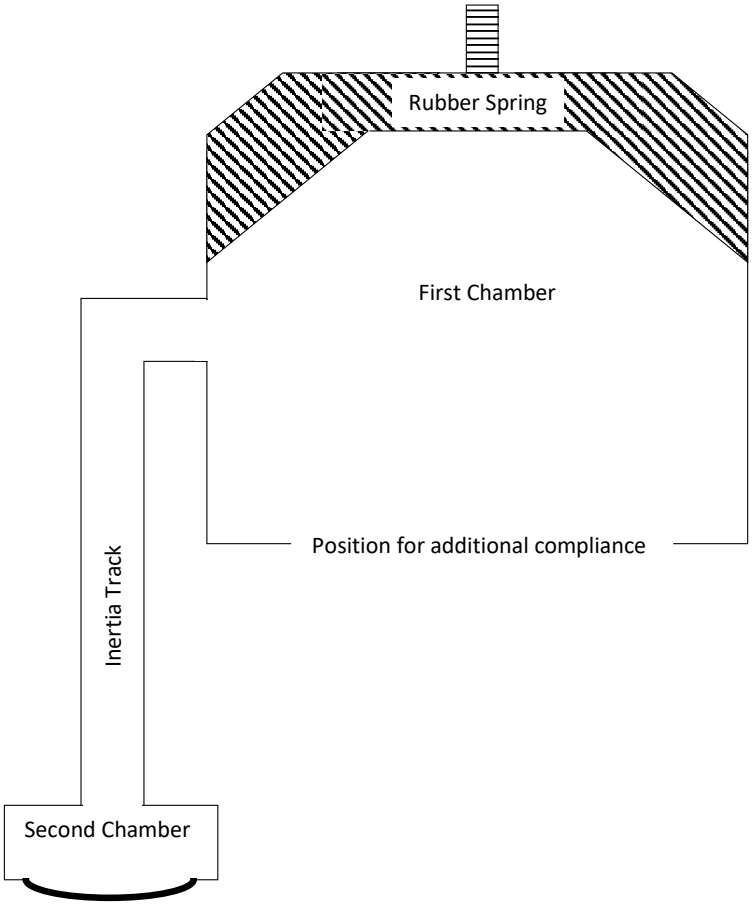

(a) Schematic diagram of the rig

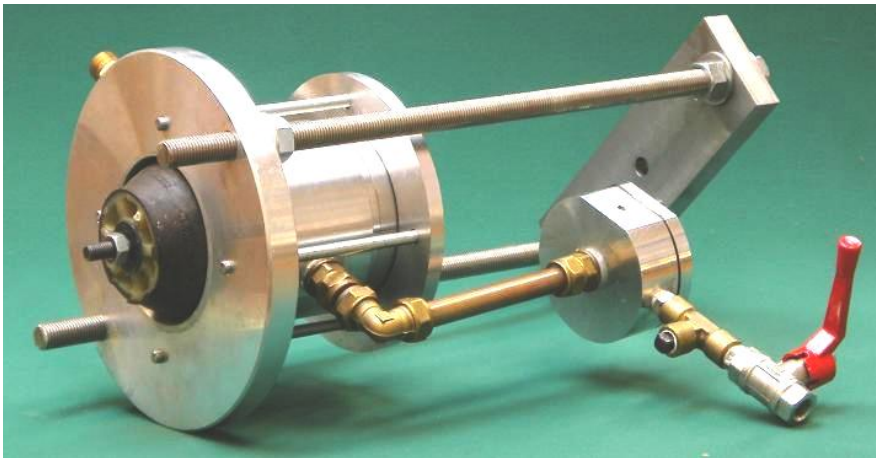

(b) Photograph of the rig

Figure 5.1: The rig used to test the switching mechanism.

attached which could be attached to the top of the magnet and direct the field towards the switching mechanism at the bottom of the first chamber. Its position could be altered with respect to the lower side of the diaphragm of the switching mechanism and can be left in place for the off-state when the magnet is removed.

All the testing was done on the VH7 Schenck (Figure 4.1) in 1 Hz steps between 1 and 50 Hz, and the dynamic displacement was measured at the top and the force at the bottom and a Solartron 1250 Frequency Response Analyser was used to find the harmonic dynamic stiffness. Two different amplitudes were tested (0.1 mm and 1 mm). The results presented typically include three conditions at each amplitude in each configuration:

- Free - there is no restriction on the movement of the diaphragm
- Off-state - as it would be in service with the ferromagnetic rod present
- On-state - as 'off-state' but with the permanent magnet beneath.

The resonance frequency of the mount is recorded. With knowledge of the inertance this is used to estimate the compliance of the system. As the compliance of the diaphragm of the second chamber is not known and there is large variation in the first chamber compliance, the assumption used in Section 4.2 that $C_1 << C_2$ may not be valid, but C_2 should be consistent throughout the different configurations. The frequency corresponding to the peak in K'' can be calculated from $\omega^2 \approx (C_1 + C_2)/(C_1 C_2 I_i)$ (Equation (4.7)). So the term $(C_1 C_2)/(C_1 + C_2)$ is used for the system compliance.

5.2.1 MCE diaphragm

The simplest configuration tried was a 2 mm-thick circular diaphragm of a proprietary formulation of MCE installed across the bottom of the first chamber (Figure 5.2). The MCE contained 470 parts of iron per one hundred parts of NR by weight. The diaphragm was stretched taut before assembly. The 'free' condition is equivalent to testing it with no switching device.

Of itself the change in stiffness of the MCE is not sufficient to effect a significant change in the compliance of the chamber as the change in stiffness is quite modest,

particularly at large strains. The design exploits restriction of movement of the diaphragm when it is attracted to the magnet, rather than the change in stiffness.

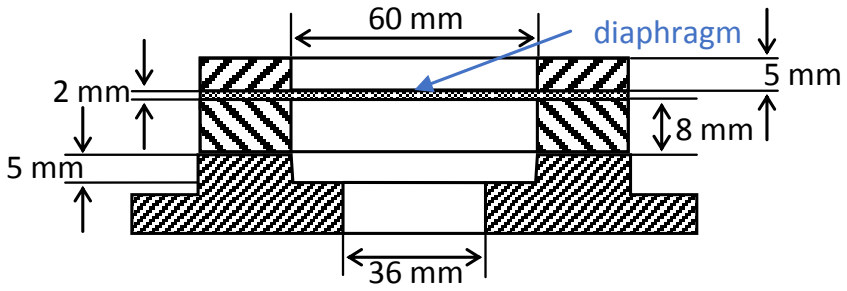

Figure 5.2: The MCE diaphragm configuration.

The results are shown in Figures 5.3 and 5.4. There is a reasonably large effect for the free condition, under which the resonance is mostly suppressed within the frequency range tested (although as the compliance has been increased the resonance frequency is reduced slightly). The suppression of the resonance is due to the diaphragm being able to absorb the majority of the volume change at the top, and keep the pressure of the chamber low, so only a small volume of fluid is forced through the inertia track. However, this does not replicate the situation in a vehicle, where the magnet will remain *in situ* and be switched on and off. In this configuration the rod was in contact with the diaphragm. The effect of leaving the metal rod in place (at the bottom of the diagram in Figure 5.2) in the off-state is that there is not a large difference compared with the on-state. This meant that this simple configuration was not considered a suitable solution. Table 5.2 gives the resonance frequencies and the system compliances for the different cases.

Amplitude mm	**Condition**	**Frequency of peak** K'' Hz	$\frac{C_1C_2}{C_1+C_2}$ $\mathrm{m^3Pa^{-1}}$
0.1	Free	12.5	6.10×10^{-11}
0.1	On	15	4.22×10^{-11}
0.1	Off	13	5.62×10^{10}
1	Free	10	9.52×10^{-11}
1	On	12	6.62×10^{-11}
1	Off	12	6.62×10^{-11}

Table 5.2: The resonance frequencies and system compliance of the MCE diaphragm

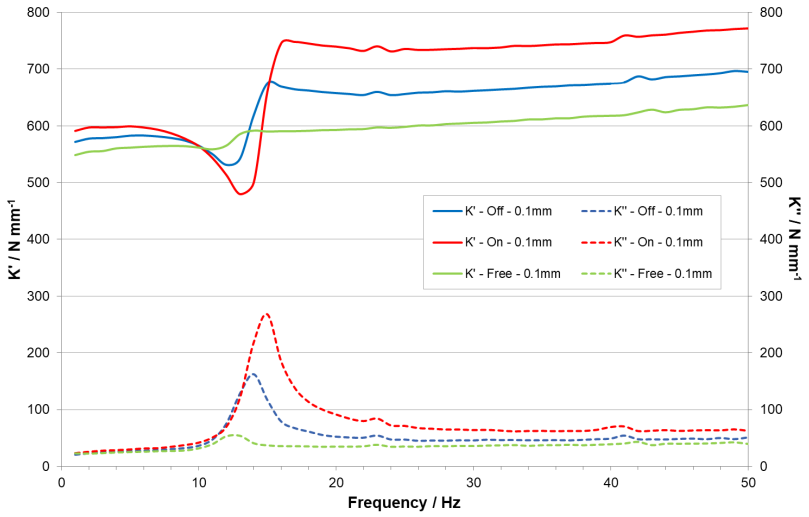

Figure 5.3: The stiffness of the configuration using an MCE diaphragm to control the first chamber compliance tested at 0.1 mm amplitude. 'On' is for the results with a magnet in place, 'Off' with the rod *in situ* and 'Free' with no restriction.

5.2.2 MCE-MRF sandwich

To encourage a stronger interaction with the magnet and take advantage of the ability of MRFs to solidify in the presence of a magnetic field, in the next configuration (shown in Figure 5.5) glycol was used with 70% by weight iron particles sandwiched between two 1 mm thick MCE diaphragms. A 1 mm thick ring of MCE was used to separate the two MCE layers.

To allow more free movement of the diaphragm in the off-state, the rod was placed at different distances away from the diaphragm. With a 1 mm gap there was very good behaviour at 0.1 mm amplitude; the resonance was suppressed in the off-state and a strong effect of the magnet was observed in the on-state as seen in Figures 5.6 and 5.7. However, at 1 mm amplitude input, where the movement of the diaphragm was greater than the 1 mm gap, the off-state behaviour was too similar to the on-state behaviour. With a 3 mm gap there is no effect of the magnet at 0.1 mm amplitude (Figure 5.8), and only a small effect at 1 mm amplitude (Figure 5.9). This configuration therefore did not provide a suitable solution. Table 5.3 gives the resonance frequencies and the system compliances for the different cases. The resonance frequencies for the 'Free' cases were not clear enough to be included.

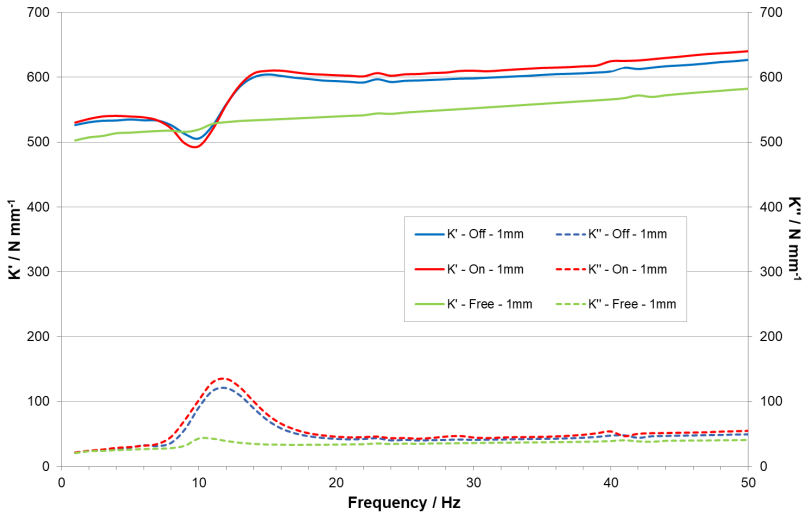

Figure 5.4: The stiffness of the configuration using an MCE diaphragm to control the first chamber compliance tested at 1 mm amplitude. 'On' is for the results with a magnet in place, 'Off' with the rod *in situ* and 'Free' with no restriction.

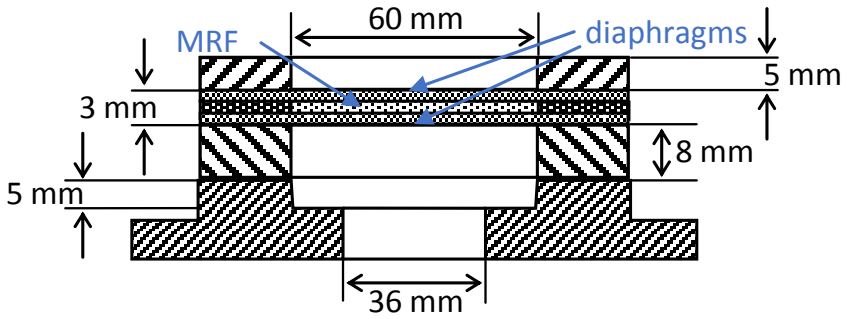

Figure 5.5: The MCE-MRF sandwich configuration.

Gap mm	**Amplitude** mm	**Condition**	**Frequency of peak** K'' Hz	$\frac{C_1+C_2}{C_1C_2}$ $\mathrm{m^3Pa^{-1}}$
1	0.1	On	14.5	4.52×10^{-11}
1	0.1	Off	12	6.62×10^{-11}
1	1	On	11	7.87×10^{-11}
1	1	Off	10	9.52×10^{-11}
3	0.1	On	indistinct	-
3	0.1	Off	indistinct	-
3	1	On	9	1.17×10^{-10}
3	1	Off	indistinct	-

Table 5.3: The resonance frequencies and system compliance of the MCE-MRF sandwich

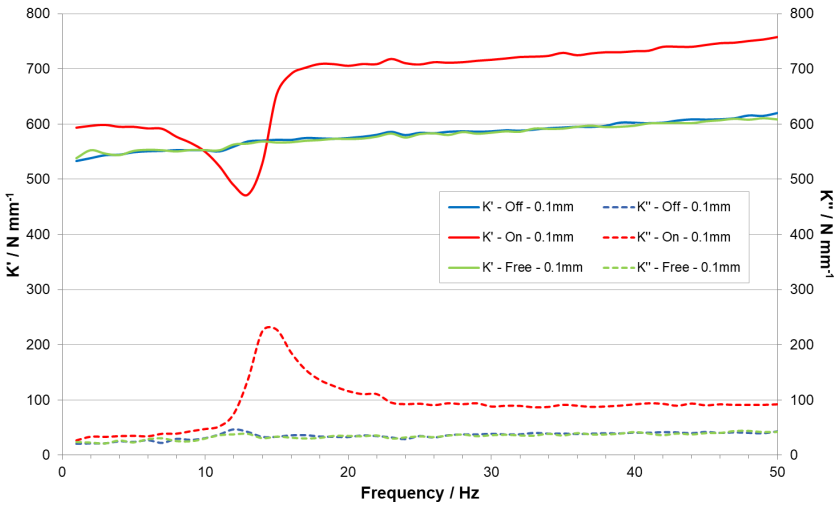

Figure 5.6: The stiffness of the configuration using an MCE-MRF sandwich to control the first chamber compliance with a 1 mm gap tested at 0.1 mm amplitude. 'On' is for the results with a magnet in place, 'Off' with the rod *in situ* and 'Free' with no restriction.

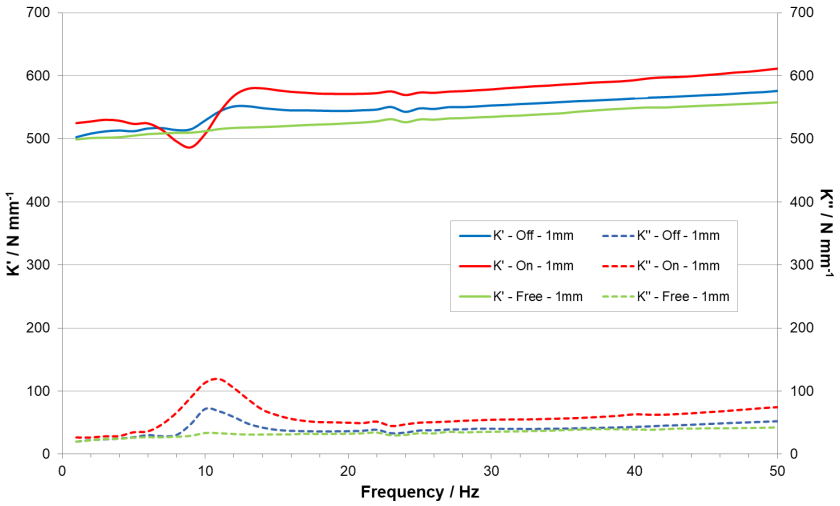

Figure 5.7: The stiffness of the configuration using an MCE-MRF sandwich to control the first chamber compliance with a 1 mm gap tested at 1 mm amplitude. 'On' is for the results with a magnet in place, 'Off' with the rod *in situ* and 'Free' with no restriction.

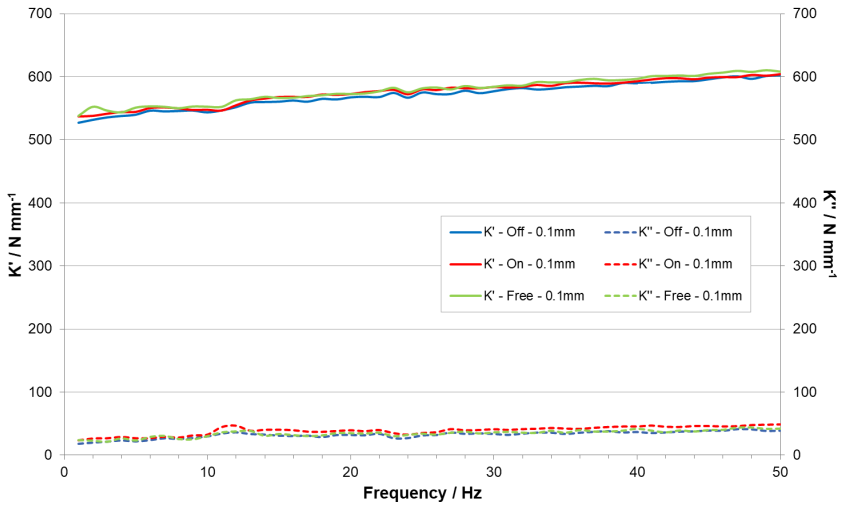

Figure 5.8: The stiffness of the configuration using an MCE-MRF sandwich to control the first chamber compliance with a 3 mm gap tested at 0.1 mm amplitude. 'On' is for the results with a magnet in place, 'Off' with the rod *in situ* and 'Free' with no restriction.

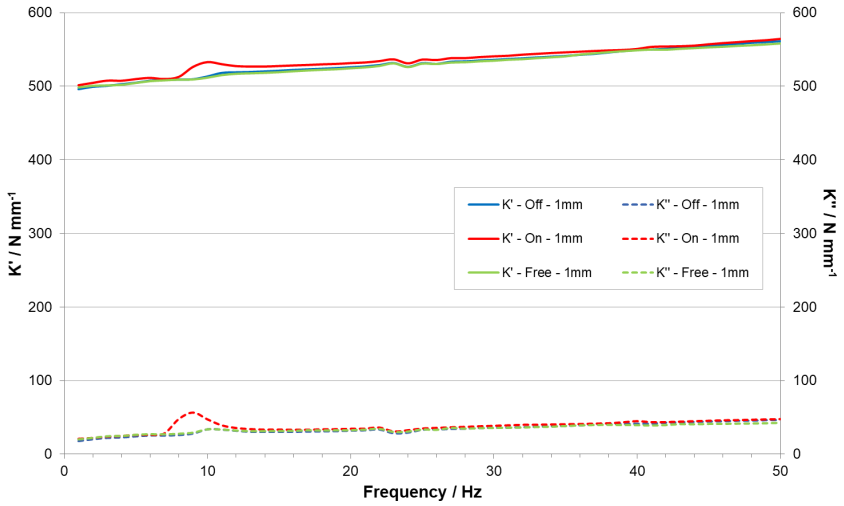

Figure 5.9: The stiffness of the configuration using an MCE-MRF sandwich to control the first chamber compliance with a 3 mm gap tested at 1 mm amplitude. 'On' is for the results with a magnet in place, 'Off' with the rod *in situ* and 'Free' with no restriction.

5.2.3 NR-MRF sandwich

There are questions about the fatigue life and ageing characteristics of the MCE. These concerns could be alleviated by using a typical natural or synthetic rubber compound, but it was uncertain how effective such a material would be in this role. To investigate this the MCE in the previous configuration was replaced with an unfilled NR compound of the same dimensions. As the stiffnesses of the rubbers will be different, the two configurations are not directly comparable. If the results were promising and the desired stiffness is known, it would be possible to design an appropriate compound. Although the amount of MRF should be similar in quantity to the previous configuration this will not be exactly the same, leading to more difficulty in direct comparison.

The results for this configuration are shown in Figures 5.10 and 5.11. Looking at these results there is not a large advantage to using the MCE. The unfilled NR compound is softer, which leads to two effects: the resonance frequency will be lower; and more of the motion of the liquid will be absorbed by the diaphragms. Consequently less fluid will be forced through the inertia track, meaning the on-state behaviour is less pronounced. This can be seen by looking at the results for the 1 mm gap. The behaviour is quite similar to that of the previous configuration, with desirable behaviour at 0.1 mm amplitude, but the 1 mm behaviour still not ideal. Table 5.4 gives the resonance frequencies and the system compliances for the different cases. The resonance frequencies for the 'Free' cases were not clear enough to be included.

Gap	**Amplitude**	**Condition**	**Frequency of peak** K''	$\frac{C_1 + C_2}{C_1 C_2}$
mm	mm		Hz	m^3Pa^{-1}
1	0.1	On	14	4.85×10^{-11}
1	0.1	Off	indistinct	-
1	1	On	10.5	8.62×10^{-11}
1	1	Off	9	1.17×10^{-10}

Table 5.4: The resonance frequencies and system compliance of the NR-MRF sandwich

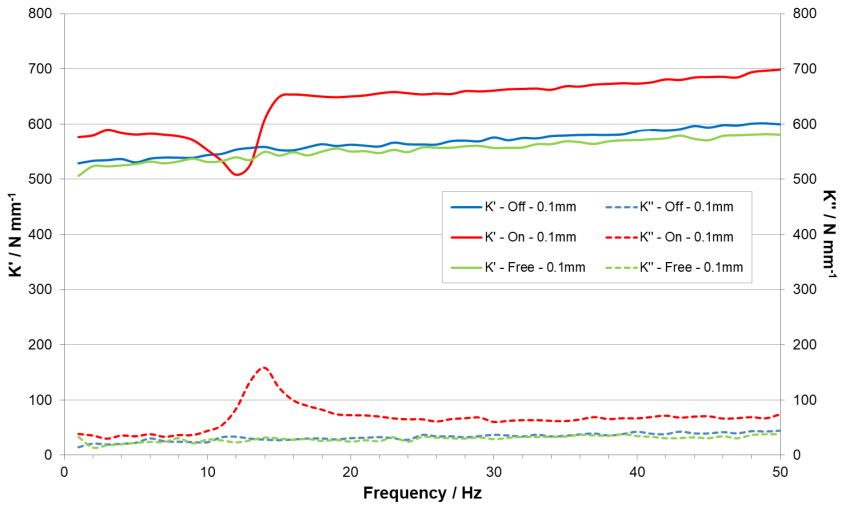

Figure 5.10: The stiffness of the configuration using an NR-MRF sandwich to control the first chamber compliance with a 1 mm gap tested at 0.1 mm amplitude. 'On' is for the results with a magnet in place, 'Off' with the rod *in situ* and 'Free' with no restriction.

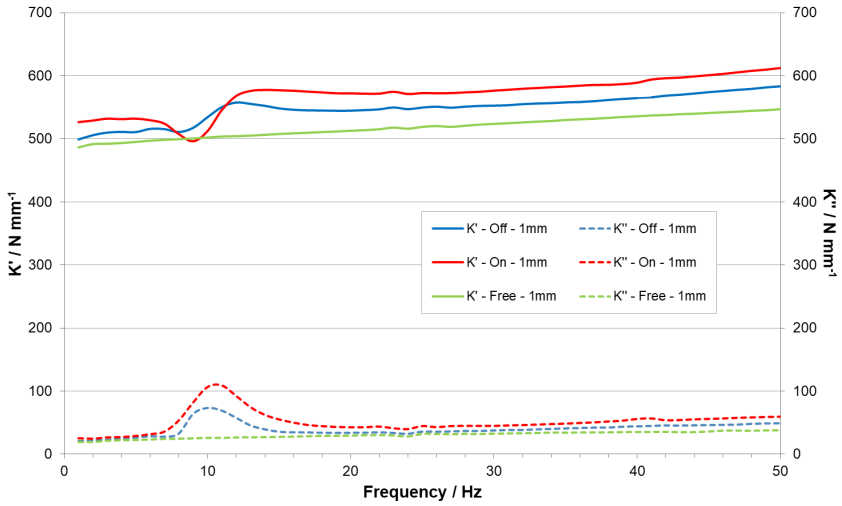

Figure 5.11: The stiffness of the configuration using an NR-MRF sandwich to control the first chamber compliance with a 1 mm gap tested at 1 mm amplitude. 'On' is for the results with a magnet in place, 'Off' with the rod *in situ* and 'Free' with no restriction.

5.2.4 MCE-MRF sandwich 2

Even though it had not been found to provide significant advantages over unfilled NR, due to the availability of the MCE sheet material used to make the diaphragms, its use was continued. The issues with the previous two configurations was at 1 mm amplitude where the movement in the off-state was too restricted. A greater space for the diaphragm at the bottom of the chamber to move might improve this behaviour. The quantity of MRF used in this next configuration was much greater, with an 8 mm cavity filled with the fluid (Figure 5.12). The diameter of the diaphragms was restricted to be 4 mm larger than the rod for the magnet. This means that the effect of the magnet should be greater across the MRF. To allow the potential for movement of the fluid in the off-state the bottom of the lower diaphragm was not constrained to a diameter of 40 mm, but around the edge of the magnet it was free to move.

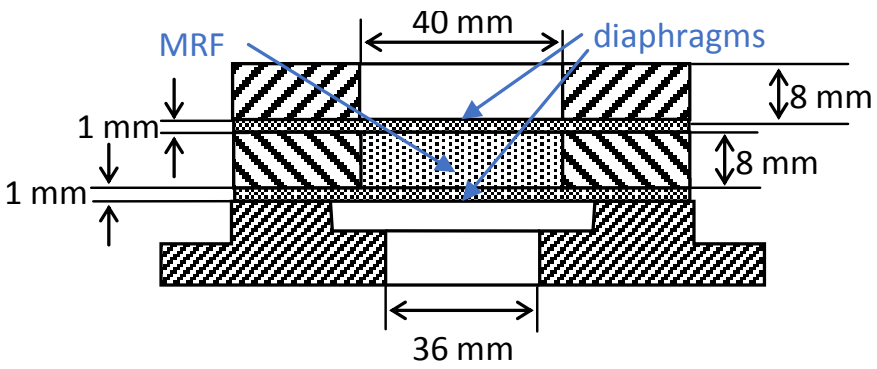

Figure 5.12: The MCE-MRF sandwich 2 configuration.

The results are shown in Figures 5.13 to 5.16 and do not include a 'free' test as the desired suppression of the resonance has been shown in previous configurations. These results show that the behaviour is not sensitive to the positioning of the rod (there is 4 mm difference in the rod positioning between the two sets of results shown, the -2 mm gap indicates that the rod has been pushed into the diaphragm). At both the 0.1 mm and the 1 mm amplitudes there is a shift in frequency between the key features of the on-state and off-state, although the resonance is not suppressed in the off-state. This suggests that the stiffness of the sandwich configuration in the off-state needs to be reduced. Table 5.5 gives the resonance frequencies and the system compliances for the different cases.

Gap mm	**Amplitude** mm	**Condition**	**Frequency of peak K''** Hz	$\frac{C_1+C_2}{C_1C_2}$ m^3Pa^{-1}
-2	0.1	On	23	1.79×10^{-11}
-2	0.1	Off	21	2.15×10^{-11}
-2	1	On	18	3.18×10^{-11}
-2	1	Off	16.5	3.49×10^{-11}
2	0.1	On	22.5	1.87×10^{-11}
2	0.1	Off	20	2.37×10^{-11}
2	1	On	16.5	3.49×10^{-11}
2	1	Off	15	4.21×10^{-11}

Table 5.5: The resonance frequencies and system compliance of the MCE-MRF sandwich 2

5.2.5 NR-MRF sandwich 2

Based on the promising results of the previous configuration, but in an attempt to make the switching mechanism softer, a slightly altered system was tried. This again used unfilled NR instead of MCE. Also the upper diaphragm was not restricted to 40 mm diameter but was 60 mm as in the earlier configurations, but the lower diaphragm was restricted with the inclusion of a metal washer beneath it, with a 40 mm diameter hole in the centre. It was thought that the larger diameter at the top of the switching mechanism would be softer than the restricted diameter of the previous configuration.

The best results were found for a 3 mm gap, as shown in Figures 5.17 and 5.18. These show excellent off-state properties with the resonance suppressed at both amplitudes. For the on-state there is a good change for both amplitudes, but there is a significant amplitude dependence and the frequency of the resonance is shifted down for the high amplitude. Table 5.6 gives the resonance frequencies and the system compliances for the different cases. The resonance frequencies for the 'Off' cases were not clear enough to be included.

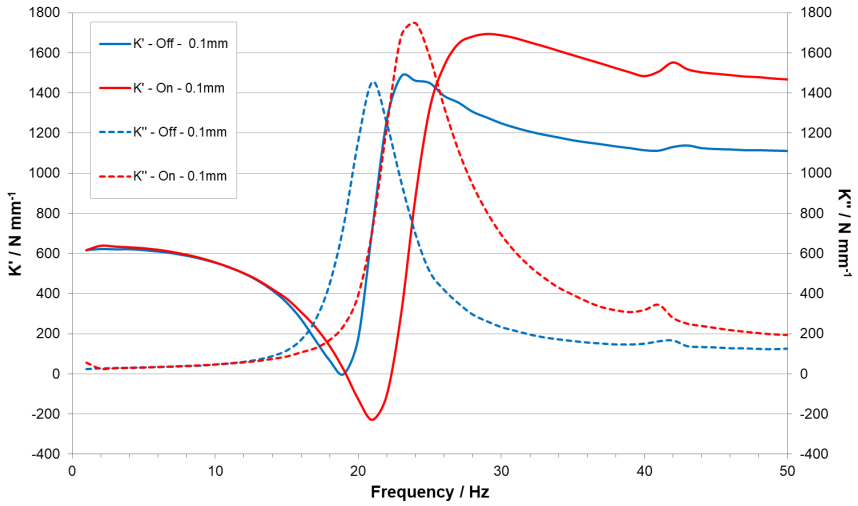

Figure 5.13: The stiffness of the configuration using an MCE-MRF sandwich to control the first chamber compliance with a -2 mm gap tested at 0.1 mm amplitude. 'On' is for the results with a magnet in place and 'Off' with the rod *in situ*.

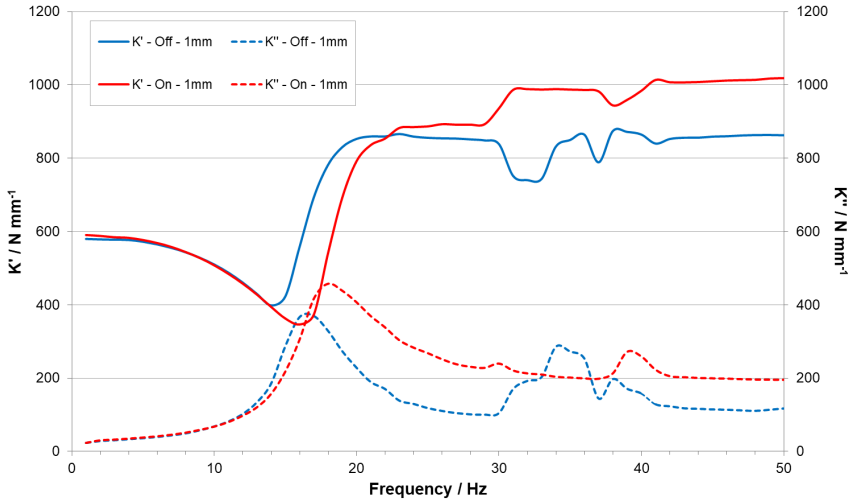

Figure 5.14: The stiffness of the configuration using an MCE-MRF sandwich to control the first chamber compliance with a -2 mm gap tested at 1 mm amplitude. 'On' is for the results with a magnet in place and 'Off' with the rod *in situ*.

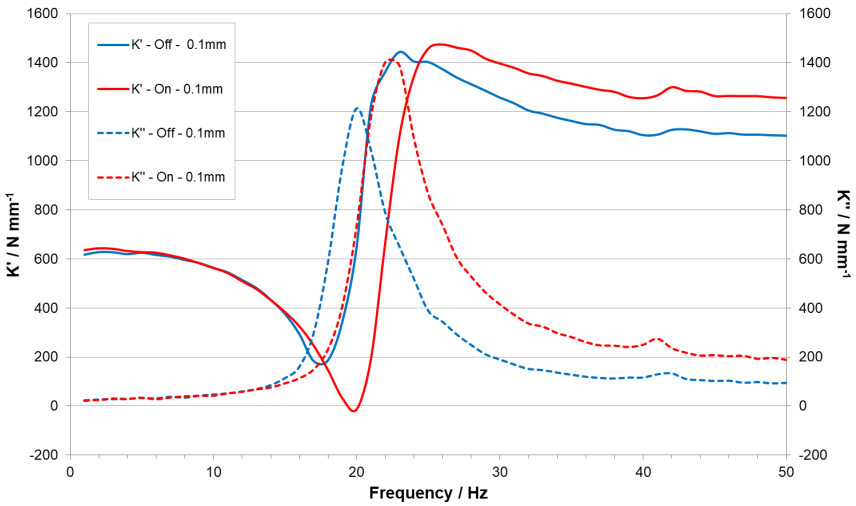

Figure 5.15: The stiffness of the configuration using a modified MCE-MRF sandwich to control the first chamber compliance with a 2 mm gap tested at 0.1 mm amplitude. 'On' is for the results with a magnet in place and 'Off' with the rod *in situ*.

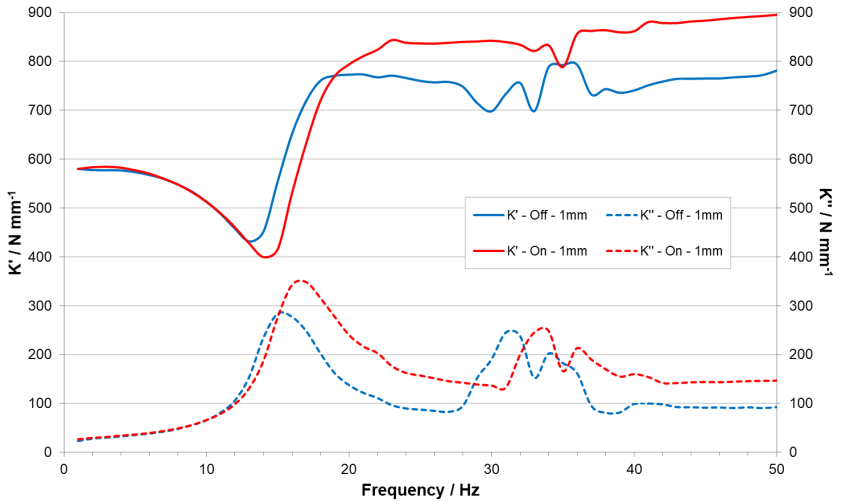

Figure 5.16: The stiffness of the configuration using a modified MCE-MRF sandwich to control the first chamber compliance with a 2 mm gap tested at 1 mm amplitude. 'On' is for the results with a magnet in place and 'Off' with the rod *in situ*.

Gap	**Amplitude**	**Condition**	**Frequency of peak K''**	$\frac{C_1+C_2}{C_1C_2}$
mm	mm		Hz	m^3Pa^{-1}
3	0.1	On	18	2.93×10^{-11}
3	1	On	11	7.87×10^{-11}

Table 5.6: The resonance frequencies and system compliance of the NR-MRF sandwich 2

5.2.6 Balloon switch

The final configuration presented here is a similar concept to the previous configuration, but uses a latex balloon filled with MRF beneath a single diaphragm at the bottom of the chamber. The balloon is set up with no gap between it and the diaphragm and no gap between it and the magnet. This would be easy to retrofit to existing mounts as the switching mechanism is contained in a separate unit. The set-up can be seen in Figure 5.19. For the off-state the balloon can be squeezed sideways to accommodate the movement of the diaphragm.

Again the results are promising with this configuration (Figures 5.20 and 5.21). The off-state behaviour is as required, with the resonance suppressed at both amplitudes. There is a clear effect of the on-state although the resonances at both amplitudes are less pronounced than the previous configuration, and at 1 mm amplitude, would benefit from being larger. Table 5.7 gives the resonance frequencies and the system compliances for the different cases. The resonance frequencies for the 'Off' cases were not clear enough to be included.

Gap	**Amplitude**	**Condition**	**Frequency of peak K''**	$\frac{C_1+C_2}{C_1C_2}$
mm	mm		Hz	m^3Pa^{-1}
3	0.1	On	13	5.62×10^{-11}
3	1	On	10	9.52×10^{-11}

Table 5.7: The resonance frequencies and system compliance of balloon switch configuration

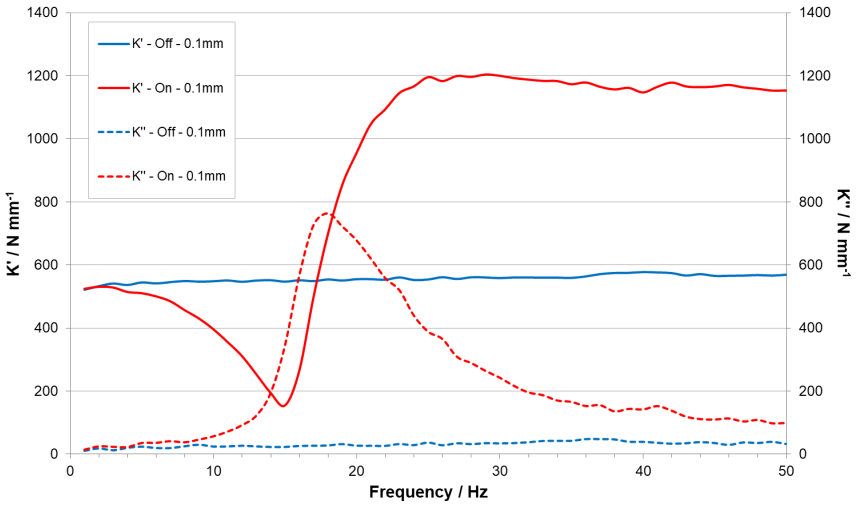

Figure 5.17: The stiffness of the configuration using a modified NR-MRF sandwich to control the first chamber compliance with a 3 mm gap tested at 0.1 mm amplitude. 'On' is for the results with a magnet in place and 'Off' with the rod *in situ*.

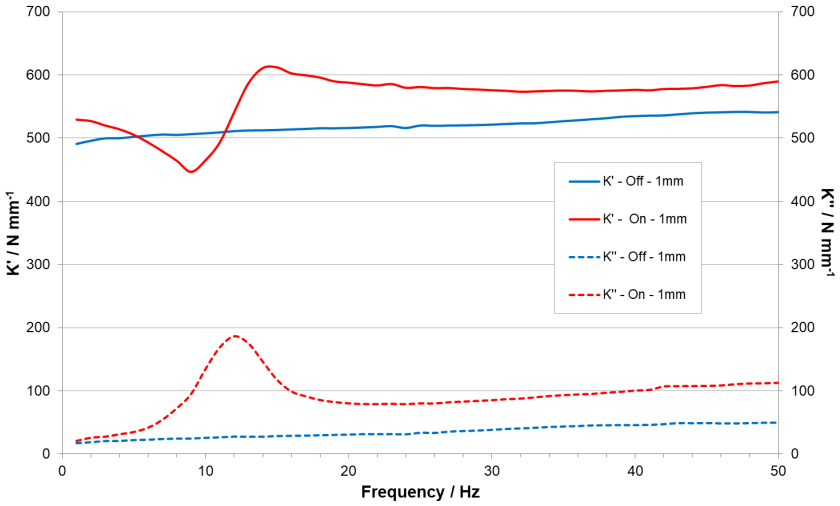

Figure 5.18: The stiffness of the configuration using a modified NR-MRF sandwich to control the first chamber compliance with a 3 mm gap tested at 1 mm amplitude. 'On' is for the results with a magnet in place and 'Off' with the rod *in situ*.

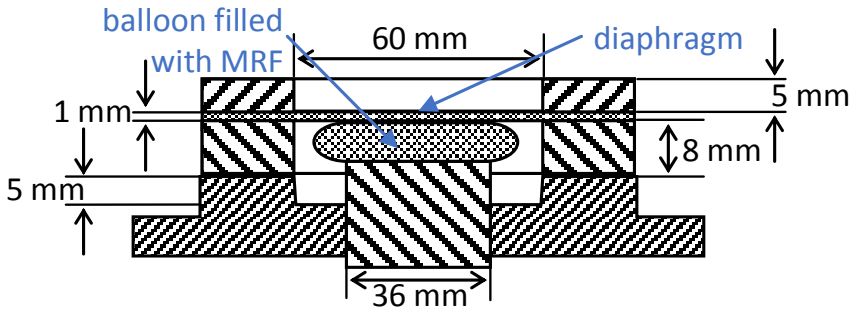

Figure 5.19: The balloon switch configuration.

5.2.7 Summary

A number of different configurations were tried with the aim of suppressing the resonance behaviour in the off-state with the usual hydromount behaviour in the on-state. The main problem to overcome was making the switching mechanism soft enough in the off-state as the presence of the magnet (even when off) restricted the movement of the diaphragm. There is a large variation in the system compliance of the configurations tested. The least variation between amplitudes in the compliance is seen for the balloon switch although the change in the stiffnesses is comparatively small.

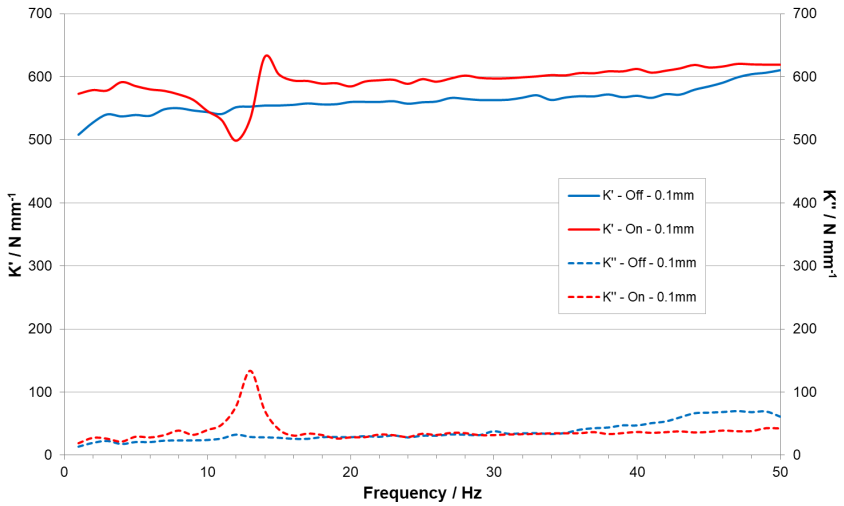

Figure 5.20: The stiffness of the configuration using a balloon switch to control the first chamber compliance tested at 0.1 mm amplitude. 'On' is for the results with a magnet in place and 'Off' with the rod *in situ*.

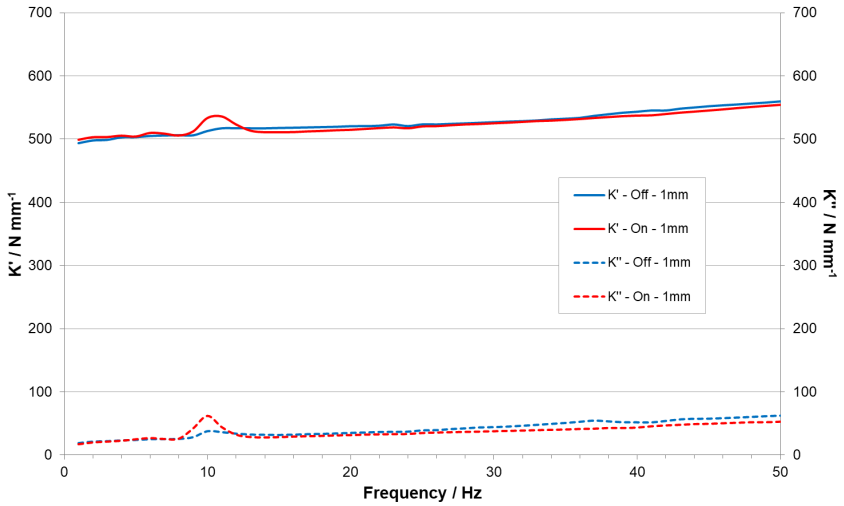

Figure 5.21: The stiffness of the configuration using a balloon switch to control the first chamber compliance tested at 1 mm amplitude. 'On' is for the results with a magnet in place and 'Off' with the rod *in situ*.

5.3 Two inertia tracks[ii]

After discussion with an automotive manufacturer, it was suggested that the current system used in vehicles frequently took advantage of having two tuned frequencies. For example, one could be at the resonance frequency of the engine on its mounts and the other at a disturbing frequency for example the engine idle frequency. This second frequency could be switched on and off as required during the use of the vehicle. It was decided to test the balloon switch developed in the previous section with this system.

5.3.1 Inertia track 1

Initially the test rig was not altered significantly, but the part used above the provide the extra compliance was turned upside down and attached to the bottom of the first chamber. This gave rise to a small second inertia track and small third chamber. A diaphragm was placed at the bottom of the new third chamber and the balloon was placed underneath this. It was hoped that this inertia track (36 mm diameter and 20 mm height) would be long enough as it was similar to some found in service. There was uncertainty regarding the stiffness of the diaphragm with the balloon. The idling frequency that this was aiming to neutralise was about 30 Hz. This configuration can be seen in Figure 5.22.

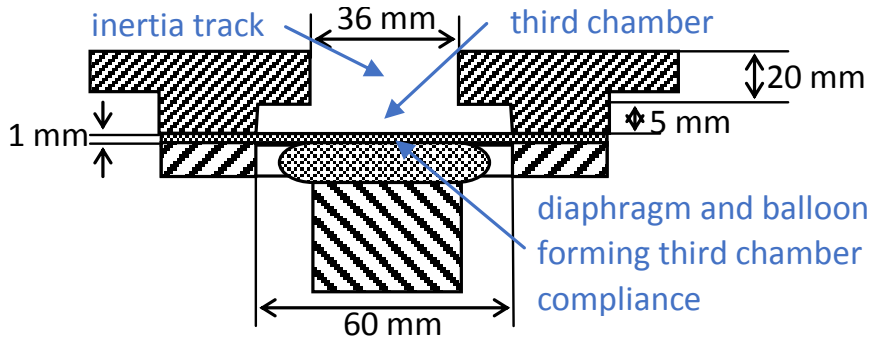

Figure 5.22: The second inertia track 1 configuration.

The test the results of which can be seen in Figure 5.23 was carried out with an electromagnet and was repeated at a few voltages, 0 V being equivalent to

[ii]There are three different configurations considered in this section. The design of the configurations was carried out by the author with input from Alan Harris. The experimental work for the first two was carried out by Luigi Borelli (as in the previous section), the last configuration was carried out by the author.

the off-state and 12 V being similar in flux density to the permanent magnet used previously in the order of 1 T. The main point to notice in the results is that there is no second resonance within the frequency range tested. Looking at the behaviour near 50 Hz, it appears likely that the second resonance may occur just beyond the test range. The second point is that changing the stiffness of the diaphragm of the bottom chamber, by changing the magnetic field strength, alters the primary resonance. It is unclear whether this is primarily due to the change in flow through the first inertia track, depending on the flow through the second, or whether the compliance of the first chamber is still being altered. As the second resonance was much greater than 30 Hz, this configuration was not considered successful.

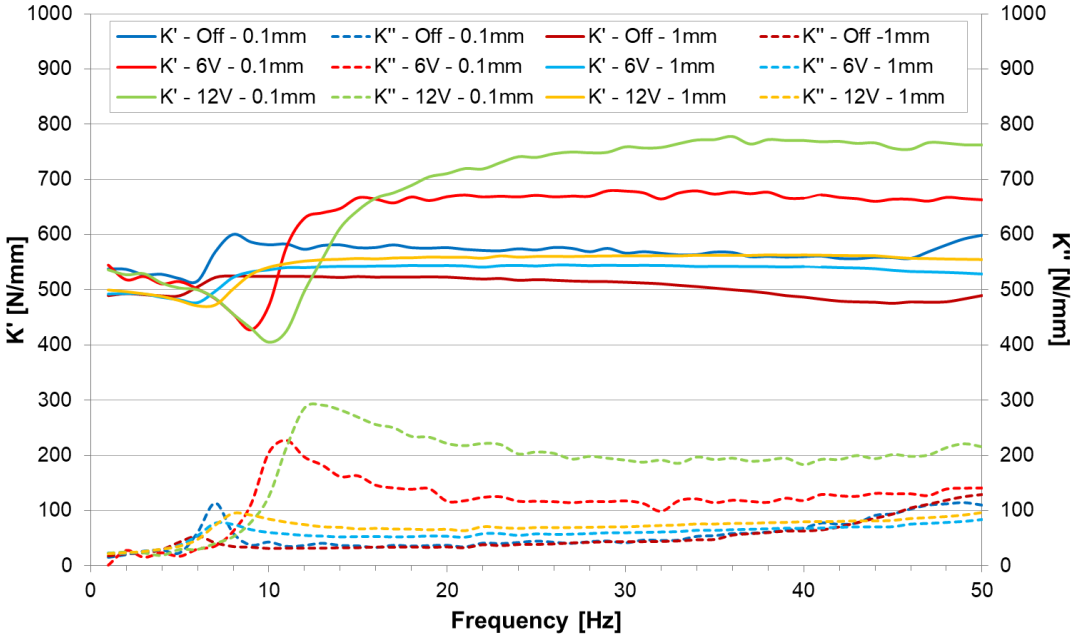

Figure 5.23: The stiffness of the configuration using the second inertia track 1 tested at 0.1 mm and 1 mm amplitude. The voltage represents the voltage supplied to an electromagnet.

5.3.2 Inertia track 2

As the resonance seemed a little beyond 50 Hz, it was hoped that by lengthening the second inertia track with a small insert the second resonance could be observed closer to 30 Hz. The insert increased the length of the inertia track to 50 mm. This configuration can be seen in Figure 5.24.

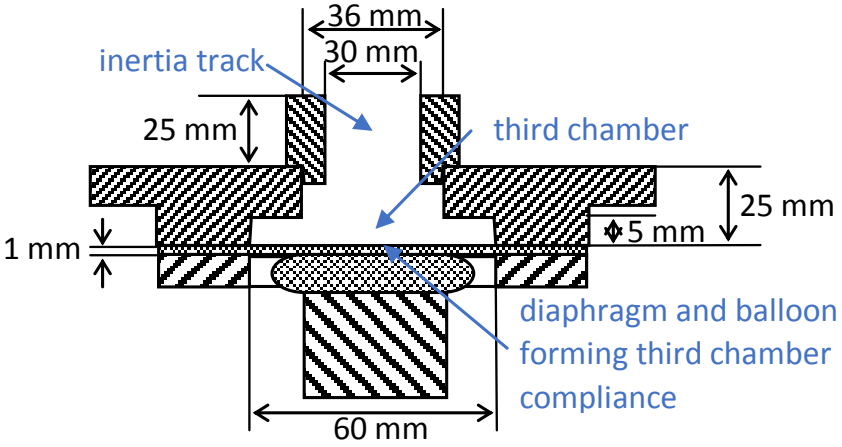

Figure 5.24: The second inertia 2 track configuration.

The results, which can be seen in Figure 5.25, were very similar to those with the smaller inertia track. However, the results for the first resonance are larger in magnitude than the previous configuration, even for the off-state.

5.3.3 Inertia track 3

The previous two configurations did not show the second resonance within the frequency range tested, so a new adaptive mount testing rig was designed. The first inertia track was 340 mm long and a had a square cross sectional area of 100 mm^2; the second chamber compliance was provided by a specially moulded sheet of rubber. The length of this inertia track was 60 mm long with a 10 mm diameter. In this case the rig was tested a) with a 50 mm diameter 1 mm thick unfilled NR diaphragm at the bottom of the tube ('free'), b) with the balloon switch in place under the diaphragm with the electromagnet off, c) with the balloon switch and the electromagnet on at 12 V and d) with the end of the inertia track blocked by piece of metal. For the final case the amplitude of testing was 0.5 mm, but it was 0.2 mm for the other cases.

The results are shown in Figure 5.26. These show the ideal behaviour, with the off-state very close to the free behaviour, and the on-state very close to the blocked behaviour. The on-state and blocked cases show a single resonance frequency with a peak in K'' at approximately 12 Hz. The free case shows a very small first resonance at approximately 4.5 Hz, but the response is dominated by a resonance at approximately 34 Hz. The off-state case is less compliant than the free state

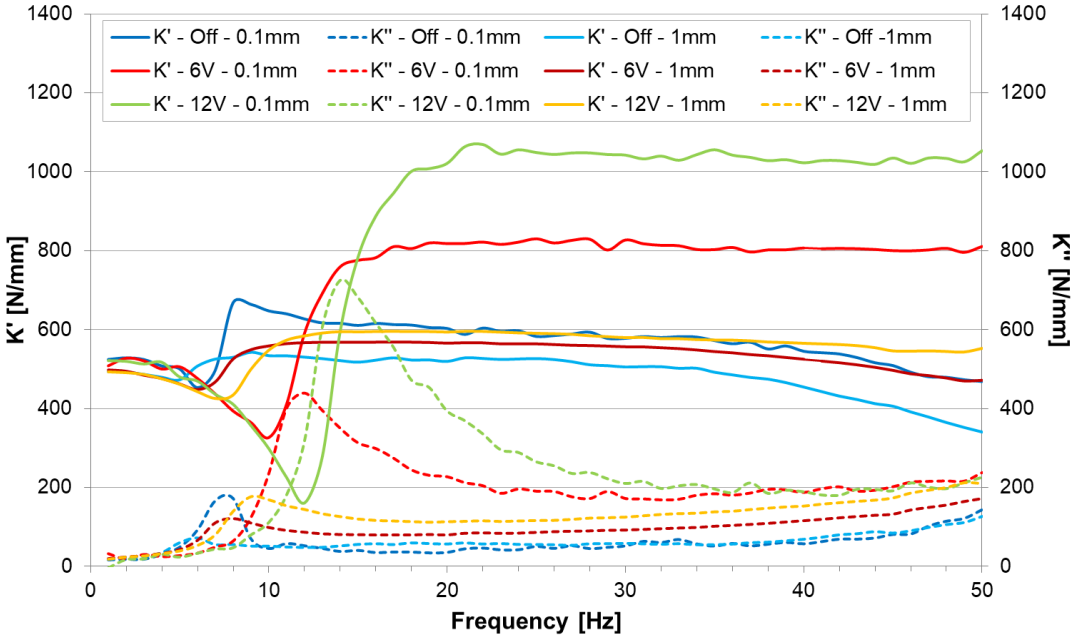

Figure 5.25: The stiffness of the configuration using a larger second inertia track tested at 0.1 mm and 1 mm amplitude. The voltage represents the voltage supplied to an electromagnet.

due to the MRF filled balloon underneath, this means the first resonance has been shifted up to approximately 9 Hz. Although the response at the first resonance frequency is small compared with the second resonance, it is much larger than for the free state. The second resonance has also been shifted up with respect to the free state the peak in K'' is found at 41 Hz, the response is a little lower at this resonance than the free state. This design proved the concept would work.

5.4 Discussion

It is possible to get close to the desired behaviour by altering the first chamber compliance. The last two configurations under that section provide promising behaviour and ideas for a potential switching mechanism. The best configuration was found to be the NR-MRF sandwich 2 with a 3 mm gap. This had a large effect with strong signals in the on-state and no resonance visible in the off-state. There was significant amplitude dependence of the resonance frequency. The balloon switch also showed potential, with the resonance not visible in the off-state. The strength of the signals in the on-state were perhaps less than ideal, but this can

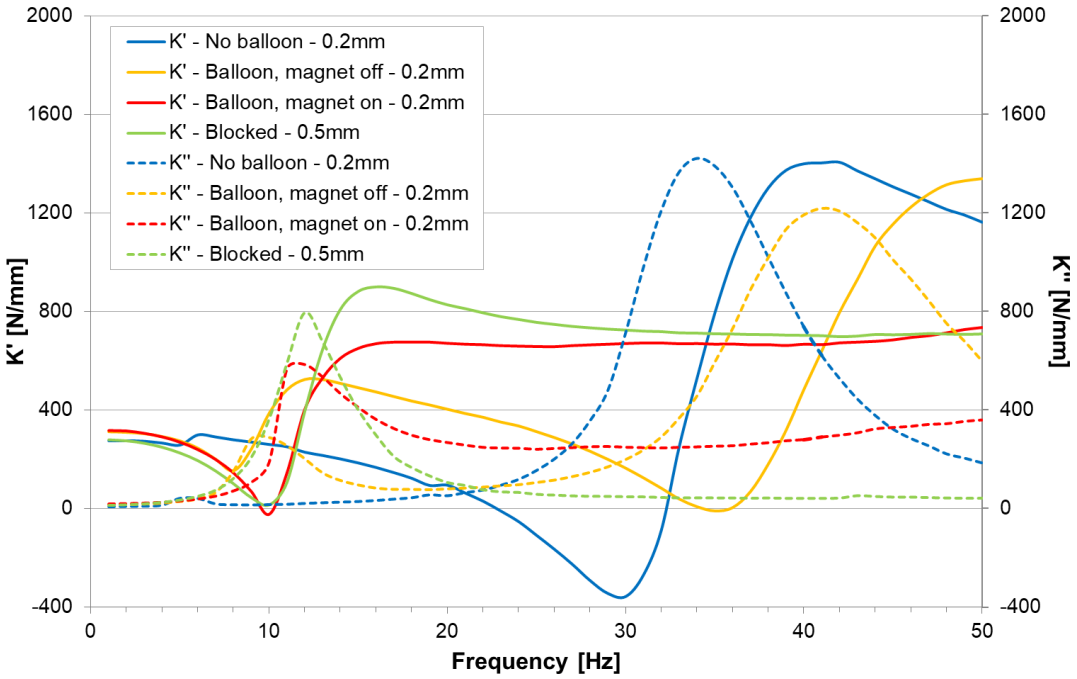

Figure 5.26: The stiffness of the configuration using a designed second inertia track tested.

be altered by changing the parameters of the mount. This did not show as much amplitude dependence. The benefits of the balloon switch are that is completely separate from the mount and can easily be added beneath a diaphragm.

The second inertia track is currently exploited to eliminate vibration caused at a specific frequency. The balloon switch shows promise for this too and a successful implementation has been demonstrated. It was possible to almost replicate the behaviour of the blocked case in the on-state, meaning that the second resonance did not appear. In the off-state it was possible to provide a resonance at both frequencies. It should be noted though that both the resonant frequencies appear to be dependent on the third chamber compliance. A better understanding of the behaviour may be found having a model for the two inertia track system.

The switching mechanism can be used to switch between the on-state and the off-state depending on predefined conditions. This allows the advantages of a passive hydromount to be used where they are desirable and either the change in stiffness by-passed (with the change in the first chamber compliance) or a second resonance frequency to be tuned. This can give advantages over a passive hydromount.

Chapter 6

Hydromounts with Two Inertia Tracks

As mentioned in the previous chapter, modern cars are increasingly being fitted with active and adaptive control of vibration. Some manufacturers are including hydromounts with two inertia tracks in their vehicles. This allows the hydromount to be tuned to two distinct frequencies, for example one tuned to be optimum for driving conditions and one tuned for the idling conditions when the car has a predictable input mainly at one frequency, twice the engine speed for a four cylinder engine, three times for a six cylinder one. Using a controllable switch allows the change between the different frequency regimes.

This chapter concentrates on developing a model for hydromounts with two inertia tracks, which was introduced in Chapter 5. This modelled is developed from the modelling of the single track hydromount in Chapter 4. To enable the modelling of the entire mount it is important to know the compliances of the chambers. To this end a theoretical approach to describe the behaviour of the diaphragms is presented. Work is also done on modelling the resistance to flow in the inertia tracks.

6.1 Model for a hydromount with two inertia tracks

The non-linear model for a hydromount with a single inertia track described in Section 4.3 can be extended to include two inertia tracks and a third compliance (see Figure 6.1). The additional assumption that is made is the two inertia tracks act independently from one another and so there is no cross-coupling.

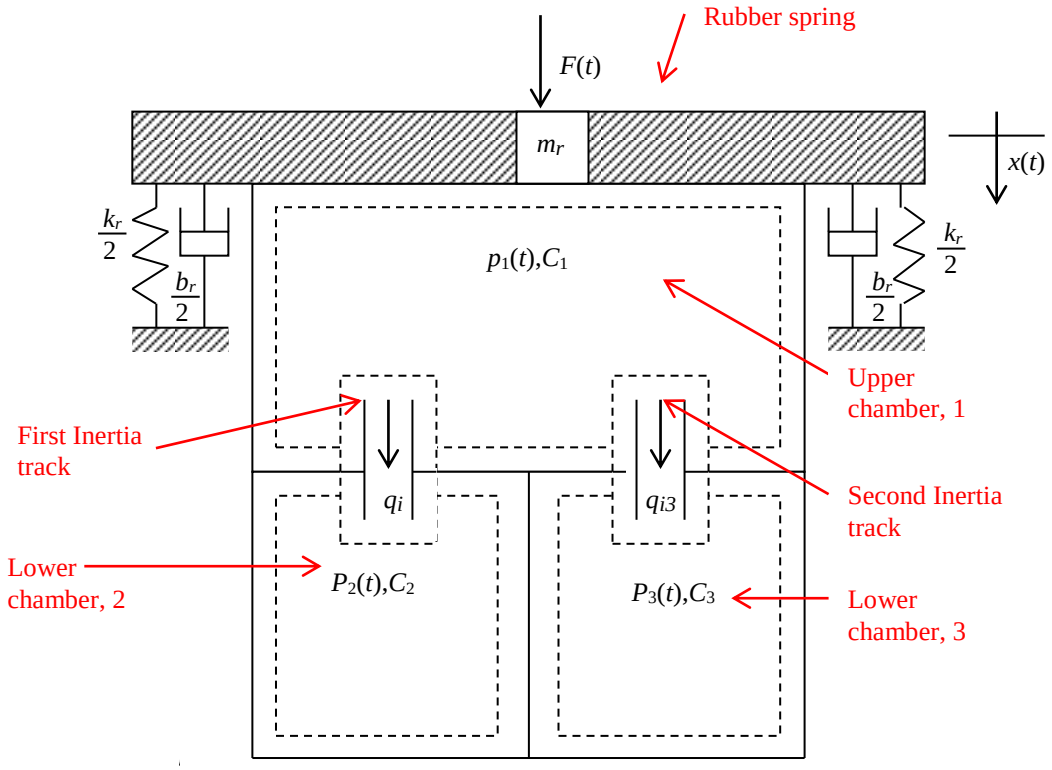

Figure 6.1: Diagram for two inertia track model

This leads to the following equations of motion for a two-inertia-track system with no decoupler are:

$$F_{\mathrm{T}}(t) = k_{\mathrm{r}}x(t) + b_{\mathrm{r}}\dot{x}(t) + A_{\mathrm{r}}p_1(t) \tag{6.1}$$

$$p_1(t) - p_2(t) = I_{\mathrm{i}}\dot{q}_{\mathrm{i}}(t) + R_{\mathrm{i}}q_{\mathrm{i}}(t) \tag{6.2}$$

$$p_1(t) - p_3(t) = I_{\mathrm{i}3}\dot{q}_{\mathrm{i}3}(t) + R_{\mathrm{i}3}q_{\mathrm{i}3}(t) \tag{6.3}$$

$$A_{\mathrm{r}}\dot{x}(t) - q_{\mathrm{i}}(t) - q_{\mathrm{i}3}(t) = C_1\dot{p}_1(t) \tag{6.4}$$

$$q_{\mathrm{i}}(t) = C_2\dot{p}_2(t) \tag{6.5}$$

$$q_{\mathrm{i}3}(t) = C_3\dot{p}_3(t) \tag{6.6}$$

where the terms for the first inertia track are the same as used in Chapter 4. The additional terms are p_3, the pressure of the third chamber; C_3, the compliance of the third chamber; $I_{\mathrm{i}3}$, the inertance of the fluid within the second inertia track; $R_{\mathrm{i}3}$, the resistance to flow through the second inertia track and $q_{\mathrm{i}3}$, the rate of flow through the second inertia track. These equations are essentially the same as the previous non-linear model, but extra terms are added to describe the flow through the second inertia track (Equations (6.3) and (6.6)).

For a linear model these equations can be solved by applying Laplace transformations. After substitution to eliminate the other variables, and following a similar procedure to that used by Singh et al.[57] for the conventional hydromount, a relation can be obtained between the transmitted force and the input displacement. This can be rearranged to give the complex transfer dynamic stiffness in the following form:

$$K^*(\omega) = \frac{F_{\mathrm{T}}(\omega)}{x(\omega)} = \frac{i\alpha_5\omega^5 + \alpha_4\omega^4 - i\alpha_3\omega^3 - \alpha_2\omega^2 + i\alpha_1\omega + \alpha_0}{\beta_4\omega^4 - i\beta_3\omega^3 - \beta_2\omega^2 + i\beta_1\omega + \beta_0} \tag{6.7}$$

where

$\alpha_5 = b_{\mathrm{r}} I_{\mathrm{i}} I_{\mathrm{i}3} C_1 C_2 C_3$,

$\alpha_4 = b_{\mathrm{r}} C_1 C_2 C_3 (I_{\mathrm{i}} R_{\mathrm{i}3} + R_{\mathrm{i}3} I_{\mathrm{i}}) + (k_{\mathrm{r}} C_1 + A_{\mathrm{r}}^2) C_2 C_3 I_{\mathrm{i}} I_{\mathrm{i}3}$,

$\alpha_3 = b_{\mathrm{r}} C_1 (C_3 I_{\mathrm{i}3} + C_2 I_{\mathrm{i}} + C_2 C_3 R_{\mathrm{i}} R_{\mathrm{i}3}) + b_{\mathrm{r}} C_3 C_2 I_{\mathrm{i}} + b_{\mathrm{r}} C_2 C_3 I_{\mathrm{i}3} + C_2 C_3 (k_{\mathrm{r}} C_1 + A_{\mathrm{r}}^2)(I_{\mathrm{i}} R_{\mathrm{i}3} + I_{\mathrm{i}3} R_{\mathrm{i}})$,

$\alpha_2 = b_{\mathrm{r}} C_1 (R_{\mathrm{i}} C_2 + R_{\mathrm{i}3} C_3) + b_{\mathrm{r}} C_2 C_3 (R_{\mathrm{i}} + R_{\mathrm{i}3}) + (k_{\mathrm{r}} C_1 + A_{\mathrm{r}}^2)(I_{\mathrm{i}3} C_3 + I_{\mathrm{i}} C_2 + R_{\mathrm{i}} C_2 R_{\mathrm{i}3} C_3) + k_{\mathrm{r}} C_2 C_3 (I_{\mathrm{i}} + I_{\mathrm{i}3})$,

$\alpha_1 = b_{\mathrm{r}} (C_1 + C_2 + C_3) + (k_{\mathrm{r}} C_1 + A_{\mathrm{r}}^2)(R_{\mathrm{i}} C_2 + R_{\mathrm{i}3} C_3) + k_{\mathrm{r}} C_2 C_3 (R_{\mathrm{i}} + R_{\mathrm{i}3})$,

$\alpha_0 = k_{\mathrm{r}} (C_1 + C_2 + C_3) + A_{\mathrm{r}}^2$,

$\beta_4 = C_1 C_2 C_3 I_{\mathrm{i}} I_{\mathrm{i}3}$,

$\beta_3 = C_1 C_2 C_3 (I_{\mathrm{i}} R_{\mathrm{i}3} + I_{\mathrm{i}3} R_{\mathrm{i}})$,

$\beta_2 = C_1 (I_{\mathrm{i}3} C_3 + I_{\mathrm{i}} C_2 + C_2 C_3 R_{\mathrm{i}} R_{\mathrm{i}3}) + C_2 C_3 (I_{\mathrm{i}} + I_{\mathrm{i}3})$,

$\beta_1 = C_1 (R_{\mathrm{i}} C_2 + R_{\mathrm{i}3} C_3) + C_2 C_3 (R_{\mathrm{i}} + R_{\mathrm{i}3}))$, and

$\beta_0 = C_1 + C_2 + C_3$.

6.2 Compliances of the upper and lower chambers

In the experimental rigs used in Chapter 5 to examine the behaviour of a mount with two inertia tracks, the lower chambers consist of circular diaphragms of rubber. The upper chamber consists of a rubber spring; it also has an annular diaphragm to increase the compliance of the chamber. A model is therefore developed for the compliance of the circular and annular diaphragms.

6.2.1 Compliance of a circular diaphragm

A circular diaphragm can be assumed to inflate to form a portion of a sphere, a spherical cap, see Figure 6.2.

Previously, Dr Julia Gough[168] has investigated the equi-biaxial inflation of rubber sheets to examine the deformation of rubber. The part of the theory that is used in this work is included in Appendix A. This gives rise to the following expression for the pressure required to inflate the spherical cap:

$$P = \frac{2Gt_0}{r}\left(1 - \lambda_1^{-6}\right) \tag{6.8}$$

where G is the shear modulus, t_0 the thickness of the rubber diaphragm, r is the radius of the sphere (Figure 6.2) and λ_1 is the principal extension ratio and is equal to a/c (a and c are defined in Figure 6.2).

To calculate the compliance, the volume of the spherical cap is required. The measurable parameters are c and h.

Using Pythagoras' Theorem:

$$r^2 = (r - h)^2 + c^2 \tag{6.9}$$

Hence

$$r = \frac{c^2 + h^2}{2h} \tag{6.10}$$

The volume of the spherical cap can be derived from the formula of the spherical

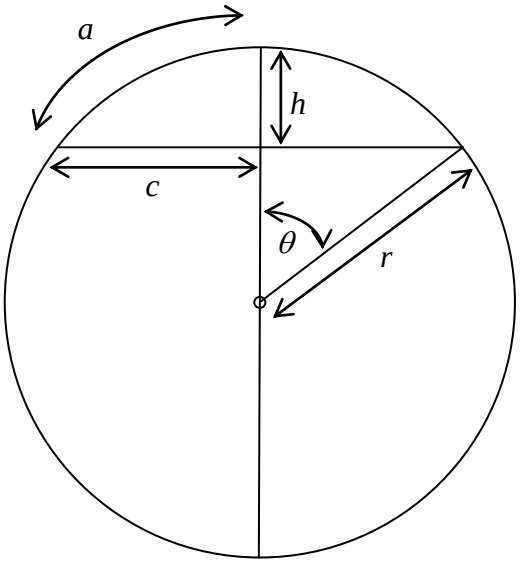

Figure 6.2: Section of circular diaphragm

sector and the formula of the cone.

$$V_{cap} = \frac{2\pi r^2 h}{3} - \frac{\pi c^2 (r-h)}{3} \tag{6.11}$$

Incorporating Equation (6.10) gives:

$$V_{cap} = \frac{\pi}{6}\left(3c^2 + h^2\right) h \tag{6.12}$$

The expression for λ_1 in terms of h and c is:

$$\lambda_1 = \frac{\theta r}{c} = \frac{c^2 + h^2}{2ch} \arcsin\left(\frac{2ch}{c^2 + h^2}\right) \tag{6.13}$$

which can be substituted into Equation (6.8).

The volumetric compliance is defined by:

$$C = \frac{\Delta V}{\Delta P}. \tag{6.14}$$

To work out ΔV, h is varied whilst c remains constant. For small changes at low P, the dependence is approximately linear. At high pressures and large inflations the neo-Hookean model[169] used for the material does not include the stiffening of the material. The pressures generally in the hydromount are near atmospheric, but with large input displacements to the mount the assumption that the material

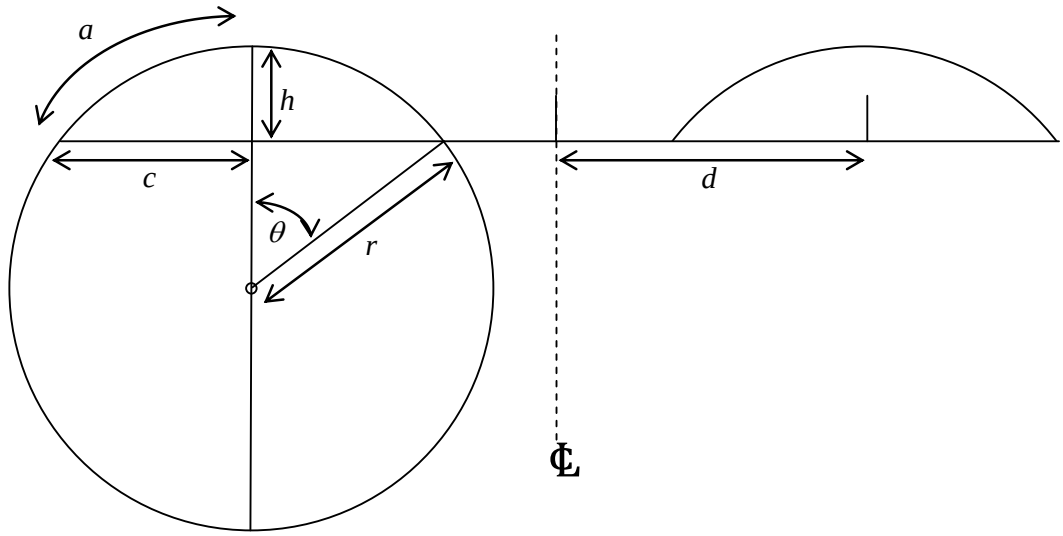

Figure 6.3: Section of annular diaphragm

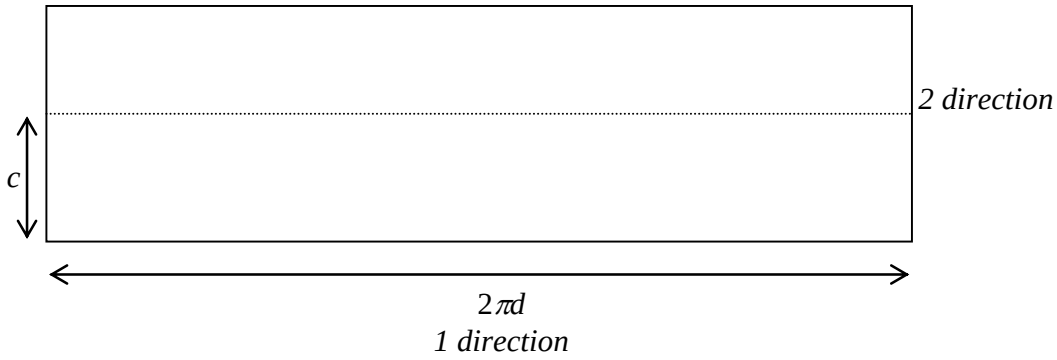

Figure 6.4: Sheet to be inflated in pure shear. 3 direction normal to paper.

is neo-Hookean may not be valid.

6.2.2 Compliance of an annular diaphragm

For an annular diaphragm, the set up is similar to that above but as the sheet is constrained in the middle, two semi-circular sections are formed, with the radius to the midpoint of the semi-circle being d, see Figure 6.3.

This can be approximated to a length of sheet that is inflated into a portion of a cylinder, see Figure 6.4. The length of the midpoint is taken as the length of the cylinder. Under inflation, the length will remain constant, but the width and thickness will alter.

The terms λ_i are the principal extension ratios, and in the case of pure shear the following applies:

$$\lambda_2 = \frac{a}{c} \tag{6.15}$$

At the centre of this inflated sheet, the sheet is in pure shear. So for stretches in the 1,2 plane $\sigma_3 = 0$, $\lambda_1 = 1$, $\lambda_2 = 1/\lambda_3$, and Equation (A.3) becomes

$$\sigma_2 = 2\left(\lambda_2^2 - \lambda_2^{-2}\right)\left(\frac{\partial W}{\partial I_1} + \lambda_1^2 \frac{\partial W}{\partial I_2}\right) \tag{6.16}$$

where W is the strain energy density and I_1 and I_2 are the strain invariants defined as

$$I_1 = \lambda_1^2 + \lambda_2^2 + \lambda_3^2 \tag{6.17}$$

$$I_2 = \lambda_1^2\lambda_2^2 + \lambda_2^2\lambda_3^2 + \lambda_3^2\lambda_1^2 \tag{6.18}$$

Also, $\lambda_1\lambda_2\lambda_3 = 1$ due to incompressibility.

For a neo-Hookean material, $\dfrac{\partial W}{\partial I_1} = \dfrac{G}{2}$ and $\dfrac{\partial W}{\partial I_2} = 0$ so

$$\sigma_2 = G\left(\lambda_2^2 - \lambda_2^{-2}\right) \tag{6.19}$$

Because f_1 acts perpendicular to the pressure, the only force that needs to be included in this consideration is f_2, leading to:

$$f_2 = \sigma_2 \lambda_3 t_0 = G t_0 \left(1 - \lambda_2^{-4}\right) \tag{6.20}$$

In the pure shear case, R_1 is ∞ so the Young-Laplace Equation (A.1) becomes

$$P = \frac{f_2}{r} \tag{6.21}$$

$$P = \frac{G t_0}{r}\left(1 - \lambda_2^{-4}\right) \tag{6.22}$$

Now, as in Equation (6.13), λ_2 can be calculated in terms of c and h from Equation

(6.15):

$$\lambda_2 = \frac{\theta r}{c} = \frac{c^2 + h^2}{2ch} \arcsin\left(\frac{2ch}{c^2 + h^2}\right). \tag{6.23}$$

Area of segment:

$$A_{seg} = \theta r^2 - cr + ch \tag{6.24}$$

Volume of cylinder fraction:

$$V_{capcyl} = 2\pi d\left(\theta r^2 - cr + ch\right) \tag{6.25}$$

6.2.3 Compliances used in this chapter

The geometry of the rubber spring used in the test rig was too complex to model analytically. This was modelled in MARC (Finite Element Software) by Dr Julia Gough. The rubber was assumed to be neo-Hookean and the shear modulus 0.5 MPa. The results are shown in Figure 6.5 along with the results if the material had a modulus of 1 MPa.

Finally, the compliances for all the diaphragms of the chambers were calculated by taking the gradient of the P - V curve. The P - V curves are shown in Figure 6.6.

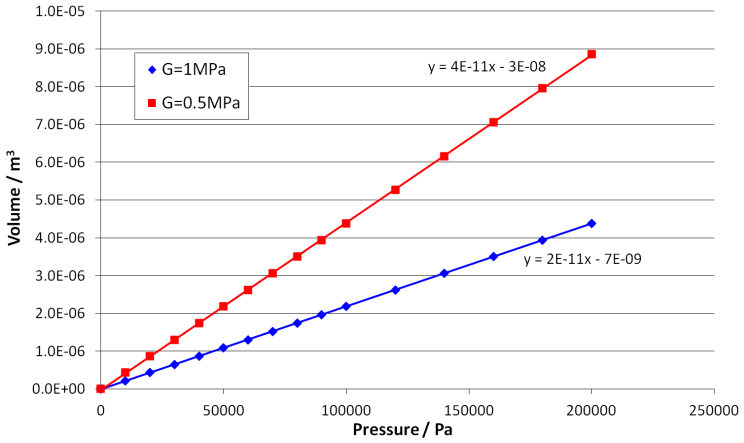

Figure 6.5: The volume-pressure relationship of the rubber spring used in the model.

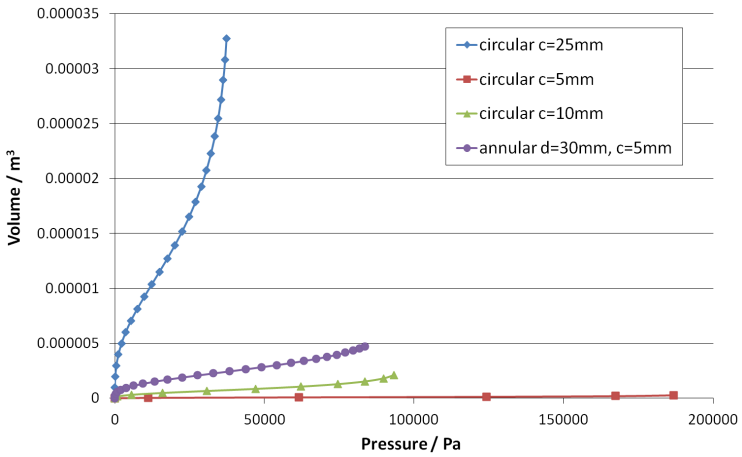

Figure 6.6: The volume-pressure relationship of the diaphragms used in the model.

6.3 Experimental results

For testing the model a hydromount simulation rig with two inertia tracks was used as described in Section 5.3. The second inertia track and the compliance of chamber 2 at the end of the first inertia track were adjustable and a number of different configurations were considered (Table 6.1). In all configurations the first inertia track had a length of 300 mm and a diameter of 12.5 mm. The diameter of the diaphragm at the bottom of the third chamber was 10 mm. All the rubber diaphragms were 1 mm thick and made of unfilled NR with a shear modulus G of approximately 0.5 MPa. A preload of 1000 N was applied and the testing was carried out on a VH7 Schenck servohydraulic machine at an amplitude of 0.1 mm at 1 Hz intervals over the frequency range 1-100 Hz. A Solartron frequency response analyser was used to calculate complex dynamic stiffness from the displacement and force output channels.

Config.	**Length - Inertia Track 2** (mm)	**Diameter - Inertia Track 2** (mm)	**Diaphragm diameter - Chamber 2** (mm)
A	12	7.5	25
B	25	5	25
C	170	20	25
D	170	20	5

Table 6.1: Configurations of the mount

The results for configuration A can be seen in Figure 6.7. Two large resonances are visible at approximately 12 Hz and 46 Hz. There are some other resonances observable particularly at approximately 23 Hz and 65 Hz. These are not the main ones caused by the two inertia tracks, but are probably due to other features within this configuration, but may be higher order non-linear effects.

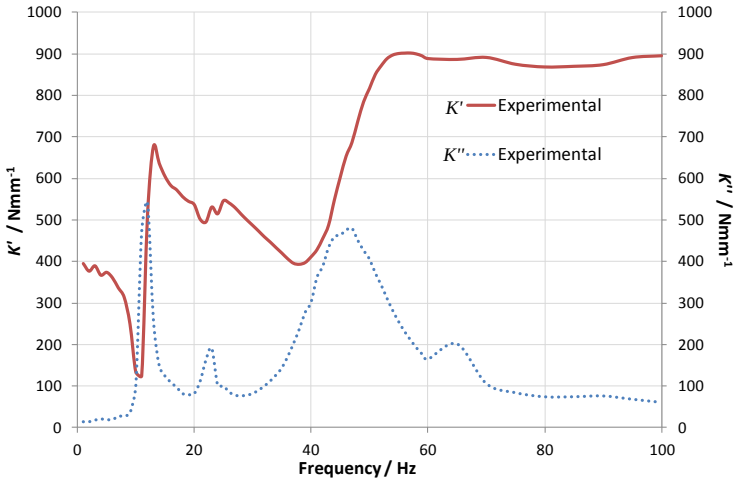

Figure 6.7: The experimental stiffnesses of configuration A.

The results for configuration B which has a longer, but narrower inertia track, can be seen in Figure 6.8. The resonance of the first inertia track has been shifted down slightly compared with configuration A and appears at 9 Hz. Given that nominally the compliances and other dimensions governing the primary resonance have remained constant, it is surprising that the resonance has shifted. A possible explanation is the interaction of the two resonances. The resonance due to the second inertia track has also been shifted down relative to configuration A to 29 Hz. This shift will be mainly due to the change in dimensions of inertia track 2. However, if the compliance of chamber 1 is higher, this may also have affected this resonance. This second inertia track resonance also results in a less significant change in K' and K'' than in configuration A. There are other resonances apparent at 16 Hz, 42 Hz and 80 Hz, which if they correspond to the same features as configuration A, also appear to be affected by the 'change' in compliance or the dimensions of inertia track 2.

Figure 6.9 shows the results for configuration C which has a much longer and wider inertia track. The first resonance appears at 7 Hz, even lower than that for configuration B, although the dimensions and compliances governing this are still nominally the same. The dimensions of inertia track 2 are much larger than

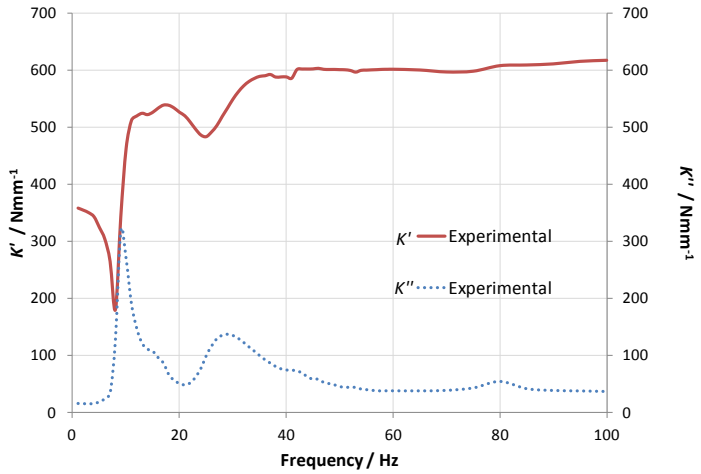

Figure 6.8: The experimental stiffnesses of configuration B.

those in configuration A and B; increasing the length will increase the inertance, but increasing the diameter will reduce it. This results in a second resonance at 35 Hz, not much different to the previous two configurations. There are no other visible resonances within the frequency range tested.

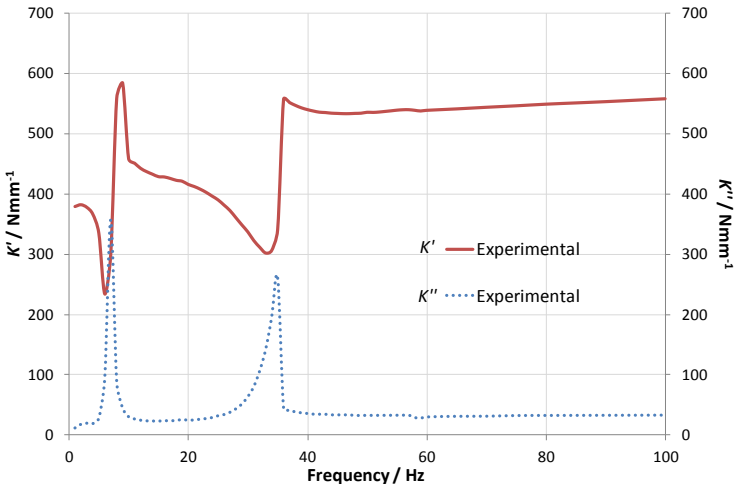

Figure 6.9: The experimental stiffnesses of configuration C.

The results for the final configuration, D, can be seen in Figure 6.10. In this configuration the second inertia track is identical to configuration C but the diaphragm in chamber 2 is reduced from 25 mm to 5 mm diameter. Here the resonance associated with the first inertia track, due to the altered second chamber compliance, is now at a similar frequency to the one from the second inertia track. The peaks in K'' occur at approximately 30 Hz and 37 Hz. Apart from a small variation in the magnitude of the response at low frequencies no other resonances

are apparent over this frequency range.

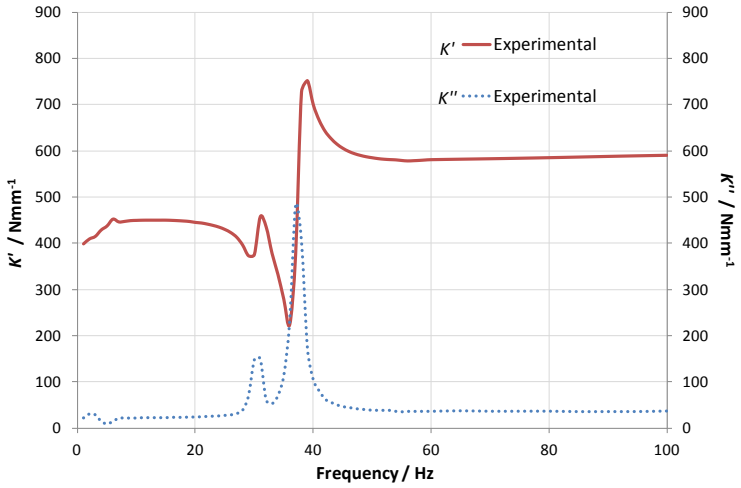

Figure 6.10: The experimental stiffnesses of configuration D.

6.4 Linear model for two inertia tracks

The linear model is given in Equation (6.7). In this section this model is used for the four configurations tested above. The parameters for the model were measured, with the exception of the compliances which were calculated as described in Section 6.2. The compliance decreases with increasing pressure until it becomes almost constant, before ultimately rising again (see Figure 6.11). The values of compliance chosen initially were from the constant compliance region. The compliances of chamber 1 and chamber 3 were estimated to be 7.51×10^{-11} $\mathrm{m^3Pa^{-1}}$ and 1.44×10^{-11} $\mathrm{m^3Pa^{-1}}$, while the values for chamber 2 can be seen in Table 6.2.

Configuration	**Compliance - Chamber 2** ($\mathrm{m^4s^2kg^{-1}}$)
A	5.34×10^{-10}
B	5.34×10^{-10}
C	5.34×10^{-10}
D	2.51×10^{-12}

Table 6.2: Compliances of the second chamber for the different configurations of the mount

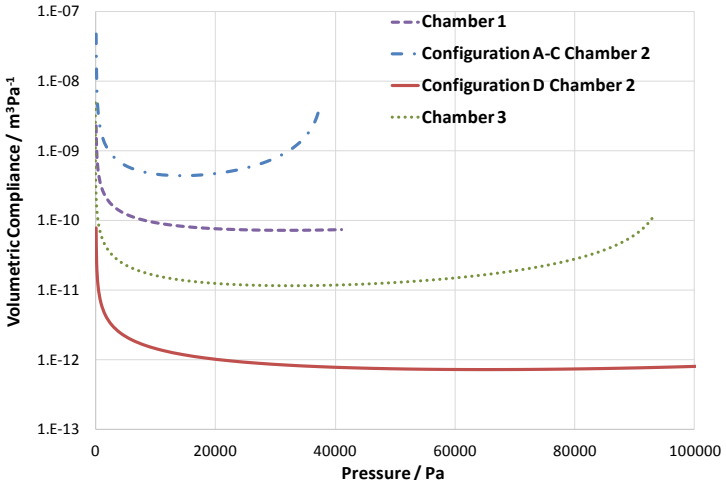

Figure 6.11: Calculated volumetric compliance of the three chambers. Pressures are relative to atmospheric pressure.

The initial results obtained for the four configurations using the linear model are shown in Figures 6.12-6.15. As the linear model does not predict the magnitude of the dynamic stiffness well, discussion of these results mainly focuses on the shape of the curves and the location of the first two resonance frequencies of the mount. The initial results for configurations A, B and C (Figures 6.12-6.14) showed reasonable agreement with the measurements in terms of the first resonance, but the second resonance was not correctly predicted, especially for configurations A and C. For configuration D (Figure 6.15), the general shape of the curves was reasonable, but both resonance frequencies are poorly predicted.

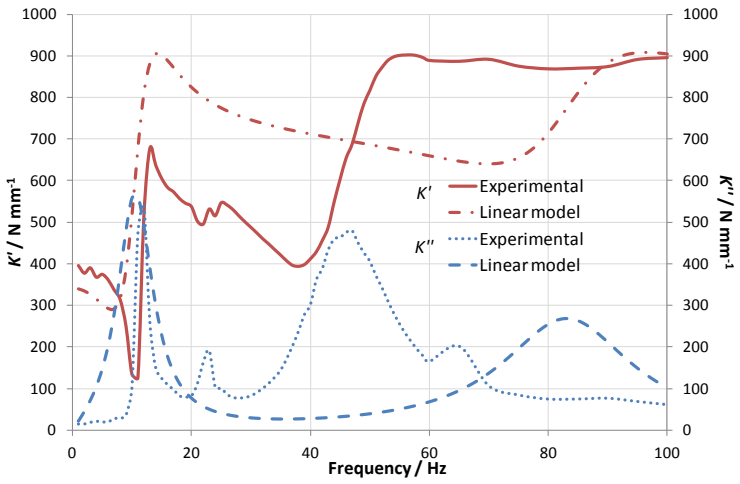

Figure 6.12: The comparison of the stiffnesses given by the linear model to the experimental data for configuration A.

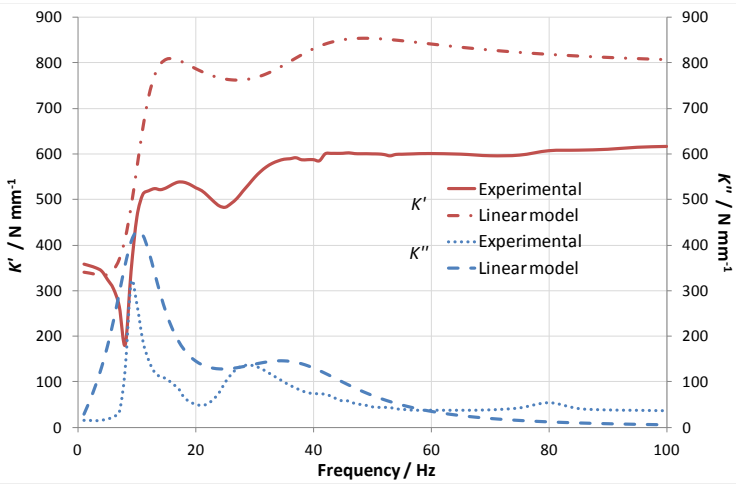

Figure 6.13: The comparison of the stiffnesses given by the linear model to the experimental data for configuration B.

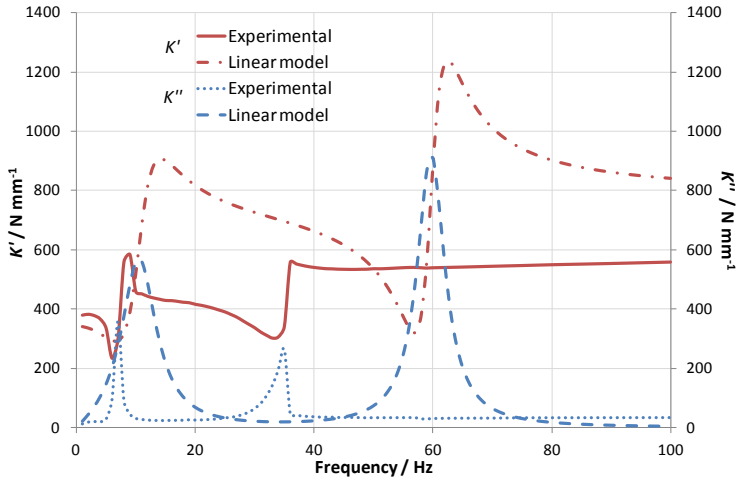

Figure 6.14: The comparison of the stiffnesses given by the linear model to the experimental data for configuration C.

The resonance frequencies are found to be very sensitive to the compliance of all three chambers as the values are so close in magnitude. The compliances were manually optimised to choose values that gave a good fit for the resonance frequencies. The new response curves can be seen in Figures 6.16-6.19.

To obtain these improved curves, the compliances were altered to the values given in Table 6.3. The values were found by trial and error; reducing compliance increases the resonance frequency and vice versa. The compliances used for chambers 1 and 3, and also for chamber 2 in configuration D, are significantly softer than the initial values chosen. This could mean that the pressure within

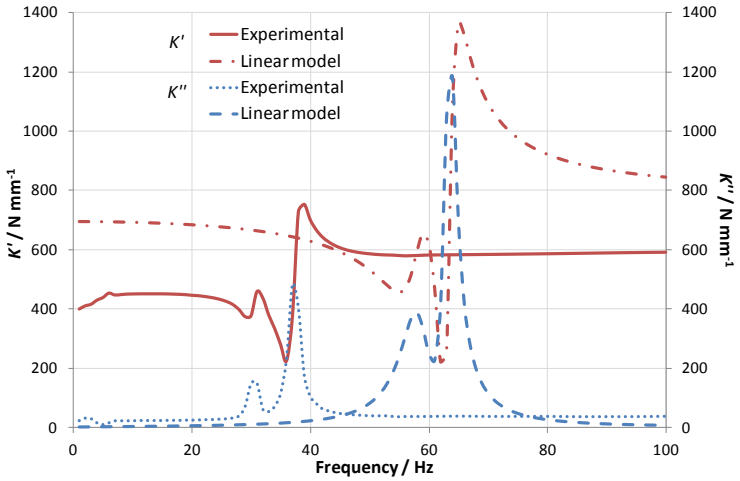

Figure 6.15: The comparison of the stiffnesses given by the linear model to the experimental data for configuration D.

these chambers was either significantly higher or lower than that chosen initially (see Figure 6.11). However, for configurations A-C the compliance of chamber 2 was overestimated, which cannot be explained by the chamber pressure. It is also different for all three configurations, despite the fact they use the same diaphragm. The method of predicting the compliance is based on the assumption that the spherical cap is not inflated beyond a hemisphere. At this point a spherical cap is no longer a reasonable model for the shape of the diaphragm. If the pressures are significantly higher than those in Figure 6.11 then this method of predicting the compliance is not valid.

	Chamber 1		**Chamber 2**		**Chamber 3**	
	($\times 10^{-10}$ $m^4s^2kg^{-1}$)		($\times 10^{-10}$ $m^4s^2kg^{-1}$)		($\times 10^{-10}$ $m^4s^2kg^{-1}$)	
	Initial	Improved	Initial	Improved	Initial	Improved
A	0.751	3.07	5.34	0.890	0.144	0.504
B	0.751	3.07	5.34	1.78	0.144	0.252
C	0.751	3.07	5.34	3.56	0.144	0.396
D	0.751	3.07	0.0251	0.113	0.144	0.346

Table 6.3: Compliances used in the model

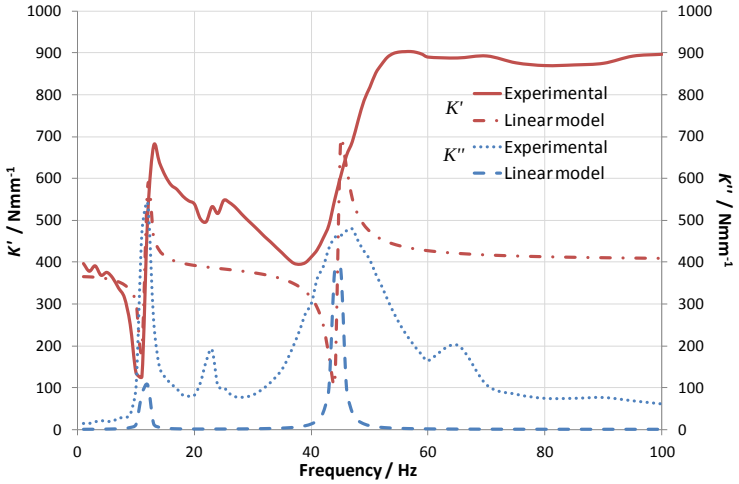

Figure 6.16: The improved stiffnesses of configuration A.

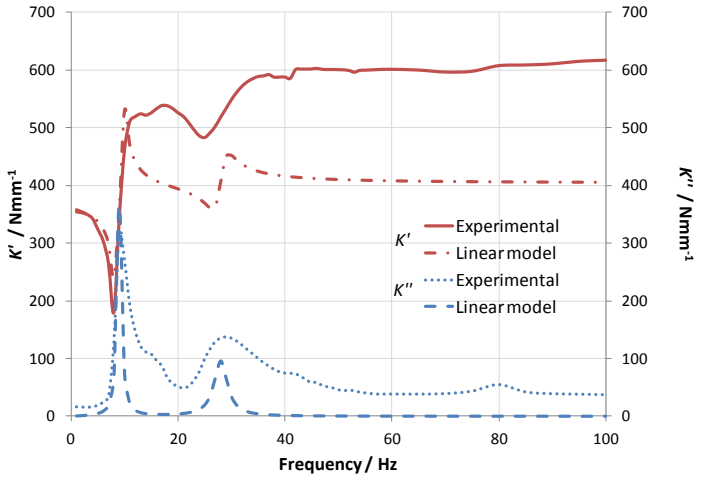

Figure 6.17: The improved stiffnesses of configuration B.

6.5 Time domain model and inclusion of non-linearities

The linear model does not provide good agreement in the magnitude of the stiffnesses, which might be improved by the inclusion of non-linearities. The time domain model also allows other parameters (such as the chamber pressure) to be found which could potentially be used to justify the chamber compliances. A time domain model was introduced in a similar way to that for the passive hydromount in Section 4.3 using the Runge-Kutta integration of Equations (6.1) to (6.6). The model was found to be unstable when used with the initial values

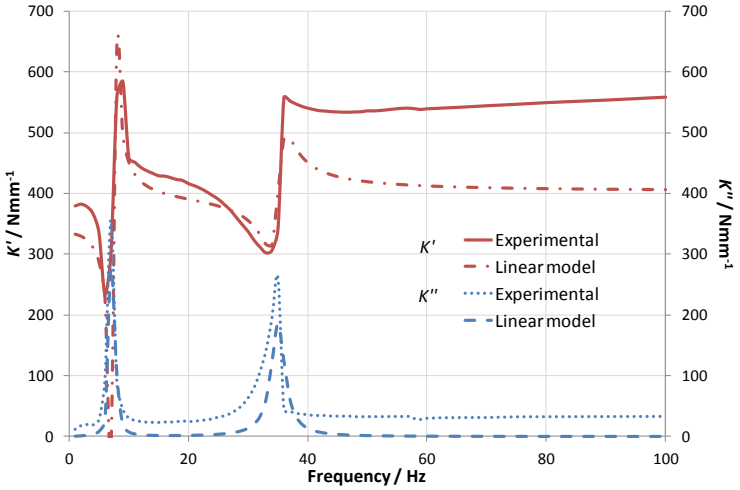

Figure 6.18: The improved stiffnesses of configuration C.

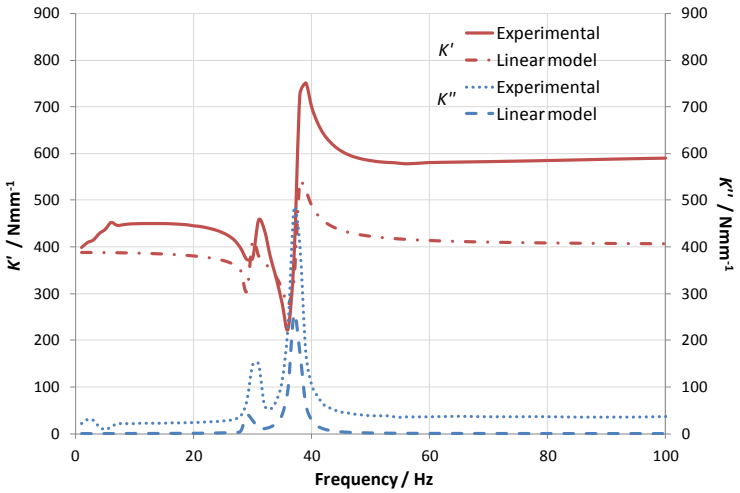

Figure 6.19: The improved stiffnesses of configuration D.

of compliance specified in Table 6.1. The values for the flow rate in the inertia tracks and the pressures within the chambers increased rapidly beyond possible physical values. However, adjusting the compliances to the new values for the improved fit, listed in Table 6.3, allowed the model to run.

Non-linearities can be included in the same way as for the simple hydromount described in Section 4.3. The vacuum phenomenon in the upper chamber was included exactly as described there. The data for the rubber spring used in the non-linear hydromount model was used here too.

6.5.1 Resistance to flow

The resistance to flow, as mentioned previously, is the gradient of the pressure-flow rate curve. In Ahmadi et al.[6] the present author demonstrated that there was good agreement between experimental data and simulations using Engineering Fluid Dynamics (a Computational Fluid Dynamics software for closed systems) for the proprietary mount in Chapter 4. As a continuation of that work, a circular cross-section pipe of a similar length to the proprietary mount inertia track was modelled as a straight length and also with three 90° corners (bent pipe) as shown in Figure 6.20. The length was 190 mm and the cross-sectional area was 100 mm^2. This was done to examine whether having bends in the adaptive mount simulation rig would be likely to affect the flow characteristics of the mount.

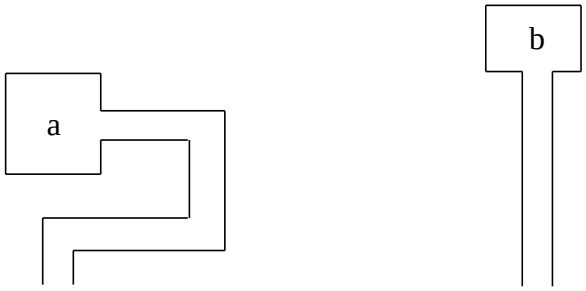

Figure 6.20: Schematic diagram of the cylindrical pipes modelled in Engineering Fluid Dynamics software. a) Pipe with corners (bent pipe) and b) Straight pipe. Not to scale).

The model was set up with a constant pressure at one end of the pipe, and atmospheric pressure at the other end. The pressure difference between the ends of the pipe, therefore, was known and the software calculated the average fluid velocity at the atmospheric pressure end, which, with knowledge of the cross-sectional area, was converted into volumetric flow rate. The results, which are shown in Figure 6.21, show that there was little effect of the corners on the resistance to flow. The second order polynomial fit is not significantly different.

The inertia tracks used in the simulation rig were therefore modelled as a straight cylindrical pipes of the appropriate dimensions with a constant pressure at one end and atmospheric pressure at the other in Engineering Fluid Dynamics as in the example above. The results can be seen in Figure 6.22 for the primary inertia track and in Figures 6.23-6.25 for the secondary inertia tracks for the different configurations. A second order polynomial trend line and equation is displayed on the graphs and these regression analysis equations are differentiated to give

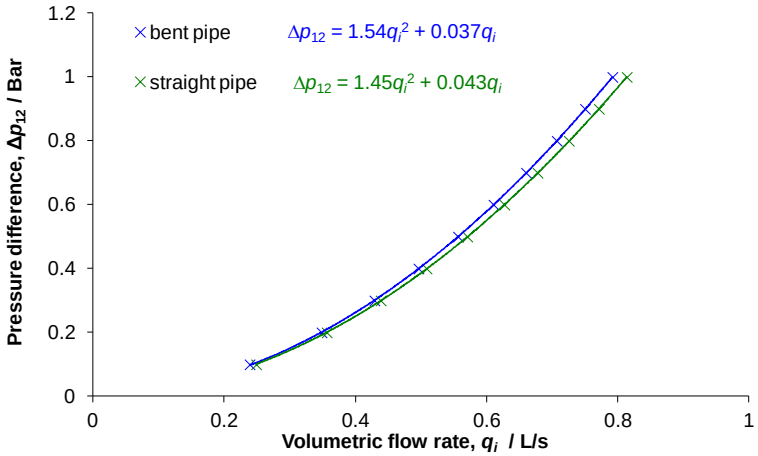

Figure 6.21: The pressure flow rate relationship for the cylindrical pipes modelled in Engineering Fluid Dynamics software.

the resistance to flow in each instance.

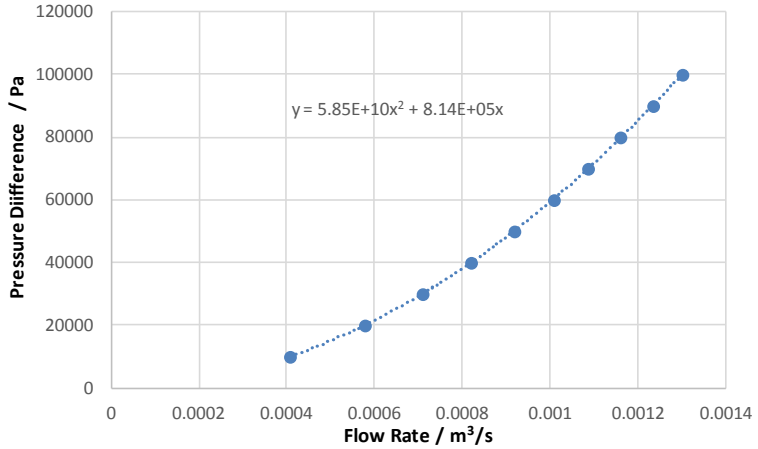

Figure 6.22: The pressure flow rate relationship for the primary inertia track (300 mm long with a diameter of 12.5 mm).

Including these non-linearities, in the time-domain model of the experimental hydromount, produced the results seen in Figures 6.26-6.29. Due to the limited number of non-linearities considered in this instance, there are still clear discrepancies between the experimental data and the model. Despite this shortcoming, the model was used to provide an estimate for the pressures in the chambers using a harmonic input. The data was taken between 1 and 50 Hz in 1 Hz intervals. The pressure was of interest to see if the improved compliances could be justified. If they were reasonable, then there would be potential for significant improvement to the model by inclusion of the non-linear behaviour of the compliance, especially if the pressure is low (see Figure 6.11).

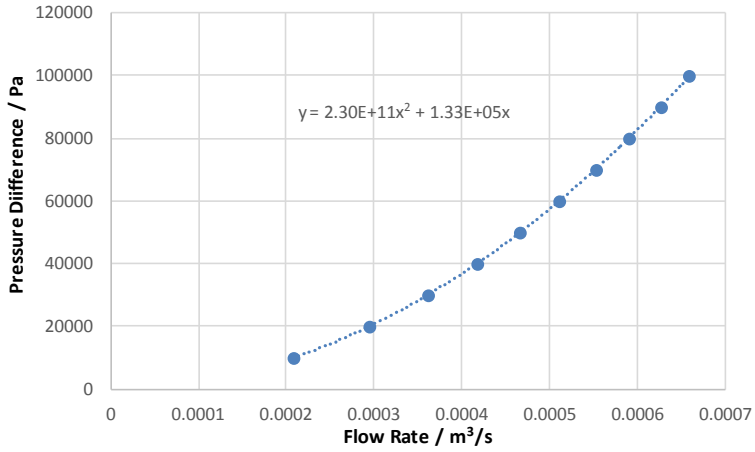

Figure 6.23: The pressure flow rate relationship for the secondary inertia track in Configuration A (12 mm long with a diameter of 7.5 mm).

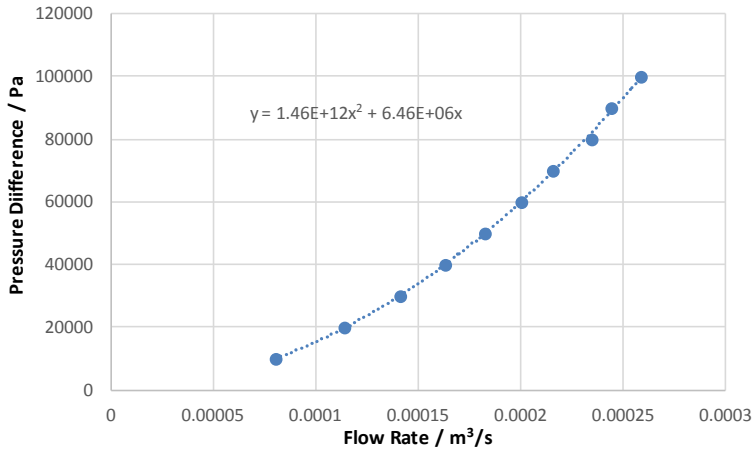

Figure 6.24: The pressure flow rate relationship for the secondary inertia track in Configuration B (25 mm long with a diameter of 5 mm).

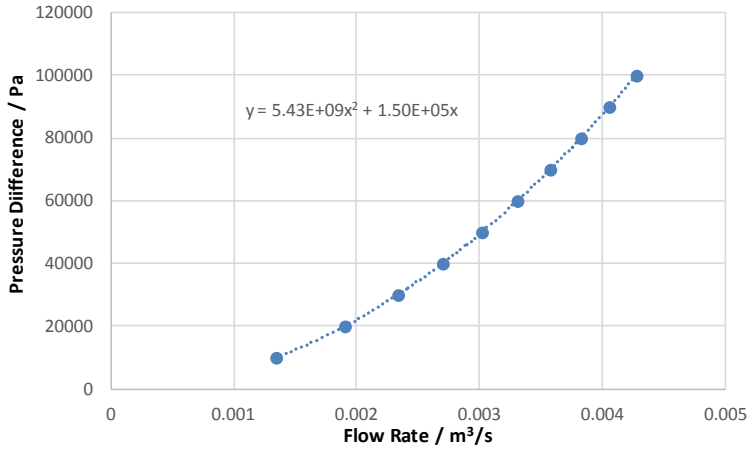

Figure 6.25: The pressure flow rate relationship for the secondary inertia track in Configurations C and D (170 mm long with a diameter of 20 mm).

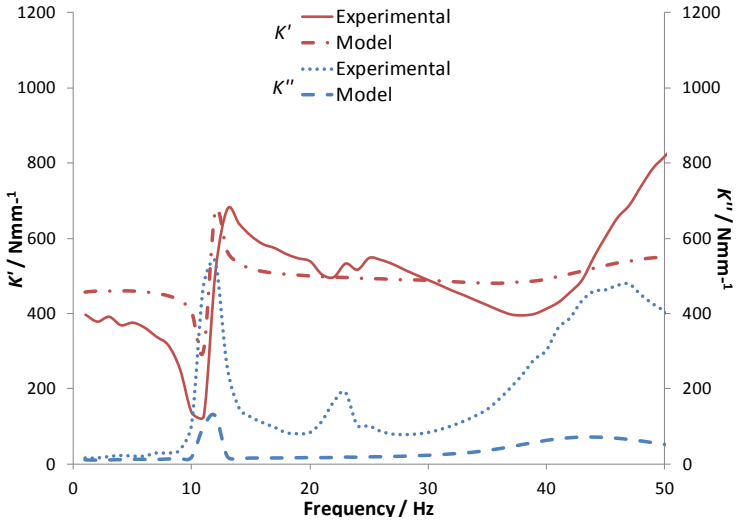

Figure 6.26: The results for the stiffnesses of configuration A.

The maximum value of pressure was determined at each excitation frequency and the results can be seen in Figures 6.30-6.32. The maximum pressure in the chambers peaks at the resonances and is different for the two resonances.

Looking first at chamber 1 (Figure 6.30), at 0.1 mm amplitude all the configurations have a similar peak value of pressure between 5 and 7.5 kPa. These values are significantly lower than those corresponding to the initial compliance. With reference to Figure 6.11, the new value of 3.07×10^{-10} m^3Pa^{-1} seems to fit better with these pressure values. For all the configurations, with the exception of C (the peak pressures of which are quite similar at both resonances), one resonance has a significantly higher pressure than the other. For A and B this is the first resonance and for D it is the second along the frequency axis. The resonance with the larger pressure corresponds to the one with the larger and sharper changes in stiffness (for configuration C the stiffnesses were similar for each resonance hence similar pressures were found). This means that the compliance of the chamber may be significantly different for each resonance and including a non-linear compliance may improve the fit.

For chamber 3 (Figure 6.31), the peak pressures are approximately 6 kPa, 8 kPa, 54 kPa and 57 kPa for configurations A, B, C and D. For configurations A and B these values are lower than those on the flat portion of the curve in Figure 6.11, and the compliances will be higher than the value initially estimated. For configurations C and D the pressures are similar to the flat portion of the curve. However, the pressure does not seem high enough to warrant the increase

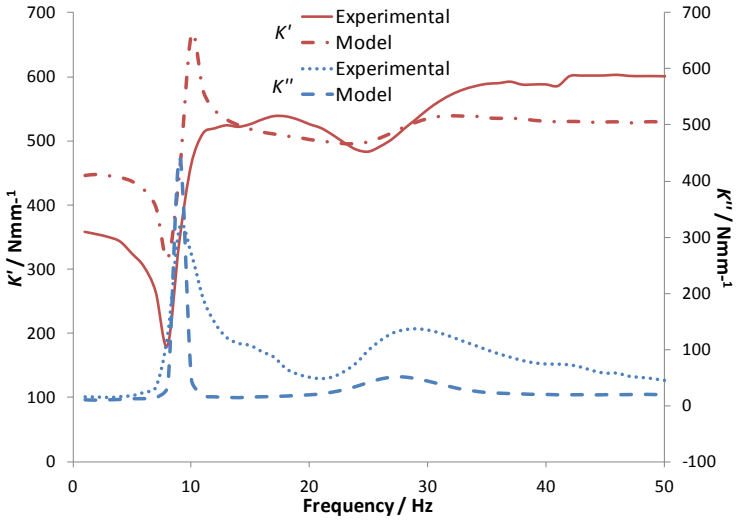

Figure 6.27: The results for the stiffnesses of configuration B.

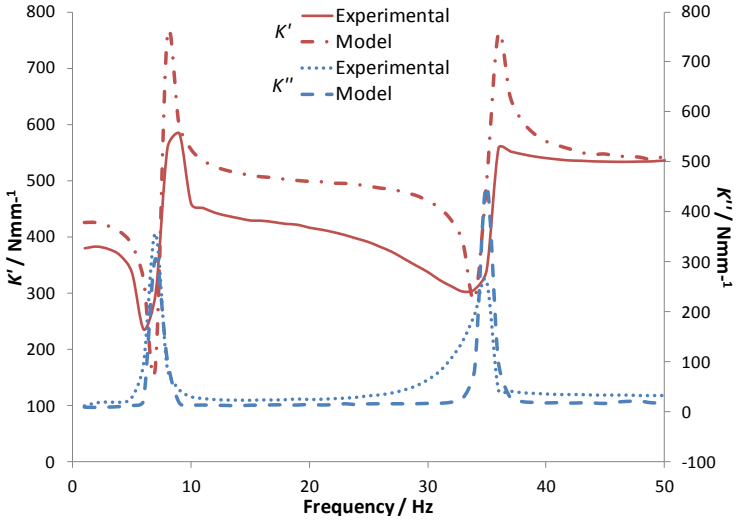

Figure 6.28: The results for the stiffnesses of configuration C.

in the compliance from the initial values to the improved values. This may be because the peak values are missed as the peaks are somewhat sharp and the increments of 1 Hz are relatively coarse, but this seems unlikely. If the peak pressure is higher the compliance could be in the high pressure upturn region observed in Figure 6.11. For configurations C and D pressure at the second resonance is much larger than the first one. In fact for D, the first resonance is not really visible in the pressure graph. For A and B the peaks of the pressure are similar at each resonance but the shape is much broader for the second. Introducing the non-linear behaviour for the compliance would have the largest effect for configurations C and D.

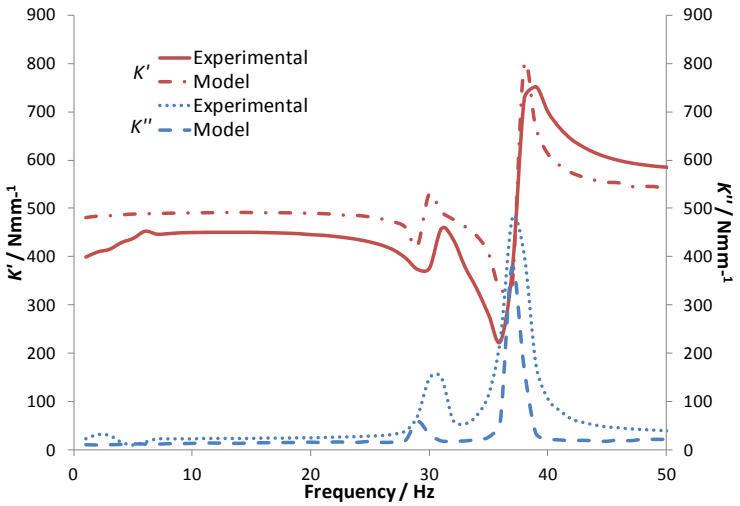

Figure 6.29: The results for the stiffnesses of configuration D.

For chamber 2 (Figure 6.32) there are two different set-ups, configurations A, B and C have one set of conditions and configuration D has a different second chamber diaphragm (and hence compliance). For configuration D the peak pressure was approximately 50 kPa, but again the peak in the pressure was quite sharp and may have been missed. The initial value seems in line with the pressure value. For configurations A, B and C the peak pressures were 16 kPa, 13 kPa and 7 kPa respectively. Although the peaks were sharp, there is not a clear justification for the reduction in the compliance. For these the first resonance was clearly dominant in the pressure curves in all configurations. The second resonance was not visible for A, B and C, and was significantly lower for D. Two reasons are considered strong possibilities for why the compliance was reduced for this chamber. One is that the diaphragm may stretch beyond a hemisphere and the calculated compliance is no longer valid and the second is that the first chamber compliance is not correct for this resonance. The latter would result in a different value for the second chamber compliance to govern the resonance frequency of the first resonance. This may be reasonable for A, B and D, but does not seem likely for C where the pressures seemed similar for the two resonances.

The peak volume change in the second chamber was estimated from the peak pressure in the second chamber and the improved values of compliance. For configuration D the estimated volume change is 565 mm^3, whereas the volume change for a fully inflated hemisphere is 262 mm^3. This means that the situation whereby the diaphragm is beyond a hemisphere is likely for this case. For configurations A to C the estimated volume changes (1424 mm^3, 2314 mm^3 and

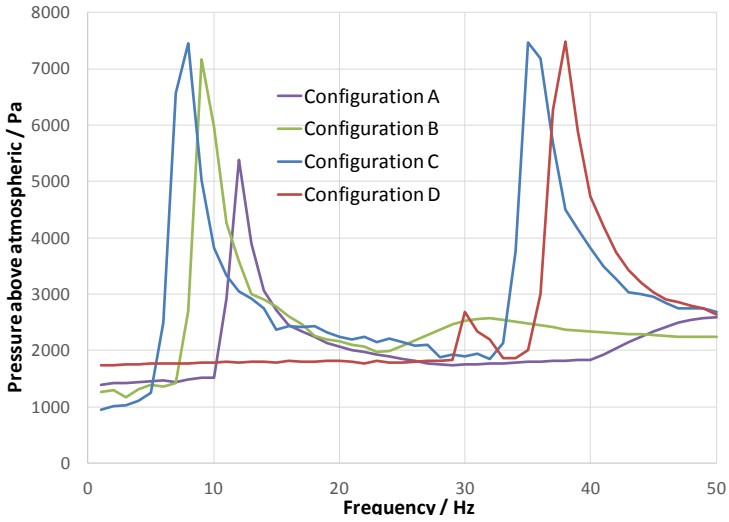

Figure 6.30: The maximum pressure in chamber 1 from the non-linear model for harmonic excitation of 0.1 mm.

2492 mm^3 respectively) are below the hemisphere volume change of 32725 mm^3.

6.6 Conclusions

The proposed two inertia track model can work well. It was possible to get good agreement for the frequency of both resonances, although the compliance was chosen to achieve this. Non-linearities can be added in the same way as for the model for the single track hydromount. The resistance to flow of the inertia track from simulation does not seem to be dependent on the number of corners in the track.

The method used to calculate the compliances for the experimental rig gives a quite a large variation with pressure. This makes the compliance hard to estimate as the pressure in the experimental rig was not known. Looking at the pressures that the non-linear model predicts there is some justification for the compliances chosen, although the theory is limited to strains below the stiffening of the polymer and inflations of the diaphragm of less than a hemisphere.

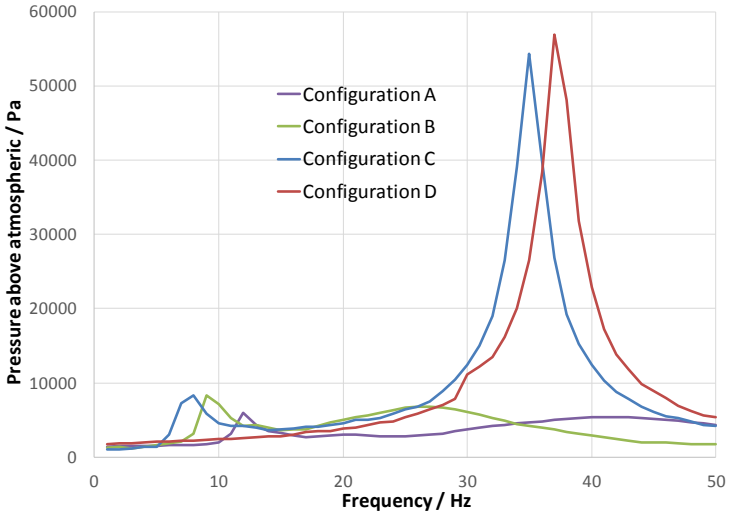

Figure 6.31: The maximum pressure in chamber 3 from the non-linear model for harmonic excitation of 0.1 mm.

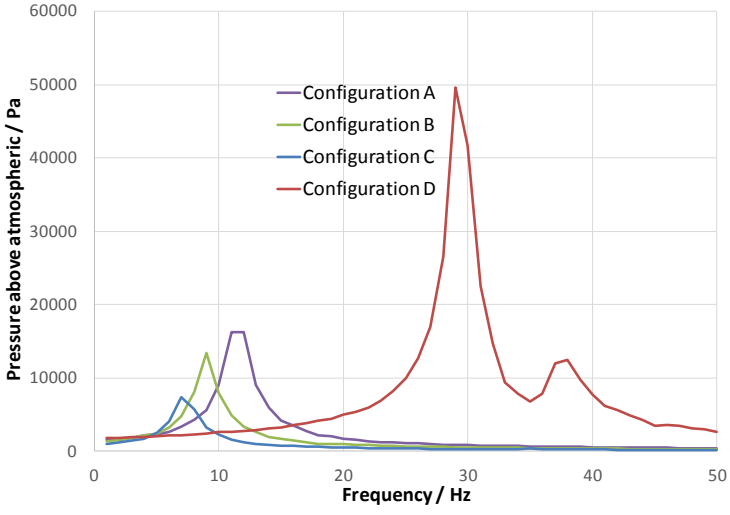

Figure 6.32: The maximum pressure in chamber 2 from the non-linear model for harmonic excitation of 0.1 mm.

Chapter 7

Hydromounts in the Quarter-Car Model

7.1 Introduction

Chapters 4 and 6 introduced models for hydromounts with one and two inertia tracks respectively. This chapter uses the linear models in the frequency domain discussed in those chapters, to explore the effect of the mounts when installed in a vehicle using the quarter car model introduced in Chapter 3.

7.2 Hydromounts with a single inertia track

The linear fluid model for hydromounts from Singh et al.[57] has been incorporated into the quarter car model. The expressions for the dynamic stiffness of the mount can be found as Equations (4.1) and (4.2). As the transfer stiffness and the point stiffnesses do not differ by much as shown in Section 4.2.2, particularly at the low frequencies where the hydromount resonance is, the transfer stiffness has been used alone, not a four pole stiffness matrix. If the rubber spring should not be considered massless, then mass should also be considered for the viscous damping cases if these are to describe a simple rubber mount.

The parameters for the hydromount used in the model, were set such that the trough in K' was at approximately the resonance frequency of the engine on the

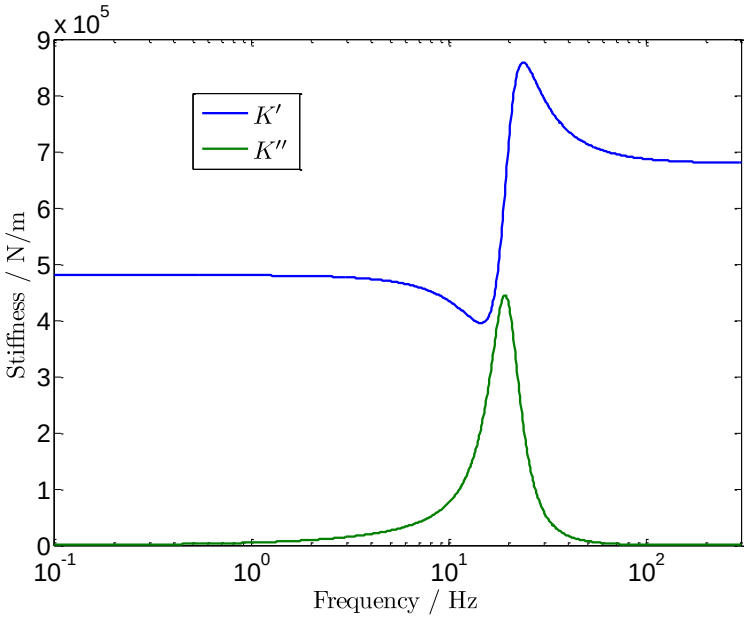

Figure 7.1: Frequency dependence of the stiffnesses of the single inertia track hydromount model

mounts used in Chapter 3 (14.2 Hz). This trough was also tuned such that the stiffness at this frequency was approximately 400 kN/m so that the resonance frequency would be similar to the cases explored earlier. The parameters used are given in Table 7.1. The stiffness behaviour can be seen in Figure 7.1.

Parameter	**Values**
b_r	0
k_r	4.8×10^5 N/m
C_1	4.79×10^{-11} Pa/m^3
C_2	3.80×10^{-8} Pa/m^3
R_i	7.69×10^7 Pa s/m^3
A_r	3.09×10^{-3} m^2
I_i	1.31×10^6 kg/m^4

Table 7.1: Parameters for the single inertia track hydromount model

To look at the changes that the hydromount makes to the performance, the results for the hydromount are compared with the spring and viscous damper with various damping levels. As they are of the most interest, only the relative motion of the engine to the chassis has been considered for the base excitation case and only the motion of the chassis for forced engine vibration case has been

considered.

Figure 7.2 shows the relative motion of the engine with respect to the chassis for the base excitation case. As discussed in Chapter 3, the ideal situation is for the engine to move in-phase and with similar amplitude to the car at low frequencies where the road input is expected to be significant. As can be seen, the hydromount acts as a tuned mass damper or vibration absorber. This has the result that the resonance present in the viscous damping examples is replaced by two peaks on either side of the original one. With the parameters used in this model, the peaks are significantly lower than in the lightly damped viscous case, but are significantly higher than for the critically damped viscous case. At high frequencies the behaviour is similar to the lightly damped case, which is ideal for vibration isolation. The height of the peaks can be controlled by the damping present in the hydromount at the new resonance frequencies of the system. For this reason it is important that there is reasonably high damping over a wide frequency range in this region. Simple rubber mounts are likely to have damping ratios of between 0.01 and 0.2, depending on the formulation.

Results for the forced vibration case, $X_1/X_{2\mathrm{f}}$, can be seen in Figure 7.3. Ideally this should be as small as possible. Again it is possible to see the tuned mass damping behaviour of the hydromount. At the resonance of the engine the benefit over the lightly damped viscous case is still present, and at high frequencies where the slope follows that of the lightly damped case, there are advantages over the more highly damped viscous cases.

As vehicles and mounts will have some inherent variability, it is clear that to allow for tuning having a broad resonance of the hydromount with high damping and the trough across a wide frequency range, is beneficial. It is also important that at higher frequencies above the resonance frequency, the stiffness is low. It is for the low amplitude vibration that this is particularly important and in this case the increase in stiffness of the mount above the resonance frequency can be avoided or mitigated by the inclusion of a decoupler (see Section 2.2).

7.3 Hydromounts with two inertia tracks

In a similar way to the single track hydromount above, the linear model for a two track hydromount (Equation (6.7)) is used in the quarter car model.

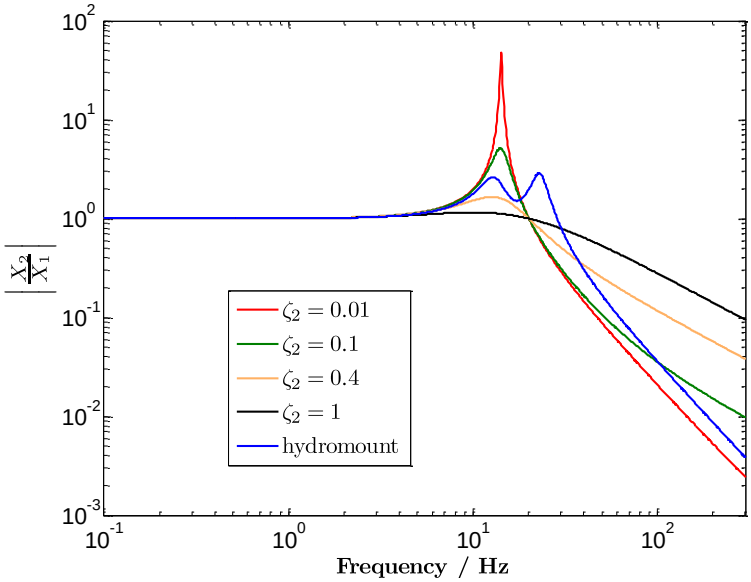

(a) $|X_2/X_1|$ versus frequency

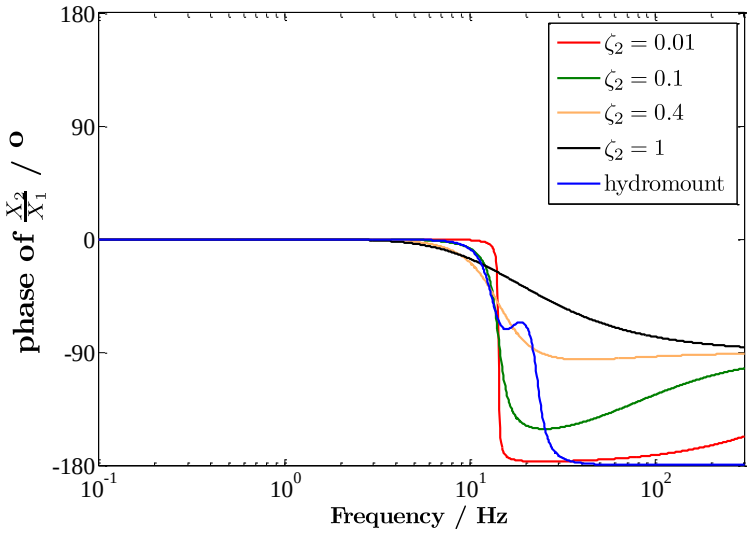

(b) Phase of X_2/X_1 versus frequency

Figure 7.2: The variation of X_2/X_1 with frequency for base excitation for viscous damping and with a single inertia track hydromount

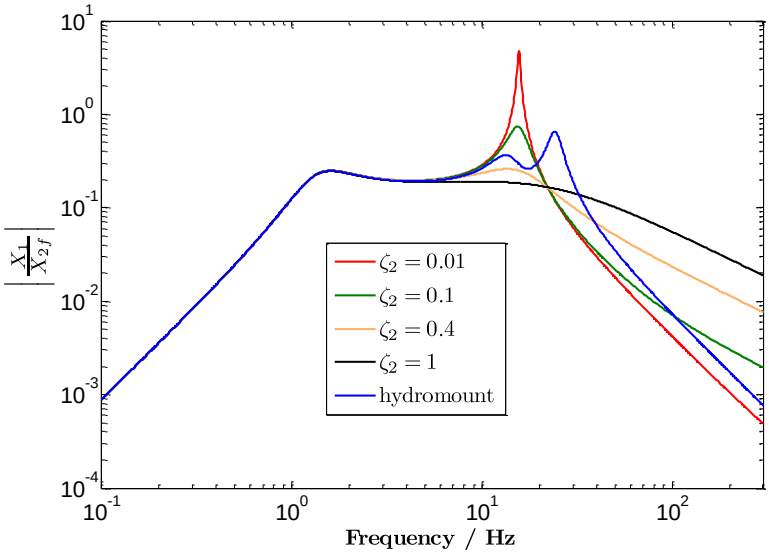

(a) $|X_1/X_{2\mathrm{f}}|$ versus frequency

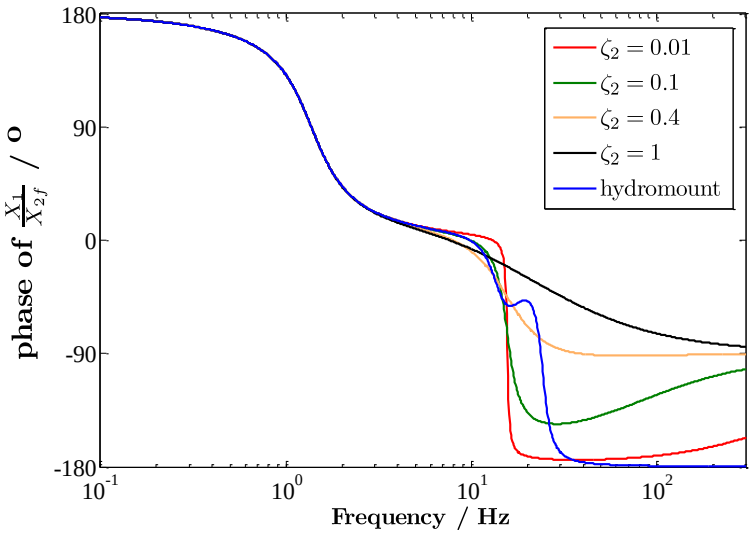

(b) Phase of $X_1/X_{2\mathrm{f}}$ versus frequency

Figure 7.3: The variation of $X_1/X_{2\mathrm{f}}$ with frequency for engine forcing for viscous damping and with a single inertia track hydromount

The parameters for the hydromount used in this section, were set so that the behaviour was similar to the one track hydromount at the first resonance frequency. To achieve this the parameters used are different from the single track mount, because of the interaction of the second resonance with the first resonance of the mount. The parameters were also chosen so that the second resonance had a trough at approximately 30 Hz as this is the engine firing frequency at idle. The parameters used are given in Table 7.2. The stiffness behaviour can be seen in Figure 7.4. The high frequency K' is larger in magnitude than that of the single inertia track hydromount.

Parameter	**Values**
b_{r}	0
k_{r}	4.4×10^5 N/m
C_1	7.67×10^{-11} Pa/m^3
C_2	2.14×10^{-10} Pa/m^3
C_3	2.52×10^{-10} Pa/m^3
R_{i}	4.51×10^7 Pa s/m^3
R_{i3}	5.25×10^7 Pa s/m^3
A_{r}	6.17×10^{-3} m^2
I_{i}	1.16×10^6 kg/m^4
I_{i3}	1.38×10^6 kg/m^4

Table 7.2: Parameters for the two inertia track hydromount model

The results for the base isolation case can be seen in Figure 7.5. The results for the viscous damping cases with $\zeta = 0.01$ and $\zeta = 1$ have been included for comparison as well as the result for the single track hydromount. Assuming that the second resonance of the hydromount is only used when the vehicle is idling, there should be no input displacement from the base, so in fact base excitation is less important than the forced vibration. However, it can be seen that the second hydromount resonance acts as a vibration neutraliser creating a minimum in the system response at approximately 30 Hz, with improved performance over the single inertia track hydromount at this frequency. Peaks are introduced in the response on either side of this frequency, which can be controlled by ensuring a broad frequency range of high damping, but this would also reduce the trough.

The forced vibration results can be seen in Figure 7.6. These show a similar outcome to the base excitation case above, with the second resonance of the

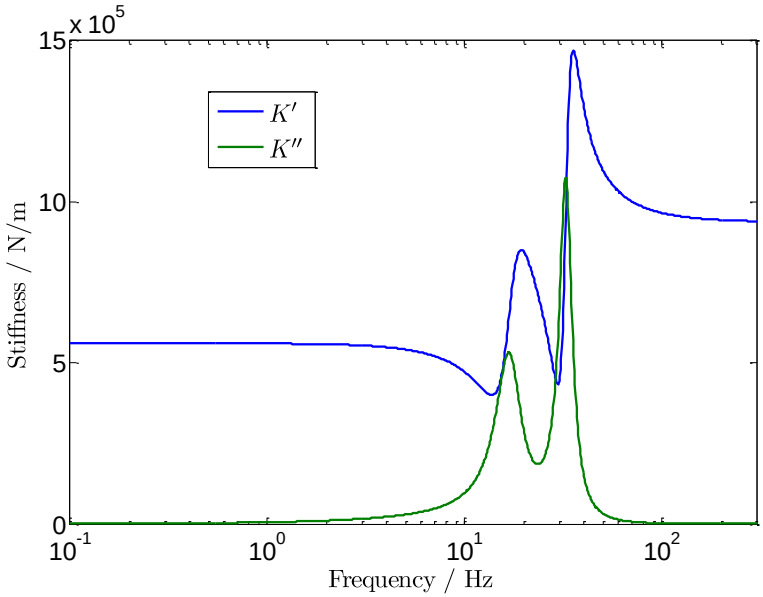

Figure 7.4: Frequency dependence of the stiffnesses of the two inertia track hydromount model

hydromount behaving as a vibration neutraliser at its tuned frequency. The behaviour is improved at this frequency over that of the single track hydromount. This could be further improved by optimisation to ensure a lower response at the main disturbing frequency. At idling the excitation frequencies should be fairly constant and the introduction of peaks at different frequencies may not be important, depending on the vehicle.

Unlike the single track hydromount, the engine vibrations above the resonance frequency of the engine on its mount are likely to be of small amplitude. This is a shortcoming of using a linear model which is necessarily tuned to the behaviour at a single amplitude. The smaller amplitude vibrations are likely to have a larger change in K' at the resonance of the second inertia track and a larger peak in K''. This could improve the behaviour at the tuned frequency further.

7.4 Summary

A single inertia track hydromount acts as a tuned mass damper, attenuating the excitation at what would be a system resonance frequency, but introducing two peaks in the response on either side. These can be controlled in height by the damping of the hydromount. Although the additional damping may reduce the

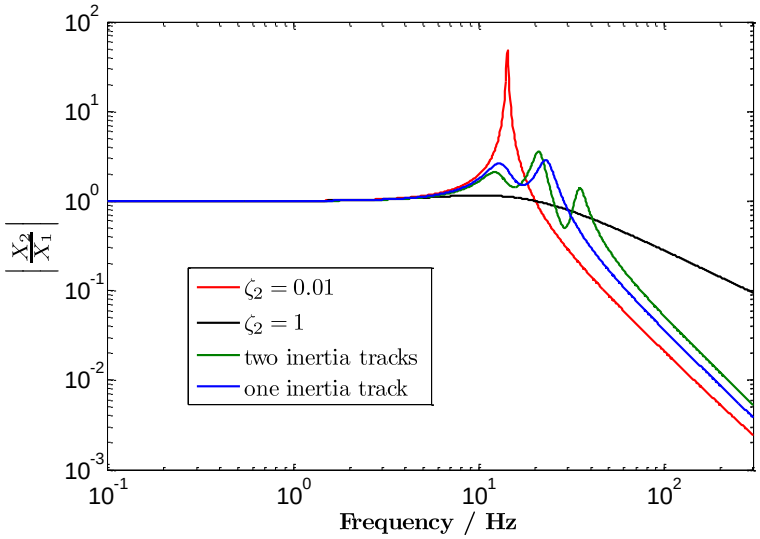

(a) $|X_2/X_1|$ versus frequency

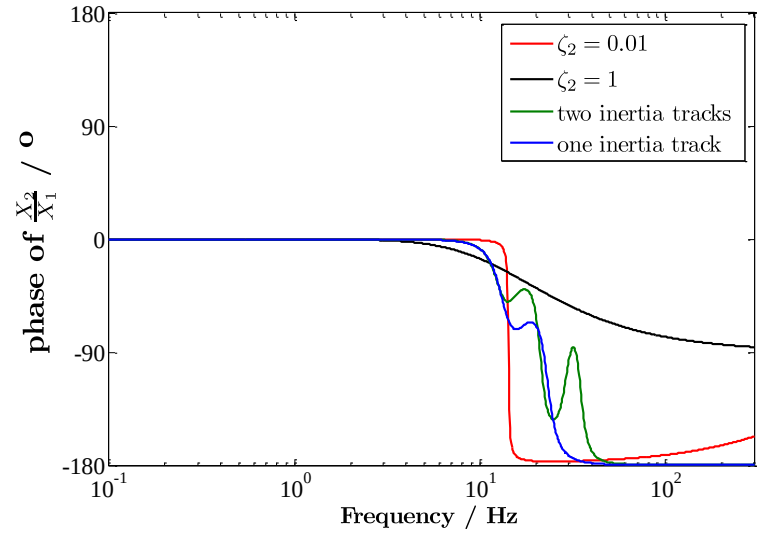

(b) Phase of X_2/X_1 versus frequency

Figure 7.5: The variation of X_2/X_1 with frequency for base excitation for viscous damping and with a two inertia track hydromount

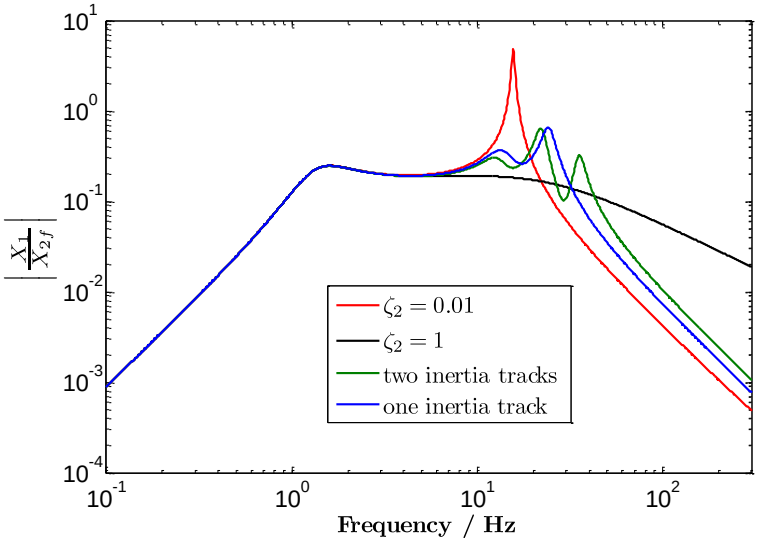

(a) $|X_1/X_{2\mathrm{f}}|$ versus frequency

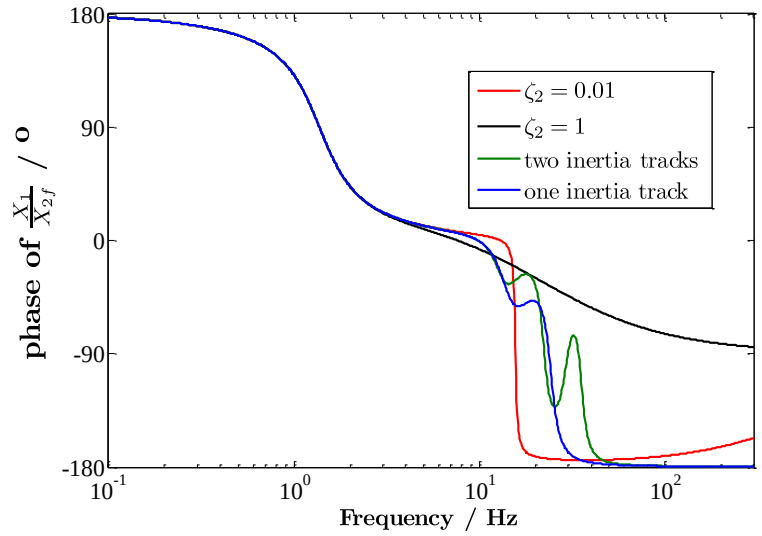

(b) Phase of $X_1/X_{2\mathrm{f}}$ versus frequency

Figure 7.6: The variation of $X_1/X_{2\mathrm{f}}$ with frequency for engine forcing for viscous damping and with a two inertia track hydromount

peaks, the response at the attenuated frequency would be increased. For single track hydromounts in this frequency region the main input is likely to be from the road and could occur at any frequency and amplitude; therefore, small magnitude peaks are probably more important than deep troughs. It then follows that it is important that the damping is high enough across a broad enough range to allow this. It is also important that at high frequencies the stiffness of the mount is not too high. This will be most significant for the small amplitude vibrations from engine excitation and this is the advantage that using a decoupler can bring as the low frequency behaviour is not so important. The low damping at high frequencies allows the hydromount to provide good isolation behaviour in this range.

Two inertia track hydromounts on the other hand, are designed such that the second inertia track provides a further resonance at a tuned frequency. At this frequency the hydromount behaves as a vibration neutraliser and it can provide benefits over a single track hydromount. If this is used to neutralise a disturbing engine vibration at idle, the low frequency behaviour is not so important, and depending on the other excitation frequencies of the engine, the introduction of the additional system response peaks on either side may also not be significant. These peaks again can be mitigated by the presence of damping, but this would worsen the behaviour at the trough.

Incorporating the switching mechanism developed in Chapter 5 into the two inertia track hydromount, allows it to switch between the single inertia track mount and the one with two inertia tracks. This means at idling the forcing frequency of the engine can be neutralised without being detrimental to the high frequency behaviour under driving conditions, where the single inertia track hydromount can be taken advantage of. Using an electromagnet would allow the switch to be operated *in situ*. The permanent magnet used in Chapter 5 was for experimental purposes only.

Chapter 8

Conclusions and Further Work

8.1 Conclusions

The aim of this project is to develop and test ideas for a switchable hydromount. The switchable hydromount has two states, one where it behaves like a passive mount, and a second where it is tuned for a disturbing frequency under specific conditions. To this end it is useful to have a working model for this hydromount and consider the potential benefits such a mount might bring.

A simplified two-degree-of-freedom system is used to represent a quarter of a car with both excitation from the base (representing the input from the ground to the wheel) and the forced vibration of the engine. This allows theoretical engine mounts different types and levels of damping and active control strategies to be examined. By comparing different types of damping, it was found that viscous damping has the disadvantage that if high damping is used to reduce the magnitude of the resonances of the system, the high frequency roll-off is adversely affected. As expected, hysteretic damping improves this as the isolation behaviour above the resonance frequencies is not dependent upon the damping, but this theoretical consideration suffers from being not causal. Using a frequency dependent stiffness makes the high damping situation more similar to that of viscous damping at high frequencies. However, there is still some advantage for high frequency roll-off when compared with the viscous damping case for low and moderate damping. In addition hypothetical groundhook and skyhoook damping configurations are considered as potential control mechanisms for an

active mount. Skyhook damping was found to give the best performance as it reduces the amplitudes at both resonance frequencies of the two degree of freedom system,

Practically, it would be hard to find an elastomeric material exhibiting a damping ratio greater than approximately 0.2, unlike the higher values of considered in the models. However, as the damping for the skyhook and groundhook cases is not a material property this could in fact be achieved using an active or potentially an adaptive system. The results are used to explain some of the desirable features of a hydromount, in particular the low damping at high frequencies, with high damping corresponding to the resonance corresponding to the engine on the mounts.

The dynamic stiffness of a proprietary single inertia track hydromount was tested. This shows a single resonance associated with the inertia track. The results show that there is strong dynamic displacement amplitude dependence of the mount when looking at the magnitude of the dynamic stiffness. However, the frequency of the resonance varies little with dynamic amplitude. A model developed by Singh et al.[57] is applied to the results of the proprietary mount. This mount showed significant amplitude-dependence in the magnitude of the real and imaginary parts of the dynamic stiffness, but did not show significant variation in the frequency dependence with changing amplitudes, with the key features appearing at similar frequencies regardless of the amplitude. Using a linear model, it is possible to achieve good agreement in predicting the frequency of the features of the response; however, the magnitude of stiffnesses was not predicted well and it was clear that the inclusion of non-linearities might improve this fit.

From the literature, potential non-linearities were identified and included into the model. As the amplitude is increased the internal resonance of the mount is shifted to slightly lower frequencies using the model, whereas this does not occur in the experimental results. The higher the amplitude, the more significant the effect is. However, generally the trends seen are similar to the experimental results, with increasing amplitude leading to reductions in the magnitude of the stiffnesses, and a wider bandwidth of the features.

The sensitivity of the dynamic stiffness to changes in the various parameters was studied. Altering the area of the rubber spring has little effect on the resonance frequency, mainly controlling the magnitude of the response above the resonance.

The area of the inertia track only affects behaviour near the resonance frequency. Changing the area can increase agreement with the response magnitude, but this will also make the fit with the resonance frequency worse. The length of the inertia track only has a direct effect on its inertance, which will have an impact on the resonance behaviour of the hydromounts, but little effect on frequencies above or below this. However, it is likely that this parameter will also affect the empirical equation for the resistance to flow through the inertia track. It should also be noted that the effective length of the inertia track is likely to vary with amplitude. Density also affects the inertance, and so will also significantly affect the resonance behaviour. Increasing the density decreases the resonance frequency and increases the magnitude of the peaks and troughs in the stiffness curves. Increasing the coefficient in the non-linear equation for resistance to flow decreases the magnitude of the peaks and troughs at the resonance, whilst leaving the high and low frequency behaviour unchanged. The vacuum phenomenon parameters do not change the behaviour much when adjusted on their own, although they could potentially be used for fine-tuning. Compliance effects in the proprietary hydromount are primarily governed by the characteristics of the compliance of the first chamber because it is much lower than that of the second chamber.

Particle swarm optimisation (PSO) was used to improve the fit of the model and to see if any further non-linearities could be identified. The cost function and fit were improved at all amplitudes, with the greatest improvements found for the higher amplitude cases. The main discrepancy between the model with the PSO parameters and the experimental data is the magnitude of the resonance peak, although the resonance frequency itself is modelled well at all amplitudes. The parameters do not show a clear trend with changing amplitude, except for the coefficient for resistance to flow through the inertia track which appears to decrease with increasing amplitude. Using the mean values for each optimised parameter improves the fit at all amplitudes, with the results at 0.1 mm and 0.2 mm amplitudes being very similar to the post-PSO values. At higher amplitudes using the mean values shifts the resonance frequency to lower values, while at 0.05 mm the peak and trough are poorly predicted. These features can be improved by using the mean values apart from for the coefficient of resistance to flow through the inertia track, which is fitted with an exponential function. The success of the optimisation technique means it has potential to be used to design a mount if the ideal behaviour is defined, as well as providing a tool to create a model with good agreement to be used in multi-body dynamics simulations of the full vehicle.

Different methods of altering the first chamber compliance to suppress the resonance of a mount in an adaptive system were investigated. The method of altering the first chamber compliance is suitable to be used to alter the properties of the mount. Although it could potentially also be used to tune the resonance frequency of the mount, this would only really be useful for fine adjustment as there are more potent ways to alter the resonance of the system at the design stage.

A two inertia track system was also considered as this allows two tuned frequencies to be used in certain circumstances: for example, the second frequency could be tuned to the engine excitation frequency when the car is idling. The second frequency could be switched on and off as required.

A promising versatile solution was found for the switching mechanism using a balloon containing MRF on top of a magnet. This allows it potentially to be retrofitted into existing devices as well as being used in potential applications other than engine mounts.

A theoretical analysis of the compliance of an annular diaphragm is used to aid in the estimation of the compliance of the chambers of the mount. A large variation was found in the calculated compliance with the chamber pressure. There were also limitations to these calculations, for example if the diaphragm expanded beyond a hemisphere.

Four different configurations of an experimental rig were used to investigate the effect of the parameters of a two inertia track mount. These showed two predominant resonances, one for each inertia track. In the three configurations where the parameters for the first inertia track and the second chamber were unchanged, there was some variation in the first resonance frequency, showing it is affected by the changes to the second inertia track.

A set of differential equations (which could be used as a linear description through Laplace transformation) was proposed for the two inertia track mount. This was compared to the data for the four experimental configurations. The sensitivity of the chamber compliances to their internal pressure is identified as a source of uncertainty, altering the compliance from that calculated for the chosen pressure allowed good agreement to be achieved. The non-linear model allowed the pressure in the chamber at each time step to be recorded. By looking at the peak pressures within the chambers some of the modified values of compliance can be explained.

This model could be used to help design mounts with two inertia tracks, and be used to describe the behaviour in multi-body dynamics simulations.

Finally, the models developed in previous chapters are applied in the quarter-car model. It is found that it is important to have a high damping with a broad spread across the frequencies to control the behaviour around the resonance. The hydromount introduces a tuned mass damper, reducing the response at the resonance of the engine on its mounts, with better behaviour at high frequencies than a simple rubber mount with similarly sized resonance peaks. The mount with a second inertia track and third compliance behaves as a vibration neutraliser at its tuned frequency, but introduces new peaks in the response. Inclusion of the switching mechanism into the mount would allow switching between the single inertia track system and the two inertia track one. This can allow the benefits both mounts to be exploited. A single inertia track hydromount would be best for normal driving conditions, but where there is a particular known forcing frequency, such as during idling, a second inertia track could provide better isolation.

8.2 Recommendations for future work

The following suggestions are made for further work, both experiments and modelling.

The switch unit developed in this thesis could be explored further. The fatigue life of a balloon containing a particle filled fluid inside is likely to be poor and a design that incorporates the same behaviour but in a container that is more robust than a latex balloon would be beneficial. It would also be of interest to explore further applications for the switch mechanism. Control strategies should also be considered, and whether feedback or feedfoward control would provide the best performance.

It is possible to improve the two-inertia track model, by expanding the model to include other non-linearities. Experimental work to determine the pressure in the chambers would be beneficial in calculating the compliance and this could be used to verify the non-linear model. Direct measurement of the chamber compliance (or diaphragm expansion with pressure) would also be informative. Particle swarm optimisation could be applied to the two inertia track model to improve the fit in the same way as has been done for the single inertia track

mount. It would be useful to apply the model to commercial instances of two inertia track mounts.

The theoretical compliance of the diaphragms could be extended to include expansion beyond a hemisphere. This would allow a greater range of pressures within the chambers to be modelled. Experimental work determining the compliance of the chambers used would also be informative.

Appendix A

Equi-biaxial inflation of rubber sheets

This contains the work previously carried out by Dr Julia Gough[168].

If no force acts normal to a tensioned surface, the surface must remain flat. But if the pressure on one side of the surface differs from the pressure on the other side, the pressure difference multiplied by the surface area results in a normal force. In order for the surface tension forces to cancel the force due to pressure, the surface must be curved. When all the forces are balanced, the resulting equation is the Young-Laplace equation:

$$\Delta P = \gamma \left(\frac{1}{R_1} + \frac{1}{R_2} \right) \tag{A.1}$$

where ΔP is the pressure difference, γ is surface tension which at the centre is equal to the force per unit length, f, and R_1 and R_2 are radii of curvature in each of the axes that are parallel to the surface. From Rivlin's theory of large strain elasticity[169] (see Treloar[170]) the differences between the true stresses for a hyperelastic, isotropic, incompressible material are given by equations of the form

$$\sigma_1 - \sigma_3 = 2\left(\lambda_1^2 - \lambda_3^2\right)\left(\frac{\partial W}{\partial I_1} + \lambda_2^2 \frac{\partial W}{\partial I_2}\right) \tag{A.2}$$

$$\sigma_2 - \sigma_3 = 2\left(\lambda_2^2 - \lambda_3^2\right)\left(\frac{\partial W}{\partial I_1} + \lambda_1^2 \frac{\partial W}{\partial I_2}\right) \tag{A.3}$$

where λ_i are the principal extension ratios, W is the strain energy density and I_1

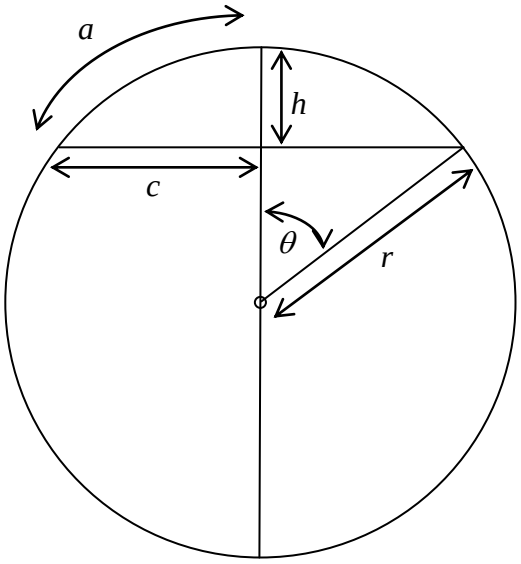

Figure A.1: Section of circular diaphragm

and I_2 are the strain invariants defined as

$$I_1 = \lambda_1^2 + \lambda_2^2 + \lambda_3^2 \tag{A.4}$$

$$I_2 = \lambda_1^2\lambda_2^2 + \lambda_2^2\lambda_3^2 + \lambda_3^2\lambda_1^2 \tag{A.5}$$

Also, $\lambda_1\lambda_2\lambda_3 = 1$ due to incompressibility.

The initial diameter of the sheet is $2c$. As it inflates a diameter on the original sheet becomes an arc of length $2a$, leading to:

$$\lambda_1 = \frac{a}{c} \tag{A.6}$$

At the centre of an inflated sheet, the sheet is in equi-biaxial extension. In equi-biaxial extension for stretches in the 1,2 plane $\sigma_3 = 0$, $\lambda_1 = \lambda_2$, $\lambda_3 = 1/\lambda_1^2$, so Equation (A.2) becomes:

$$\sigma_1 = 2\left(\lambda_1^2 - \lambda_1^{-4}\right)\left(\frac{\partial W}{\partial I_1} + \lambda_1^2\frac{\partial W}{\partial I_2}\right) \tag{A.7}$$

For a neo-Hookean material, $\frac{\partial W}{\partial I_1} = \frac{G}{2}$ and $\frac{\partial W}{\partial I_2} = 0$ so

$$\sigma_1 = G\left(\lambda_1^2 - \lambda_1^{-4}\right) \tag{A.8}$$

where G is the shear modulus.

The tension force, f_1, in the 1 direction, across a line of unit length, is given by

$$f_1 = \sigma_1 t \tag{A.9}$$

where the rubber thickness, $t = t_0\lambda_3$ where t_0 is the initial rubber thickness. Hence, from (A.9),

$$f_1 = Gt_0\left(1 - \lambda_1^{-6}\right) \tag{A.10}$$

When R_1 and R_2 from Equation (A.1) are equal in the case of equi-biaxial extension, the equilibrium fluid pressure, P, is given by

$$P = \frac{2f_1}{r} \tag{A.11}$$

where r is the radius of curvature of the sheet. This leads to:

$$P = \frac{2Gt_0}{r}\left(1 - \lambda_1^{-6}\right) \tag{A.12}$$

References

[1] Electrostrictive ceramics, Accessed:15/05/2017. URL `www.trstechnologies.com/Materials/Electrostrictive-Ceramics`.

[2] H Tuller. Electroceramics. In Mel Schwartz, (Ed), *Encyclopedia of Smart Materials*, pages 337–356. John Wiley and Sons, Inc., New York, 2002.

[3] H Eda and L Zhou. Giant magnetostrictive materials. In Mel Schwartz, (Ed), *Encyclopedia of Smart Materials*, pages 503–519. John Wiley and Sons, Inc., New York, 2002.

[4] J Van Humbeeck and R Stalmans. Shape memory alloys, types and functionalities. In Mel Schwartz, (Ed), *Encyclopedia of Smart Materials*, pages 951–964. John Wiley and Sons, Inc., New York, 2002.

[5] R Sakurai, H See, T Saito, and M Sumita. Effect of matrix viscoelasticity on the electrorheological properties of particle suspensions. *Journal of Non-Newtonian Fluid Mechanics*, **81**:235–250, 1998.

[6] HR Ahmadi, A Ismail, C Lajim Sayung, and JK Picken. Development of smart engine mounts. In *International Rubber Conference 2008, Kuala Lumpur, Malaysia*, 2008.

[7] WM Winslow. *Method and Means For Translating Electrical Impulses Into Mechanical Force*, US Patent, US2417850, 1947.

[8] WM Winslow. Induced fibration of suspensions. *Journal of Applied Physics*, **20**:1137–1140, 1949.

[9] J Rabinow. The magnetic fluid clutch. *AIEE Transactions*, **67**:1308–1315, 1948.

[10] J Rabinow. *Magnetic Fluid Torque and Force Transmitting Device*, US Patent, US2575360, 1951.

[11] JD Carlson, DM Catanzarite, and KA St. Clair. Commercial magneto-rheological fluid devices. *International Journal of Modern Physics B*, **10**: 2857–2866, 1996.

[12] MR Jolly, JW Bender, and JD Carlson. Properties and applications of commercial magnetorheological fluids. In *SPIE 5th Annual Int. Symposium on Smart Structures and Materials, San Diego, CA*, 1998.

[13] PW Atkins. *Physical Chemistry*. Oxford University Press, Oxford, 4th Edition, 1990.

[14] YT Choi, JU Cho, SB Choi, and NM Wereley. Constitutive models of electrorheological and magnetorheological fluids using viscometers. *Smart Materials & Structures*, **14**:1025–1036, 2005.

[15] SS Papell. *Low viscosity magentic fluid obtained by the colloidal suspension of magenetic particles*, US Patent, US3215572, 1965.

[16] AJ Millar Henrie and JD Carlson. Magnetorheological fluids. In Mel Schwartz, (Ed), *Encyclopedia of Smart Materials*, pages 597–600. John Wiley and Sons, Inc, New York, 2002.

[17] MR Jolly, JD Carlson, and BC Muñoz. A model of the behaviour of magnetorheological materials. *Smart Materials & Structures*, **5**:607–614, 1996.

[18] JD Carlson. What makes a good MR fluid? In *8th International Conference on Electrorheological (ER) Fluids and Magneto-rheological (MR) Suspensions, Nice*, 2001.

[19] RC Bell, JO Karli, AN Vavreck, DT Zimmerman, GT Ngatu, and NM Wereley. Magnetorheology of submicron diameter iron microwires dispersed in silicone oil. *Smart Mater*, **17**:015028, 2008.

[20] S Genç. *Synthesis and Properties of Magnetorheological (MR) Fluids*. PhD thesis, University of Pittsburgh, USA, 2002.

[21] Q Zhang, X Liu, Y Ren, L Wang, and Y Hu. Effect of particle size on the wear property of magnetorheological fluid. *Advances in Materials Science and Engineering*, **ID 4740986**, 2016.

[22] R Stanway, JL Sproston, MJ Prendergast, JR Case, and CE Wilne. ER fluids in the squeeze-flow mode: an application to vibration isolation. *Journal of Electrostatics*, **28**:89–94, 1992.

[23] T Hong, XP Zhao, and L Shu. Design and performance research of an adaptive damper composed of electrorheological fluids and piezoelectric ceramics. *Smart Materials & Structures*, **12**:347–354, 2003.

[24] GY Zhou and JR Li. Shear properties of a magnetorheological elastomer. *Smart Materials & Structures*, **12**:139–146, 2003.

[25] JD Carlson and MR Jolly. MRF, foam and elastomer devices. *Mechatronics*, **10**:555–569, 2000.

[26] P Blom. *Magneto-sensitive rubber in the audible frequency range*. PhD thesis, Kungliga Tekniska Högskolan, Sweden, 2006.

[27] P Blom and L Kari. Amplitude and frequency dependence of magneto-sensitive rubber in a wide frequency range. *Polymer Testing*, **24**:656–662, 2005.

[28] L Kari and P Blom. Magneto-sensitive rubber in a noise reduction context exploring the potential. *Plastics, Rubber and Composites*, **34**:365–371, 2005.

[29] M Lokander and B Stenberg. Improving the magnetorheological effect in isotropic magnetorheological rubber materials. *Polymer Testing*, **22**: 677–680, 2003.

[30] M Lokander and B Stenberg. Performance of isotropic magnetorheological rubber materials. *Polymer Testing*, **22**:245–251, 2003.

[31] X Guan, X Dong, and J Ou. Magnetostrictive effect of magnetorheological elastomer. *Journal of Magnetism and Magnetic Materials*, **320**:158–163, 2008.

[32] LC Davis. Model of magnetorheological elastomers. *Journal of Applied Physics*, **85**:3348–3351, 1999.

[33] GY Zhou and Q Wang. Study on the adjustable rigidity of magneto rheological-elastomer-based sandwich beams. *Smart Materials & Structures*, **15**:59–74, 2006.

[34] Y Shen, MF Golnaraghi, and GR Heppler. Experimental research and modeling of magnetorheological elastomers. *Journal of Intelligent Material Systems and Structures*, **15**:27–35, 2004.

[35] SV Kankanala and N Triantafyllidis. On finitely strained magnetorheological elastomers. *Journal of the Mechanics and Physics of Solids*, **52**: 2869–2908, 2004.

[36] A Dorfmann and RW Ogden. Magnetoelastic modelling of elastomers. *European Journal of Mechanics A - Solids*, **22**:497–507, 2003.

[37] A Dorfmann and RW Ogden. Nonlinear magnetoelastic deformations. *Quarterly Journal of Mechanics and Applied Mathematics*, **57**:599–622, 2004.

[38] IA Brigadnov and A Dorfmann. Mathematical modeling of magneto-sensitive elastomers. *International Journal of Solids and Structures*, **40**: 4659–4674, 2003.

[39] H See, R Sakurai, T Saito, S Asai, and M Sumita. Relationship between electric current and matrix modulus in electrorheological elastomers. *Journal of Electrostatics*, **50**:303–312, 2001.

[40] P Ludeelerd, S Niamlang, R Kunaruksapong, and A Sirivat. Effect of elastomer matrix type on electromechanical response of conductive polypyrrole/elastomer blends. *Journal of Physics and Chemistry of Solids*, **71**: 1243–1250, 2010.

[41] AN Gent, S Kawahara, and J Zhao. Crystallisation and strength of natural rubber and synthetic *cis*-1,4-polyisoprene. *Rubber Chemistry and Technology*, **71**:668–678, 1998.

[42] T Puvanatvattana, D Chotpattananont, P Hiamtup, S Niamlang, A Sirivat, and AM Jamieson. Electric field induced stress moduli in polythiophene/polyisoprene elastomer blends. *Reactive & Functional Polymers*, **66**:1575–1588, 2006.

[43] B Liu, SA Boggs, and MT Shaw. Electrorheological properties of anisotropically filled elastomers. *IEEE Transactions on Dielectrics and Electrical Insulation*, **8**:173–181, 2001.

[44] T Shiga, A Okada, and T Kurauchi. Electroviscoelastic effect of polymer blends consisting of silicone elastomer and semiconducting polymer particles. *Macromolecules*, **26**:6958–6963, 1993.

[45] Lord Rayleigh. The theory of the Helmholtz resonator. *Proceedings of the Royal Society of London Series A*, **92**:265–275, 1916.

[46] A Geisberger, A Khajepour, and F Golnaraghi. Non-linear modelling of hydraulic mounts: Theory and experiment. *Journal of Sound and Vibration*, **249**:371–397, 2002.

[47] SJ Gau and JD Cotton. Experimental study and modeling of hydraulic engine mount system. Technical report, SAE Technical Paper Series 951348, 1995.

[48] M Bernuchon. A new generation of engine mounts. Technical report, SAE Technical Paper Series 840259, 1984.

[49] PE Corcoran and GH Ticks. Hydraulic engine mount characteristics. Technical report, SAE Technical Paper Series 840407, 1984.

[50] K Kadomatsu. Hydraulic engine mount for shock isolation at acceleration on the FWD cars. Technical report, SAE Technical Paper Series 891138, 1989.

[51] FY Yi and MZ Xie. Objective evaluation of engine mounting isolation. *AASRI Procedia*, **3**:49–53, 2012.

[52] RM Brach and AG Haddow. On the dynamic response of hydraulic engine mounts. Technical report, SAE Technical Paper Series 931321, 1993.

[53] YH Yu, NG Naganathan, and RV Dukkipati. A literature review of automotive vehicle engine mounting systems. *Mechanism and Machine Theory*, **36**:123–142, 2001.

[54] J Christopherson and GN Jazar. Dynamic behavior comparison of passive hydraulic engine mounts. Part 1: Mathematical analysis. *Journal of Sound and Vibration*, **290**:1040–1070, 2006.

[55] T Ushijima, K Takano, and H Kojima. High performance hydraulic mount for improving vehicle noise and vibration. Technical report, SAE Technical Paper Series 880073, 1988.

[56] KH Lee, YT Choi, and SP Hong. Performance design of hydraulic mount for low frequency engine vibration and noise control. Technical report, SAE Technical Paper Series 941777, 1994.

[57] R Singh, G Kim, and PV Ravindra. Linear analysis of automotive hydro-mechanical mount with emphasis on decoupler characteristics. *Journal of Sound and Vibration*, **158**:219–243, 1992.

[58] G Kim. *Study of passive and adaptive hydraulic engine mounts*. PhD thesis, Ohio State University, USA, 1992.

[59] M Clark. Hydraulic engine mount isolation. Technical report, SAE Technical Paper Series 851650, 1985.

[60] TJ Royston and R Singh. Periodic response of nonlinear engine mounting systems. Technical report, SAE Technical Paper Series 951297, 1995.

[61] K Seto, K Sawatari, A Nagamatsu, M Ishurama, and K Dol. Optimum design method for hydraulic engine mounts. Technical report, SAE Technical Paper Series 911055, 1991.

[62] H Yarmohamadi and V Berbyuk. Computational model of conventional engine mounts for commercial vehicles: validation and application. *Vehicle System Dynamics*, **49**:761–787, 2011.

[63] WC Flower. Understanding hydraulic mounts for improved vehicle noise, vibration and ride qualities. Technical report, SAE Technical Paper Series 850975, 1985.

[64] Q. Li, J-C Zhao, B. Zhao, and X-S Zhu. Parameter optimization of a hydraulic engine mount based on a genetic neural network. *Proceedings Of The Institution Of Mechanical Engineers Part D-Journal Of Automobile Engineering*, **223**:1109–1117, 2009.

[65] J. Marzbanrad and A. Jamali. Design of ANFIS networks using hybrid genetic and SVD methods for modeling and prediction of rubber engine mount stiffness. *International Journal of Automotive Technology*, **10**: 167–174, 2009.

[66] J-H Lee, M-S Bae, and K-J Kim. Limitations of mechanical model with a lumped mass in representing dynamic characteristics of hydraulic mount. Technical report, SAE Technical Paper Series 2003-01-1466, 2003.

[67] L-R Wang, Z-H Lu, and H Ichiro. An elementary simulation of vibration isolation characteristics of hydraulically damped rubber mount of car engine. Technical report, SAE Technical Paper Series 2001-01-1453, 2001.

[68] H Adiguna, M Tiwari, R Singh, HE Tseng, and D Hrovat. Transient response of a hydraulic engine mount. *Journal of Sound and Vibration*, **268**:217–248, 2003.

[69] JH Lee and KH Kim. An efficient technique for design of hydraulic engine mount via, design, variable-embedded damping modeling. *Journal of Vibration and Acoustics - Transactions of the ASME*, **127**:93–99, 2005.

[70] LR Wang, JC Wang, and I Hagiwara. An integrated characteristic simulation method for hydraulically damped rubber mount of vehicle engine. *Journal of Sound and Vibration*, **286**:673–696, 2005.

[71] WB Shangguan and ZH Lu. Experimental study and simulation of a hydraulic engine mount with fully coupled fluid-structure interaction finite element analysis model. *Computers & Structures*, **82**:1751–1771, 2004.

[72] WB Shangguan and ZH Lu. Modelling of a hydraulic engine mount with fluid-structure interaction finite element analysis. *Journal of Sound and Vibration*, **275**:193–221, 2004.

[73] YQ Zhang and WB Shangguan. A novel approach for lower frequency performance design of hydraulic engine mounts. *Computers & Structures*, **84**:572–584, 2006.

[74] LR Wang, JC Wang, ZH Lu, and I. Hagiwara. Finite element-based parameter estimations for a characteristic simulation model of a hydraulically damped rubber mount for vehicle engines. *Proceedings of the Institution of Mechanical Engineers Part D - Journal of Automobile Engineering*, **221**:1273–1286, 2007.

[75] YK Ahn, YC Kim, BS Yang, M Ahmadian, KK Ahn, and S Morishita. Optimal design of an engine mount using an enhanced genetic algorithm with simplex method. *Vehicle System Dynamics*, **43**:57–81, 2005.

[76] J Christopherson and GN Jazar. Dynamic behavior comparison of passive hydraulic engine mounts. Part 2: Finite element analysis. *Journal of Sound and Vibration*, **290**:1071–1090, 2006.

[77] S He and R Singh. Approximate step response of a nonlinear hydraulic mount using a simplified linear model. *Journal of Sound and Vibration*, **299**:656–663, 2007.

[78] JE Colgate, CT Chang, YC Chiou, WK Liu, and LM Keer. Modeling of a hydraulic engine mount focusing on response to sinusoidal and composite excitations. *Journal of Sound and Vibration*, **184**:503–528, 1995.

[79] AR Ohadi and G Maghsoodi. Simulation of engine vibration on nonlinear hydraulic engine mounts. *Journal of Vibration and Acoustics - Transactions of the ASME*, **129**:417–424, 2007.

[80] T Ushijima and T Dan. Nonlinear BBA for predicting vibration of vehicle with hydraulic engine mount. Technical report, SAE Technical Paper Series 860550, 1986.

[81] MF Golnaraghi and GN Jazar. Development and analysis of a simplified nonlinear model of a hydraulic engine mount. *Journal of Vibration and Control*, **7**:495–526, 2001.

[82] PA Baillio. True sharp edge orifices. Technical report, Bird Precision Data Sheet, 2003.

[83] S He and R Singh. Discontinuous compliance nonlinearities in the hydraulic engine mount. *Journal of Sound and Vibration*, **307**:545–563, 2007.

[84] LR Wang, ZH Lu, and I Hagiwara. Analytical analysis approach to nonlinear dynamic characteristics of hydraulically damped rubber mount for vehicle engine. *Nonlinear Dynamics*, **61**:251–264, 2010.

[85] G Kim and R Singh. Nonlinear-analysis of automotive hydraulic engine mount. *Journal of Dynamic Systems Measurement and Control-Transactions of the ASME*, **115**:482–487, 1993.

[86] JH Lee and R Singh. Critical analysis of analogous mechanical models used to describe hydraulic engine mounts. *Journal of Sound and Vibration*, **311**:1457–1464, 2008.

[87] JH Lee and R Singh. Nonlinear frequency responses of quarter vehicle models with amplitude-sensitive engine mounts. *Journal of Sound and Vibration*, **313**:784–805, 2008.

[88] JH Lee and R Singh. Existence of super-harmonies in quarter-vehicle system responses with nonlinear inertia hydraulic track mount given sinusoidal force excitation. *Journal of Sound and Vibration*, **313**:367–374, 2008.

[89] MS Foumani, A Khajepour, and M Durali. Application of sensitivity analysis to the development of high performance adaptive hydraulic engine mounts. *Vehicle System Dynamics*, **39**:257–278, 2003.

[90] G Kim and R Singh. A study of passive and adaptive hydraulic engine mount systems with emphasis on nonlinear characteristics. *Journal of Sound and Vibration*, **179**:427–453, 1995.

[91] TQ Truong and KK Ahn. A new type of semi-active hydraulic engine mount using controllable area of inertia track. *Journal of Sound and Vibration*, **329**:247–260, 2010.

[92] SR Hong, SB Choi, and MS Han. Vibration control of a frame structure using electro-rheological fluid mounts. *International Journal of Mechanical Sciences*, **44**:2027–2045, 2002.

[93] TG Duclos. Design devices using electrorheological fluids. Technical report, SAE Technical Paper Series 881134, 1988.

[94] S Morishita and J Mitsui. An electronically controlled mount using electro-rheological fluid. Technical report, SAE Technical Paper Series 922290, 1992.

[95] EW Williams, SG Rigby, JL Sproston, and R Stanway. Electrorheological fluids applied to an automotive engine mount. *Journal of Non-Newtonian Fluid Mechanics*, **47**:221–238, 1993.

[96] SB Choi and YT Choi. Sliding mode control of a shear-mode type ER engine mount. *KSME International Journal*, **13**:26–33, 1999.

[97] SB Choi and HJ Song. Vibration control of a passenger vehicle utilizing a semi-active ER engine mount. *Vehicle System Dynamics*, **37**:193–216, 2002.

[98] SB Choi, YT Choi, CC Cheong, and YS Jeon. Performance evaluation of a mixed mode ER engine mount via hardware-in-the-loop simulation. *Journal of Intelligent Material Systems and Structures*, **10**:671–677, 1999.

[99] SR Hong, SB Choi, WJ Jung, IB Ham, and DK Kim. Vibration control of an ER mount subjected to high static loads. *Journal of Sound and Vibration*, **242**:740–748, 2001.

[100] WB Jeong, WS Yoo, and WJ Jung. Vibration and noise control of structural systems using squeeze mode ER mounts. *KSME International Journal*, **17**:1949–1960, 2003.

[101] WJ Jung, WB Jeong, SR Hong, and SB Choi. Vibration control of a flexible beam structure using squeeze-mode ER mount. *Journal of Sound and Vibration*, **273**:185–199, 2004.

[102] SR Hong, SB Choi, and DY Lee. Comparison of vibration control performance between flow and squeeze mode ER mounts: Experimental work. *Journal of Sound and Vibration*, **291**:740–748, 2006.

[103] PL Graf and R Shoureshi. Modeling and implementation of semi-active hydraulic engine mounts. *Journal of Dynamic Systems, Measurement, and Control*, **110**:422–429, 1988.

[104] T Ushijima, K Takano, and T Noguchi. Rheological characteristics of ER fluids and their application to anti-vibration devices with control mechanism for automobiles. Technical report, SAE Technical Paper Series 881787, 1988.

[105] NK Petek, RI Goudie, and FR Boyle. Actively controlled damping in electro-rheological fluid-filled engine mounts. Technical report, SAE Technical Paper Series 881785, 1988.

[106] YK Ahn, M Ahmadian, and S Morishita. On the design and development of a magneto-rheological mount. *Vehicle System Dynamics*, **32**:199–216, 1999.

[107] M Brigley, YT Choi, NM Wereley, and SB Choi. Magnetorheological isolators using multiple fluid modes. *Journal of Intelligent Material Systems and Structures*, **18**:1143–1148, 2007.

[108] D York, XJ Wang, and F Gordaninejad. A new MR fluid-elastomer vibration isolator. *Journal of Intelligent Material Systems and Structures*, **18**:1221–1225, 2007.

[109] SB Choi, SR Hong, KG Sung, and JW Sohn. Optimal control of structural vibrations using a mixed-mode magnetorheological fluid mount. *International Journal of Mechanical Sciences*, **50**:559–568, 2008.

[110] C Ciocanel, T Nguyen, and M Elahinia. Design and modeling of a mixed mode magnetorheological (MR) fluid mount. In M Ahmadian, (Ed), *Active and Passive Smart Structures and Integrated Systems 2008*, volume 6928 of *Proceedings of the Society of Photo-Optical Instrumentation Engineers (SPIE)*, 2008.

[111] DE Barber and JD Carlson. Performance characteristics of prototype MR engine mounts containing LORD glycol MR fluids. *Journal of Physics: Conference Series*, **149**:012035, 2009.

[112] QH Nguyen, SB Choi, YS Lee, and MS Han. Optimal design of high damping force engine mount featuring MR valve structure with both annular and radial flow paths. *Smart Materials & Structures*, **22**:115024, 2013.

[113] K Doi. *Electrorheopectic fluid filled vibration damping mount for use with automotive engines and the like*, US Patent, US5088699, 1992.

[114] V Härtel. *Active two-chamber engine mount with hydraulic damping*, US Patent, US4759534, 1988.

[115] V Härtel. *Active two-chamber engine mount*, US Patent, US4757981, 1988.

[116] M Ahmadian and YK Ahn. Performance analysis of magneto-rheological mounts. *Journal of Intelligent Material Systems and Structures*, **10**: 248–256, 1999.

[117] EJ Breitbach and T Grützmacher. *Engine mount, particularly for a propeller-driven aircraft, comprising a tubular frame structure*, US Patent, US6123293, 2000.

[118] PJ Jones and MW Downing. *Adaptive fluid mount*, US Patent, US5197692, 1993.

[119] R Tikani, N Vahdati, and S Ziaei-Rad. Two-mode operation engine mount design for automotive applications. *Shock and Vibration*, **19**(6):1267–1280, 2012.

[120] M Wang, GF Yao, JZ Zhao, and M Qin. A novel design of semi-active hydraulic mount with wide-band tunable notch frequency. *Journal of Sound and Vibration*, **333**:2196–2211, 2014.

[121] B Barszcz, JT Dreyer, and R Singh. Experimental study of hydraulic engine mounts using multiple inertia tracks and orifices: Narrow and broad band tuning concepts. *Journal of Sound and Vibration*, **331**:5209–5223, 2012.

[122] N Vahdati. Double-notch single-pumper fluid mounts. *Journal of Sound and Vibration*, **285**:697–710, 2005.

[123] R Tikani, S Ziaei-Rad, and N Vahdati. Effective reduction of stiffness at peak frequency in hydraulic engine mounts by using magneto-rheological fluids. *Journal of Vibroengineering*, **14**:866–879, 2012.

[124] JH Koo and M Ahmadian. Qualitative analysis of magneto-rheological tuned vibration absorbers: Experimental approach. *Journal of Intelligent Material Systems and Structures*, **18**:1137–1132, 2007.

[125] B Widrow, JR Glover, JM McCool, J Kaunitz, CS Williams, RH Hearn, JR Zeidler, E Dong, and RC Goodlin. Adaptive noise cancelling: Principles and applications. *Proceedings of the IEEE*, **63**:1692–1975, 1975.

[126] SJ Elliot. *Signal Processing for Active Control*. Academic Press, London, 2001.

[127] AJ Hills, AJL Harrison, and DP Stoten. A comparison of two adaptive algorithms for the control of active engine mounts. *Journal of Sound and Vibration*, **286**:37–54, 2005.

[128] DP Stoten and SA Neild. The error-based minimal control sythesis algorithm with integral action. *Proceedings of the Institution of Mechanical Engineers Part I-Journal of Systems and Control Engineering*, **217**:187–201, 2003.

[129] C Olsson. Active automotive engine vibration isolation using feedback control. *Journal of Sound and Vibration*, **294**:162–176, 2006.

[130] BH Lee and CW Lee. Model based feed-forward control of electromagnetic type active control engine-mount system. *Journal of Sound and Vibration*, **323**:574–593, 2009.

[131] JE Huber, NA Fleck, and MF Ashby. The selection of mechanical actuators based on performance indices. *Proceedings of the Royal Society of London A: Mathematical, Physical and Engineering Sciences*, **453**: 2185–2205, 1997.

[132] BP Trease and S Kota. A survey and comparison of smart material linear actuators, 2001 (Accessed 17/05/2017). URL `www-personal.umich.edu/~btrease/share/Trease_Actuator_Report.pdf`.

[133] C Togashi and M Nakano. *Hydraulic active engine mount*, Japanese Patent, JP2001280409, 2001.

[134] C Togashi and M Nakano. *Hydraulic active mount*, Japanese Patent, JP2001280408, 2001.

[135] C Togashi and M Nakano. *Active mount device for engine*, Japanese Patent, JP2001187534, 2001.

[136] C Togashi, H Ozawa, and M Nakano. *Engine Mount*, Japanese Patent, JP2001153176, 2001.

[137] M Gugsch. *Active vibration absorber*, US Patent, US5718418, 1998.

[138] LR Miller, M Ahmadian, CM Nobles, and DA Swanson. Modeling and performance of an experimental active vibration isolator. *Journal of Vibration and Acoustics - Transactions of the ASME*, **117**:272–278, 1995.

[139] Y Nakaji, S Satoh, T Kimura, T Hamabe, Y Akatsu, and H Kawazoe. Development of an active control engine mount system. *Vehicle System Dynamics*, **32**:185–198, 1999.

[140] YW Lee and CW Lee. Dynamic analysis and control of an active engine mount system. *Proceedings of the Institution of Mechanical Engineers Part D - Journal of Automobile Engineering*, **216**:921–931, 2002.

[141] H Ichikawa, A Muramatsu, and Y Takayoshi. *Vibration controller for active vibration insulators and method for controlling vibrations for the same*, US Patent, US2005228574, 2005.

[142] K Okumura and K Kato. *Active fluid inclusion type engine mount*, Japanese Patent, JP2005239084, 2005.

[143] A Saito. *Active liquid-sealed vibration damper*, Japanese Patent, JP2004251389, 2004.

[144] M Gugsch, R Langof, and P Indlekofer. *Active elastic mount*, US Patent, US5452884, 1995.

[145] H Mansour, S Arzanpour, and F Golnaraghi. Design of a solenoid valve based active engine mount. *Journal of Vibration and Control*, **18**:1221–1232, 2012.

[146] AM Hosseini, S Arzanpour, F Golnaraghi, and AM Parameswaran. Solenoid actuator design and modeling with application in engine vibration isolators. *Journal of Vibration and Control*, **19**:1015–1023, 2013.

[147] TA Baudendistel, SG Tewani, MW Long, and JE Dingle. *Vacuum actuated active decoupler mount*, US Patent, US6422545, 2002.

[148] Y Takeda. *Mounting device of internal combustion engine*, Japanese Patent, JP2000255277, 2000.

[149] H Yamazoe and F Murakami. *Electronically controlled engine mount device*, Japanese Patent, JP2003214484, 2003.

[150] H Kojima. *Vibration-proofing device*, Japanese Patent, JP2001221287, 2001.

[151] WE Gossman and MJ Burke. *Dual chambered, active vibration damper with reactive force producing pistons*, US Patent, US5332203, 1994.

[152] Y Hagino, K Goto, and T Suzuki. *Fluid-filled active elastic engine mount*, US Patent, US6527262, 2001.

[153] V Härtel. *Active hydraulically damped engine mount*, European Patent, EP0464599, 1992.

[154] V Härtel, M Richter, M Stoppert, and M Gugsch. *Active hydraulically damped engine mount*, European Patent, EP0464597, 1992.

[155] J Tobias. *Vibration isolation support mounting system*, US Patent, US5101929, 1992.

[156] J Tobias. *Vibration isolation supsupport mounting system*, US Patent, US5310017, 1994.

[157] L Sui, X Xiong, and GC Shi. Piezoelectric actuator design and application on active vibration control. *Physics Procedia*, **25**:1388–1396, 2012.

[158] J Jeon, YM Han, DY Lee, and SB Choi. Vibration control of the engine body of a vehicle utilizing the magnetorheological roll mount and the piezostack right-hand mount. *Proceedings of the Institution of Mechanical Engineers Part D - Journal of Automobile Engineering*, **227**:1562–1577, 2013.

[159] DY Lee, YK Park, SB Choi, and HG Lee. Design and vibration control of vehicle engine mount activated by MR fluid and piezoelectric actuator. In *Proceedings of the SPIE - The International Society for Optical Engineering*, volume 7493, 2009.

[160] TD Gillespie. *Fundamentals of vehicle dynamics*. Society of Automotive Engineers, Inc., 1992.

[161] KD Marshall. Tire noise and vibration. In AN Gent and JD Walter(Eds), *The Pneumatic Tire*, chapter 9, pages 364–407. NHTSA, 2006.

[162] W Weaver, SP Timoshenko, and DH Young. *Vibration Problems in Engineering*. Wiley and Sons, Inc, 5th edition Edition, 1990.

[163] NW Tschoegl. *The Phenomenological Theory of Linear Viscoelastic Behavior. An Introduction*, chapter 8. Interconversion of the linear viscoelastic functions, pages 430–431. Springer-Verlag, Berlin, 1989.

[164] Gough J. Section 3.9: Dynamic behaviour. In *Engineering Design with Rubber*, page 15. Tun Abdul Razak Research Centre, Hertford, 2015.

[165] HR Ahmadi and AH Muhr. Modelling dynamic properties of filled rubber. *Plastics, Rubber and Composites: Processing and Applications*, **26**:452–461, 1997.

[166] J Kennedy and R Eberhart. Particle swarm optimisation. In *Proceeedings of the IEEE International Conference on Neural Networks*, Perth, Australia, 1995.

[167] Implementation of Particle Swarm Optimisation (PSO) in MATLAB, March 2017. URL `www.yarpiz.com/50/ypea102-particle-swarm-optimisation`.

[168] J Gough. *Inflation of rubber sheet*. TARRC Internal Laboratory Report, December 2000.

[169] RS Rivlin. Large elastic deformations of isotropic materials Part 1. Fundamental concepts. *Philosophical Transactions of the Royal Society of London, Series A Mathematical and Physical Sciences*, **240**:459–490, 1948.

[170] LRG Treloar. *The Physics of Rubber Elasticity*. Oxford University Press, Oxford, Third Edition, 1975.